Multinuclear Cobalt Schiff Base Complexes and their Activity Towards the Oxygen Reduction Reaction

A thesis submitted to the University of East Anglia

For the degree of Doctor of Philosophy

Submitted September 2022

Charles Andrew James

This thesis is dedicated to my Father,

Andrew Paul Milton

My Grandmother,

Marie Swain

And my Friend,

Hannah Lucy Eke

Acknowledgements

Firstly, I would like to thank my supervisor Dr. John Fielden for his guidance, patience, and friendship over the past four years. You have had a unique ability to inspire me with new ideas over the course of this work, while keeping me grounded and on track throughout.

I would also like to thank Dr. Joseph Wright for his support throughout this work. You always listened to my extended ramblings about my chemistry, despite the fact you only came into the office to make a cup of tea.

I am grateful to Tom Foster, whose generous donation funded this research, thank you for your support and interest.

To my colleagues, particularly my good friend Bethany Hood, thank you for being there for me. Undertaking this research has been immeasurably easier with you to consult, brainstorm, and often rage about complex chemistry problems when things weren’t going to plan.

To my family, it has been your belief and support in my chosen path that has put me where I am today You made me realise that I had the ability to pursue my interests in science, despite my consistently terrible report cards and test results during my school years. Thank you for making me who I am.

To the best group of friends anyone could hope for, Alistair, Charlotte, Moss, Sam, Jordan, Ieva and James; Each one of you has reassured me through difficult times, and celebrated with me through the good times, and distracted me (usually with beer, games and importantly, chess) when I simply needed to not think about this work for an evening. Thank you all. Order!

Finally, to Jess, you have been the only constant in my life over the course of this work. I don’t know how I would have gotten through this without you, your reassurance, love and warmth through tough times has kept me motivated, positive and most importantly, happy throughout these years. This work is as much yours as it is mine.

Abstract

The cathodic oxygen reduction reaction (ORR) remains to be the most challenging aspect of hydrogen fuel cell (HFC) research. The ORR is a sluggish, multi-electron process which currently uses large loadings of platinum to achieve required current densities. With the high cost and low availability of platinum, much effort has been directed towards developing non-precious metal catalysts for the ORR. While good progress has been made, heterogeneous precious metal-free catalysts often show poor selectivity to the four-electron ORR to water, and commonly generate hydrogen peroxide as a by-product which can damage the sensitive fuel cell components. Understanding the mechanism of heterogeneous catalysts can be difficult and as such manipulating the selectivity of the ORR for these systems can be challenging. Studying the ORR for homogeneous molecular catalysts can allow for closer examination of the specific mechanism of the ORR, and make it possible to determine factors which contribute to generation of the two ORR pathways.

In this work, a dinuclear cobalt complex bearing a new heptadentate Schiff base ligand was designed with the intention of influencing the system towards four-electron pathway selectivity. In addition, the catalyst design was inspired by known Co^{II}salen complexes' ability to reach low overpotentials whilst retaining their catalytic activity.

The catalytic activity of the new complexes was determined spectrophotometrically by the use of a homogeneous chemical reductant, and selectivity was determined by iodometric titration. Overpotentials were estimated by cyclic voltammetry and assessing the standard potential of the ORR pathways using previously established thermodynamic data.

Remarkably, it was found that the selectivity of the ORR catalysed by these complexes was dependent on the identity of the proton source used, where high four-electron pathway selectivity was observed when the proton source was a carboxylic acid. When the non-coordinating NH_4PF_6 was used, almost quantitative selectivity towards the two-electron pathway was observed. The selectivity was also determined to be a result of the identity of the conjugate base, rather than the strength of the Brønsted acid. To the best of our knowledge, such an anion-based selectivity dependence has not yet been observed for the ORR and presents a new consideration when developing catalysts for the ORR.

Access Condition and Agreement

Each deposit in UEA Digital Repository is protected by copyright and other intellectual property rights, and duplication or sale of all or part of any of the Data Collections is not permitted, except that material may be duplicated by you for your research use or for educational purposes in electronic or print form. You must obtain permission from the copyright holder, usually the author, for any other use. Exceptions only apply where a deposit may be explicitly provided under a stated licence, such as a Creative Commons licence or Open Government licence.

Electronic or print copies may not be offered, whether for sale or otherwise to anyone, unless explicitly stated under a Creative Commons or Open Government license. Unauthorised reproduction, editing or reformatting for resale purposes is explicitly prohibited (except where approved by the copyright holder themselves) and UEA reserves the right to take immediate ‘take down’ action on behalf of the copyright and/or rights holder if this Access condition of the UEA Digital Repository is breached. Any material in this database has been supplied on the understanding that it is copyright material and that no quotation from the material may be published without proper acknowledgement.

List of Abbreviations

AcOH	Acetic acid
B.M.	Bohr Magneton
BFPP	1,3-bis(2-formylphenoxy)-2-propanol
bpy	Bipyridyl
CCO	Cytochrome C oxidase
Cp	Cyclopentadienyl
Cp*	Pentamethylcyclopentadineyl
CV	Cyclic voltammetry
DCM	Dichloromethane
DFT	Density functional theory
DMF	*N*,*N*-dimethylformamide
DMSO	dimethylsulfoxide
DTBC	Di-*tert*-butylcatechol
DTBQ	Di-*tert*-butylquinone
E	Reduction potential
E^0	Standard reduction potential
EtOH	Ethanol
EU	European Union
EV	Electric vehicle
f	Frequency
F	Faraday's constant/spectrometer frequency
GHG	Greenhouse gas
GW	Gigawatt
HER	Hydrogen evolution reaction
HFC	Hydrogen fuel cell
HOR	Hydrogen oxidation reaction
HT-PEMFC	High-temperature polymer electrolyte membrane fuel cell
IR	Infrared

J	Manetic exchange interaction
L	Orbital angular momentum
MCFC	Molten carbonate fuel cell
Me	Methyl
MEA	Membrane electrode assembly
MeCN	Acetonitrile
MeOH	Methanol
NMR	Nuclear magnetic resonance spectroscopy
NZHF	Net-zero hydrogen Fund
OAc	Acetate
ORR	Oxygen reduction reaction
OTf	trifluoromethylsulfonate
PAFC	Phosphoric acid fuel cell
PCET	Proton coupled electron transfer
PEMFC	Polymer electrolyte membrane fuel cell
PhCN	Benzonitrile
PSII	Photosystem II
PV	Photovoltaic
S	Spin quantum number
s	Spin
SMM	single molecule magnet
SOFC	Solid oxide fuel cell
tAm	*tert*-amyl
TBA	tetrabutylammonium
TBAOAc	tetrabutylammonium acetate
tBu	*tert*-butyl
TFA	Trifluoroacetic acid
TLC	Thin layer chromatography
TOF	Turn over frequency
TON	Turn over number
Tyr	Tyrosinyl

VO	Vanadyl
WOC	Water oxidation catalyst
WOR	Water oxidation reaction
Xm	Molar magnetic susceptibiliy
XRD	X-ray diffractometry
μ	magnetic moment

Contents

Chapter 1
Introduction to Hydrogen Fuel and Oxygen Reduction

1.1 The Global Climate Crisis

It is now common knowledge among the general population that global warming triggered by emissions of greenhouse gases (GHGs) poses an extreme and very real threat to the way we live over the next century. The average global temperature has risen steadily by 0.08 ^oC per decade since 1880 following the start of the industrial revolution. In recent times, this value has more than doubled to 0.18 ^oC per decade since 1981.[1] Overall, the global average temperature currently is 1 ^oC higher than the 20th century average. Climate scientists suggest that to avoid catastrophic and irreversible changes to the global ecosystems, sea levels and extreme weather events, the global average temperature rise should remain below 2 ^oC and ideally below 1.5 ^oC.[2,3]

The main contributor to GHG emissions is CO_2 derived from the burning of fossil fuels. In response to this global threat, G20 members have pledged to reduce GHG emissions with the Paris Climate Agreement.[4,5] The UK has pledged to reduce GHG emissions by at least 68% compared to the 1990 levels by 2030, and the USA has pledged to reduce its GHG emissions by 50% compared to its 2005 levels by 2030. In order to achieve these lofty goals, a paradigm shift in the way that we produce, store and use energy is necessary. Energy derived from renewable sources such as solar or wind power is the most promising alternative to the burning of fossil fuels. In 2020 in the UK, wind power accounted for 21% of the total energy production, an almost ten-fold increase from its value of 2.7% in 2010. Solar energy production in the UK is lower than wind, accounting for only 1.65% of the total energy production in 2020, however this value is growing much more rapidly than wind where <0.01% of grid energy in 2010 came from solar power. Global solar energy capacity has increased drastically over the past decade from 40 GW in 2010 to 710 GW in 2020 and the global proportion of energy produced from solar sources has increased from 0.06% in 2010 to 1.36% in 2020.[6]

Despite these advances in renewable energy capacity and generation, alongside the decreasing cost per watt of renewable energy where large scale photovoltaic (PV) electricity generation is now the cheapest energy generation method and can cost as low cost as $0.70 USD per watt,[7] a major roadblock in the widespread use of these renewable sources is the storage of the generated power. Currently, the grid is supplied with energy in accordance with demand, if the demand for energy increases, more fuel is burned to meet that demand. However, with wind and solar power, response to an increased demand is more difficult to facilitate due to the inconsistent patterns of wind strength in particular regions and sunlight exposure to PV panels. To mitigate the problems with inconsistent power generation from renewable and carbon-free sources, many energy storage solutions have been investigated in which inconsistently produced energy is stored, either mechanically or in the form of a photoelectro, or electrogenerated fuel. The most widely explored of these fuels is hydrogen, the production of which from large scale PV energy can now cost less than methane reformation.[8]

In the UK and EU, there has been a considerable drive to increase the production and use of renewable, low carbon fuels. Aside from the clear and significant environmental benefits of using low carbon fuels, there are also geopolitical benefits associated with a centralised production of green fuels within the UK and EU.[9] The fallout of the COVID-19 pandemic has clearly shown that reliance on fossil fuel imports during times of economic uncertainty can destabilise fuel supply chains and costs to the consumer.[10,11] In addition, the invasion of Ukraine has resulted in a global disruption in fossil fuel supplies due to volatile trade relationships with Russia.[12] The EU in particular is experiencing a dilemma where the Union is strongly opposed to Russia's actions, but relies on their vast natural resource supply to provide 45% of their natural gas imports. It is for this reason that the EU has developed the REPowerEU centralised power strategy.[13] REPowerEU has set aside €210 billion to develop renewable fuels to end reliance on Russian exports by 2027. In the UK, a target has been set to facilitate the production of 10 GW of electrolytic hydrogen by 2030, achieved by significant funding into low carbon water electrolysis through the net-zero hydrogen fund (NZHF).[14]

1.1.1 Hydrogen as a Green Fuel and Polymer Electrolyte Membrane Fuel Cells

Hydrogen gas has an extraordinarily high gravimetric energy density of 120 $MJ\cdot kg^{-1}$, much greater than that of diesel or liquid petroleum (40 and 45 $MJ\cdot kg^{-1}$) and as such is an attractive fuel.[15,16] However, since H_2 is a gas at atmospheric pressure, its volumetric energy density is orders of magnitude lower than that of liquid fossil fuels.[17] When stored cryogenically in its liquid state however, the energy density of H_2 is brought much closer to that of liquid fossil fuels.[18] Energy can be extracted from hydrogen by burning with O_2 to directly generate heat, or by electrochemical oxidation of H_2 to release the electrons from the protons. The former of these processes is now being implemented in home heating systems as a green alternative to natural gas where hydrogen ready boilers where by 2025. Many boilers will burn a 20:80 blend of H_2 and natural gas. By 2035, it is expected that a transition to 100% hydrogen will be used on the gas grid.[19] Electrochemical extraction of the energy from hydrogen in the form of a hydrogen fuel cell (HFC) is both more well-known and more efficient. The efficiency of an internal combustion engine is normally around 30%, while HFCs can achieve efficiencies of up to 60%. However, implementation of hydrogen fuel cells into everyday, general public use poses many infrastructure and technological challenges.

The widespread use of HFCs is limited by several factors. In order to understand these issues, it is important to understand the fundamental concepts of a HFC, more specifically, the simplest and most widely researched HFC - the polymer electrolyte membrane fuel cell (PEMFC). Firstly, the oxidation of H_2 into its constituent $2H^+$ and $2e^-$ is performed at the anode. This oxidation process requires efficient catalysis and thus the anode is normally comprised of a high surface area graphitic material impregnated with Pt metal, or alloys containing Pt.[20] Secondly, the liberated H^+ migrates across the proton conductive electrolyte membrane, normally a perfluorinated sulfonate polymer such as Nafion™, to the cathode.[21–23] At the cathode, O_2 from the air is reduced by the electrons from the oxidation of H_2 which migrate as a current across the circuit and combined with the protons to form H_2O as the product.[24] This cathodic reduction process also requires catalysis and is much more sluggish than the H_2 oxidation. As a result, much higher Pt loadings are required at the cathode.[25] This basic PEMFC concept is outlined in Fig 1.1.1

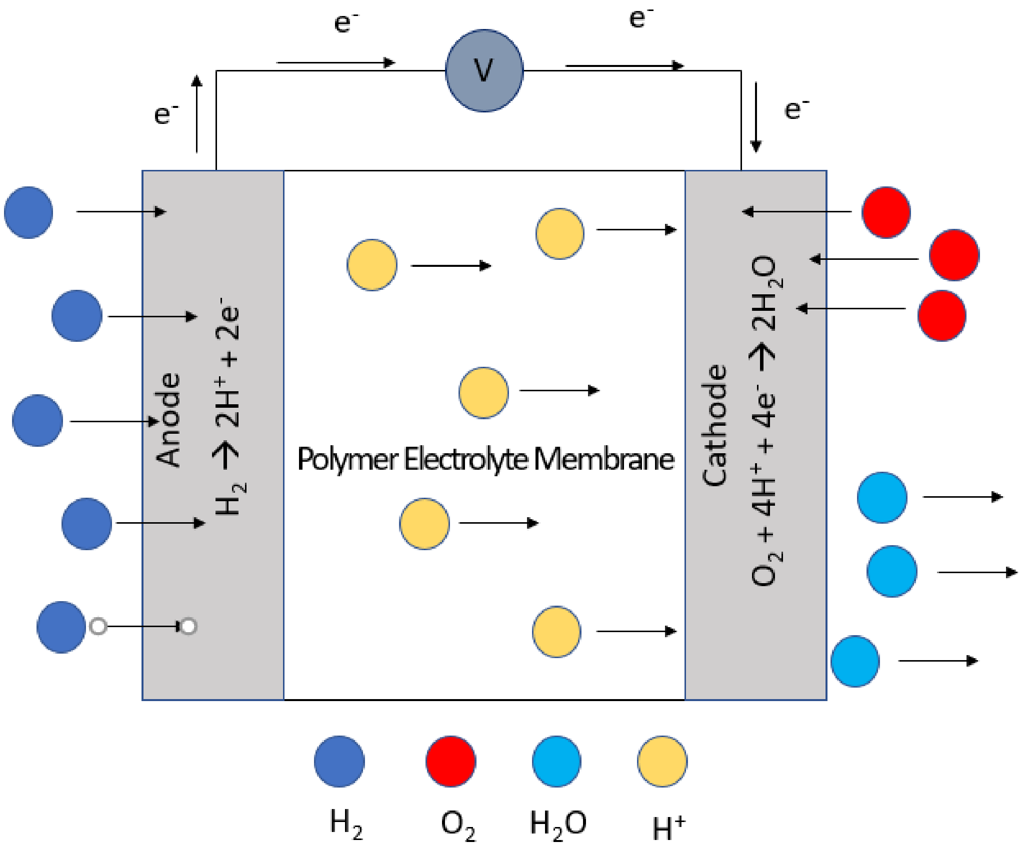

Figure 1.1.1 Schematic representation of the processes involved in a PEMFC

The main issues for the widespread use of PEMFCs in providing power to personal and commercial vehicles include but are not limited to the following:

- GHG emission free production of H_2 gas; safe storage and transport of H_2 gas;[26,27]
- Cost and availability of Pt and other precious metals used in the electrode materials;[28–30] and
- Poisoning of the catalyst materials by common contaminants found in H_2 gas such as CO and MeOH.[31–33]

In addition to these technical issues, there is also market competition with well-established electric vehicles (EVs) which are currently seen as a suitable green alternative to ICE vehicles. While this may be true for personal vehicles, EVs do not have sufficient energy capacity for long range commercial applications such as in trucks, trains, ships or planes. EVs also require long charging times, particularly for long range vehicles which can take hours to charge, whereas hydrogen fuel cells can be refuelled in a matter of minutes.

While all of these issues pose significant challenges to commonplace use of HFCs in vehicles, perhaps the most significant and fundamental challenge posed to chemists is the catalysis of the oxygen reduction reaction (ORR). The ORR is a sluggish multi-electron, multi-proton process and in order to achieve the high thermodynamic efficiency required by a HFC, a catalyst with a very low overpotential is required. Typically, as previously stated, the catalyst for the ORR in a PEMFC is Pt or a Pt containing alloy, but due to the scarcity of Pt metal in Earth's crust, large scale production and use of PEMFCs is unrealistic without developing a catalyst system which does not use precious metals.

1.1.2 Other fuel cell technologies

While PEMFCs are by far the most well-known class of fuel cell due to their relevance to the transport sector, there are other fuel cell systems which may be equally important to a fully decarbonised and circular hydrogen economy. It is important to understand that when developing electrocatalysts to enable the electrochemical use of hydrogen fuels, there are more considerations and options than just the most popular PEMFC. Within the EU, further research into the following fuel cell technologies is particularly important due to the potential restriction of the manufacture and use of perfluorinated alkyl substances. Nafion™ falls into the scope of this restriction, and as a result the production of PEMFCs in the EU may be limited.

Solid Oxide Fuel Cells (SOFCs)[34–36] are a highly efficient class of fuel cell which operate at very high temperatures (>600°C) and use a solid oxide ceramic material as the membrane rather than a polymer electrolyte membrane. The high operating temperature allows oxygen to be reduced directly to O^{2-} at the cathode. O^{2-} then migrates in the ceramic material to the anode where it is combined with oxidised H_2 to form H_2O. SOFCs are particularly attractive as they do not require platinum group metal catalysts and as such are very cost efficient. However, their high operating temperature and large start up times limit their use in personal vehicles. On the other hand, in heavy-duty applications such as air and maritime travel, the weight and heat management of SOFCs becomes less of an issue so they are currently being researched further.

Molten Carbonate Fuel Cells (MCFCs)[37–40] are another class of very high temperature fuel cell. The MCFC operates in a similar way to SOFCs, however at the cathode O_2 is reduced with CO_2 to form CO_3^{2-}. The formed CO_3^{2-} migrates through an electrolyte of molten Na_2CO_3 or K_2CO_3 to the anode where it is combined with oxidised H_2, generating H_2O and CO_2. MCFCs have a unique application in that they can be added to the exhaust stacks of fossil fuel power plants to prepare exhaust CO_2 for capture. The flue gas of fossil fuel plants is only ca. 10% CO_2, MCFCs selectively extract CO_2 from a mixture and regenerates the CO_2 at the anode where it is in high (>90%) concentration which is high enough for carbon capture methods.

Phosphoric Acid Fuel Cells (PAFCs)[41,42] were among the earliest commercial fuel cell technologies used. PAFCs use liquid phosphoric acid suspended in a microporous matrix as the electrolyte rather than a polymer electrolyte. Phosphoric acid is only able to conduct protons at higher temperatures (>150°C) and still require platinum catalysts to facilitate both the HOR and the ORR. While PAFCs are still used in some stationary applications, their corrosive electrolyte and relatively low efficiency has caused them to be replaced by other fuel cell technologies in recent years.

High-Temperature Polymer Electrolyte Membrane Fuel Cells (HT-PEMFCs)[43–45] are a more recent technology and are essentially a hybrid between PEMFCs and PAFCs. HT-PEMFCs use a solid membrane comprising of phosphoric acid doped polybenzimidazole in which protons are conducted by ‘proton hopping’ between protonated and deprotonated nitrogen atoms of imidazole moieties. HT-PEMFCs are of particular interest as they allow the fuel cell to operate at higher temperatures than fuel cells containing Nafion™ as the electrolyte, since protons can be conducted without the need for hydration of the membrane like in Nafion™. The higher temperature of operation means that expensive and heavy cooling systems are not necessary, resulting in higher specific energy and power densities. The weight saving is even effective enough to allow HT-PEMFCs to be used as aircraft propulsion systems, an area where standard PEMFCs have not yet proved technically feasible.[46] HT-PEMFCs have been proposed as a high priority technology on the journey towards a fully decarbonised transport sector. HT-PEMFCs still currently still use platinum catalysts for both the HOR and the ORR, however due to their higher operating temperature, there is a much higher possibility that HT-PEMFCs will be able to use non-precious metal catalysts in the near future. In addition, due to the increased stability of the polybenzimidazole membrane, HT-PEMFCs are more resistant to CO contamination in the fuel gas and H_2O_2 production from the ORR.

1.2 Requirements of Oxygen Reduction Catalysis for Fuel Cells

1.2.1 Overpotential of ORR Catalysts

The overpotential of an electrochemical transformation is defined as additional potential above the thermodynamic potential of a reaction to drive that reaction at a specific rate.[47,48] The standard reduction potential (the reduction potential at standard pressure, temperature and at a pH of 0) of the ORR in aqueous acidic media is +1.23 V, as such, the reduction of oxygen is thermodynamically favourable. However, due to an extremely high kinetic barrier, the overpotential required to drive the ORR is greater than 1.23 V (i.e. the cell uses all of its excess potential to simply overcome activation energy)[49] and thus the ORR does not occur spontaneously without catalysis (i.e. if an inert graphite electrode is used). In the context of a hydrogen fuel cell, the overpotential is related to the output efficiency of the cell (i.e., the useful energy obtained compared to the theoretical maximum). If the oxygen reduction reaction requires a large driving force to overcome the activation energy associated with O-O bond fission, then less of the energy associated with the conversion from O_2 to H_2O can be used as useful work to power the load.[50] It is important to note that the specific equilibrium potential of the ORR is dependent on the specific conditions used. In many cases, a pH of 0 may decompose the catalyst used, and therefore any adjustment to the acidity of the system should be accounted for in the standard potential using the Nernst equation (discussed in detail in Chapter 4). In the context of fuel cells, a low overpotential means that each membrane electrode assembly (MEA, an individual cell of the overall fuel cell stack) is able to provide a high electromotive force, therefore a low overpotential means that fewer MEAs can be used in a fuel cell, reducing the cost and the use of expensive catalysts and membrane materials.

1.2.2 Turnover Frequency

The turnover frequency (TOF) of a catalyst is the kinetic parameter which describes the number of substrate to product transformations performed per equivalent of catalyst per second.[47,51,52] The TOF is intrinsic to the catalyst system, that is to say, that under the same conditions, if two catalysts demonstrate different TOF values, then that difference is related to the catalyst's activity, rather than external influences.[53] While a TOF can technically be determined under any reaction conditions, the most robust form of TOF is the TOF_{max} which is defined as the TOF when all other reactants are at such a high concentration that they show a zero order contribution to the rate of reaction, otherwise known as saturation kinetics. Saturation kinetics are most commonly seen in enzymatic catalysis, where the substrate is in such high concentration compared to the enzyme, that at any instance the active site of all the enzymes are occupied. In the context of a fuel cell, a high TOF translates to a high current passage through the system, and therefore the TOF should be sufficiently high as to meet the amperage requirements of the fuel cell's load.

1.2.3 Oxygen Binding to Metal Complexes

In order for a material to be considered as an ORR catalyst, it must show some degree of binding towards O_2. This binding must be strong enough that oxygen remains bound for a sufficient amount of time for reduction to take place, but not so strong that any oxide products formed after reaction with oxygen are not able to regenerate back to the original active catalyst.[53]

Many transition metal complexes with a vacant geometric site available for coordination will bind oxygen to some degree due to the highly reactive nature of O_2, however the metal ions normally associated with the reversible binding of O_2 are Co^{II} [54,55] and Fe^{II} [56] and in many other cases, complexes of manganese[57,58] and copper.[59–61]

The high reactivity and binding capabilities of dioxygen can be explained by a molecular orbital (MO) theory treatment of its electronic structure (figure 1.2.1),[57,62] in which the degeneracy of the π^* antibonding orbitals results in the highest energy electrons being unpaired. The partially occupied π^* orbital means that O_2 demonstrates π Lewis acidity and is able to readily accept an unpaired electron from a metal ion, forming a superoxide-metal complex where one unpaired electron remains associated with the bound O_2.[56] Since a bound superoxide still contains an unpaired electron, the superoxide continues to demonstrate π acidity, and as such, the superoxide may be further reduced by either the same, or a separate metal ion to form a peroxo-bound complex.

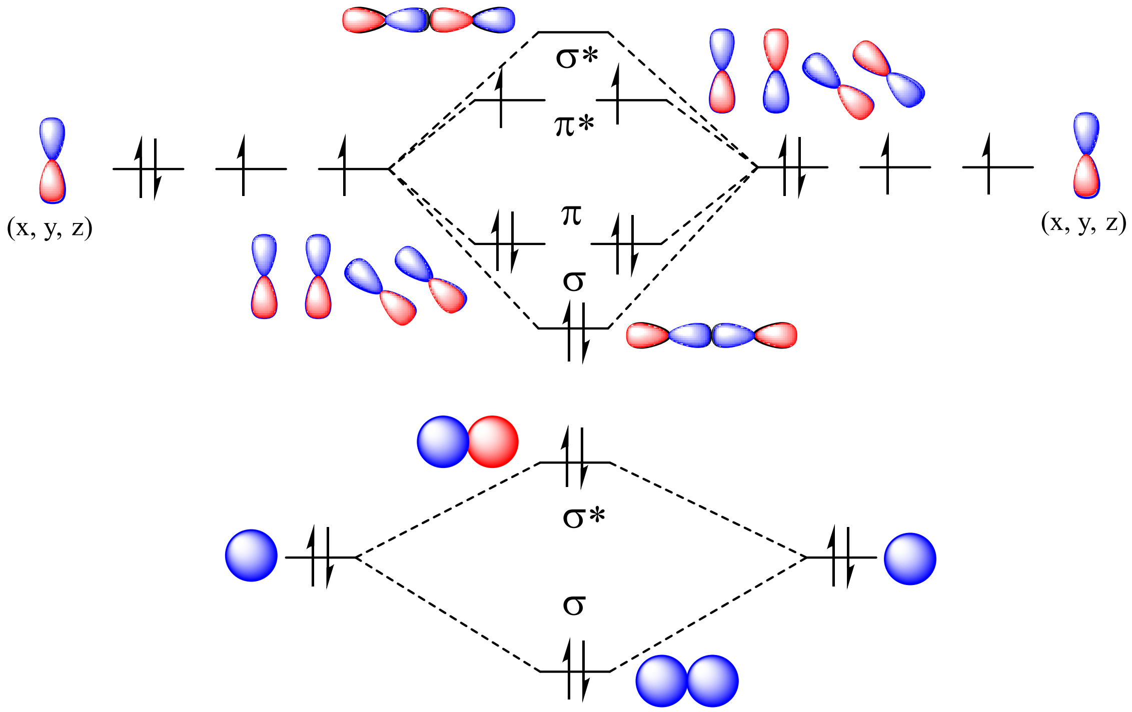

Figure 1.2.1 Molecular orbital theory representation of bonding interactions in O_2.

This multiple electron acidity of O_2 therefore generates multiple binding modes which can be adopted with metal complexes, which are summarised in figure 1.2.2.[63]

End-on Mononuclear (superoxide)

Side-on Mononuclear (peroxide)

Bridging Dinuclear (peroxide)

Bridging Side-on Dinuclear (peroxide)

Figure 1.2.2 Summary of coordination modes of O_2 towards transition metal ions

Reversible, mononuclear binding of O_2 is best known in iron porphyrin complexes which are the oxygen binding components in the active site of haem and haemoglobin proteins. The reversibility of O_2 binding towards haem is essential to its action as an oxygen carrier where, in the case of land animals, oxygen is bound to haem in the lungs and transported via the blood to destination organs.[64] Once at their destination, the O_2-haem must be labile enough to decoordinate O_2, where it is then used in the cellular metabolism which is undertaken by enzymes which include a similar porphyrin motif in their active site such as cytochrome oxidases.[65–67] The binding of

O_2 to porphyrins, both natural and synthetic, can be regulated by the inclusion of an axial base. If the axial base is weakly to moderately electron donating, such as imidazole or histidine, then the binding of O_2 is reversible. However, if the axial base is strongly coordinating, then O_2 binding becomes irreversible and O_2 remains fixed to the complex.[68–70] This is an important consideration when designing ORR catalysts, since if the reaction between the oxygen activating complex results in highly stable oxidation products, regeneration of the catalyst will be slow or impossible. Conversely, if the binding of O_2 is too weak, the activation of oxygen may be too slow for the catalyst to be considered useful.

1.2.4 Product Selectivity

The ORR proceeds via two pathways in acidic media, the four-electron pathway which generates water as the sole product,[71–73] and the two-electron pathway which generates hydrogen peroxide.[74–76] The four-electron pathway is highly preferable to the two-electron pathway, particularly in the a fuel cell context, since hydrogen peroxide is well known to decompose sensitive and expensive parts of the fuel cell assembly particularly the electrolyte membrane, Nafion™ via generation of hydroxyl radicals.[77,78] The four-electron pathway is also approximately twice as exothermic as the two-electron pathway with a standard reduction potential of 1.23 V versus 0.68 V for the two-electron pathway. Commonly used platinum catalysts are well known to rapidly and effectively catalyse the four-electron process,[30,79] however non-noble heterogeneous catalysts such as first-row transition doped graphite often show much lower selectivities. Designing a non-noble metal catalyst which shows high selectivity towards the four-electron pathway has been the focus of many studies over the past decade. Despite these efforts however, there has not yet been a well-established pattern between the structure of heterogeneous catalysts and product selectivity. In more recent years, there has been more focus on studying homogeneous systems where the structure activity relationships can be studied in more detail, with the hope of applying the lessons learned from homogeneous catalysis into heterogeneous catalysts for application in commercially viable fuel cells.

1.2.5 Stability to Contaminants

While electrolytically produced H_2 can be obtained in very high purity without need for further processing, steam reformed hydrogen generally contains non-negligible contaminants of CO and MeOH. These contaminants are well known to poison platinum catalysts, reducing their activity and overall lifetime. As such, the hydrogen used in PEMFCs must be particularly high purity to avoid catalyst decomposition. The need to only use electrolytic or expensively processed hydrogen undoubtably limited the growth in popularity in HFCs over their development. In an ideal scenario, hydrogen obtained from any source would be used in a HFC. To achieve this, any catalyst developed should be stable to both MeOH and CO. In addition, HT-PEMFCs are often used with an on-board reformer, allowing green fuels such as MeOH to be used, and in this case it is of even greater importance that the catalyst is stable to MeOH contamination. Many first-row transition metal based catalytic materials have been shown to be more resistant to poisoning by CO and MeOH.

1.3 Biological ORR Catalysts

Undoubtably, the best ORR catalysts are designed by nature and are found in aerobic organisms where the oxygen transport chain is essential to aerobic respiration. With many catalyst systems, it is reasonable to take inspiration from nature's catalysts when designing a new homogeneous catalyst system. Indeed, this method has proven successful in many applications. In particular hydrogenase active sites have been effectively mimicked or served as inspiration for a number of mononuclear or dinuclear Fe or Ni proton reduction catalysts. The active site of photosystem II has also been synthetically mimicked and shows good activity towards the photocatalytic water oxidation reaction.

For the ORR, biological systems such as cytochrome C oxidase (CCO) have been studied and have given rise to the extremely broad field of metalloporphyrin ORR catalysts. To a lesser extent, the oxygen reducing laccase enzyme has been synthetically mimicked with the intention of exploiting the structure's incredibly low ORR overpotential.

1.3.1 Laccase

Laccase is a tri-copper metalloenzyme belonging to a family of multi-copper oxidases and is found in plants such as *Rhus vernicifera*, *Rhus succedanea,* and *Pinus taeda* as well as fungus species such as *Polyporus versicolor*.[80] Laccase is well known for its ability to catalyse the four-electron reduction of oxygen to water and is often studied as an electrocatalyst adsorbed or covalently bound to either carbonaceous materials or gold electrodes.[81]

Laccase demonstrates a remarkably low overpotential for the ORR, and as a result has been the subject of multiple investigations into the enzyme's mechanism and potential use in biological fuel cells and biosensors.[82–85]

One drawback to the use of laccase as an ORR catalyst (and the use of enzymes as electrocatalysts in general) is the large area of inactive protein which is not directly related to the active site, limiting the specific activity of the enzymatic electrocatalyst. As a result, multiple attempts to mimic the laccase active site have been attempted. One study by Gewirth and co-workers synthesised a number of laccase models including mononuclear models bearing a dipicolylamine ligand and multinuclear models where the dipicolylamine donor sets are linked by an alkyl (for dinuclear complexes), bipyridyl or terpirydyl (for trinuclear complexes) linker (Figure 1.3.1).[84] Despite activity ORR activity being observed for each model, the group reported no substantial increase in activity for the multinuclear models when compared to the simple mononuclear complex, indicating that simply modelling the geometric aspects of the laccase active site is not sufficient to replicate the high activity of laccase.

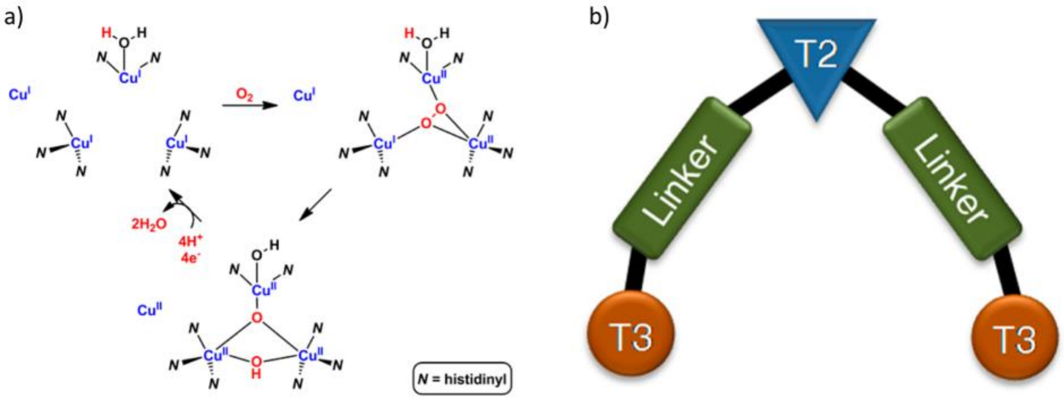

Figure 1.3.1 Simplified representation of the laccase active site (a) and the design motif of synthetic laccase inspired ORR catalysts where T2 and T3 represent metallic sites (b). Reprinted with permission from reference 84. Copyright 2014 American Chemical Society.

1.3.2 Cytochrome Oxidase

Cytochrome C oxidase (CcO) is the terminal enzyme in the respiratory chain of eukaryotic cells which is responsible for the reduction of oxygen to water within mitochondrial systems.[66,86] The structure of the CcO active site is bimetallic with a porphyrinic iron centre and a pendant histidine copper complex. The mechanism of the ORR by CcO involves proton coupled electron transfer from the nearby tyrosine (TyrOH) moiety induces O-O cleavage to form Fe^{IV}=O and Cu-OH intermediates and a TyrO· species.[87]

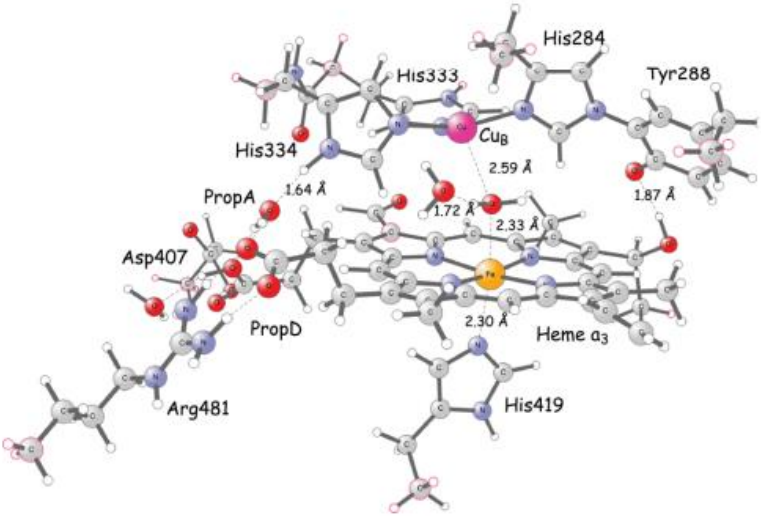

Figure 1.3.2 Model of the bimetallic active site of CcO. Reprinted with permission from reference 87. Copyright 2016 American Chemical Society.

There have been numerous studies where the active site of CcO has been mimicked for the ORR where iron porphyrin complexes are designed to be in close proximity to a secondary copper site. These mimics can either be homogeneous catalysts in solution or heterogeneous when bound to a gold electrode by a suitable linker group.[88,89] or when physiadsorbed onto edge plane graphite.[90] Success has also been shown when incorporating the nitrogen rich iron-copper motif into graphitic nanoparticle systems, further demonstrating that inspiration from molecular catalysts can prove valuable when designing heterogeneous systems.[91]

1.4 Molecular ORR Catalysts

1.4.1 Porphyrin ORR Catalysts

Porphyrins are fully conjugated 18π electron macrocyclic organic compounds comprising of four alternating pyrrole and methine moieties. They are synthesised by the condensation between an aldehyde and a dipyrrolylmethane and can be functionalised before formation using substituted reactants or post-synthetically using strongly nucleophilic reagents such as Grignard reagents or lithiated compounds.[92] The planar N_4 core of the porphyrin has made them an extremely common ligand, both in nature and synthetic chemistry. The porphyrin is composed such that two of the pyrrole moieties are protonated in its neutral state and can be deprotonated to form a dianionic ligand. Due to their presence in many biological ORR systems, porphyrin complexes have been at the epicentre of synthetic molecular ORR catalysis for well over half a century.

Stahl and co-workers studied the relationship between Brønsted acidity of the proton source used in ORR catalysis and the product selectivity observed.[93] For the same mononuclear Co^{II}-porpyrin complex, a range of acids over a pKa range between 2 and 8 were used as the proton source in DMF. As the pKa increased, the TOF of the ORR decreased, which is to be expected when reducing the acidity of the proton source in a protic reaction. Interestingly however, when the pKa of the acid is increased from 3.5 to 5.0, the selectivity of the reaction inverts from almost quantitative H_2O_2 selectivity to almost quantitative H_2O selectivity.

The reason for this switch in selectivity is based in the thermodynamics of the system, further investigation by the group found that the reduction potential of the catalyst is independent of acid strength, while the equilibrium potentials of the two-electron and four-electron pathways show a Nernstian and co-linear decrease with increasing pKa. The switch in selectivity coincides with the equilibrium of the two-electron pathway becoming more negative than the reduction potential of the catalyst. i.e., the two-electron pathway would be operating at an *underpotential* (Figure 1.4.1). The production of H_2O_2 therefore becomes unfavourable and the four-electron pathway to produce H_2O dominates.

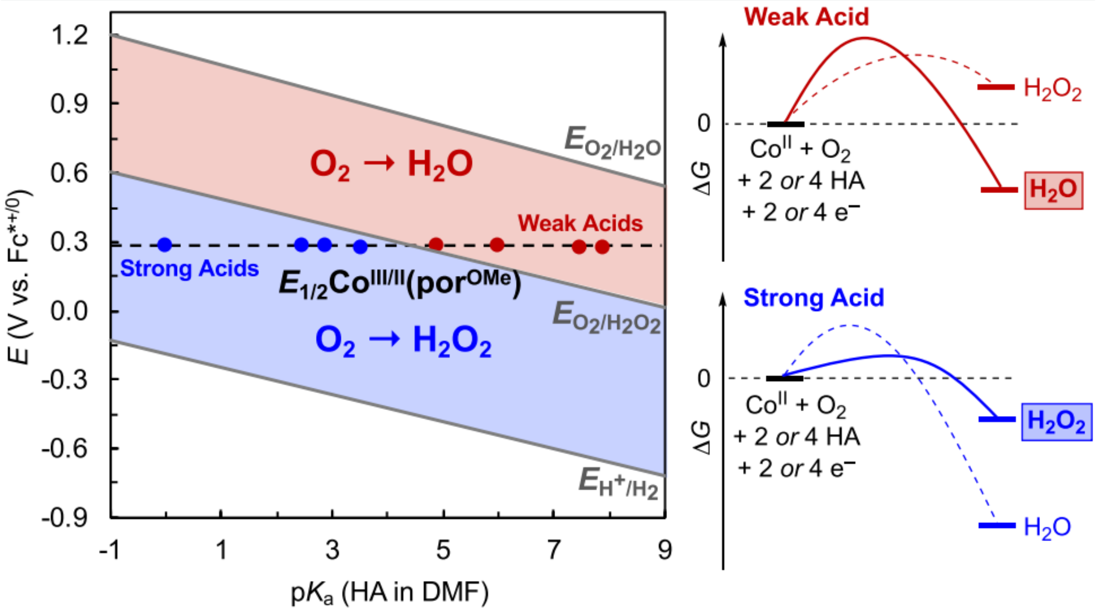

Figure 1.4.1 A graph showing the relationship between pKa and equilibrium potentials of the two-electron and four-electron pathways of the ORR in DMF as well as the $E_{1/2}$ of the Co^{II}porphyrin catalyst and its effect on product selectivity. Reprinted with permission from reference 87. Copyright 2019, American Chemical Society, Washington, DC.

This work demonstrates that thermodynamic considerations can be just as important as catalyst design when attempting to influence the selectivity of a redox reaction.

In a similar study, Pegis and Meyer investigated the TOF vs overpotential correlation for the ORR catalysed by a series of iron(II) porphyrin complexes in acetonitrile and DMF solution.[94–97] (Figure 1.4.2) The complexes studied were distinguished by variations in the substitutions at the four methine carbon atoms on the porphyrin ligand. The overpotential and TOF were determined electrochemically using the well-established foot-of-the-wave analysis (discussed further in chapter 4) which is a convenient method of determining the rate of an electrocatalytic reaction which is sufficiently rapid such that the electrocatalytic current response is approximately an order of magnitude greater than the current response of the catalyst under electrochemically reversible conditions.

Varying the methine substituents of the ligand resulted in a range of catalyst reduction potentials between -0.362 and -0.630 V in DMF solution, while in MeCN the reduction potentials ranged between -0.280 and -0.375 V. These changes in catalyst reduction potential relate to an overpotential range between 0.91 and 1.18 V for DMF systems and between 1.11 and 1.21 V for MeCN systems using 20 mM [DMF-H]OTf as the proton source. The TOF response across these overpotential ranges was exceedingly steep. For DMF systems, the TOF of the ORR began at 3.0×10^{0} s^{-1} for the lowest overpotential catalyst up to an impressive 2.0×10^{3} s^{-1} for the highest. For the MeCN systems, the TOF ranged from 2.2×10^{2} s^{-1} up to 2.2×10^{6} s^{-1} which remains, to date, the highest TOF for a homogeneous ORR electrocatalyst.

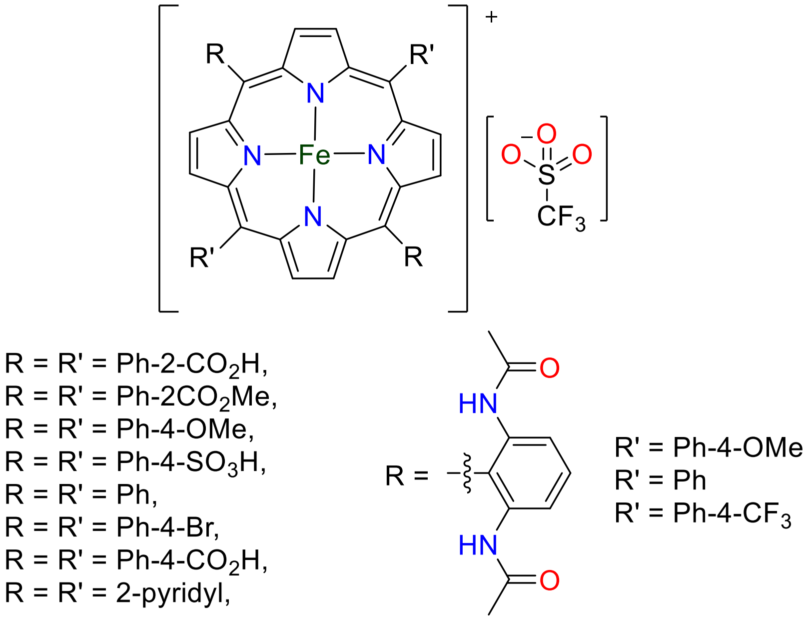

Figure 1.4.2 Structures of the Fe^{III} porphyrin ORR electrocatalysts investigated by Pegis and Meyer[94–97]

For this study, all catalysts were fully selective towards the four-electron pathway. It is generally accepted that iron porphyrin ORR electrocatalysts are selective to H_2O production, however due to the steep TOF vs. overpotential slope, these catalysts are not able to catalyse the ORR at low overpotentials, while on the other hand, mononuclear cobalt complexes, (including porphyrins, but also non-porphyrin complexes) will generally catalyse the two-electron reduction of oxygen unless thermodynamically influenced otherwise.

1.4.2 Cofacial Diporphyrins

In the previous section, it was seen that in the majority of cases, mononuclear cobalt complexes of porphyrins and other planar macrocyclic ligands tend to produce H_2O_2 as the product of the ORR unless thermodynamically influenced otherwise. This trend extends to most other mononuclear cobalt complexes. It was postulated that if a second cobalt site was included into the O_2 binding site that cleavage of the O-O bond may be more facile, indeed, many enzymatic ORR active sites contain more than one active metal centre and are mostly always selective to the four-electron pathway.[66,67] This postulation led to the development of a series of cofacial diporphyrin complexes, where two cobalt macrocycles are covalently linked by a spacer moiety. Multiple studies have adopted this method and as a result the range of diporphyrin or dimacrocycle cobalt complexes have been examined for the ORR.[98–101]

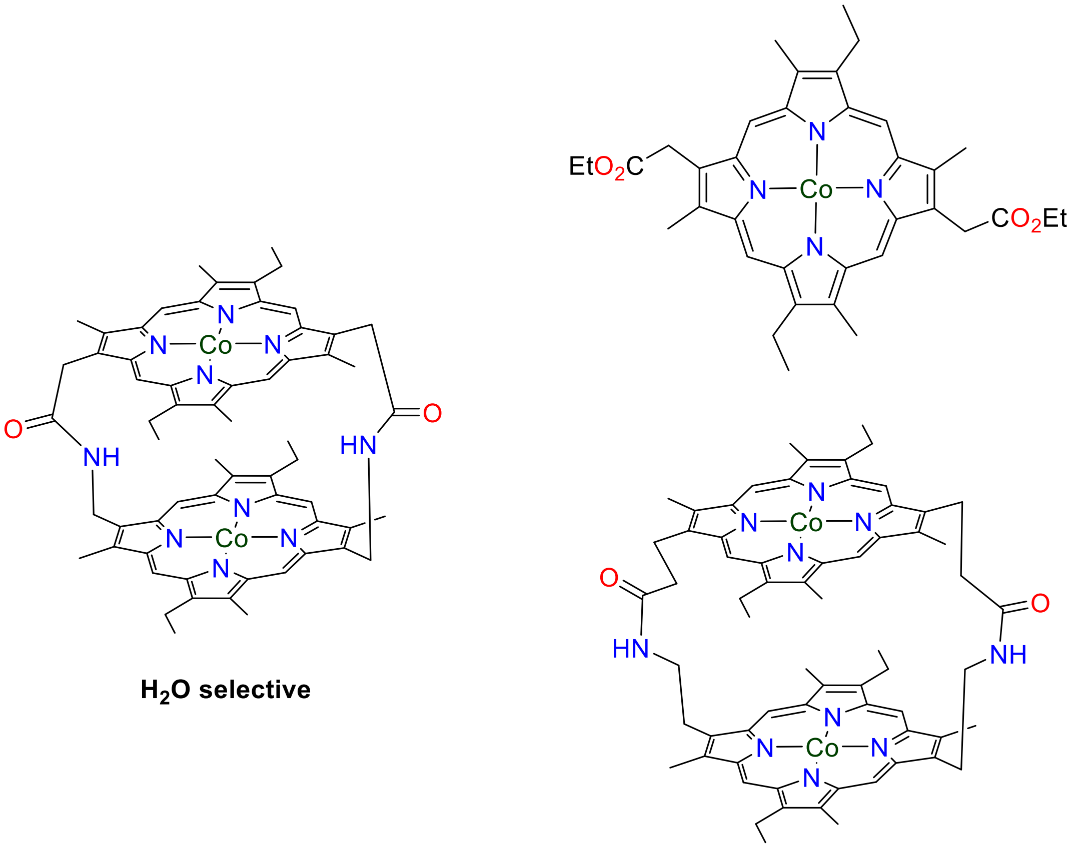

H_2O selective

H_2O_2 selective

Figure 1.4.3 Water selective cofacial diporphyrin complex (left) and H_2O_2 selective porphyrin complexes (right) studied by Anson and co-workers in 1979.

The first such dinuclear cobalt macrocycles were examined in 1979 by Anson and co-workers where cofacial porphyrin complexes were covalently tethered by amide linkages, providing a bimetallic active site (Figure 1.4.3).[102] These rudimentary cofacial complexes were examined electroanalytically for ORR activity by adsorption onto a graphite electrode and it was found that only minimal amounts of hydrogen peroxide were formed. When a mononuclear porphyrin analogue was analysed by the same method, almost quantitative formation of hydrogen peroxide was observed. In addition, another diporphyrin complex in which the tethering amide had a longer chain (i.e. the Co-Co distance was increased) resulted in a poor selectivity than the short chain complex. This was the first instance where an ORR catalyst was developed with the intention of forming a peroxo bridged dimer between two cobalt ions to improve selectivity towards the four-electron pathway.

1.4.3 Polypyridyl ORR Catalysts

As seen with porphyrin complexes, metal complexes bearing ligands with a large number of N-heterocyclic donor groups have an increased affinity towards the binding of O_2 due to an increased electron density located at the metal centres. This observation naturally led to the development and investigation of non-porphyrin N-heterocycle rich ligands towards the binding and reduction of oxygen.[103]

This area of study has been particularly successful in the development of complexes which are able to produce stable adducts between the complex and O_2. Wada and co-workers designed a dinuclear homogeneous catalyst system where a ligand comprising two terpyridyl moieties spaced by a xanthene or anthracene bridge forms a dinuclear complex following reaction with two equivalents of $CoSO_4$ and 2,2-bipyridyl (Figure 1.4.4 left).[104] During the complexation, reaction of the formed complex with oxygen from the air results in the formation of a μ-O_2 bridge between the two cobalt (III) ions where the remaining coordination sphere of each ion comprises of five pyridyl donors. The bridging structure of the bound O_2 was confirmed by XRD studies. In addition, the reversibility of the binding of O_2 was confirmed by comparing the Raman spectra between $^{16}O_2$ and $^{18}O_2$ saturated MeCN solutions. Catalytic activity was examined by the chemical reductant method using $Fe(CpMe)_2$ in PhCN solution containing $HClO_4$ as the proton source. Selectivity of the homogeneous ORR was determined using the spectrophotometric Ti-porphyrin method[105] and was found to have almost quantitative selectivity towards the four-electron pathway.

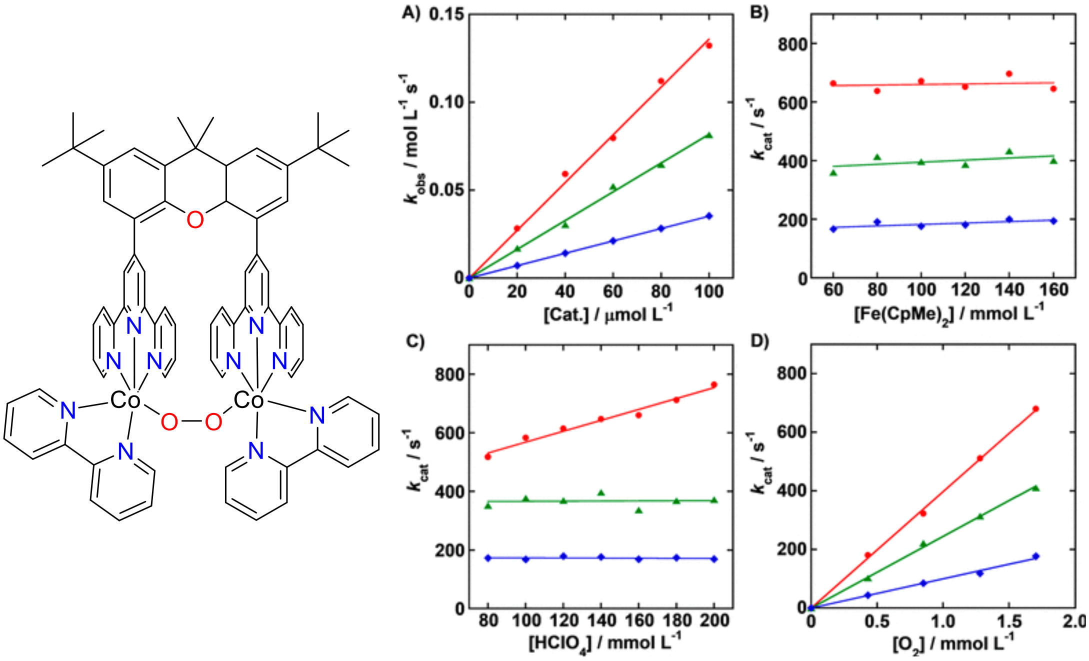

Figure 1.4.4 Structure of a polypyridyl peroxo-bridged dinuclear four-electron pathway selective ORR catalyst (left) studied by Wada and co-workers, and kinetic studies showing the oxygenation rate determining step where figures A), B), C), and D) show the rate of ORR with varying concentrations of catalyst, reducing agent, perchloric acid and O_2 respectively. Coloured traces represent the different catalytic species, with the red trace representing the catalyst species shown. Reprinted with permission from reference 112. Copyright 2021 American Chemical Society.

Kinetic studies revealed that the rate of O_2 reduction showed a first-order dependence on the concentrations of the catalyst complex and the O_2 concentration but was independent on the concentrations of $HClO_4$ and the $Fe(CpMe)_2$ reducing agent. This showed that the rate determining step of the catalysis was the binding of oxygen between the two Co^{II} ions (Figure 1.4.4 right). Of the complexes studied, the catalyst which used a xanthene spacer showed the highest TOF of 6.8×10^2 s^{-1}. While electrochemical studies were performed, an overpotential of the catalysis was not estimated in the study, likely due to the irreversibility of the redox feature which was associated with catalytic turnover.

The decadentate polypyridyl motif is relatively common amongst dinuclear O_2 binding and reduction complexes. Llobet and co-workers developed a ligand in this family where a pyridazine bridging group separates two cobalt ions and pyridylic arms occupy the remaining four coordination sites per cobalt ion.[106] If the complexation is done with two equivalents of $Co(OTf)_2$ in an O_2-free atmosphere and subsequent salt metathesis with NH_4PF_6, the final coordination site of the cobalt ions remains vacant as determined by XRD studies. Upon exposure of the complex to air, the complex binds oxygen, forming a similar μ-O_2 bridge between the two cobalt ions.

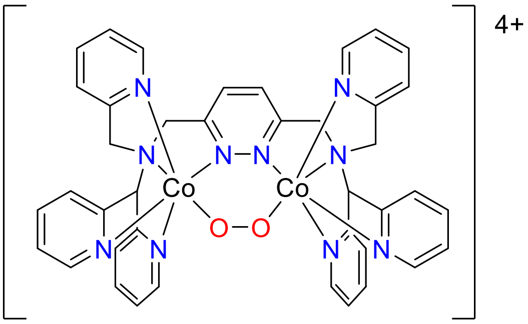

H_2O_2 selective

Figure 1.4.5 Structure of the dinuclear peroxo-bridged dinuclear cobalt complex bearing a decadentate polypyridyl ligand studied by Llobet and co-workers as a two-electron pathway selective ORR catalyst.

Interestingly, despite the similarity of the coordination environement between this complex and the previously discussed complex, catalytic studies revealed exclusive formation of H_2O_2 as the product. This result shows that despite the inclusion of a second oxygen-binding cobalt centre, it is not definitive that the formation of a peroxo-bridged intermediate guarantees four-electron pathway selectivity.

1.4.4 Salen ORR Catalysts

Metal complexes of salen ligands have been used extensively for catalysis and small molecule activation for many decades.[107–110] Normally bearing two imine donors and two phenolate donors, salen ligands often form square planar complexes, or complexes with a tetradentate basal plane where the axial sites can be occupied by Lewis basic solvents such as pyridine. The presence of a vacant or labile site means that complexes of many transition metal ions such as Co^{II} or Mn^{II} are able to bind oxygen through the modes discussed in section 1.2.3. In addition, salen ligands are simple to synthesise and normally are obtained in high yield and purity from mixing a diamine and two equivalents of a salicylaldehyde derivative in an alcohol solvent. This ease of synthesis means that many structural variants of salen ligands can be examined with few changes to the synthetic procedures.

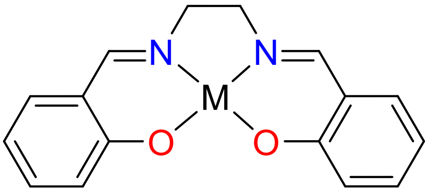

Figure 1.4.6 Structure of Msalen, the typical salen complex derived from salicylaldehyde and ethylenediamine

While salen complexes have been known to bind oxygen since the mid-20th century,[111] examination of their ORR activity was not examined in detail until recent years. The lack of ORR examination of salen complexes in the academic landscape is likely due to their poor electrocatalytic response by conventional means such as foot-of-the-wave analysis (explained in detail in Chapter 4). Only recently, a new generally accepted spectrophotometric method for quantifying the rate of ORR catalysis has been established which involves using ferrocene derivatives as the reducing agent (explained in detail in chapter 5).[112] This newly established method of quantification of the ORR has allowed complexes, for which the TOF is too slow for electrochemical analysis, to be examined. In addition, this method is convenient for developing a deeper understanding of the ORR mechanism by study of the reaction kinetics.[73,113]

One of the complexes which falls into this category is the family of Co^{II}-salen complexes. Stahl and co-workers have previously examined a cooperative electrocatalytic interaction between Co^{II}-salophen and hydroquinone, where the rate of electrocatalytic ORR by Co^{II}-salophen is enhanced by the electron and proton transfer characteristics of hydroquinone.[114] The group proposed that hydrogen atom transfer from hydroquinone quenches the bound superoxide intermediate, followed by PCET from hydroquinone, initiating O-O bond fission and generating benzoquinone as the product. Since benzoquinone is more readily reduced at the electrode than the Co^{III}-salophen-superoxide intermediate, the rate associated with the reduction of oxygen is enhanced. This cooperative catalysis essentially allows O_2 to be reduced in bulk solution, then the homogeneous reductant is rapidly regenerated at the electrode (Figure 1.4.7). While this research demonstrated the importance of electron and proton transfer kinetics in both the rate and selectivity of the ORR, the technique is not sufficient to fully quantify the electrocatalytic activity and examine overpotential and TOF of Co^{II}-salophen alone.

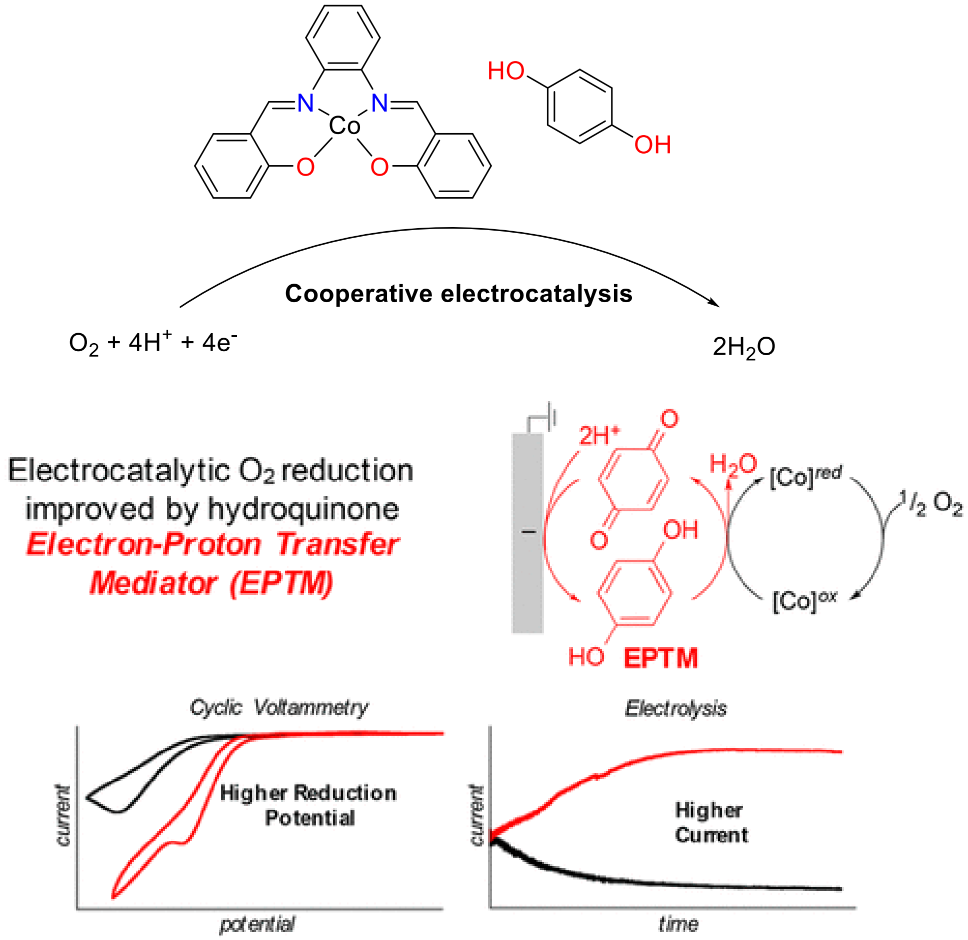

Figure 1.4.7 Structures, mechanism and electrochemical behaviour of a cooperative catalytic system using Co^{II}salophen and hydroquinone for the four-electron reduction of O_2. Reprinted with permission from reference 104. Copyright American Chemical Society 2017

To fully quantify the kinetics of the ORR catalysed by Co^{II}salophen and a wider family of salen complexes, Stahl and co-workers used the relatively new spectrophotometric method developed by Fukuzimi and Guillard where the catalytic aerobic oxidation of ferrocene derivatives can be monitored by the spectrophotometry. Using this method, Stahl showed that the selectivity of the ORR catalysed by the Co^{II}salen family (Figure 1.4.8) is almost quantitative towards the $2e^-$ pathway for both complexes containing electron donating and electron withdrawing groups, with TOF values ranging from 0.027 to 5.5 s^{-1} at overpotentials calculated between 90 and 550 mV respectively.[115] In addition, it was also shown that the LogTOF scales linearly with overpotential, where, as the reduction potential of the catalyst becomes more negative, the rate of reduction of oxygen is increased exponentially.

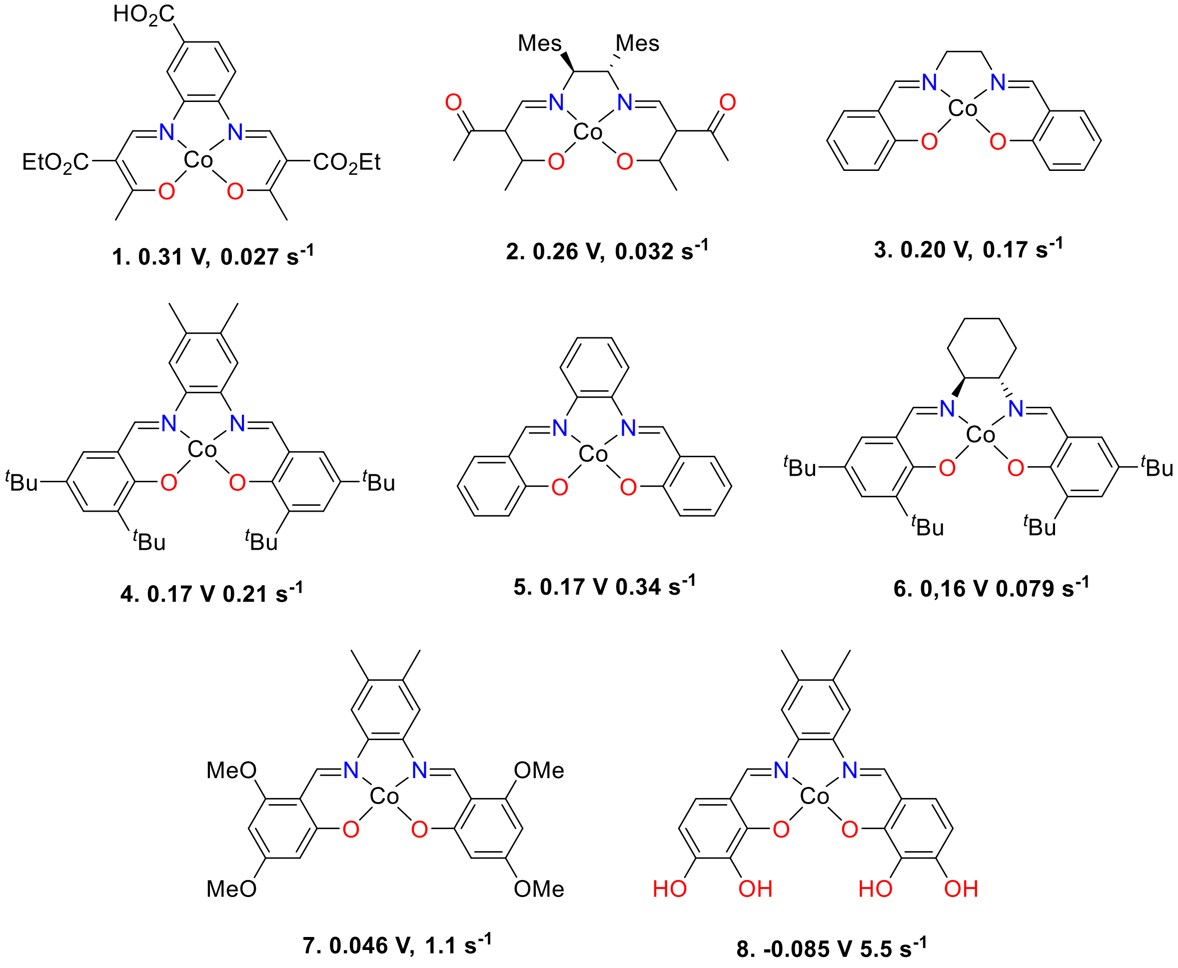

Figure 1.4.8 Structures, half wave potentials, and ORR TOFs of the eight two-electron selective Co^{II}salen oxygen reduction catalysts studied by Stahl and co-workers.

The work also showed that the two-electron reduction of oxygen could be performed at relatively low overpotentials at appreciable TOF values. It is proposed that if a porphyrin catalyst such as Co(por^{Me}) was used under conditions such that the overpotential was modified to match that of these Co^{II}salen complexes, the rate of oxygen reduction would be minimal. It is therefore clear that the Co^{II}salen motif is excellent for accessing very low overpotentials for the ORR, whilst conserving TOF. In addition, a robust trend between TOF and overpotential was observed, indicating that the main factor dictating the rate of ORR was the $E_{1/2}$ of the complex, rather than steric influences arising from the incorporation of bulky alkyl groups. In a subsequent study by the same group, it was found that the rate limiting step of the catalytic H_2O_2

production was the second protonation of the proximal oxygen atom of the bound Co-OOH species (the oxygen atom bound to the metal centre), while oxygen binding to the cobalt centre was found to be spontaneous and rapid as determined by Clark electrode studies. Differential pulse voltammetry studies also showed a significant response of an oxygenated solution of the Co^{II}-salen complex to the addition of acetic acid both in the presence and absence of decamethylferrocene as an electron transfer mediator.

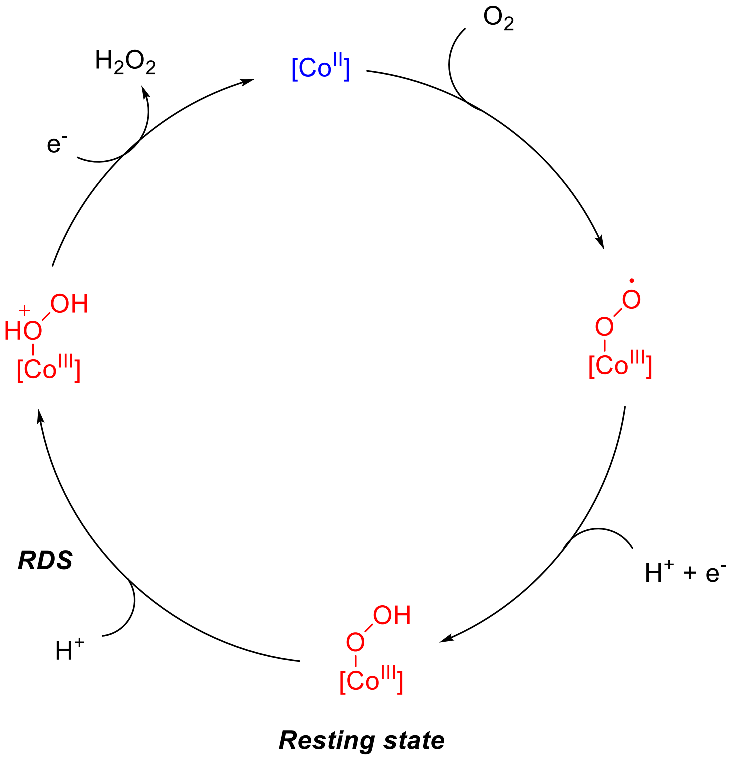

Figure 1.4.9 Catalytic cycle proposed by Stahl and co-workers for the two-electron reduction of oxygen catalysed by Co^{II}-salen complexes.

Density functional theory (DFT) calculations also support the observation that protonation of the distal oxygen atom proceeds spontaneously while the second protonation event occurring at the proximal site represents a maximum on the Gibbs free energy profile.[116]

While a few other studies which quantify the ORR catalysed by N_2O_2 donor set Schiff base complexes exist, little work has been done to attempt to switch their selectivity towards the four-electron pathway.

Recently, Machan and co-workers developed a bipyridyl backboned N_2O_2 donor set cobalt complex (Figure 1.4.10, (a)) which was examined for ORR activity by the same method.[117] The study found that this complex was more selective towards the four-electron pathway than the Co^{II}-salen complexes showing a H_2O product selectivity of 71% at a TOF of 1.03×10^{-3} s^{-1}. However due to poorly reversible electrode kinetics as shown by a peak separation in the cyclic voltammogram of ca. 500 mV, the overpotential was found to be 1.24 V, much higher than their salen counterparts. However, it is important to note that comparison of overpotential between $4e^-$ and $2e^-$ selective catalysts should not be done, since both pathways are distinct chemical processes and have differing equilibrium potentials. In a subsequent study by the same group, a bipyridyl backbone N_2O_2 cobalt complex, this time bearing methyl ether substituents at the 2-position of the phenolate rings, facilitated the two-electron pathway despite the similar ligand structure.[118] It was proposed that the cause of this H_2O_2 selectivity is hydrogen bonding between the ether and the proximal oxygen atom of the bound complex, encouraging H_2O_2 release before O-O bond fission can occur.

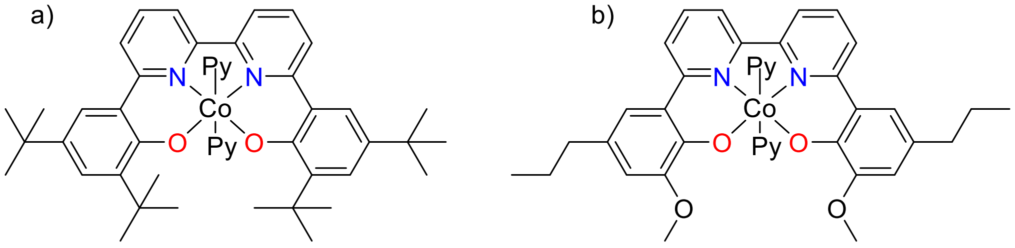

71% H_2O selectivity

76 - 87% H_2O_2 selectivity

Figure 1.4.10 Bipyridyl backbone cobalt N_2O_2 complexes studied by Machan and co-workers showing opposite selectivities between structures (a) and (b).

Despite these relatively recent advances in salen based ORR electrocatalysts this type of ligand system has been known and examined for at least 20 years. At the turn of the millennium, Liu and co-workers developed an oxovanadium(IV)salen catalyst (Figure 1.4.11 left) which is able to reduce oxygen to water in acetonitrile or dichloromethane solution in the presence of triflic acid.[119,120] The ORR facilitated by VOsalen was examined thoroughly by electrochemical analysis and found that the reduction takes place via a complex mechanism beginning with the acid induced disproportionation of two equivalents of the complex to generate V(V) and V(III) species. The latter of these species is capable of binding O_2 via a peroxo bridged dimer. Regeneration of the catalyst takes place by homolytic bond fission of the peroxo bridged dimer, as well as reduction of the V(V) species at the electrode (Figure 1.4.11 right). The research surrounding VOsalen complexes for the ORR appears to have concluded in the early 21st century due to the slow rate of catalysis and the complex mechanism.

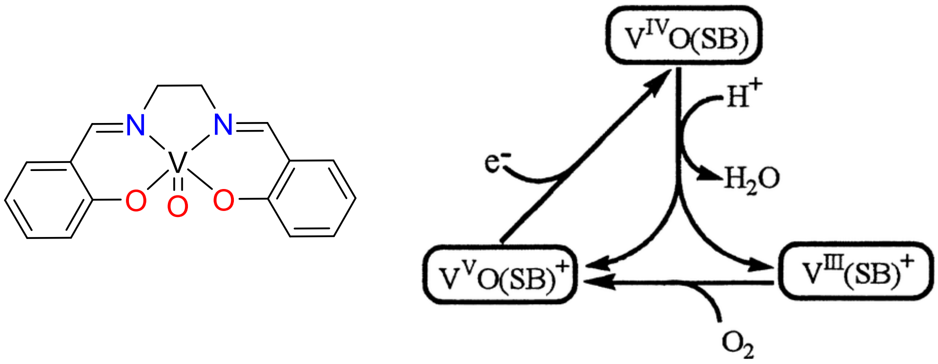

Figure 1.4.11 VOsalen complex and ORR mechanism studied by Anson and Liu for ORR catalysis where the catalytic species are generated by acid induced disproprtionation of the $V^{IV}O$ species. Reprinted with permission from reference 118. Copyright American Chemical Society 2001

1.5 Salen Complexes in Non-ORR catalysis

As described in the previous section, salen-like complexes (i.e., those with an imine phenolate donor set) are able to catalyse the oxygen reduction reaction and access high TOF values for their low η_{eff}. While there are only a handful of examples of salen complexes tested for ORR activity, they have seen much attention in other catalytic reactions relevant to renewable fuels such as the hydrogen evolution reaction (HER)[121,122] and the water oxidation reaction (WOR)[123] and CO_2 reduction,[124,125] as well as organic catalysis such as catalytic olefin epoxidation by Jacobsen type complexes.[126,127] While not directly related to the oxygen reduction reaction, understanding the use of Co(salen) and similar Schiff base complexes in these reactions is both important to the hydrogen economy, of which the ORR is a part, and understanding the design of Schiff base catalysts for energy relevant transformations.

1.5.1 Schiff Base Complexes for Hydrogen Production

Currently, hydrogen gas is generated mainly by the steam reformation of methane or the gasification of coal. Of course, methane is a fossil fuel and thus any hydrogen economy which uses methane or coal gasification as its source of hydrogen is not renewable. Generating hydrogen gas from renewable sources such as the electrolysis of water by solar power, therefore, is of vital importance to the possible transition into a sustainable hydrogen economy. The concept of obtaining hydrogen gas from the electrolysis of water is in its essence the reverse reaction of that occurring within a HFC, an oxidising potential is applied to water, causing it to oxidise at the anode to O_2, and release protons. These protons are then reduced at the cathode to release H_2 gas. Development of catalytic systems for the WOR and HER half reactions are therefore pivotal to the production of water splitting systems for H_2 production.

The HER has been efficiently catalysed by several first-row transition metal complexes, and many involve ligand systems which require difficult and expensive synthesis. Schiff base complexes, however, are easily tuneable, inexpensive and simple to synthesise. In the mononuclear case, McNamara and co-workers synthesised a simple cyclohexyl ‘half-salen’ motif which is able to produce H_2 from trifluoroacetic acid in MeCN solution at an overpotential of 350 mV (Figure 1.5.1 left) with a moderate rate.[128] In a subsequent study by the same group, the ligand structure was easily tuned to even lower overpotentials of 280 (Figure 1.5.1 right) and 120 mV (Figure 1.5.1 bottom) by modifying the ligand backbone and adding more electron-withdrawing groups.[129]

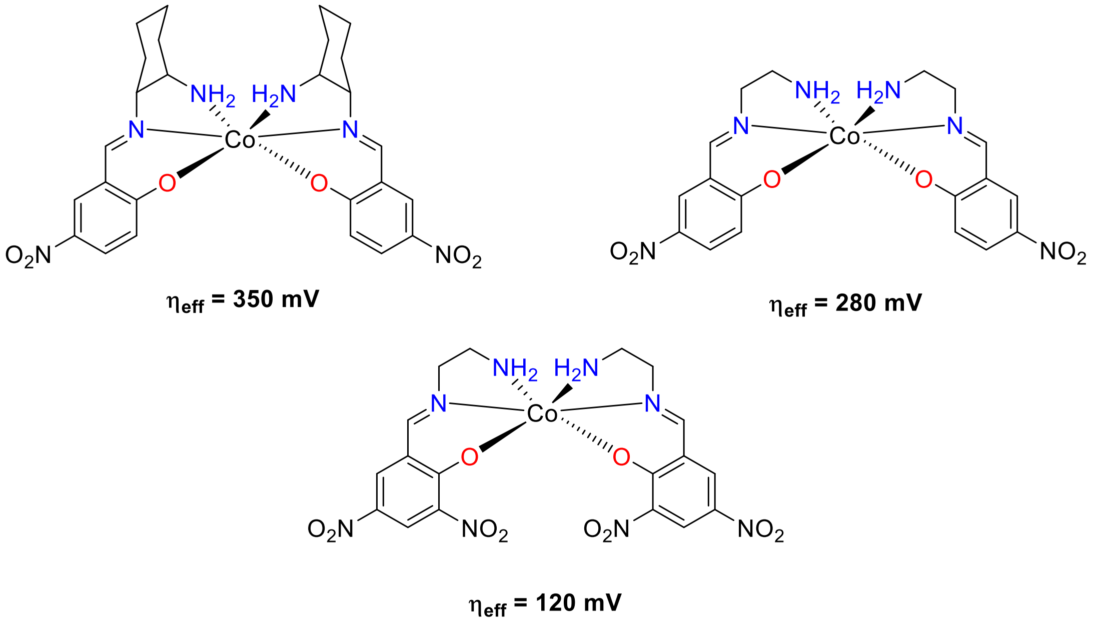

η_{eff} = 350 mV

η_{eff} = 280 mV

η_{eff} = 120 mV

Figure 1.5.1 Schiff base cobalt complexes studied by McNamara and co-workers for the low-overpotential electrocatalytic reduction of protons to hydrogen.

The simplest Co(salen) was tested for the homogeneous photocatalytic WOC by Ma and co-workers where aqueous solutions containing Co(salen) (< 2.4 µM), $[Ru(bpy)_3](ClO_4)_2$ (1 mM) and $Na_2S_2O_8$ (5 mM) were irradiated with 420 nm light at ca. 16 mW. The number of moles of O_2 generated was then determined periodically by gas chromatography to determine TOF and TON of 6.4 s^{-1} and 854 respectively.[130,131] However, stability studies indicate that under photocatalytic conditions, Co(salen) decomposes to form nanoparticulate cobalt oxides which are the true catalytically active species. This decomposition of the proposed catalyst to a nanoparticulate catalyst is not uncommon within molecular catalysis and it is important to understand the stability of potential catalytic complexes under highly oxidising or reducing conditions.[132]

1.5.2 Dinuclear Schiff Base Complexes for Hydrogen Production

The HER is proposed to take place via two main pathways, the heterolytic and homolytic routes.[133] The heterolytic route involves reduction of a mononuclear active site followed by protonation of the metal centre to form a metal hydride, then reaction of the hydride with a second proton releases H_2 from the oxidised metal centre which is free to be regenerated by reduction at the electrode. For the homolytic route, two metal centres are reduced and subsequently protonated to form a $2M_{ox}$-H species followed by reductive elimination of H_2 and regeneration of the catalytically active sites. The homolytic pathway clearly presents the question of whether a dinuclear active site can promote the homolytic pathway, and whether doing so affects catalytic activity.

Dinolfo and co-workers designed a macrocyclic dicobalt Schiff base HER electrocatalyst for which both heterolytic or the homolytic pathways are possible in MeCN in the presence of AcOH or TFA.[134] While the operating overpotential of the system was high considering its Faradaic efficiency and TOF, DFT studies reveal that the HER in fact most likely follows a heterolytic pathway in which a bridging hydride between the cobalt centres is protonated to release H_2 rather than the homolytic pathway, much like the mechanism observed in Fe-Fe or Fe-Ni hydrogenase mimics.[135,136]

The WOR in particular suffers from the same sluggish nature as the ORR where the formation of the O-O bond is accompanied by a large kinetic barrier. As well as the kinetic limitations, the WOR involves a high thermodynamic barrier with the standard oxidation potential of water to oxygen at a large 1.23 V. Therefore, any WOC must be effective at very low overpotentials to allow the WOR to be a viable method of generating H_2 gas. Complexes of salen and salen-like ligands have been studied as possible WOCs, in the case of electrocatalytic water oxidation, salen complexes are often electrodeposited onto a surface[137] or incorporated into a metal organic framework[138] and act as heterogeneous catalysts, whereas in the photocatalytic WOR, photosensitisers are used in conjunction with a sacrificial oxidant which would be replaced with an electrode within an electrolytic device.[139]

1.6 Literature Summary and Thesis Aims

The literature surrounding homogeneous ORR catalysts is diverse, and there have been multiple methods to influence the selectivity of catalysts. The selectivity of the ORR can be influenced by either the specific design of the catalyst, or through changes made to the catalytic environment. For example, mononuclear Fe^{III}porphyrin catalysts generally facilitate the four-electron pathway, where O-O bond cleavage is driven by the formation of a Fe=O intermediate, followed by hydrolysis which regenerates the active catalyst and releasing H_2O. While these Fe^{III}porphyrin catalysts exhibit particularly high rates of oxygen reduction, the overpotential required to drive this catalysis is considerably high c.a. 1 V.

Cobalt complexes can access lower overpotentials while retaining their catalytic activity, however, mononuclear cobalt complexes are generally selective towards the two-electron pathway. Since cobalt (III) complexes have a greater number of d-electrons than iron (III) complexes, formation of Co=O intermediates following O-O bond fission is disfavoured. As a result, O-O bond cleavage in mononuclear cobalt complexes is slow and release of H_2O_2 is often preferred.

Facilitating O-O bond cleavage in mononuclear cobalt complexes can be achieved by two main methods: Firstly, thermodynamic bracketing of the ORR by influencing the reaction conditions such that the formation of H_2O_2 would be operating at an underpotential results in the two-electron pathway being thermodynamically disfavoured, leaving the four-electron pathway as the only thermodynamically feasible option. Secondly, co-catalysis of the ORR with a proton-electron transport mediator can allow rapid PCET to a bound hydroperoxide intermediate in bulk solution, initiating O-O bond fission before release of H_2O_2 can take place.

Dinuclear cobalt complexes such as cofacial or pacman diporphyrins, as well as dinuclear polypyridyl complexes have been shown to have increased selectivity towards the four-electron pathway. The formation of a bridging peroxo intermediate between the two cobalt ions both weakens the O-O bond due to increased donation to the π^* orbitals of dioxygen, and allows distribution of each oxygen atom to individual cobalt centres, meaning that formation of high energy Co=O species is not required for O-O bond fission.

Another method of improving the selectivity of mononuclear cobalt complexes towards the four-electron pathway is to incorporate a proton relay which directs protons to the distal oxygen atom of the bound hydroperoxide species. This method has been effective at improving the H_2O selectivity of cobalt porphyrin complexes, but has seldom been applied to other non-porphyrin catalyst systems.

Cobalt complexes of salen ligands or similar phenolate imine ligands are also able to catalyse the ORR, however, since these complexes are generally mononuclear, the only salen complexes tested for the ORR catalyse the two-electron pathway. Co^{II}salen complexes have been shown to carry out the ORR to H_2O_2 at particularly low overpotentials with some reaching overpotentials as low as 90 mV.

With the impressive ORR activity of salen complexes at their low overpotential, it seems appropriate to attempt to modify the catalyst system through the known methods of influencing ORR selectivity to design a salen based ORR catalyst which is active at low overpotentials but is selective towards the four electron pathway. Surprisingly, there are very few examples of salen or phenolate imine ORR catalyst which make use of either proton relay systems or dinuclear active sites to bias the system towards four-electron selectivity.

In this work, we aim to design a new dinuclear catalytic system where the salen inspired motif allows access to relatively low ORR overpotentials, while the dinuclear structure biases the selectivity of the catalysis towards the four-electron pathway.

As a starting point, the inorganic coordination chemistry literature was reviewed for possible dinuclear Schiff base motifs where first-row transition metals could be accommodated with a suitable metal-metal distance which would allow for the binding of oxygen between the two metal centres via the peroxo-bridging coordination mode. The selected motif was then adapted to incorporate beneficial features of salen complexes, where both phenolate and imine moieties are utilised in the donor set of the ligand.

Once a suitable complex had been designed and synthesised, structural characterisation was carried out to confirm the predicted coordination mode of the ligand. Further structural investigation was carried out for complexes when subjected to a variety of synthetic conditions.

Subsequent electrochemical studies characterised the redox behaviour of the synthesised complexes. Voltametric studies of the complexes allowed for estimation of the operating overpotential of the catalysts, as well as development of insights into their behaviour when introduced to O_2.

Catalytic studies were carried out to determine the rate of ORR catalysis, selectivity and mechanism under various conditions. In addition, the catalyst system was screened for activity towards catalytic aerobic oxidation of organic substrates, which could have particular relevance to catalytic industrial processes.

In a separate branch of this work, a mononuclear Co^{II}salen complex bearing a ligand in which we had incorporated a non-coordinating pyridyl moiety to act as a proton relay was synthesised in an attempt to improve the four-electron pathway selectivity of the Co^{II}salen motif.

Chapter 2

Design, Synthesis and Coordination Chemistry

2.1 Schiff Base Phenolate Complexes in Catalysis

2.2 Ligand Design

Among the ORR catalysts found in the literature, one finds a trend between ligand structure, overpotential, turnover frequency (TOF), and selectivity. Often these trends operate with a ‘trade-off’ in each metric. For example, an electron rich ligand normally results in a catalyst with a high TOF but with a high operating overpotential, while electron poor ligands operate at lower overpotentials at the sacrifice of TOF.[52,140] It is also often the case that modifying the overpotential and TOF of an ORR catalyst also influences selectivity.[93] Understanding these trends in ligand activity is of vital importance to the conscious design of a catalyst which fits the desired criteria. In the previous chapter, we have seen that complexes of salen ligands and similar Schiff bases are able to access low overpotentials for the ORR, however mononuclear Schiff base complexes often only catalyse the two-electron ORR pathway. Improving the four-electron pathway selectivity has been achieved in other ligand systems by introducing a second metal ion to the active site of the catalysis. Interestingly however, there has been very little research done in developing dinuclear Schiff base complexes for the ORR with the intention of improving their selectivity towards the four-electron pathway. With this in mind, we set out to develop such a complex.

Following a review of possible ligand motifs, it was decided that a ligand containing a bridging µ-alkoxide would be the simplest way of obtaining a coordination environment in which the two metal atoms are held in close proximity to one-another to facilitate a bridging oxygen binding mode. A few reports show dinuclear Schiff base complexes that fit this criterion with the use of 1,3-bis(2-formylphenoxy)-2-propanol (BFPP) (figure 2.2.1) as the ligand backbone and the precursor to the Schiff base ligand.

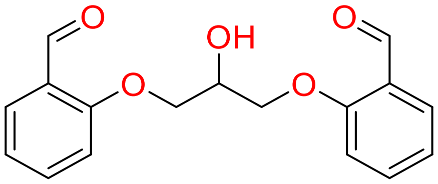

Figure 2.2.1 Structure of BFPP the precursor to Schiff base ligands used to synthesise multinuclear complexes in this work.

Hosseini-Yazdi and co-workers describe a variety of Zn(II) dinuclear Schiff base complexes formed from a template synthesis containing BFPP, $ZnCl_2$ or $Zn(NO_3)_2$ and either ethylene diamine or 1,2-diaminopropane.[141] XRD data of complexes derived from $Zn(NO_3)_2$ and ethylenediamine (Zn-1) or 1,2-diaminopropane (Zn-2) both show distorted octahedral environments with a μ-alkoxide bridging moiety, then coordination of one phenolate ether, imine, and terminal amine occupying the basal plane of each Zn centre. Both Zn-1 and Zn-2 also contain a bridging nitrate anion axially between the two zinc atoms. The final axial site of each zinc atom is filled by either H_2O in the case of Zn-1 or NO_3^- in the case of Zn-2 (Figure 2.2.2).

In a similar set of studies, Golbedaghi and co-workers synthesised a number of dinuclear complexes where the ligand is formed by imine condensation with two equivalents of ethanolamine. Complexation of this ligand with $Cd(NO_3)_2$, $Zn(ClO_4)_2$ or $Cu(ClO_4)_2$ results in the formation of complexes similar in structure to Zn-1 and Zn-2.[142]

All of the studies of complexes with this motif, however, are entirely structural, and voltammetry or catalytic studies were not undertaken. Nonetheless, we decided that modifying this ligand system by using 2-aminophenol derivatives in the imine condensation step instead of alkyl-diamines or ethanolamine could afford the desired salen-like dinuclear motif where the final ligand contains both phenolate and imine donors. The proposed ligand design is shown in Scheme 2.2.1. This type of phenolate-imine ligand derived from BFPP has not yet been reported, however there are similar mononucleating ligands synthesised from salicylaldehyde derivatives and 2-aminophenols,[143,144] however none of these have been examined for ORR activity.

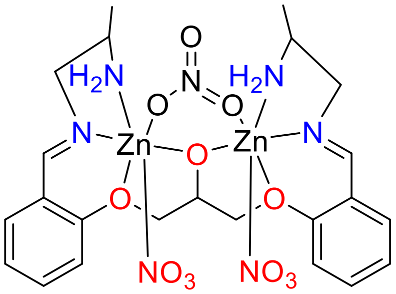

Zn-1

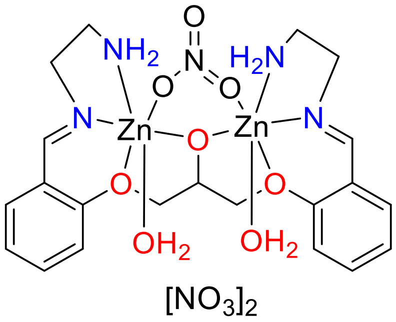

Zn-2

Figure 2.2.2 Structures of dinuclear Zn(II) complexes obtained from BFPP

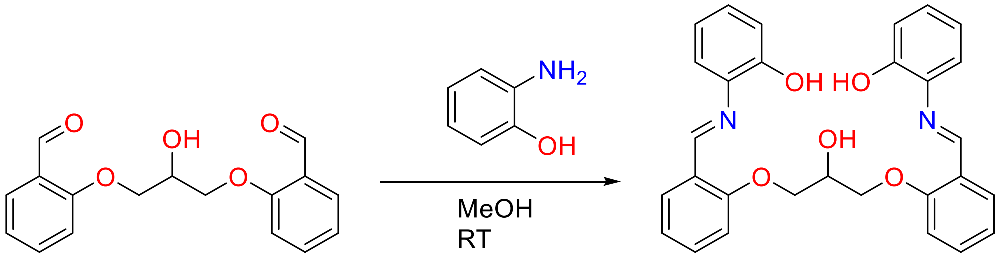

Scheme 2.2.1 Design and structure of the imine phenolate Schiff base system used in this work.

2.3 Ligand Synthesis

2.3.1 Synthesis of 1,3-bis(2-formylphenoxy)-2-propanol

BFPP was easily obtained via a modified literature procedure in which salicylaldehyde is dissolved in warmed aqueous NaOH followed by the dropwise addition of epichlorohydrin.[145] Subsequent nucleophilic attacks (Scheme 2.3.1) by deprotonated salicylaldehyde both substitute the chloride and open the epoxide ring of epichlorohydrin, resulting in the separation of a yellow oil that solidifies upon standing overnight. Recrystallisation from MeOH/H_2O mixtures affords BFFP in 25-35% yields. ^1H NMR of BFPP is shown in Appendix 1.

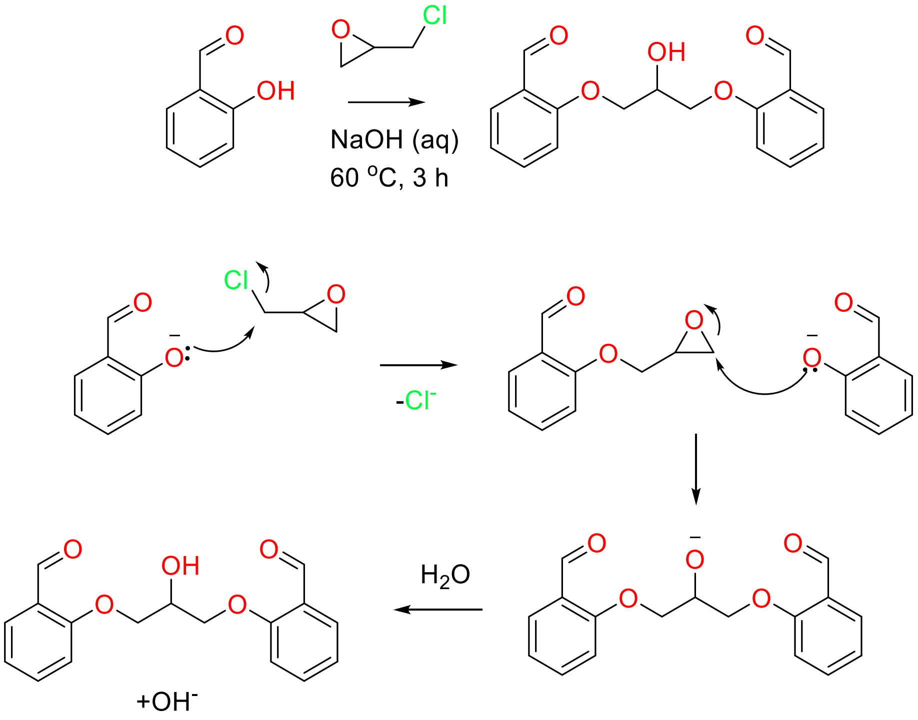

Scheme 2.3.1 Possible mechanism for the formation of BFPP from salicylaldehyde and epichlorohydrin.

The synthesis of BFPP is both highly scalable and inexpensive due to the industrial relevance of the starting materials. In particular, epichlorohydrin is a readily available synthetic building block due to its primary use in the synthesis of epoxy resins.[146]

2.3.2 Attempted synthesis of substituted dialdehyde precursors

We attempted to derivatise BFPP to obtain ligand backbones with varying steric and electronic properties, however in the majority of cases, reactions produced mixtures of unidentified products and polymeric gels. One case in which the undesired product could be characterised was seen when replacing salicylaldehyde in the reaction with 3,5-di-tert-butylsalicylaldehyde. An off-white crystalline material precipitates from the reaction mixture within an hour following addition of epichlorohydrin. ^{1}H NMR of this material shows alkyl signals normally attributed to rigid heterocyclic aliphatic compounds with a great deal less magnetic symmetry than expected of the target compound. Most notably, the absence of a signal with the characteristic aldehyde HCO singlet at 10 ppm indicates a reaction at the carbonyl function. The presence of seven separate signals between 6.0 and 1.75 ppm suggests an unsymmetrical aliphatic chain whereas the predicted spectrum of the target compound should be similar to that of BFPP with only a pentet and doublet in the aliphatic region. Despite all attempts to modify reaction conditions to bias the reaction away from intramolecular cyclisation, such as temperature variance, and very slow addition of epichlorohydrin, the same crystalline off-white product precipitated from the reaction under all circumstances.

With the loss of aldehyde functionality and asymmetry in mind, we consider a reaction in which the alkoxide intermediate following initial ring opening of the epichlorohydrin epoxide attacks the electrophilic aldehyde carbon, then the generated hemiacetal undergoes a second intramolecular cyclisation via nucleophilic substitution of the terminal chloride (Scheme 2.3.2).

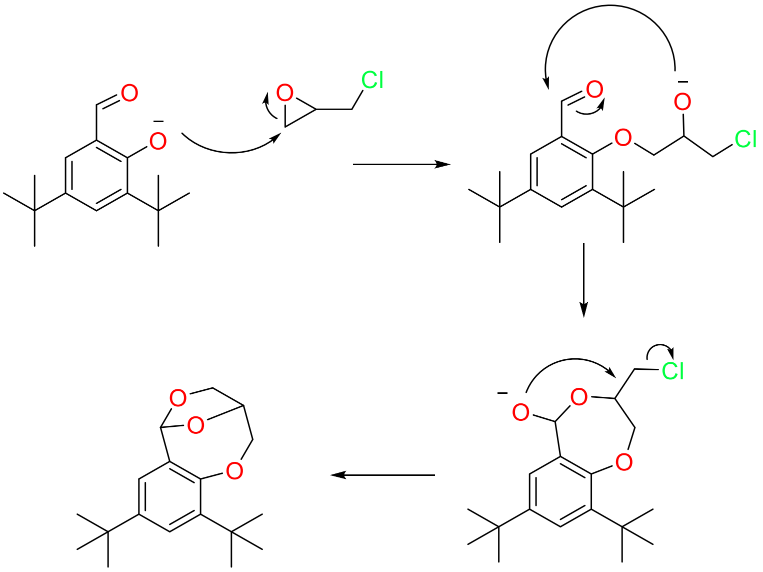

Scheme 2.3.2 Possible mechanism for the intramolecular bicyclic acetal formation from 3,5-di-*tert*-butylsalicylaldehyde and epichlorohydrin

This suggested reaction was confirmed by XRD of the product (figure 2.3.1), showing the predicted bicyclic acetal structure. While this undesired reaction is one of a few that may hinder formation of BFPP derivatives, it is clear that steric hinderance and electronic differences in the starting materials has an influence on the outcome on the range of products obtained from the reaction between epichlorohydrin and salicylaldehyde derivatives and upon further literature search, this undesired intramolecular cyclisation is a common pathway for the reaction between salicylaldehyde derivatives and epichlorohydrin.[147] For this reason, we decided it would be more convenient to alter electronics and sterics by substitution of the 2-aminophenol used in ligand synthesis.

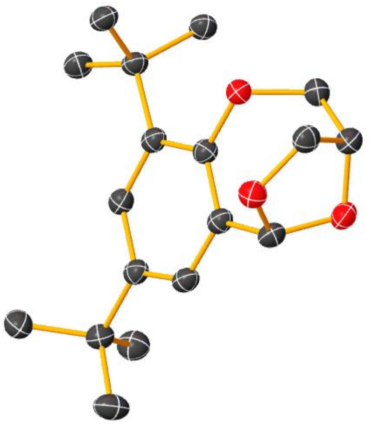

Figure 2.3.1 X-ray crystal structure of the bicyclic acetal product. Thermal displacement ellipsoids are set at the 50% probability level C = grey, O = red.

2.4 Dinuclear Cobalt complexes

2.4.1 Attempts to obtain the organic ligand

The synthesis of the Schiff base ligand from condensation reaction between BFPP and two equivalents of a 2-aminophenol derivative was attempted. While an immediate colour change was observed upon mixing of the two colourless starting materials in MeOH at reflux, no precipitation of the ligand took place. If the reaction solvent was concentrated, the colour of the solution changed from orange-brown to wine red. Upon full removal of the solvent, a burgundy oil remained. ^{1}H NMR of this oil was complex and indicated a mixture of products. Due to the unsuitability of the Schiff base complex towards purification by column chromatography, it was decided that a one-step ligand synthesis and metalation was most appropriate to properly form the desired ligand.

2.4.2 Metalation with $Co(OAc)_2$ and 2-amino-4-methylphenol

Template synthesis of **$Co_2L^{Me}OAc$** to cobalt was achieved by first refluxing $Co(OAc)_2 \cdot 4H_2O$ and BFPP in a 2:1 molar ratio in MeOH to establish an interaction between the metal ions and the O atoms of each coordination compartment in BFPP. Adding a MeOH solution containing two equivalents of substituted 2-aminophenol results in a rapid colour change from purple to dark orange-brown (scheme 2.4.1). After refluxing the solution for two hours, the vivid yellowish brown **$Co_2L^{Me}OAc$** complex is precipitated by the dropwise addition of diethyl ether to the concentrated reaction solution.

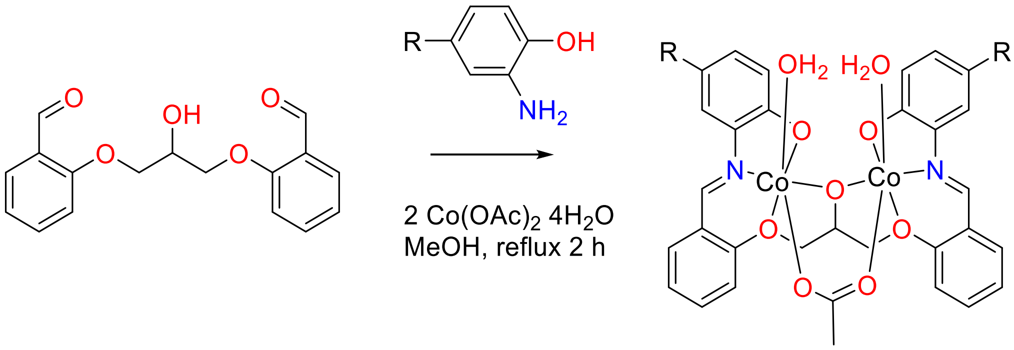

Scheme 2.4.1 Synthesis and proposed structure of **$Co_2L^{Me}OAc$** via template synthesis from BFFP, $Co(OAc)_2$ and 2-amino-4-methylphenol

2.4.3 Characterisation of Co$_2$L^{Me}OAc

Elemental analysis of **Co$_2$L^{Me}OAc** is in good agreement with the proposed structure. ESI-MS for each complex shows a *m/z* value relating to the $[M – OAc^-]^+$ fragment, indicating that ionisation is achieved with the loss of OAc^-. Interestingly, the isotope pattern proceeds in half integer values (i.e., a $[M]_2^{2+}$ ion), this is indicative of a dimerization process where the detected ion fragment is one with twice the mass and twice the charge of the monomer. Of course, the question arises of whether this dimer is the native structure of the complex with two acetates coordinated (i.e. **Co$_4$L^{Me}$_2$(OAc)$_2$**) or if the dimerization process occurs within the mass spectrometer itself. Unfortunately attempts to obtain single crystals of **Co$_2$L^{Me}OAc** suitable for XRD failed and therefore the dimerization phenomenon could not be directly explained at this stage.

Infrared spectroscopy of **Co$_2$L^{Me}OAc** shows the expected loss of the aldehyde band and the gain of a band at 1598 cm^{-1}, relating to coordinated C=N stretching frequencies. The band at 1570 cm^{-1} relates to the asymmetric stretching frequency of the acetate ligand. The position of this band gives information on the acetate binding mode. Different binding modes of mono and dinuclear complexes (figure 2.4.1) show slightly differing infrared bands where asymmetric stretching frequencies range between 1523 and 1630 cm^{-1}.[148] The asymmetric acetate stretching frequency of 1570 cm^{-1} found in **Co$_2$L^{Me}OAc** indicates that the acetate binding mode is likely the predicted bridging between the two cobalt centres.

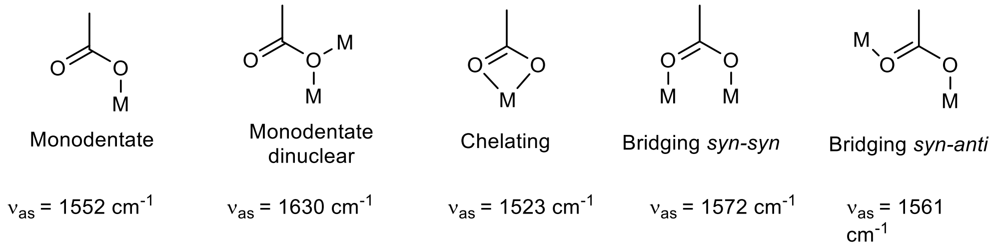

Figure 2.4.1 Summary of the infrared asymmetric stretching frequencies for different coordination modes of acetate ligands

2.4.4 Synthesis of Substituted Co_2L^ROAc complexes

In order to explore the effects of varying the electron donor properties of the ligand, a variety of different 2-aminophenols with different substituents at the 4-position were used in the complexation reaction. The 2-aminophenol derivatives used were: 2-aminophenol, 2-amino-4-*tert*-butylphenol, 2-amino-*tert*-amylphenol, 2-amino-4-trifluoromethylphenol and 2-amino-4-fluorophenol. The reactions were carried out under the same conditions where BFFP was stirred in refluxing MeOH with two equivalents of $Co(OAc)_2{\cdot}4H_2O$ before addition of a MeOH solution containing two equivalents of the substituted 2-aminophenol. A colour change from purple to dark brown was observed in all cases and the product was obtained by concentrating the reaction solution and precipitating the solid with diethyl either.

All complexes obtained by this method showed ESI-MS data consistent with that for Co_2L^{Me}OAc, where the parent ion peak was associated with the predicted mass of the appropriate dinuclear complex with the loss of the bridging acetate. In addition, each complex underwent the same *in situ* dimerization process where the isotope pattern proceeds in half integer values. Calculated and found values for the peak relating to the $[M – OAc^-]^+$ ions for the five complexes are shown in Table 2.4.1.

Complex	m/z [M-OAc]+ calcd.	m/z Found
Co_2L^HOAc	597.03	597.0269
Co_2L^{tBu}OAc	709.2	709.1621
Co_2L^{tAm}OAc	737.2	737.201
Co_2L^FOAc	633.01	633.013
Co_2L^{CF3}OAc	733.1	733.21

Table 2.4.1 Calculated and found ESI-MS values for the $[M – OAc^-]^+$ ion fragments for the family of Co_2L^ROAc complexes.

Elemental analysis of **Co_2L^{CF3}OAc** was consistent with the calculated value for the predicted structure. However, for Co_2L^{tBu}OAc, Co_2L^{tAm}OAc, Co_2L^FOAc and Co_2L^HOAc, elemental analysis was significantly far from the expected values and attempts to fit the data to other possible structures was unsuccessful. In addition, attempts to further purify these complexes did not improve the elemental analysis data.

This unfortunate result meant that while the complexes could be electrochemically characterised and screened for catalytic activity under the assumption that the unidentified impurity was not electroactive, any catalytic studies with these complexes could not be quantitatively analysed to any degree of accuracy.

Infrared spectroscopy of the four complexes showed similar stretching frequencies to $Co_2L^{Me}OAc$. Imine stretching frequencies at c.a. 1600 cm^{-1}, for all complexes indicate that the imine moieties in all cases are coordinated to the metal centres. Bands at c.a. 1570 cm^{-1} are attributed to the acetate ligand, which likely adopts the bridging mode in all circumstances.

2.4.5 NMR study of $\mathbf{Co_2L^{Me}OAc}$

^1H NMR in D_3COD shows the expected paramagnetic broadening for a complex with two d^7 Co(II) ions which are likely in a high spin state.[149] The spectrum is complex and difficult to assign, likely due to conformational flexibility of the ligand, paired with paramagnetic broadening. The ^1H NMR shown in Figure 2.4.2 shows several distinct resonances outside of the normal range for diamagnetic complexes (0-15 ppm). However, also seen are a number of resonances within the diamagnetic region. These resonances can be attributed to either: ^1H nuclei which are situated a suitable distance from the paramagnetic ions to not be paramagnetically shifted; or the ^1H nuclei of a proportion of $\mathbf{Co_2L^{Me}OAc}$ species which have been oxidised by atmospheric oxygen and are therefore diamagnetic. The latter case is supported by the fact that the diamagnetic resonance for imine protons which are situated by only three bonds from the cobalt ions can be observed in their usual position at 10.1 ppm.

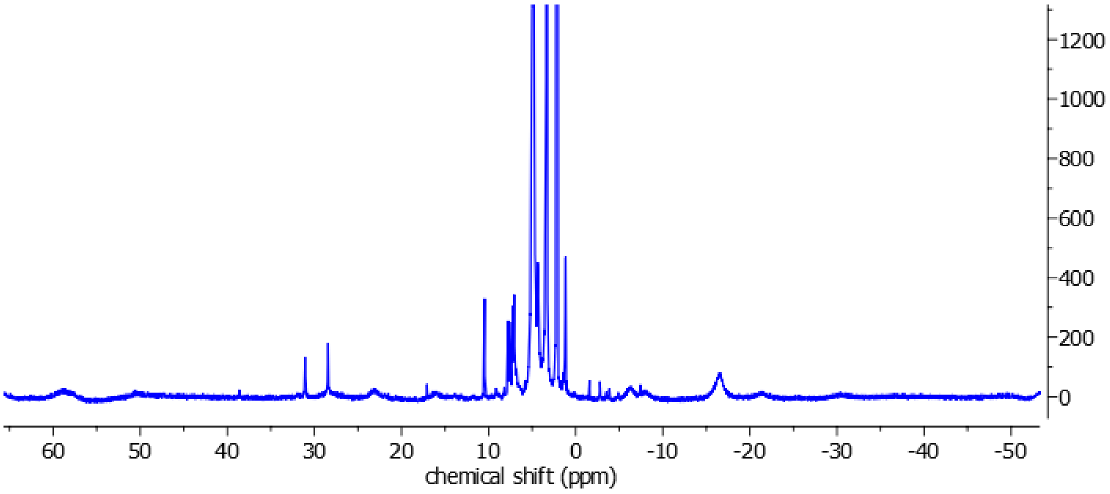

Figure 2.4.2 Paramagnetic ^{1}H NMR of **$Co_2L^{Me}OAc$** in D_3COD

While a classical approach to NMR gives a complicated and difficult to assign spectrum, another NMR method often used to analyse paramagnetic compounds is the Evans' method.[150,151] This method allows determination of magnetic susceptibility and therefore unpaired electron number of a complex by simultaneously measuring the chemical shift of a reference solvent in the presence and absence of a paramagnetic complex.

The Evans' method is performed by inserting a sealed capillary containing a mixture of proteo and deuterated solvent (e.g. 50:1 v/v $CDCl_3$:$CHCl_3$) into an NMR sample with known concentration of the paramagnetic complex in the same solvent mixture and acquiring a ^{1}H NMR spectrum. (Figure 2.4.3) The difference in chemical shift between the reference solvent in the capillary and the solvent containing the paramagnetic complex relates directly to the molar magnetic susceptibility (X_m) via equation 2.3.1

$$X_m = \frac{3\Delta f}{4\pi Fc} \qquad \text{Eqn. 2.3.1}$$

Where Δf is the difference in chemical shift in Hz, *F* is the spectrometer operating radiofrequency in Hz and c is the concentration of complex in mol•cm^{-3}.

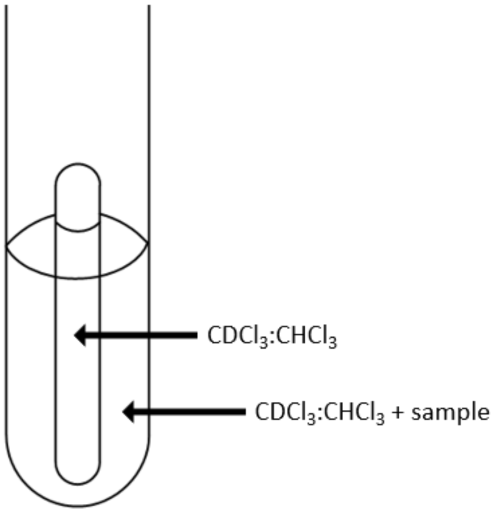

Figure 2.4.3 Diagram of the Evans' method NMR sample containing a capillary of reference solvent

The Evans' method ^{1}H NMR spectrum for a 2.65×10^{-5} mol cm^{-3} solution **$Co_2L^{Me}OAc$** in 50:1 $CDCl_3$:$CHCl_3$ shows two signals relating to $CHCl_3$, one at the expected chemical shift of 7.26 ppm, and another broad signal at 9.30 ppm, relating to the shifted $CHCl_3$ resonance in the presence of a paramagnetic complex. Converting the shift from ppm to Hz and applying equation 1.3.1 gives a X_m value of 0.0184 cm^{3}mol^{-1}, which can be converted to a magnetic moment (μ) via equation 2.3.2.

$$\mu = \sqrt{8X_m T} \qquad \text{Eqn. 2.3.2}$$

Where T is the probe temperature of the spectrometer in K. This gives a magnetic moment of 6.65 B.M. The magnetic moment of a complex relates to its electronic structure via equation 2.3.3

$$\mu = 2\sqrt{[(S+1)] + \left[\frac{1}{4}L(L+1)\right]} \qquad \text{Eqn. 2.3.3}$$

Where S and L are the spin and orbital quantum numbers respectively. However, since first row transition metals tend to have a low orbital contribution to the magnetic moment, equation 2.3.3 can often be simplified to only include contributions from spin (Equation 2.3.4). The Evans' method NMR spectrum of **$Co_2L^{Me}OAc$** is shown in figure 2.4.4.

$$\mu_s = 2\sqrt{S(S+1)} = \sqrt{n(n+2)} \qquad \text{Eqn. 2.3.4}$$

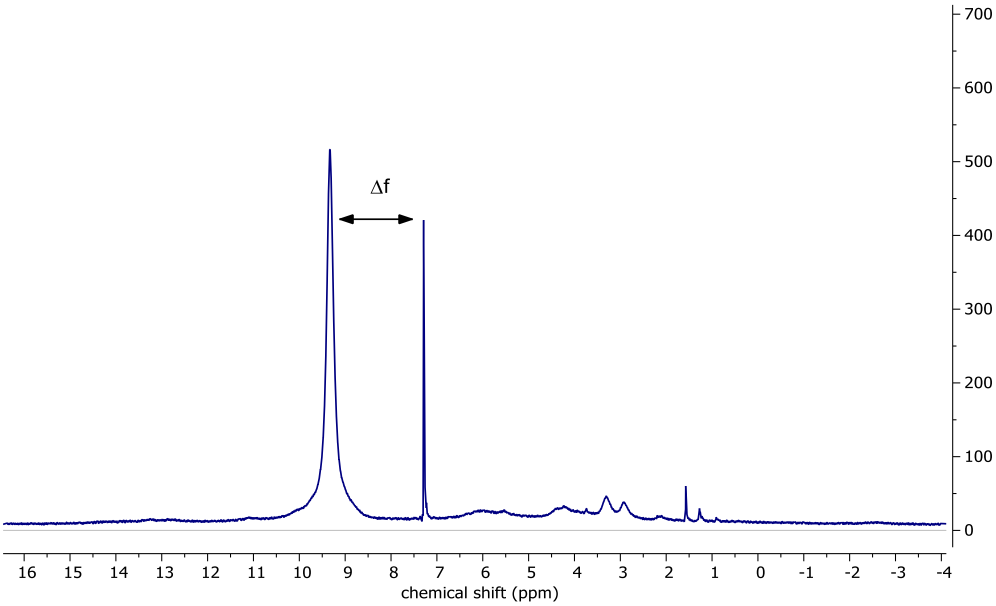

Figure 2.4.4 Evans' method ^{1}H NMR spectrum of **$Co_2L^{Me}OAc$** in 50:1 $CDCl_3$:$CHCl_3$

This is the spin only equation and is the most commonly used equation to determine the number of unpaired electrons in a mononuclear complex. The theoretical spin only magnetic moment for a multinuclear system (μ_M) where magnetic centres do not interact is given by equation 2.3.5.

$$\mu_M = \sqrt{\sum_i \mu_i^2} \qquad \text{Eqn 2.3.5}$$

Where μ_i is the μ_s for each individual magnetic centre. For example, a dinuclear system with two non-interacting S = 3/2 cobalt ions will be estimated to have a total magnetic moment of 5.47 B.M. The magnetic moment of **$Co_2L^{Me}OAc$** was found to be 6.63 B.M, larger than that expected if the two cobalt ions were non interacting. This suggests a contribution from the orbital angular momentum to the ground spin state which is common for Co(II) species. It is also possible that there is some degree of ferromagnetic coupling between the two Co(II) ions, which would increase the overall magnetic susceptibility of the complex.

The magnetic moment of 6.63 B.M. indicates the presence of at least 6 unpaired electron. For a dinuclear d^7 complex, 6 unpaired electrons suggests that both cobalt centres are high spin, with either octahedral or square pyramidal geometry depending on whether the solvent molecules found from elemental analysis are coordinated to the metal centres.

2.5 Trinuclear cobalt complexes

2.5.1 Synthesis of Co$_3$L^{Me}(OAc)$_3$

While attempts to obtain single crystals of **Co$_2$L^{Me}OAc** failed, if the reaction solvent contained an excess of Co(OAc)$_2$, or if vapor diffusion crystallisation was set up with a solution containing 1:1 **Co$_2$L^{Me}OAc** and Co(OAc)$_2$, a small amount of dark brown block shaped crystals were be obtained. The X-ray structure of these crystals (figure 2.5.1) shows a trinuclear structure where the third cobalt atom is coordinated between the two phenolate O atoms, bolstered by bridging between acetates of the two imine coordinated cobalt centres. The coordination sphere of the third cobalt ion is completed by coordination of methanol. The coordinated methanol also exhibits hydrogen bonding to the acetate bound to the second cobalt ion.

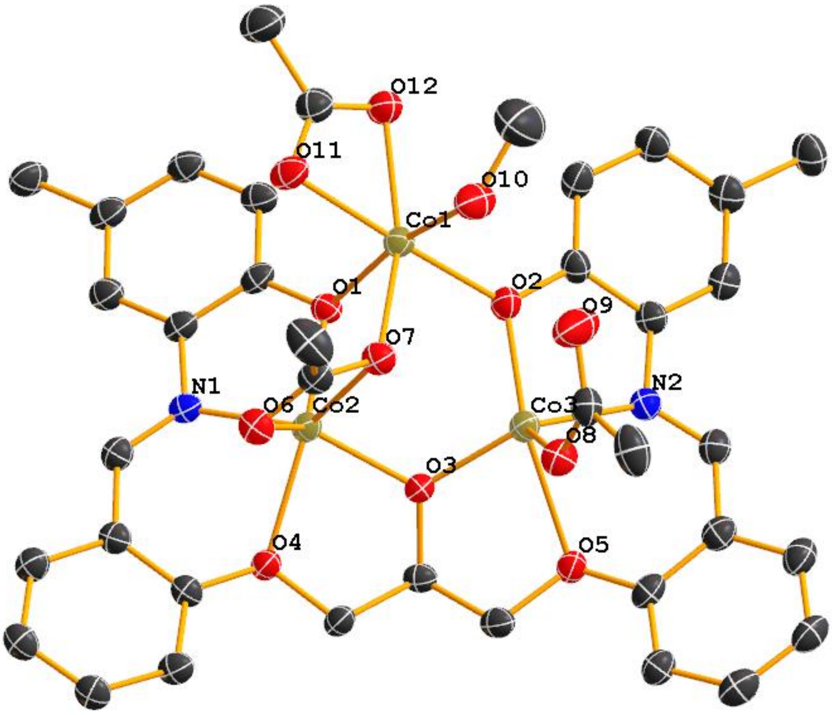

Figure 2.5.1 X-ray crystal structure of **Co$_3$L^{Me}(OAc)$_3$**. Thermal displacement ellipsoids are set at the 50% probability level. Hydrogen atoms are omitted for clarity. C = grey, N = blue, O = red, Co = yellow.

The cyclic trinuclear core of **Co$_3$L^{Me}(OAc)$_3$** contains alternating cobalt and oxygen atoms in a distorted chair structure where the Co2-O3-Co3 angle between the cobalt atoms bridged by the alkoxide is 118.47(14)$^{\circ}$, more obtuse than a classical cyclohexane ring, while the O1-Co1-O2 angle of the third cobalt atom between the phenoxide O atoms is more acute at 87.91(12)°. Co2 shows a four-coordinate NO_3 basal plane consisting of the phenolate (O1), alkoxide (O3) and ether O (O4) atoms and the imine N atom (N1), and is axially coordinated by a chelating acetate ligand (O6, O7). Co3 shows a similar environment however the axial acetate ligand is monodentate (O8), with the second O atom (O9) of the acetate instead hydrogen bonding to the coordinated methanol (O10) of Co1. Both Co2 and Co3 are slightly raised above their four coordinate basal planes and bonds between ether O atoms and their respective cobalt atoms are elongated with lengths of 2.217(3) and 2.331(3) Å respectively. Co1 exhibits a tripodal geometry with the two phenolate O atoms and the acetate ligand of Co2, then a pseudo-octahedral environment is completed with coordination of methanol and the final chelating acetate. Selected bond lengths relating to the coordination environment of **$Co_3L^{Me}(OAc)_3$** are shown below in Table 2.5.1.Relevant bond angles are found in Appendix 3, Table A.4.

Table 2.5.1 Bond lengths of the coordination environment of **$Co_3L^{Me}(OAc)_3$**

Atom	Atom	Length/Å
Co2	O4	2.217(3)
Co2	O1	2.033(3)
Co2	O3	1.976(3)
Co2	O7	2.286(3)
Co2	O6	2.146(3)
Co2	N1	2.077(4)
Co3	O3	1.962(3)
Co3	O2	2.000(3)
Co3	O5	2.331(3)
Co3	N2	2.079(3)
Co3	O8	1.984(3)
Co1	O1	2.072(3)
Co1	O2	2.034(3)
Co1	O7	2.126(3)
Co1	O10	2.103(3)
Co1	O11	2.171(3)
Co1	O12	2.093(4)

If the reaction to obtain **$Co_2L^{Me}OAc$** is carried out with three equivalents of cobalt acetate instead of two, and at room temperature instead of reflux, a brown precipitate forms within a few hours and gives **$Co_3L^{Me}(OAc)_3$** in 79% yield. IR spectroscopy of the bulk **$Co_3L^{Me}(OAc)_3$** powder showed two bands at 1578 and 1556 cm^{-1} demonstrating a variety of acetate binding modes.

The magnetic moment of **$Co_3L^{Me}(OAc)_3$** was calculated to be 7.79 B.M. This value is higher than the calculated value for a tris-d^7 compound (6.61 B.M). The value of 7.79 B.M. suggests a greater contribution of the orbital angular momentum to the overall magnetic susceptibility in the trinuclear complex.

2.5.2 Structure of $Co_3L^{tBu}Cl_3$

If three equivalents of $CoCl_2$ are used in the complexation a similar crystal structure can be obtained for **$Co_3L^{tBu}Cl_3$** (Figure 2.5.2) where the same distorted chair conformation is adopted; however, Co2 and Co3 exist in a more truly square pyramidal structure where the axial sites are occupied by chloride ligands. Co1 is now tetrahedral with only coordination between phenolate O atoms, one chloride and a water molecule. Bond angles of the tetrahedron range between 95.3(3) and 121.6(2)°. Non-classical hydrogen bonding from the water molecule to the chloride ligand of Co3 is the only interaction further supporting the coordination of Co1.

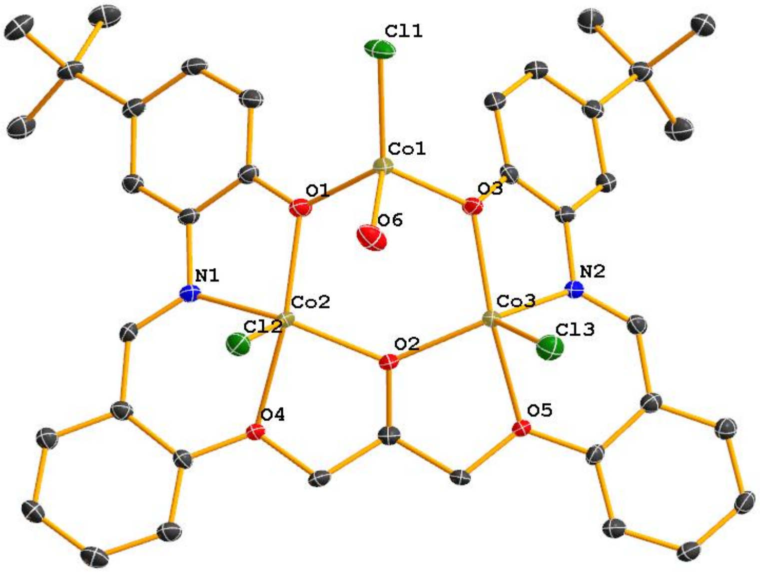

Figure 2.5.2 X-ray crystal structure of **$Co_3L^{tBu}Cl_3$**. Hydrogen atoms are omitted for clarity. Thermal displacement ellipsoids are set at the 50% probability level where C = grey, N = blue, O = red, Co = yellow Cl = green.

While a few suitable crystals of $Co_3L^{tBu}Cl_3$ could be obtained, the bulk product of the reaction did not give an elemental analysis which was consistent with the crystal structure, indicating significant impurity. The source of this impurity is likely a result of formation of both the dinuclear and trinuclear species. Selected bond lengths relating to the coordination environment of **$Co_3L^{tBu}Cl_3$** are shown below in Table 2.5.2. Relevant bond angles are listed in Appendix 3, Table A.5

Table 2.5.2 Bond lengths of the coordination environment of **$Co_3L^{tBu}Cl_3$**

Atom	Atom	Length/Å
Co3	Cl3	2.278(3)
Co3	O3	2.059(6)
Co3	O2	1.998(7)
Co3	O5	2.216(6)
Co3	N2	2.051(8)
Co2	Cl2	2.292(3)
Co2	O2	1.966(7)
Co2	O1	2.035(6)
Co2	O4	2.209(6)
Co2	N1	2.045(8)
Co1	Cl1	2.227(2)
Co1	O3	1.940(7)
Co1	O1	1.956(7)
Co1	O6	2.001(7)

The bond lengths between Co2 and Co3 and the alkoxide bridge are 1.966(7) and 1.998(7) Å respectively, slightly longer than the corresponding bonds in **$Co_3L^{Me}(OAc)_3$**. The bond lengths of Co1 with the two phenolate donors (O1 and O3) are 1.956(7) and 1.940(7) Å respectively, approximately 0.05 Å shorter than the corresponding bonds in **$Co_3L^{Me}(OAc)_3$** This reduction in bond length is likely attributed to the increased electron density about the phenolate moieties arising from the inductively donating *tert*-butyl groups in place of methyl groups in **$Co_3L^{Me}(OAc)_3$**. Bonds between Co2 and Co3 with imine donors N1 and N2 are 2.045(8) and 2.051(8) Å respectively, again slightly shorter than the corresponding bonds in **$Co_3L^{Me}(OAc)_3$** due to increased donation from *tert*-butyl groups.

2.5.3 Structure of $Co_3L^H(OAc)_3$

While bulk powders of **$Co_3L^H(OAc)_3$** could not be obtained in sufficient purity for further studies, it was possible to obtain a few crystals suitable for diffractometry by vapour diffusion of Et_2O into a concentrated MeOH solution of the crude complex.

The crystal structure of **$Co_3L^H(OAc)_3$** shows interesting structural differences to its analogue **$Co_3L^{Me}(OAc)_3$**. Where **$Co_3L^{Me}(OAc)_3$** crystallises as a relatively open-structured planar structure where the two imine bonded cobalt ions show square pyramidal geometry, **$Co_3L^H(OAc)_3$** crystallises as a closed structure where the imine coordinated cobalt atoms (Co2 and Co3) display distorted trigonal bipyramidal geometry. The ligand is twisted out of planarity and two acetates bridge between imine coordinated cobalt ions and the third cobalt ion. The overall structure has a rotational axis of C2v symmetry which runs from the C-C bond of the non-bridging acetate and through the C-O bond of the alkoxide bridging group. Views of the symmetrical $Co_3L^H(OAc)_3$ structure are shown in Figure 2.5.3.

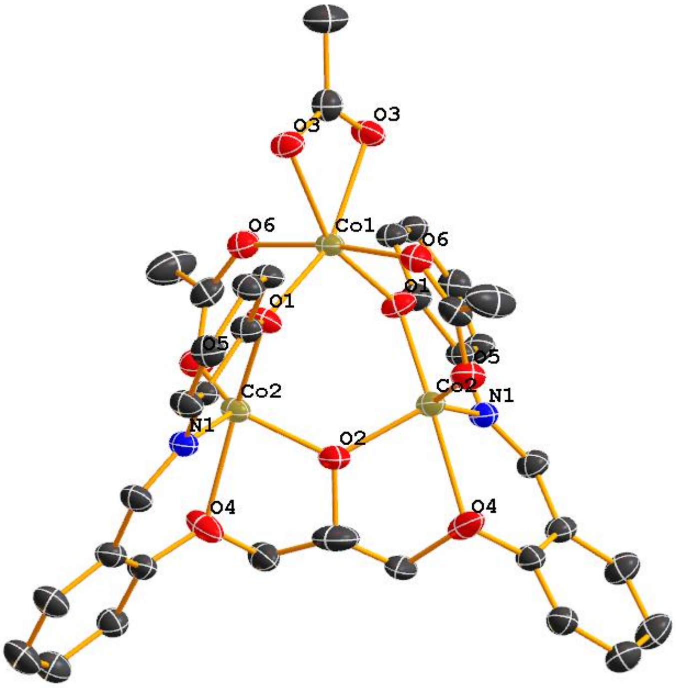

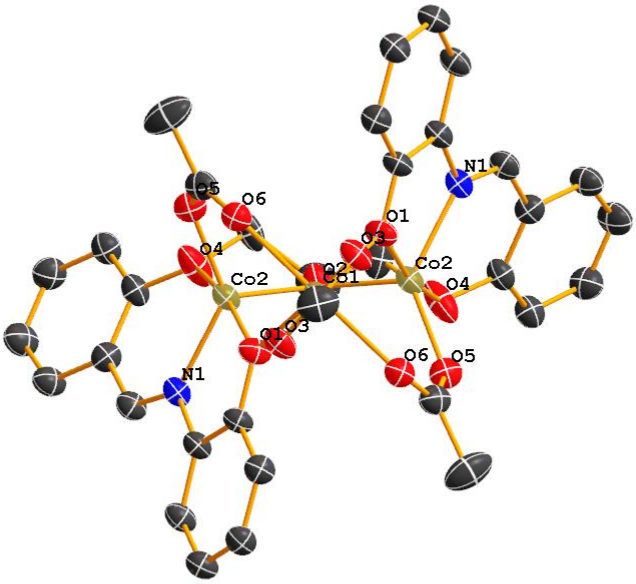

Figure 2.5.3 Crystal structure of $Co_3L^{H}(OAc)_3$ represented as a front view (top) and a view down the C2v axis of symmetry (bottom) Hydrogen atoms are omitted for clarity. Thermal displacement ellipsoids are set at the 50% probability level where C = grey, N = blue, O = red, Co = yellow

Due to the C2v symmetry of **$Co_3L^{H}(OAc)_3$** the asymmetric unit contains half of the full trinuclear complex and as such atoms duplicated from the combination of two asymmetric units are equivalent. Selected bond lengths relating to the coordination environment of **$Co_3L^{H}(OAc)_3$** are shown below in Table 2.5.3. Relevant bond angles are listed in Appendix 3, Table A.6

Table 2.5.3 Bond lengths of the coordination environment of **$Co_3L^{H}(OAc)_3$**

Atom	Atom	Length/Å
Co1	O3	2.165(3)
Co1	O1	2.016(3)
Co1	O6	2.116(3)
Co2	O5	1.959(3)
Co2	O2	1.944(2)
Co2	N1	2.056(3)
Co2	O4	2.240(3)

The bond length between Co2 and the alkoxide bridge (O2) is 1.944(2) Å, slightly shorter than the corresponding bonds in **$Co_3L^{Me}(OAc)_3$**. The bond length between Co1 and the phenolate donor (O1) is 2.016(3) Å, slightly shorter than the corresponding bond in **$Co_3L^{Me}(OAc)_3$** despite the reduced electron donation from the *para* group to the phenolate moiety. The bond length between Co2 and the imine donor atom is 2.056(3), slightly longer than the corresponding bonds in **$Co_3L^{Me}(OAc)_3$**, likely due to the reduced electron donation from the *para* H atom in place of methyl groups of the phenolate moiety.

2.6 Tetranuclear Cobalt Complexes

2.6.1 Tetranuclear Complexes in Catalysis

Cubane-like structures of metal complexes with ligands containing multiple oxygen donors are relatively common in the literature and arise from the availability of the lone pairs of O atoms to coordinate to the metal centres of other monomers present.[152–154] The different forms of cubane structures are presented in figure 2.6.1.

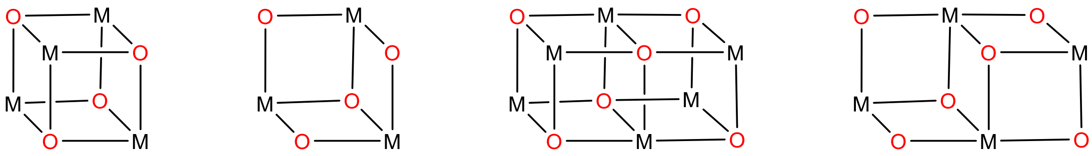

Cubane Defective Cubane Dicubane Defective Dicubane

Figure 2.6.1 Structures of four cubane clusters

The most well-known of these structures is the pure cubane in which four metal ions and four non-metal donors occupy alternating vertices of a cube. The active site of nature's highly efficient photosynthesis catalyst, photosystem II (PSII)[155,156], adopts this geometry with a Mn_3CaO_4 core and facilitates photocatalytic water oxidation with a TOF of 10^7 s^{-1} and a TON of 500.[157] As a highly active water oxidation catalyst (WOC), much research has been undertaken to mimic the active site of PSII. One notable biomimetic catalyst of PSII was synthesised by Patzke and co-workers in 2013 where a simple $Co^{II}_4O_4$ cubane (figure 1.5.4) bearing 2-hydroxymethylpyridine and acetate ligands photocatalyses the oxidation of water in the presence of $[Ru(bpy)_3]^{2+}$ as a photosensitiser and $Na_2S_2O_8$ as the sacrificial oxidant with moderate TON of 40 and competitive TOF 7 s^{-1} in slightly alkaline conditions.[158]

The oxygen evolution mechanism of PSII has been proposed to operate via the lability of the Mn-O bond where partial abstraction of the oxygen atom from the cubane structure by the pendant Mn ion. Coordination of a water molecule to the cubane Mn ion and subsequent deprotonation generates a hydroxyl ligand. Oxidative coupling of the hydroxo and oxyl ligands in close proximity yields the hydroperoxo intermediate which can undergo a PCET step to liberate O_2 and reform the cubane structure.[159]

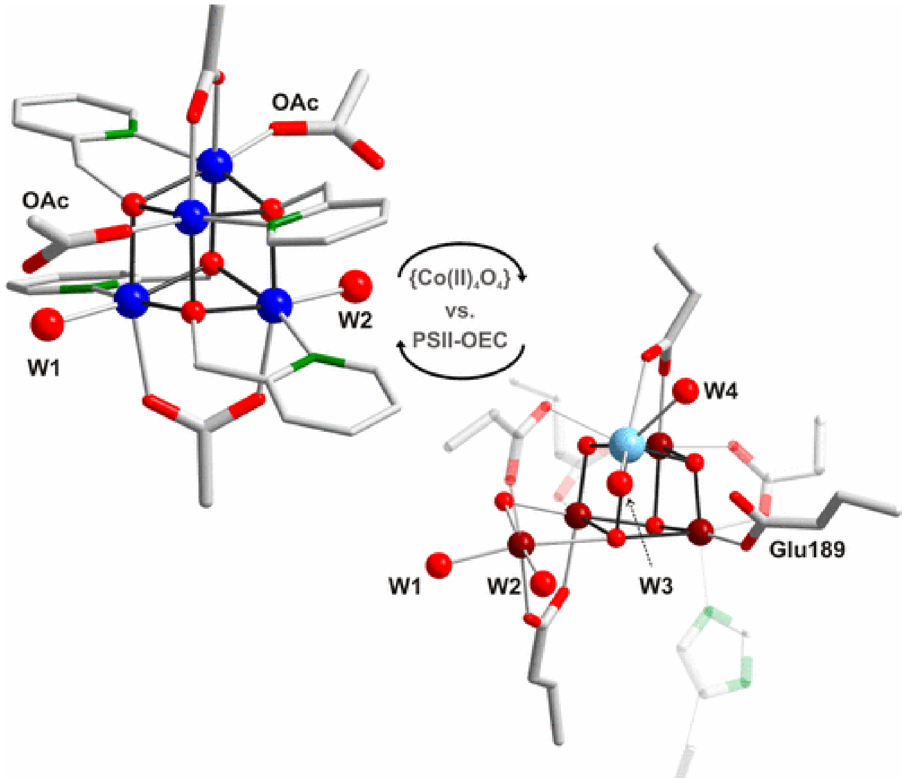

Figure 2.6.2 Crystal structure of a biomimetic WOC synthesised by Patzke and co-workers (Co, blue; O, red; N, green; C, grey) (Left) and the active site of PSII (Mn, dark red; Ca, light blue) (right). Reprinted with permission from reference 157. Copyright 2022 American Chemical Society.

The presence of the pendant Mn ion outside of the cubane core of PSII is vital to the oxygen evolving activity of the complex. It has been proposed that the Co clusters studied by Patzke operate via a mechanism where two aqua ligands are deprotonated in close proximity where they can form either a peroxo bridge if the aqua ligands were on separate cobalt ions, or a side on peroxo ligand if both aqua ligands are on the same cobalt ion. Through this mechanism, it is not necessary for the cubane structure to become opened by oxo extraction and explains the moderate WOC activity of stable Co_4O_4 cubane clusters without pendant groups.

While cubane catalysis, particularly WOC[160,161] is prosperous in the literature,[162] M_4-O_6 defective dicubane structures are less widely studied. The most common catalytic reactions studied with defective dicubane clusters are those undertaken in biology by catechol oxidase[163] or phenoxazinone synthase[164] where substrates such as 3,5-di-*tert*-butylcatechol (DTBC) are oxidised to the corresponding 3,5-di-*tert*-butylquinone (DTBQ) or 2-aminophenol is oxidatively homocoupled to form aminophenoxazinone (APX) respectively. It is important to note however that while these catalysts show a defective dicubane structure in the solid state, upon dissolution it is not uncommon for a mononuclear active site to be liberated by solvolysis of the cluster.

One such example of a defective dicubane complex in the solid state was synthesised by Ghosh and co-workers where a hexadentate ligand produced by Mannich reaction between 2-methoxyphenol and N,N'-dimethylethylenediamine.[165] Complexation of the ligand with two equivalents of cobalt acetate in the presence of sodium azide or sodium thiocyanate yields a tetranuclear defective dicubane complex comprising of two mononuclear units which each coordinate to both amines and phenolates of the ligand. The two units are linked together by cobalt ions coordinated to the 2-methoxyphenolate portions of each ligand and further supported by bridging of azide or thiocyanate ligands.

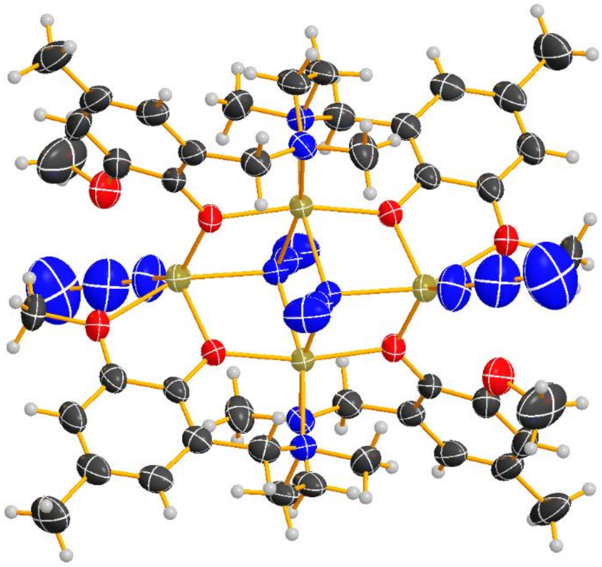

Figure 2.6.3 Crystal structure of the defective dicubane complex synthesised by Ghosh and co-workers demonstrating phenoxazinone synthase activity in MeOH solution.

Mass spectrometry results, however, show that upon dissolution into MeOH, the same solvent used for catalytic reactions with 2-aminophenol, the $Co_4L_2(N_3)_4$ tetranuclear structure is not retained and the catalytically active species is a neutral mononuclear CoL with likely release of $Co(N_3)_2$.

2.6.2 Magnetism of Cubane Clusters

Aside from catalysis, multinuclear cobalt clusters see most attention in the field of single molecule magnets (SMM).[166,167] SMMs have interesting applications in data storage and computing as potential qubits[168] and are defined as a complex with a non-zero magnetic ground state ($S > 0$) and a large energy separation between the ground and excited states. In multinuclear complexes, a non-zero magnetic ground state can be achieved by influencing the exchange interaction (J) between metal centres where ferromagnetic exchange interactions (i.e. spins are aligned in the ground state) give higher ground states and antiferromagnetic coupling (i.e. spins are opposing in the ground state) give lower or zero ground states as depicted for a simple dinuclear system in Figure 2.6.4.

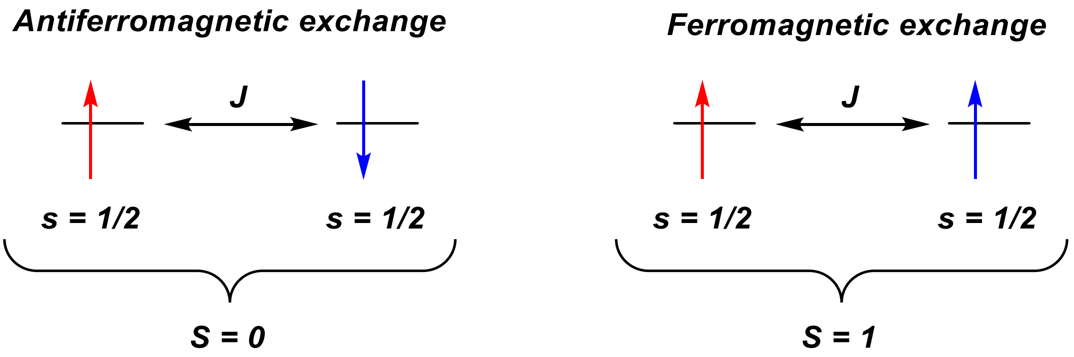

Figure 2.6.4 Diagram illustrating the ground spin state for ferromagnetic and antiferromagnetic exchange interactions in a simple system where two unpaired electrons are coupled by an exchange interaction J

Antiferromagnetic interactions often dominate in multinuclear systems, however there is a higher tendency for complexes where the M-L-M bond angle is close to 90° to prefer ferromagnetic interactions due to favourable overlap of the magnetic orbitals.[169,170] The geometry of cubane clusters means that these complexes normally satisfy this favourable magnetic orbital overlap criteria to encourage ferromagnetic exchange interactions. Cubane clusters, including defective dicubane clusters therefore commonly have non-zero magnetic ground states and often are examined for SMM properties.[171]

2.6.3 Synthesis of $\mathbf{Co_4L^{Me}{}_2(BF_4)_2}$

To compare the characteristics of the $\mathbf{Co_2L^{R}OAc}$ monomer and the $\mathbf{Co_4L^{R}{}_2(OAc)_2}$ dimer, a structural analogue must be synthesised. Since by mass spectrometry, the dimer clearly forms upon loss of OAc^-, dimerization should be achieved by abstraction of OAc^- via salt metathesis. This was initially undertaken with $\mathbf{Co_2L^{Me}OAc}$ in which a saturated solution of $NaBF_4$ was added dropwise to a concentrated methanol solution of the complex. Over the next hour, large, brown, block shaped crystals suitable for analysis by XRD formed.

The crystal structure of the salt metathesis product (Figure 2.6.5) confirms the formation of $\mathbf{Co_4L^{Me}{}_2(BF_4)_2}$ where the structure can indeed be considered a dimer of two $\mathbf{Co_2L^{Me+}}$ units, bound together by coordination of the remaining lone pairs of

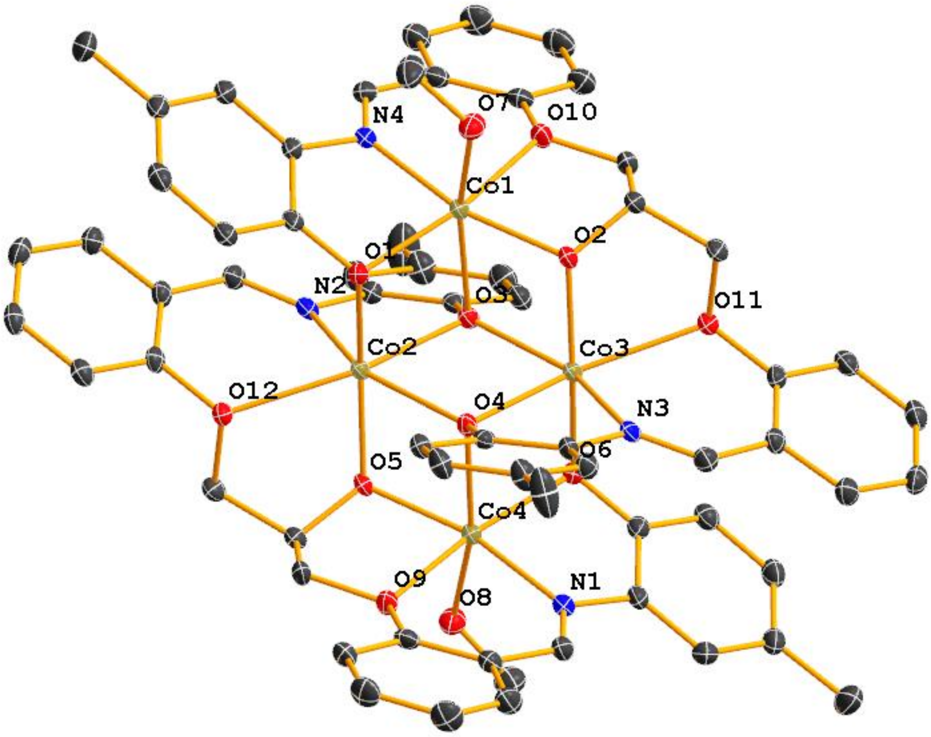

Figure 2.6.5 X-Ray crystal structure of $\mathbf{Co_4L^{Me}{}_2(BF_4)_2}$. Non-coordinating BF_4^- counter ions and hydrogen atoms are omitted for clarity. Thermal ellipsoids are set at the 50% probability level where C = grey, N = blue, O = red, Co = yellow.

phenoxy O atoms in the ligand of the first monomer unit with the vacant Co coordination sites of the second monomer unit. The asymmetric unit of the tetranuclear complex comprises only of half the complex, i.e., one **Co_2L^{Me}** unit. Each **Co_2L^{Me+}** unit shows a similar coordination mode to the trinuclear analogues, where each cobalt centre is coordinated to a phenolate O atom, an imine N atom and the neutral ether O atom. Each cobalt atom of the defective dicubane exhibits distorted octahedral geometry The two cobalt atoms are bridged by a µ-alkoxide as shown in the zinc complexes from the literature discussed earlier this chapter. The ligand structure around the dimer shows three layers of coordination. The top and bottom layers are symmetrical where four chelators of the same ligand occupy the square basal plane. The cobalt ions in the top and bottom coordination layers are also coordinated axially by methanol, and by the phenolate of the ligand that is not involved in the basal plane. The middle coordination layer includes two cobalt ions which are both equidistant from the top and bottom cobalt ions. Each cobalt in the middle layer has a square basal plane consisting of three chelators from the same ligand, and the fourth from the other ligand. Axial sites in this case are occupied by the phenoxide and alkoxide found in the basal plane of the top and bottom layers. Torsion angles between aryl rings from salicyclaldehyde and 2-aminophenol moieties of the same coordination pocket are 30-31^o in the top and bottom layers, while those of the middle layer lie 41-42^o out of planarity.

Selected bond lengths relating to the coordination environment of **$Co_4L^{Me}{}_2(BF_4)_2$** are shown below in Table 2.6.1. Relevant bond angles are listed in Appendix 3, Table A.7

Table 2.6.1 Bond lengths of the coordination environment of **$Co_4L^{Me}{}_2(BF_4)_2$**

Atom	Atom	Length/Å
Co2	O4	2.0964(15)
Co2	O1	1.9750(16)
Co2	O3	2.2439(16)
Co2	O5	2.0047(16)
Co2	O11	2.3208(16)
Co2	N3	2.1020(2)
Co1	O2	2.0536(15)
Co1	O1	1.9726(16)
Co1	O3	2.2077(16)
Co1	O7	2.1258(18)
Co1	O10	2.1939(16)
Co1	N4	2.0450(2)
Co3	O4	2.1812(16)
Co3	O2	2.0331(16)
Co3	O3	2.0861(15)
Co3	O12	2.3123(16)
Co3	O6	1.9977(16)
Co3	N2	2.1010(19)
Co4	O4	2.2504(16)
Co4	O5	2.0408(15)
Co4	O6	1.9636(16)
Co4	O9	2.2030(15)
Co4	O8	2.1514(18)
Co4	N1	2.050(2)

The bonds between Co1 and Co4 and their respective phenolate donors (O1 and O6) are 1.9726(16) and 1.9636(16) Å respectively, shorter than those present in **$Co_3L^{Me}(OAc)_3$**, signifying a significant stabilisation of these bonds when the structure is dimerised, likely due to the complex adopting a sterically and electronically preferential structure. This trend in the reduction of bond lengths in the coordination environment between trinuclear and tetranuclear structures continues for Co-N and Co-O (ether donor) bonds, however, the Co-O (alkoxide donor) bonds are longer in the tetranuclear than the trinuclear. Co-O bond lengths occupy approximately the same range for all four cobalt ions, suggesting all exist in the same oxidation state, whereas known mixed valence Co(II)-Co(III) defective dicubanes show variable Co-O bond lengths depending on the oxidation state of the cobalt ions.[172]

The Co_4O_6 core (depicted more clearly in Figure 2.6.6) adopts a 'defective dicubane' geometry (i.e., two facially fused cubane structures where the two extreme vertices are missing) where cobalt ions in the defective dicubane core are alternated by O atoms either from the alkoxide or phenolates in the ligand. The alkoxides bridge cobalt ions originating from the same monomer **Co_2L^{Me+}** unit, and phenolates bridge cobalt ions from the two different **Co_2L^{Me+}** units.

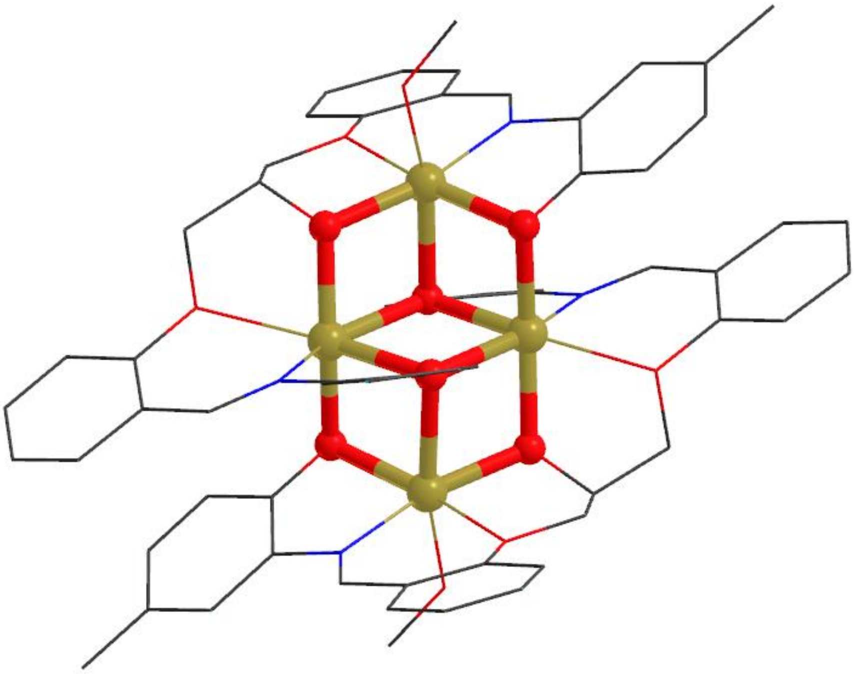

Figure 2.6.6 X-Ray crystal structure of **$Co_4L^{Me}{}_2(BF_4)_2$** highlighting the defective dicubane Co_4O_6 core of the complex.

The salt metathesis reaction was also performed with NH_4PF_6 and $NaClO_4$ with the aim of altering the solubility of the resulting tetranuclear complexes. Similar results were obtained in each case, with supporting crystal structures confirming isostructurality regardless of the counter ion introduced, however **$Co_4L^{Me}{}_2(BF_4)_2$** remained the most soluble in all solvents and is only completely soluble in DMF and DMSO.

Other tetranuclear crystal structures were obtained by varying the substituted 2-aminophenol. Through this method, it was possible to obtain XRD data for **$Co_4L^{H}{}_2(PF_6)_2$** and **$Co_4L^{OMe}{}_2(PF_6)_2$**. Both showed the same defective dicubane structure as seen before, with similar bond angles and lengths. **$Co_4L^{H}{}_2(PF_6)_2$** was crystallised from MeCN solution and shows coordinated MeCN in the positions occupied by MeOH in other tetranuclear structures. The crystal structures for these two complexes are shown in Figure 2.6.7. Relevant bond lengths and angles of

$Co_4L^{OMe}{}_2(PF_6)_2$ are given in Appendix 3, Table A.8 and Table A.9 respectively and **$Co_4L^{H}{}_2(PF_6)_2$** are given in Appendix 3, Table A.10 and A.11 respectively.

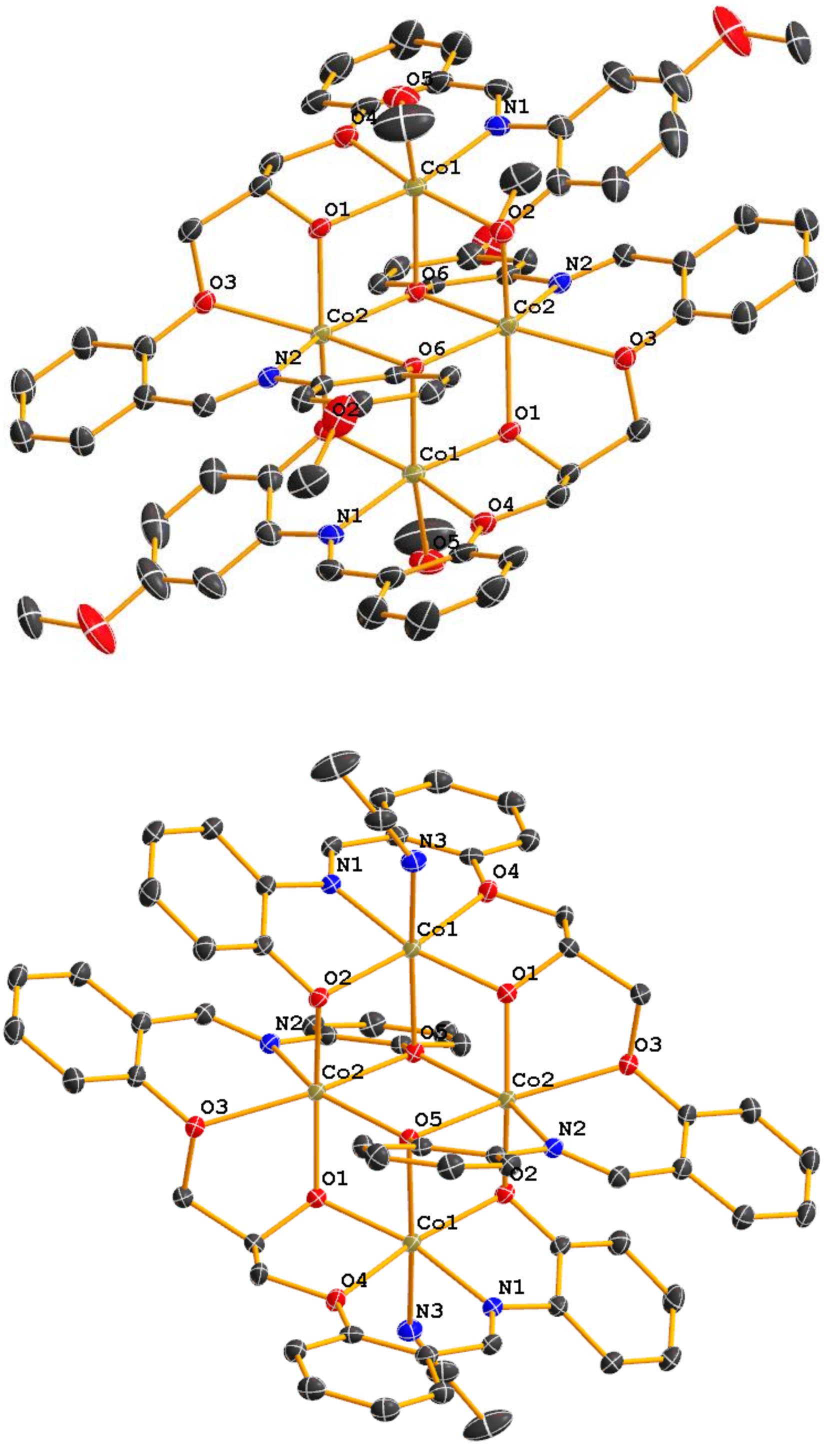

Figure 2.6.7 X-ray crystal structures of **$Co_4L^{OMe}{}_2(PF_6)_2$** (top) and **$Co_4L^{H}{}_2(PF_6)_2$** (bottom). Hydrogen atoms and non-coordinating solvents and anions are omitted for clarity. Thermal ellipsoids are set at the 50% probability level where C = grey, N = blue, O = red, Co = yellow.

While abstraction of acetate from **$Co_2L^{Me}OAc$** by NH_4PF_6 in MeOH results in dimerization to form a stable tetranuclear complex, we were interested in abstracting acetate without dimersation. To achieve this, the axial sites of the dinuclear complex should be occupied by an external ligand before coordination of phenolate O atoms can initiate dimerization. When **$Co_2L^{Me}OAc$** is dissolved in pyridine, no visible reactions occur and no colour changes are observed over several days, however when a large excess of NH_4PF_6 is added to the solution, a gradual colour change from yellow-brown to wine red is observed over a few days. Removal of the solvent and subsequent washing with diethyl ether yields a burgundy diamagnetic solid, indicating complete oxidation of the Co(II) centres to Co(III) in the presence of atmospheric oxygen. This result indicates that spontaneous oxidation of the Co(II) centres is slow and reversible while the bridging acetate is present, even in highly electron rich pyridine solution. If only a stoichiometric amount of pyridine is added to a methanol solution of **$Co_2L^{Me}OAc$** before addition of NH_4PF_6 however, the same tetranuclear as if no pyridine is present was obtained, where methanol still occupies the axial sites of the defect dicubane cluster.

While the resulting diamagnetic complex was difficult to characterise and any structural proposal would be dubious, it is an important consideration that spontaneous, irreversible oxidation of the Co(II) centres only proceeds following the abstraction of the acetate ligand.

2.6.4 Magnetic properties of $Co_4L^{Me}{}_2(BF_4)_2$

The solution state magnetic susceptibility of $Co_4L^{Me}(BF_4)_2$ was obtained by the same method as di and trinuclear complexes, the magnetic moment of 9.20 B.M at 300 K. is higher than the theoretical value for four non-interacting cobalt atoms (7.64 B.M.). All three structures (di, tri, and tetranuclear) have approximately the same difference between theoretical and experimental magnetic moments at room temp, showing that exchange interactions and orbital angular momentum contributes to the magnetism by a similar amount as the number of metal centres increases.

2.7 Coordination to Other Metals

2.7.1 Metalation to Zinc

When $Zn(OAc)_2$ is used in the template synthesis with BFPP and 4-methyl-2-aminophenol in MeOH solution, a bright yellow solid precipitates within minutes, unlike the analogous reaction with $Co(OAc)_2$ which requires precipitation with diethyl ether. Elemental analysis of the sample is out of agreement with the calculated values for a **$Zn_2L^{Me}(OAc)$**, however good agreement is achieved when considering the trinuclear complex **$Zn_3L^{Me}(OAc)_3$** (Scheme 2.7.1).

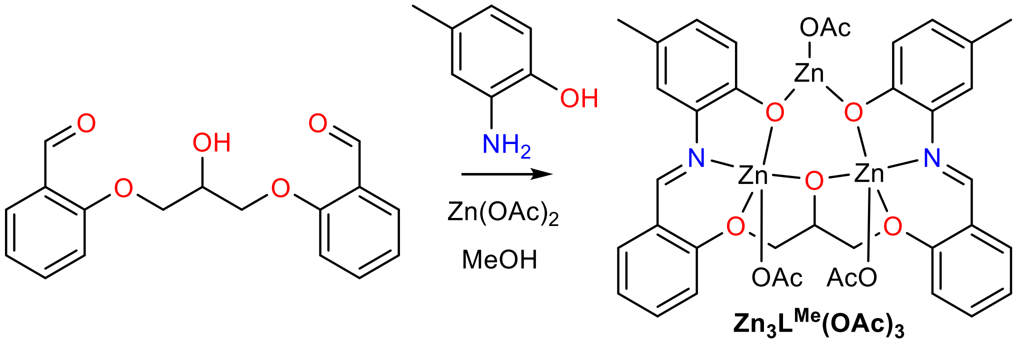

Scheme 2.7.1 Synthesis of $Zn_3L^{Me}(OAc)_3$

The formation of **$Zn_3L^{Me}(OAc)_3$** is supported by the ^1H NMR spectrum in d_6-DMSO (Figure 2.7.1) which shows five signals in the aromatic region. The signals at 7.30 and 6.95 ppm each integrate to four protons, indicating the overlapping of two different environments in each case, resulting in a total of seven aromatic proton environments. The broad multiplet at 4.57 ppm is assigned to the proton of the carbon bearing the alkoxide bridge, and the signals of the adjacent alkyl protons appear at 4.43 and 4.24 ppm. The separation between these two signals indicates structural asymmetry of the alkyl chain upon coordination to Zn(II). The signal at 1.63 is attributed to the CH_3 protons of acetate, this signal integrates to 9, showing the presence of three acetate equivalents, supporting the elemental analysis data. The formation of a trinuclear complex even when only two equivalents of $Zn(OAc)_2$ are used indicates that the trinuclear zinc structure is thermodynamically favoured, contradictory to that seen by coordination of cobalt where three equivalents of metal salt must be used to obtain the trinuclear structure.

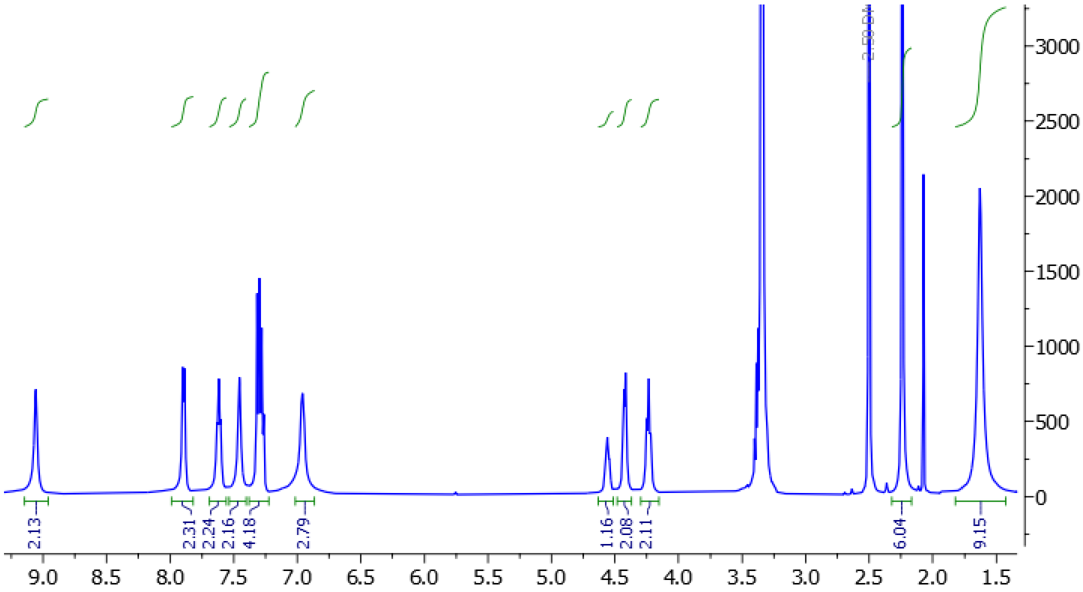

Figure 2.7.1 ^{1}H NMR spectrum of **$Zn_3L^{Me}(OAc)_3$**

Infrared spectroscopy shows similar bands to that of **$Co_2L^{Me}OAc$**, most notably, a band at 1570 cm^{-1}, indicating that acetate ligands coordinate with either a bidentate or chelating binding mode shown in figure 1.3.2.

Single crystals of **$Zn_3L^{Me}OAc_3$** were obtained by vapour diffusion of diethyl ether into a DMF solution. XRD confirms the trinuclear structure (Figure 2.7.2), however unlike **$Co_3L^{Me}(OAc)_3$** and **$Co_3L^{tBu}(OAc)_3$**, the ligand is twisted between the two aryl regions such that the two phenolate moieties are almost orthogonal to one another. The twisting of the ligand is due to the difference in configuration between Zn2 and Zn3. Zn2 has the alkoxide O3 and the imine N2 *cis* to one another, while Zn3 has the alkoxide O3 and the imine N1 *trans* to one another. In **$Co_3L^{Me}(OAc)_3$**, both of these configurations are *trans* and therefore the ligand has increased planarity. Zn2 and Zn3 adopt a square pyramidal geometry where the axial site is coordinated by a monodentate acetate in the case of Zn3, and for Zn2, an acetate which bridges between Zn2 and Zn1. Zn1 is coordinated by the two phenoxy O atoms, a chelating acetate, and the bridging acetate to Zn2. Interestingly, unlike **$Co_3L^{Me}(OAc)_3$** and **$Co_3L^{tBu}Cl_3$**, **$Zn_3L^{Me}(OAc)_3$**, the Zn_3O_3 core of the complex adopts a boat-like conformation instead of a chair.

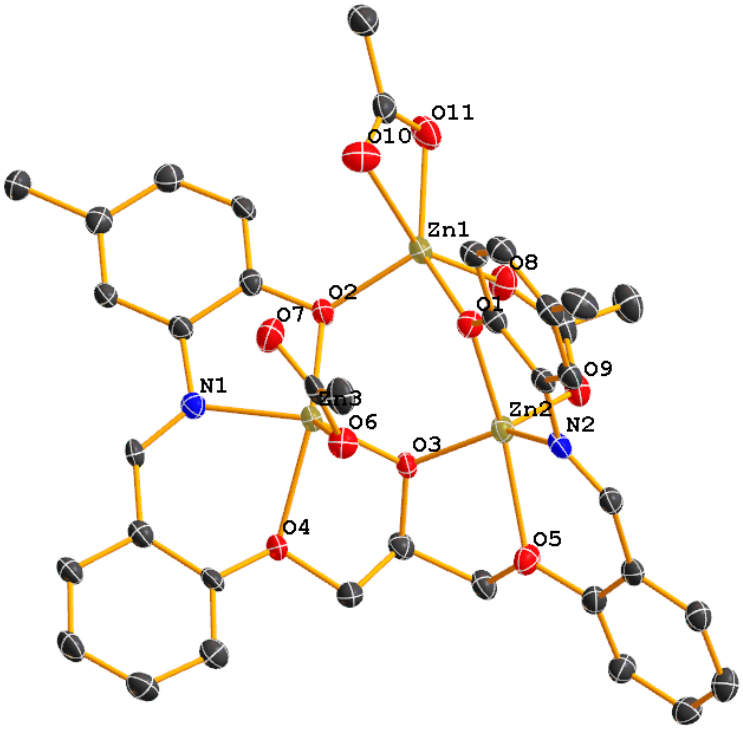

Figure 2.7.2 X-Ray crystal structure of **Zn$_3$L^{Me}(OAc)$_3$**. Hydrogen atoms are omitted for clarity. Thermal ellipsoids are set at the 50% probability level where C = grey, N = blue, O = red, Zn = yellow.

Relevant bond lengths of **Zn$_3$L^{Me}(OAc)$_3$** are given below in Table 2.7.1. Relevant bond angles are given in Appendix 3, Table A.12.

Table 2.7.1 Bond lengths relating to the coordination environment of **Zn$_3$L^{Me}(OAc)$_3$**

Atom	Atom	Length/Å
Zn3	O3	2.006(3)
Zn3	O4	2.246(3)
Zn3	O6	1.956(3)
Zn3	O2	2.032(3)
Zn3	N1	2.056(3)
Zn2	O3	1.933(3)
Zn2	O1	2.017(3)
Zn2	O5	2.228(3)
Zn2	O9	1.971(3)
Zn2	N2	2.034(4)
Zn1	O1	1.987(3)
Zn1	O8	2.065(3)
Zn1	O2	1.976(3)
Zn1	O10	2.248(4)
Zn1	O11	2.040(4)

2.7.2 Mononuclear Nickel Complex

Reaction of BFPP, $Ni(OAc)_2$ and 2-amino-4-methylphenol in a 1:2:2 molar ratio, similar to that used to obtain dinuclear cobalt complexes, gives a dark yellow solution which upon concentration of the solvent and precipitation with diethyl ether yields a yellow solid with similar physical characteristics to those of **$Co_2L^{Me}OAc$**. Vapor diffusion of diethyl ether into a concentrated methanol solution of the complex gives single crystals suitable for XRD studies, which interestingly reveal that the crystallised complex is in fact a mononuclear octahedral complex where the two phenolate moieties of the ligand coordinate orthogonally to the Ni(II) centre, resulting in an overall neutral complex without anionic acetate ligands present Figure 2.7.3.

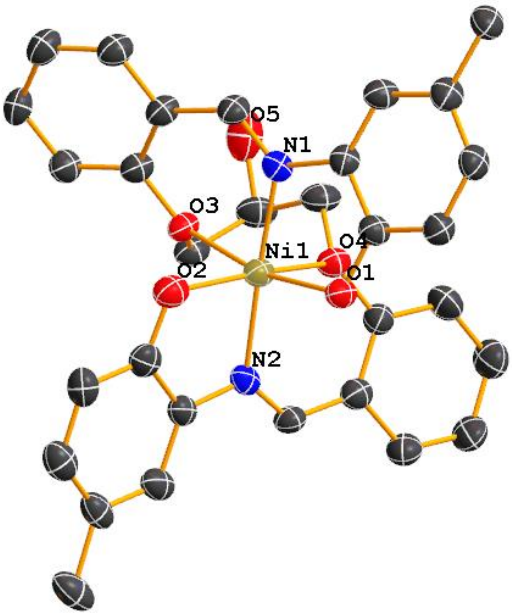

Figure 2.7.3 X-Ray crystal structure of **NiL^{Me}** where thermal ellipsoids are set at the 50% probability level. Hydrogen atoms are omitted for clarity. C = grey, N = blue, O = red, Ni = yellow.

Bond lengths relating to the coordination environment of **NiL^{Me}** are given below in Table 2.7.2. Relevant bond angles are given in Appendix 3, Table A.13.

Table 2.7.2 Bond lengths relating to the coordination environment of NiL^{Me}

Atom	Atom	Length/Å
Ni1	O4	2.169(5)
Ni1	O1	2.008(4)
Ni1	O2	1.975(5)
Ni1	O3	2.149(4)
Ni1	N1	2.008(4)
Ni1	N2	2.022(4)

While single crystals of **NiL^{Me}** could be obtained, it is likely that the bulk material contained a mixture of both **NiL^{Me}** and **$Ni_2L^{Me}OAc$**, and only the mononuclear complex was able to crystallise from the mixture.

2.7.3 Tetranuclear Nickel Complex

Following the same procedure as other tetranuclear complexes, the reaction of BFFP, 2-amino-4-methylphenol and $Ni(OAc)_2$ in a 1:2:2 molar ratio, followed by salt metathesis with NH_4PF_6 results in the formation of single crystals of $\mathbf{Ni_4L^{Me}(PF_6)_2}$. The crystal structure is like that of $\mathbf{Co_4L^{Me}(BF_4)_2}$, where the complex adopts a defective dicubane core (Figure 2.7.4).

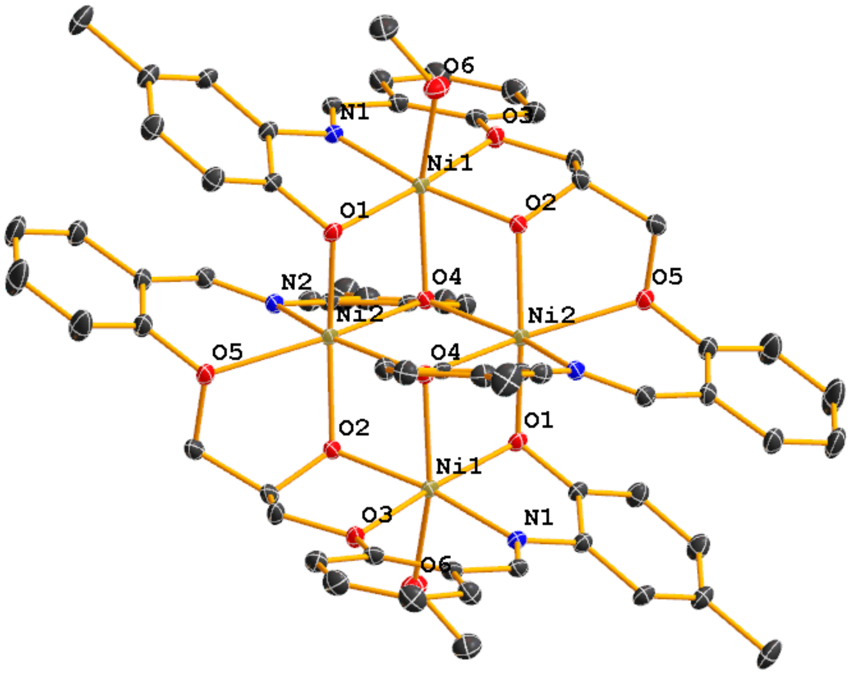

Figure 2.7.4 X-Ray crystal structure of $\mathbf{Ni_4L^{Me}{}_2(PF_6)_2}$ where thermal ellipsoids are set at the 50% probability level. Non-coordinating PF_6^- counter ions and hydrogen atoms are omitted for clarity. C = grey, N = blue, O = red, Ni = yellow.

Bond lengths relating to the coordination environment of $\mathbf{Ni_4L^{Me}(PF_6)_2}$ are given below in Table 2.7.3. Relevant bond angles are given in Appendix 3, Table A.13.

Ni-O bond lengths present in $\mathbf{NiL^{Me}{}_2(PF_6)_2}$ are consistent with those for known examples of defective dicubane complexes comprising of four Ni(II) ions and O-rich Schiff base ligands.[173]

Table 2.7.3 Bond lengths relating to the coordination environment of **$Ni_4L^{Me}{}_2(PF_6)_2$**

Atom	Atom	Length/Å
Ni1	O2	1.9750(19)
Ni1	O4	2.1608(19)
Ni1	O1	2.0353(19)
Ni1	O3	2.1021(19)
Ni1	O6	2.106(2)
Ni1	N1	1.994(2)
Ni2	O2	1.9930(19)
Ni2	O4	2.0726(18)
Ni2	O1	2.0124(19)
Ni2	O5	2.2838(19)
Ni2	N2	2.050(2)

2.8 Attempted ligand variations

2.8.1 Replacing Aldehyde with Amine

We briefly investigated alternate ligand backbone structures, one such variation was to replace the carboxaldehyde functionality of the BFPP backbone with an amine, allowing the ligand to be formed by condensation with salicylaldehyde derivatives. This was achieved by ring opening of epichlorohydrin with two equivalents 2-nitrophenol, followed by reduction of the nitro group to an amine by the Pd/C hydrazine method.

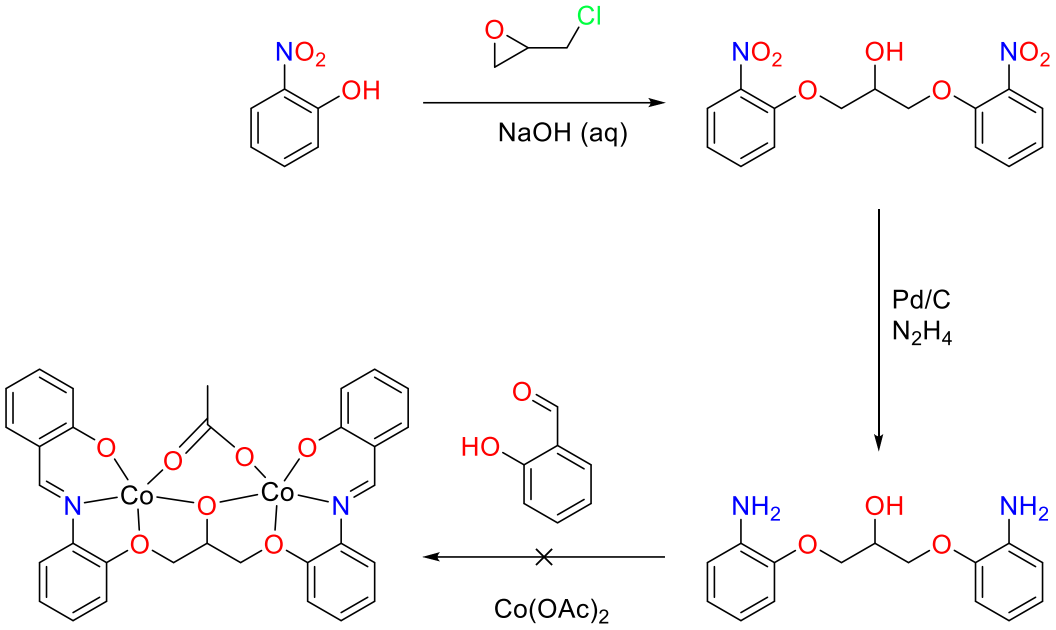

Scheme 2.8.1 Attempted synthetic pathway to obtain a ligand variation where salicylaldehyde is used as the phenolate donor instead of 2-aminophenols

While this allowed access to the diamine, template complexations with metal salts and salicylaldehydes only ever resulted in insoluble coordination polymers, likely due to the poor coordination geometry between the phenolate-imine part of the ligand and the alcohol and ether part.

2.8.2 Attempted Complexation of a Polypyridyl Ligand from BFFP

While the main focus of this work was to investigate complexes of N_2O_7 ligands, it is difficult to ignore the prevalence of polypyridyl complexes in ORR catalysis. For this reason, we designed a ligand which contains a polypyridyl N_6O_3 coordination environment derived from BFPP by reductive amination with dipicolylamine. While this ligand could be obtained, the following complexation reactions appeared to only yield a small amount of paramagnetic mauve solid, for which preliminary oxygen reduction measurements indicated no catalytic activity, and therefore no further work to optimise the complexation reaction was undertaken.

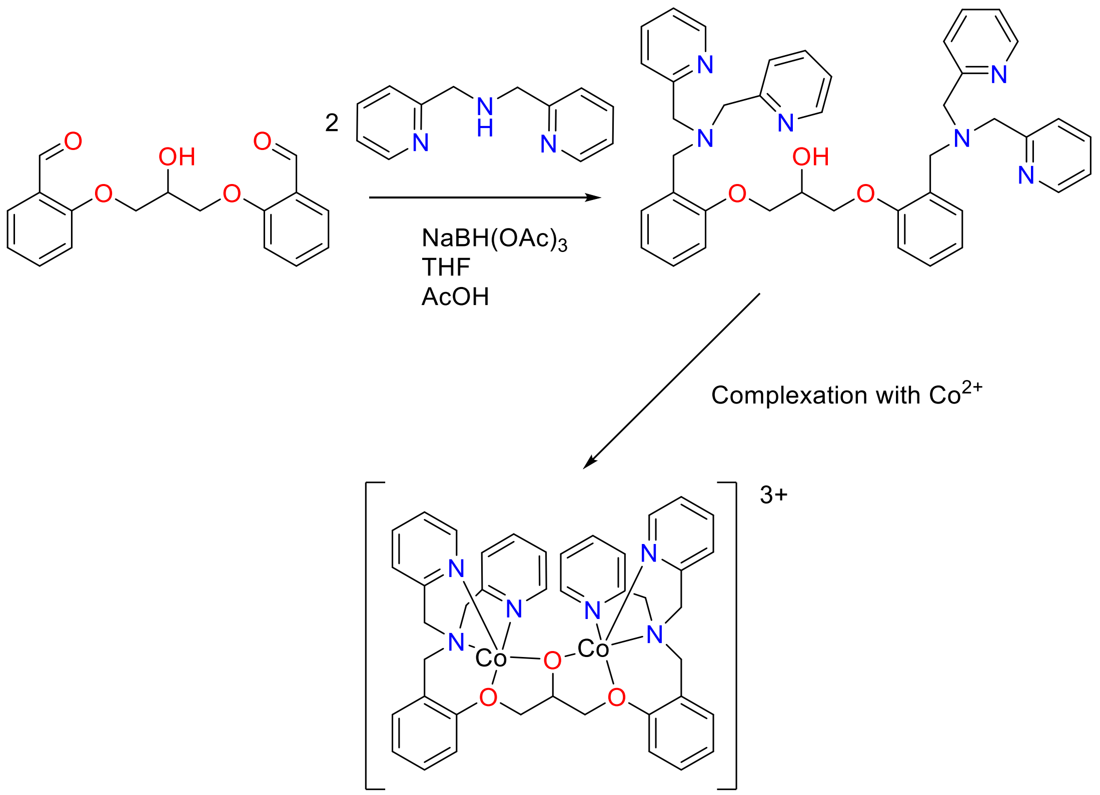

No ORR activity - not studied further

Scheme 2.8.2 Attempted synthesis of a dinuclear polypyridyl complex by reductive amination of dipicolylamine onto BFPP.

2.9 Conclusions

A new heptadentate Schiff base complex was designed, taking inspiration from a combination of Co^{II}salen ORR catalysts and work where BFPP was used as a precursor to multinuclear metal complexes. **$Co_2L^{Me}OAc$** was synthesised in good yield by templated condensation between BFPP, 2-amino-4-methylphenol and cobalt(II) acetate. Complexation reactions using a variety of 2-aminophenol derivatives resulted in the formation of the corresponding family of Co_2L^ROAc complexes, however many of these were not of sufficient purity for catalytic studies. While attempts to obtain XRD quality crystals of **$Co_2L^{Me}OAc$** failed, elemental analysis, mass spectrometry and IR studies supported the suggested structure. If the complexation reaction was carried out with three equivalents of cobalt salt, a trinuclear complex was formed and was studied by XRD. If the coordinated acetate anion was abstracted from the complex via salt metathesis with non-coordinating salts, a tetranuclear complex formed by coordination between the vacant octahedral sites of the cobalt ions with the lone pairs of oxygen atoms at the phenolate moieties of the ligand. XRD studies of these tetranuclear complexes revealed that the complex adopts a defective dicubane motif which has potential applications as a single molecule magnet.

Variations to the ligand, including formation of a polypyridyl analogue, and derivatisation of the BFPP backbone were attempted, however these lead to impure and uncharacterisable products where purification attempts failed. Any crude materials obtained were screened for ORR activity. No catalytic activity was observed for any of these crude species, so further attempts to obtain fully characterised complexes were not attempted.

Chapter 3

Mononuclear Salen Complexes bearing a Pendant Base Moiety

3.1 Introduction

The use of salen and salen-like complexes to catalyse the oxygen reduction reaction has been studied in good detail. Their ease of synthesis and high thermodynamic efficiency makes these complexes good candidates for homogeneous oxygen reduction, as well as their potential to be electropolymerized onto an electrode for heterogeneous catalysis. However, under normal conditions, i.e. in organic solvent with a weak acid as a proton source, the ORR catalysed by salen complexes is almost always selective towards the two electron reduction and formation of hydrogen peroxide. While electroreduction of oxygen to hydrogen peroxide is desirable as an alternative to the anthraquinone process of hydrogen peroxide synthesis,[174] it is not the ideal product in the context of fuel cells. The selectivity determining step in the ORR catalysed by mononuclear complexes is often the protonation of either the proximal or distal oxygen atom of a metal bound hydroperoxo species, where if the oxygen proximal to the metal centre is protonated rapidly, H_2O_2 is released, whereas if the distal oxygen is protonated, O-O bond cleavage is facile, and H_2O is generated.[175]

One method to facilitate distal oxygen atom protonation is to incorporate a flexible proton relay which operates within the second coordination sphere of the metal complex.[176–178] While this treatment has seen some success with other ligand systems, notably hangman porphyrins,[179–181] there are yet to be any salen-like complexes which bear a pendant base catered towards the oxygen reduction reaction. The lack of pendant base bearing salen complexes is likely due to the inherent planarity of the ligand structure – it is difficult to design a system in which the pendant base can reach the second coordination sphere in the axial position of the metal centre. On the other hand, Machan and co-workers modified a H_2O selective Co-N_2O_2 bipyridyl ORR catalyst with ether functionalities at the *ortho* positions of the ligand's phenolic rings, resulting in a flip in selectivity to H_2O_2 due to protonation of the proximal oxygen atom of the bound species, facilitated by hydrogen bonding to the ether functionalities.[118]

We based our ligand design on previous work in the Fielden research group in which a 1,3-cyclohexyl backboned Schiff base complex is able to catalyse the reduction of H^+ from AcOH to H_2, albeit at a low Faradaic efficiency due to a side reaction in which the acetonitrile was reduced to ethylamine.[182] If a pendant proton relay was incorporated proximally to the active site, the reduction of protons to H_2 is enhanced, increasing the Faradaic efficiency from 15 to 38%, and reducing the Faradaic efficiency for acetonitrile reduction from 22% to 11%.

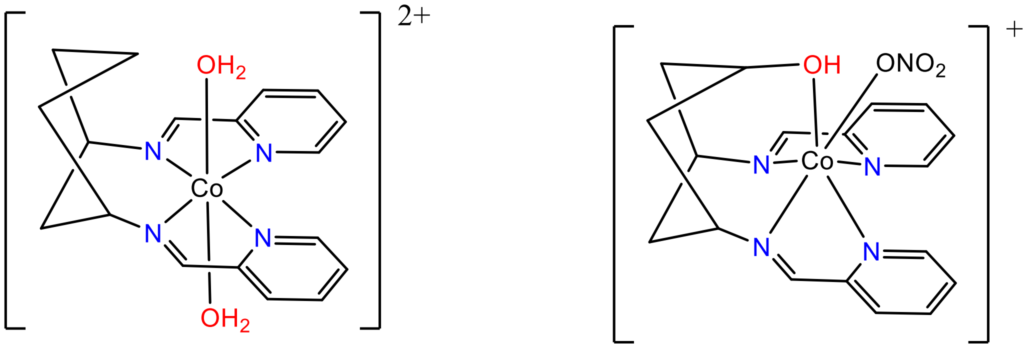

Faradaic efficiency (H_2) = 15%

Faradaic efficiency ($EtNH_2$) = 22%

Faradaic efficiency (H_2) = 38%

Faradaic efficiency ($EtNH_2$) = 11%

Figure 3.1.1 Co 1,3-cyclohexyl backboned N_4 iminopyridine complexes previously studied by our group where a proton relay increased selectivity towards hydrogen evolution rather than acetonitrile reduction.

It was decided to take a similar action in this work and study whether incorporating a flexible proton relay into the salen-like structure, which was already well known to reduce O_2 to H_2O_2 in the presence of AcOH; increases the selectivity towards H_2O production.

3.2 Ligand Design and Synthetic Pathway

The synthetic pathway used in previous work was used as a basis for the synthesis a pendant amine bearing salen-like ligand is shown in scheme 3.2.1.

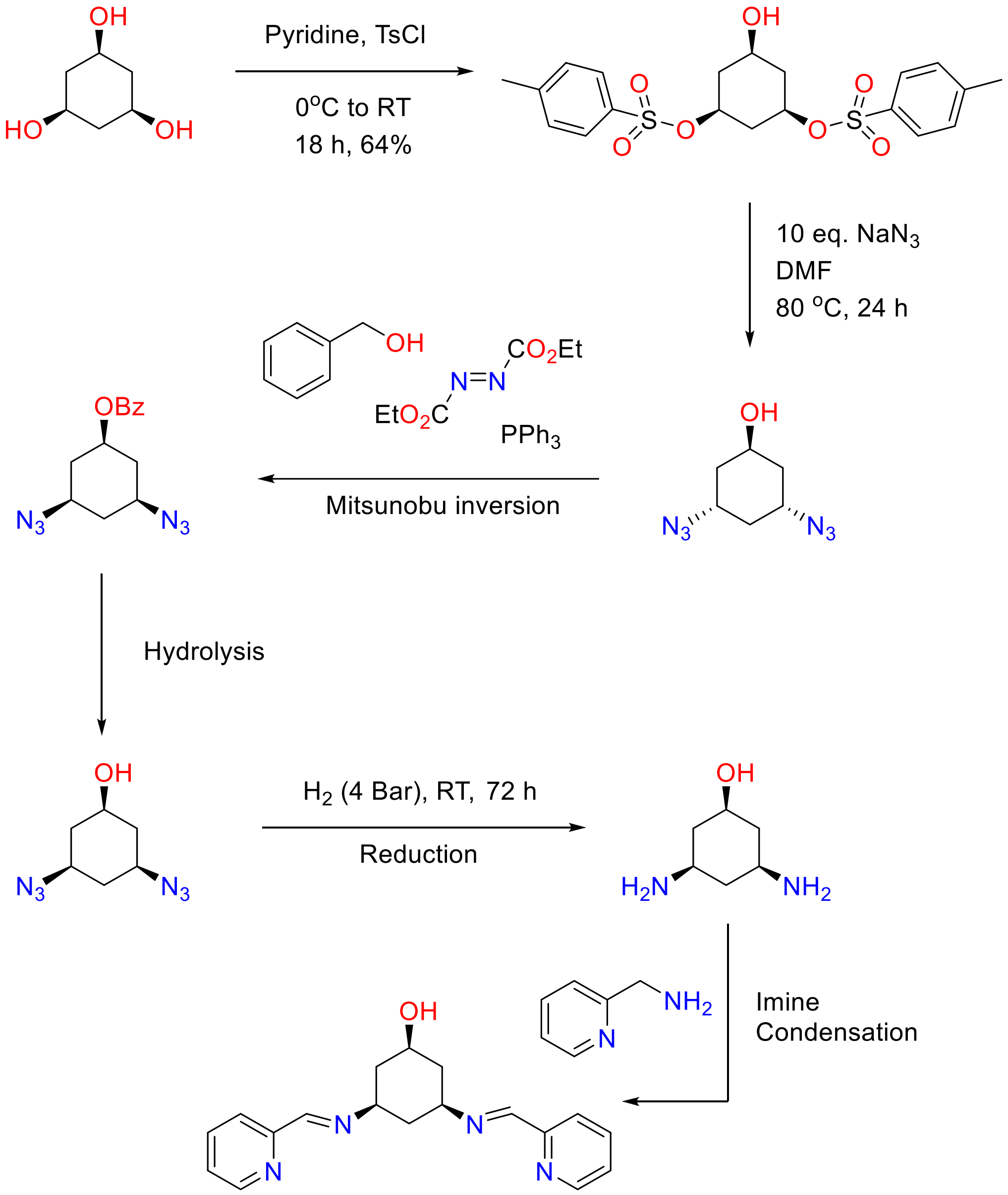

Scheme 3.2.1 Outline of the synthetic pathway undertaken in our group's previous work to obtain bis-iminopyridine complexes for proton reduction and acetonitrile reduction.

In the previous work, a Mitsunobu inversion[183] was performed on cis-trans-1,3-diazidocyclohexan-5-ol to form cis-cis-1,3-diazidocyclohexane-5-ol. This places the final hydroxyl group in close proximity to the coordination pocket of the ligand, resulting in coordination of the pendant alcohol to the metal centre. With the goal being to protonate the substrate in the second coordination sphere, it was decided to instead incorporate a longer, more flexible proton relay which is unable to coordinate to the metal centre. To achieve this, we decided to leave the cyclohexanol as *cis*-*trans* and instead add an ether linkage to a pendant amine. Following this the desired salen ligand could be synthesised by reduction of the azide groups to amines, followed by imine condensation with 3,5-di-*tert*-butylsalicylaldehyde instead of pyridine-2-carboxyaldehyde as to establish the salen-like ligand.

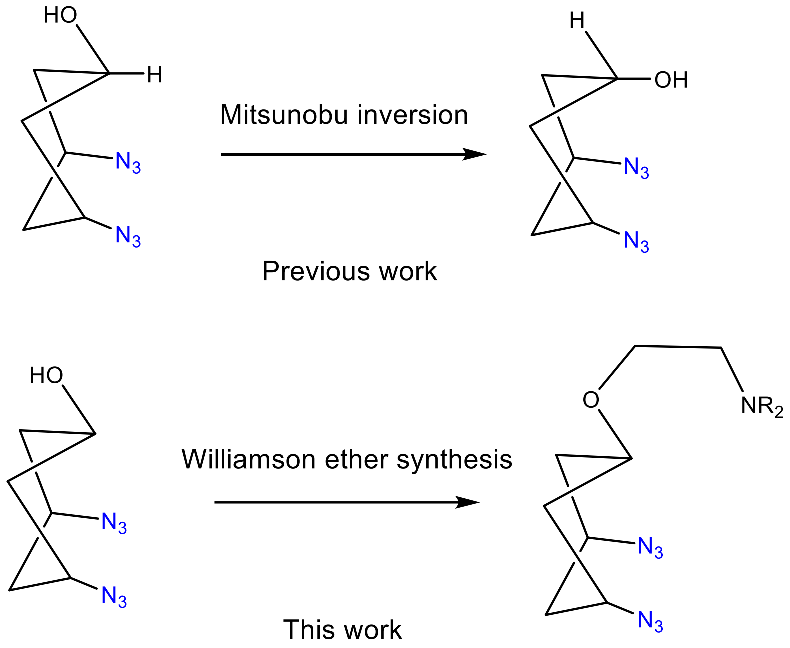

3.3 Ligand synthesis

3.3.1 Cis,cis-3,5-ditosyloxycyclohexanol

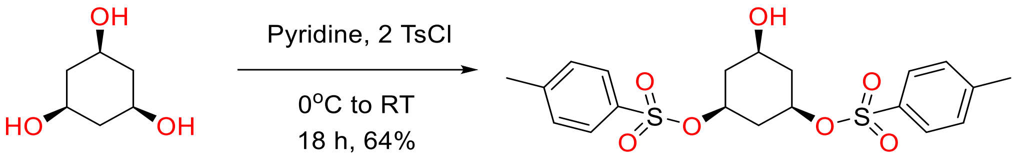

Compund 3-1

Scheme 3.3.1 Tosylation of *cis,cis*-cyclohexane-1,3,5-triol to form *cis*-1,3-ditosyloxy-*cis*-5-hydroxycyclohexane.

To obtain *cis*-1,3-ditosyloxy-*cis*-5-hydroxycyclohexane (**3-1**), our group's previous method of direct tosylation of *cis*-cyclohexane-1,3,5-triol with two equivalents of *p*-toluenesolfonyl chloride in pyridine was used. The alternative in which one alcohol of the starting material is protected before tosylation is possible, but the slight gain in yield obtained from the protection pathway was outweighed by the simplicity of direct tosylation. Tosylation of *cis*-cyclohexane-1,3,5-triol occurs with complete stereoconservation i.e. the overall stereoisomerism remains *cis*-*cis* and thus *cis*-1,3-ditosyloxy-*cis*-5-hydroxycyclohexane could be obtained in 57% yield, where the monotosylated by-product could also be isolated from the products mixture by column chromatography. ^{1}H NMR of **3-1** is shown in Appendix 1.

3.3.1 *Cis,trans*-diazidocyclohexanol

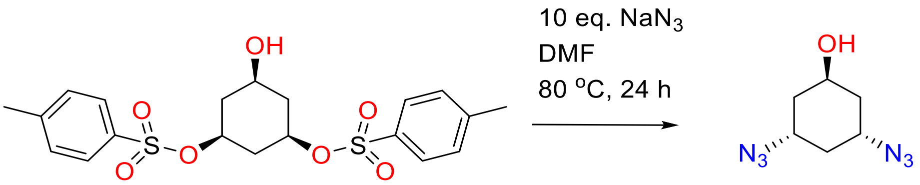

Compund 3-2

Scheme 3.3.2 Nucleophilic substitution of *cis*-1,3-ditosyloxy-*cis*-5-hydroxycyclohexane to obtain *cis*-3,5-diazido-*trans*-cyclohexanol (**3-2**).

Nucleophilic substitution of the tosyl leaving groups with NaN_3 in DMF at 80 °C afforded *cis*-1,3-diazido-*trans*-5-hydroxycyclohexane (**3-2**) with complete stereoinversion of the 1 and 3 positions. It is important at this stage to note the high azide number of the product, and to limit risk of explosions, was only ever synthesised in small batches the day before the following step. ^{1}H NMR of **3-2** is shown in Appendix 1.

3.3.2 Williamson Ether Synthesis to Incorporate Pendant base

Addition of the pendant amine was achieved via an ether linkage onto *cis*-1,3-diazido-*trans*-5-hydroxycyclohexane. Initially, *N*,*N*-dimethyl-2-amino-1-bromoethane was chosen as the precursor for the pendant base, which had the desired product **3a**. Ether formation was undertaken by deprotonation of *cis*-1,3-diazido-*trans*-5-hydroxycyclohexane by NaH, followed by addition of *N*,*N*-dimethyl-2-amino-1-bromoethane at room temperature. Unfortunately for a number of conditions tested such as varying the solvent, reaction temperature NaH and *N*,*N*-dimethyl-2-amino-1-bromoethane concentrations, no product was recovered, and only a mixture of starting materials and by-products were obtained.

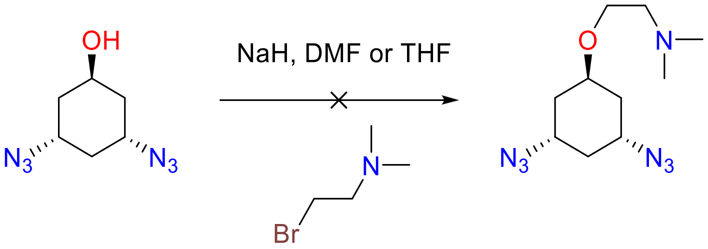

Scheme 3.3.3 Attempted Williamson ether synthesis with **2** and 2-*N,N*-dimethylaminobromoethane to obtain the pendant base functionalised intermediate.

The expected cause of this failed reaction is due to the mismatched latent polarity of the amine and the required polarity following the loss of bromide. To account for this, 2-bromomethylpyridine was used to form the pendant base instead of *N*,*N*-dimethyl-2-amino-1-bromoethane, where latent polarity effects are dampened by the electron withdrawing nature of the aryl ring. As a result, attachment of the pendant pyridyl group proceeded to afford slightly impure **3-3** following column chromatography to remove excess mineral oil. **3-3** was used in the next step without further purification. ^{1}H NMR of **3-3** is shown in Appendix 1.

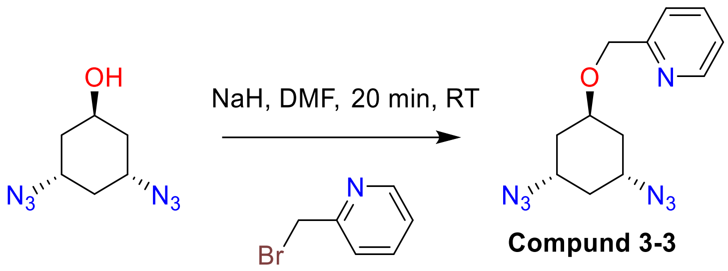

Scheme 3.3.4 Williamson ether synthesis from **2** and 2-bromomethylpyridine to obtain the pendant pyridyl functionalised intermediate **3-3**.

3.3.3 Reduction of Azides to Amines

Several reduction methods to form amines from the azide groups were attempted. With the fear of disrupting the ether linkage of **3-3** by reduction by hydrogenation, the reaction was first attempted with more gentle methods of reduction. Firstly, the Staudinger reaction in which PPh_3 reduces azides to amines through formation of an azide-phosphine adduct which releases N_2 and forms an iminophosphorane which is then hydrolysed during aqueous workup to form thrphenylphosphine oxide and the desired amine.[184]

While this could effectively reduce the azides to amines as shown by TLC using ninhydrin as a stain to detect produced amines, removal of the triphenylphosphine oxide proved to be very challenging due to the similar solubilities of the diamine product **3-4** and the triphenylphosphine oxide, along with the instability of **3-4** towards column chromatography.

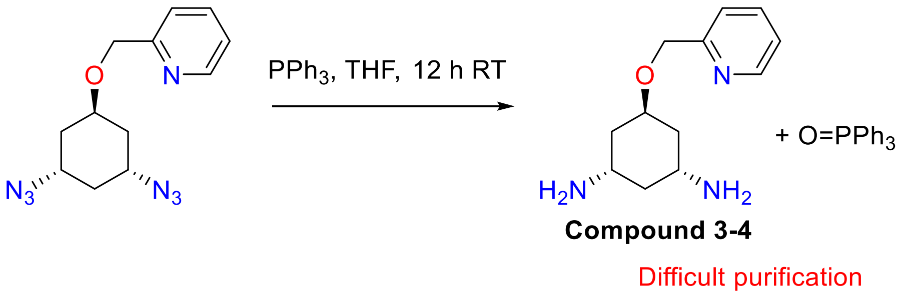

Scheme 3.3.5 Attempted Staudinger reaction method to reduce azides of **3-3** to amines to afford **3-4**.

Secondly, magnesium metal was used as a reducing agent in MeOH solution,[185] and while the formation of hydrogen from the reaction mixture was a clear indicator that reduction of the azide groups was taking place, the reaction mixture precipitated an insoluble sol-gel substance which was likely a coordination polymer between the reduced diamine product and magnesium metal. Attempts to decoordinate the product from the magnesium metal, including acid washing and Soxhlet extraction were unsuccessful.

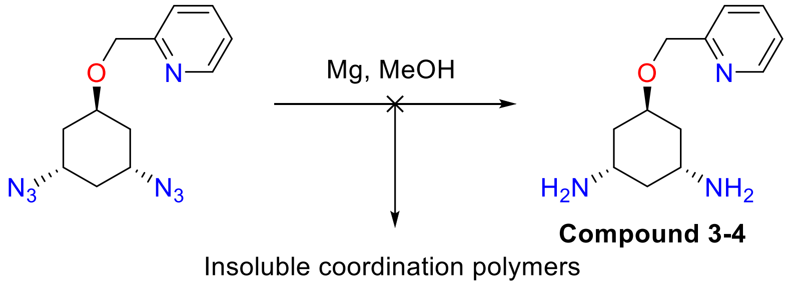

Scheme 3.3.6 Attempted reduction of the azides of **3-3** by reaction with magnesium metal in MeOH.

Finally, selective reduction of azides was achieved by hydrogenation under a mild pressure of 4 Bar over 72 h at room temperature, under these gentle conditions, the target diamine was obtained in near quantitative yields without disruption to the ether linkage. Formation of the diamine was confirmed by IR spectroscopy, where the 2083 cm^{-1} band relating to the azide groups in the starting material disappeared in the product, and a band at 1619 cm^{-1} relating to the N-H stretching frequency of the primary amines was formed. ^{1}H NMR of **3-4** is shown in Appendix 1.

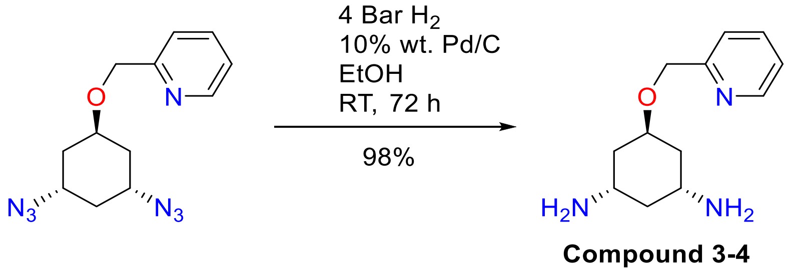

Scheme 3.3.7 Reduction of the azides of **3-3** by Pd catalysed hydrogenation to afford the diamine **3-4**.

3.3.4 Salcn-Py ligand and Complexation

To obtain the final 1,3-cyclohexyl backboned salen-like ligand, diamine **3-4** was refluxed in MeOH with two equivalents of 3,5-di-*tert*-butylsalicylaldehyde, to obtain the final ligand **5** in 55% yield. ^{1}H NMR of Salcn-Py is shown in Appendix 1.

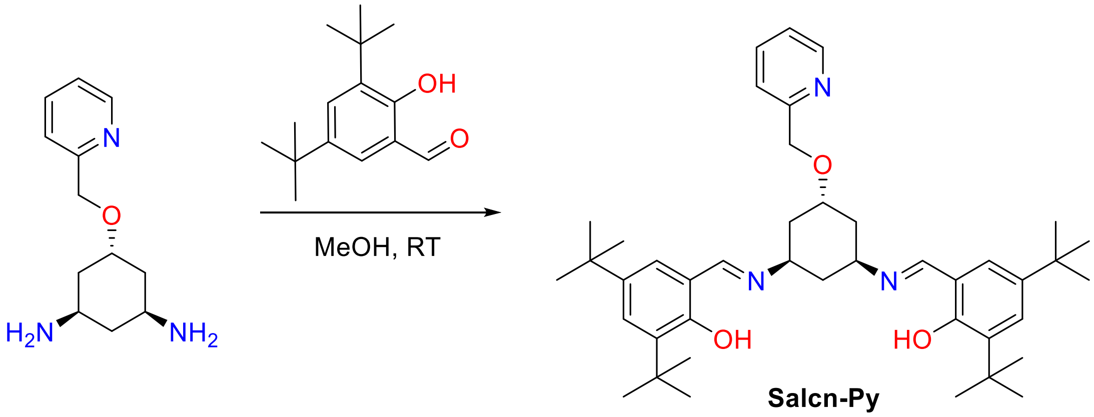

Scheme 3.3.8 Schiff base condensation of **3-4** with 3,5-di-*tert*-butylsalicylaldehyde to obtain the final salen ligand Salcn-Py

Finally, complexation was achieved by adding a solution of either cobalt (II) acetate terahydrate or copper (II) acetate monohydrate in MeOH to a solution of the ligand in DCM at room temperature. CoSalcn-Py was obtained in 80% yield and the structure was supported by mass spectrometry and elemental analysis. Infrared spectroscopy showed imine stretching frequencies of 1587 cm^{-1} which indicates that the imine groups are metal coordinated.

Attempts to crystallise CoSalcn-Py resulted in only microcrystalline solids with large degrees of twinning and were unsuitable for XRD studies. However, if a DCM/MeOH solution CuSalcn-Py was slowly evaporated over the course of a day, the copper complex crystallised as large, green single crystals suitable for diffractometry.

The crystal structure of CuSalcn-Py shows the expected four-coordinate distorted square planar geometry. The torsion angle between the N-Cu-N and the O-Cu-O planes is 22.7^o and as a result the aryl rings of the phenolate moieties lie out of plane with one another. Relevant bond lengths and angles of Cu(salcn-Py) are given in Appendix 3, Table A.14 and Table A.15 respectively.

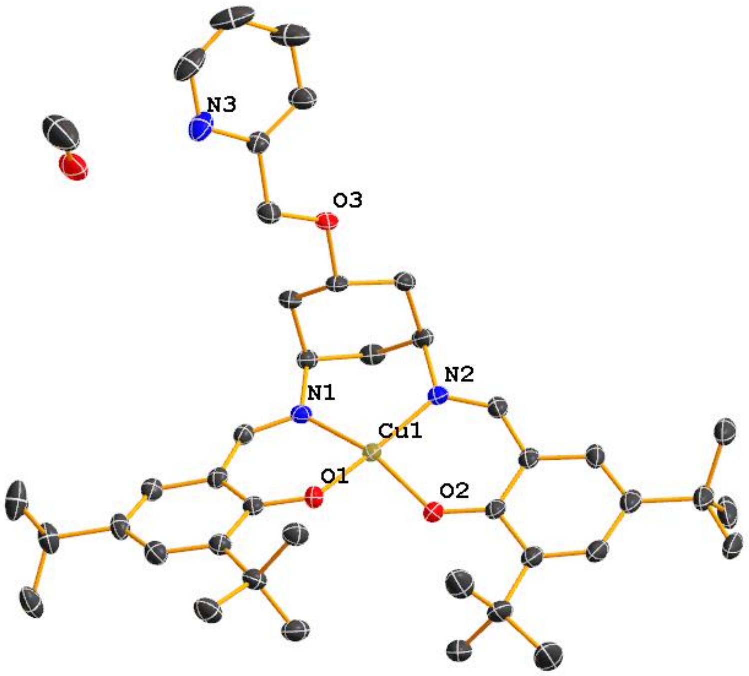

Figure 3.3.1 X-Ray crystal structure of Cu(salcn-Py). Thermal ellipsoids are set at the 50% probability level. Hydrogen atoms are omitted for clarity. C = grey, O = red, N = blue, Cu = yellow.

3.3.5 ORR Screening of Salcn-Py Complexes

Both the cobalt and copper complexes of Salcn-Py were preliminarily examined for the ORR both by both electrochemical and spectrophotometric means. Unfortunately, in both cases, no ORR activity was observed under the conditions tested. This lack of activity is surprising considering the structural similarities between Salcn-Py complexes and their standard salen analogues. While the lack of ORR activity for these complexes was both disappointing and unexpected this motif may be used in a number of other applications where salen complexes are used and a pendant functionality would be beneficial.

Chapter 4

Electrochemistry and Electrocatalysis

4.1 Introduction to Electrochemistry

Electrochemical analysis is an extremely useful method of determining the redox properties of organic and inorganic complexes and their reactivity with an extensive range of substrates. The use of electrochemistry as a method of characterisation is growing rapidly, however, to make full use of these versatile analytical techniques, an in-depth understanding of the theory surrounding the subject is required. This chapter will first describe some of the fundamentals of electrochemical analysis. These methods are then applied to the complexes described in the previous chapter and their relevance to the ORR will then be discussed.

4.1.1 Redox Processes and the Nernst Equation

For a reduction process where A undergoes a single electron reduction to B (Eqn. 4.1.1)

$$\mathrm{A} \underset{\text{-e-}}{\overset{\mathrm{e}^-}{\rightleftharpoons}} \mathrm{B} \qquad \text{(Eqn. 4.1.1)}$$

at an electrode surface, there exists a standard reduction potential (E^0) which is the electrochemical potential required to establish a dynamic equilibrium between A and B, that is, where the net change in Gibbs free energy (ΔG^0) of the system is zero.[186] The value of E^0 is measured under standard conditions ([A] = [B] = 1 M, 298 K) quoted with respect to the potential of the standard hydrogen electrode (SHE) which is defined as 0 V. If the concentrations of A and B or the temperature are non-standard, however, the reduction potential is shifted in accordance with the Nernst equation (Eqn. 4.1.2)

$$E = E^0 - \frac{RT}{nF} ln\left(\frac{[B]}{[A]}\right) \qquad \text{(Eqn. 4.1.2)}$$

which relates the non-standard potential (E) to E^0 and the actual reaction conditions where R is the ideal gas constant, T is temperature, n is the number of electrons transferred in the process and F is faraday's constant. In voltametric analysis, concentrations of reactants and products are constantly changing over the course of a redox process, and thus the Nernst equation underpins many of the phenomena seen during analysis.

4.1.2 Diffusion

Most voltammetry measurements are undertaken in stationary solutions (i.e., not stirred) and therefore the contents of the solution at the electrode can be different to the contents of the bulk solution. As a result of this disparity in species at the electrode and in bulk solution, a concentration gradient is formed. The diffusion of a species across this gradient is defined by Fick's laws of diffusion, the first of which describes the diffusive flux (j) at a point in solution (x) shown in Eqn. 4.1.3.

$$j = -D\frac{\partial c}{\partial x} \qquad \text{(Eqn. 4.1.3)}$$

Where c is the concentration of the diffusing species and D is the diffusion coefficient of that species. D is the measure of how quickly the species diffuses across a concentration gradient in a specific solvent and at a specific temperature and is often inversely proportional to the hydrodynamic radius of the species.

Fick's second law of diffusion relates to the change in concentration at a specific point, x, over time. This law is dependent on the shape of the diffusion layer, and in the case of a circular disc electrode (as is most common in voltammetry) takes the form shown in Eqn. 4.1.4.

$$\frac{\partial c}{\partial t} = D\left(\frac{\partial^2 c}{\partial r^2} + \frac{1}{r}\frac{\partial c}{\partial r} + \frac{\partial^2 c}{\partial z^2}\right) \qquad \text{(Eqn. 4.1.4)}$$

Where r and z are the radius and the height of the diffusion layer respectively.

Diffusion of substrate towards the electrode is often the slowest step during the redox process, and as a result the flow of current across a voltametric cell is dictated by the flux of substrate to the electrode.

4.1.3 Cyclic Voltammetry

Cyclic voltammetry (CV) is the most widely used and versatile electrochemical experiment, it allows for rapid determination of the equilibrium potentials of reversible processes, as well as insight into the reversibility of redox reactions and their response to the addition of substrates.[187–190] The principle of CV is to sweep the potential of an electrode at a constant rate (υ, Vs^{-1}) from a starting potential $E_{initial}$ to a vertex potential E_{vertex} and then back down to a final potential E_{final}, commonly the same value as $E_{initial}$ (Figure 4.1.1)

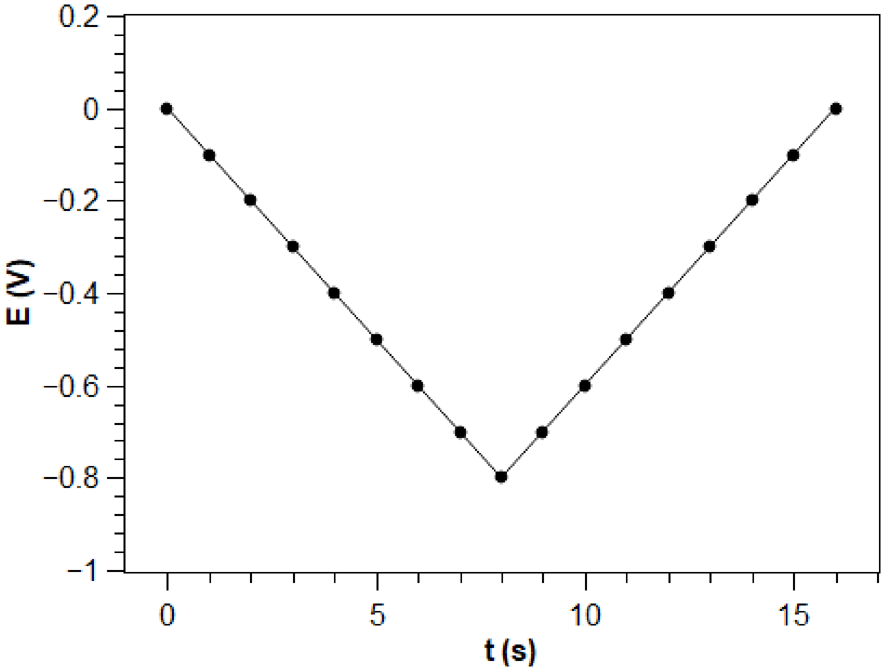

Figure 4.1.1 Potential (E) vs. time profile for a CV scan from 0 V to a vertex potential of -0.8 V and back to a final potential of 0 V with a scan rate (v) of 0.1 Vs^{-1}

As the potential is swept from $E_{initial}$ to E_{vertex} a redox process may occur, in this example, we consider the reduction of A to B in Eqn. 4.1.1. As the potential of the electrode approaches and exceeds the reduction potential of A, the current response increases until a limit (i_{pc}) at E_{pc}. After this point, the concentration of A at the electrode is depleted, and further reduction of A is dependent on slow diffusive transport of A across the diffusion layer to the electrode surface. After the potential of the electrode reaches E_{vertex}, the direction of the scan is reversed and swept back to E_{final}. During this sweep, the reduced product B that is present at the electrode following reduction of A is oxidised back to A in a similar manner, with the current response reaching a peak (i_{pa}) at E_{pa} before diminishing to its mass transport limited value.

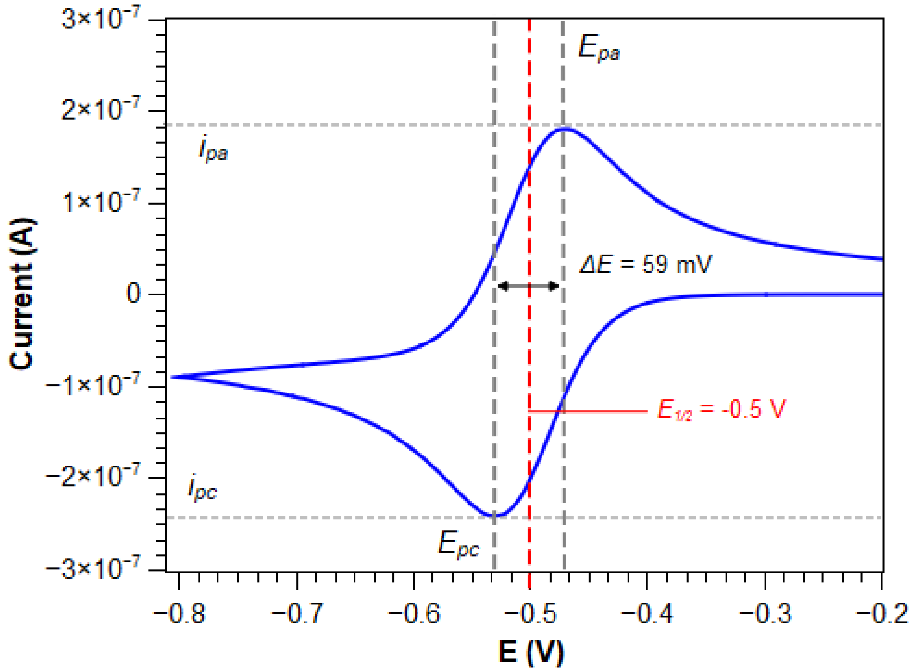

Figure 4.1.2 Simulated CV of the ideal reversible one-electron reduction of A to B where the vertical dashed lines represent the potential of notable redox events, and the horizontal dashed lines represent the maximum current response of those events. Simulated using Limhes ECsim Open Source Software.[191]

The separation between E_{pc} and E_{pa} for a fully reversible system is 59 mV and is the typical value for a fully reversible single electron transfer.

This ‘duck’ shaped voltammogram shown above is typical for an ideal, reversible electrochemical process which has a high rate of electron transfer (k_e). The k_e value of an electron transfer can be explained by Marcus theory[186], where if the potential energy surfaces for A and B are similar with respect to the reaction coordinate (e.g., bond lengths or angles) then the transition state energy (E_{TS}) and thus activation energy (E_a) is low and electron transfer is facile (Fig 4.1.2).[192]

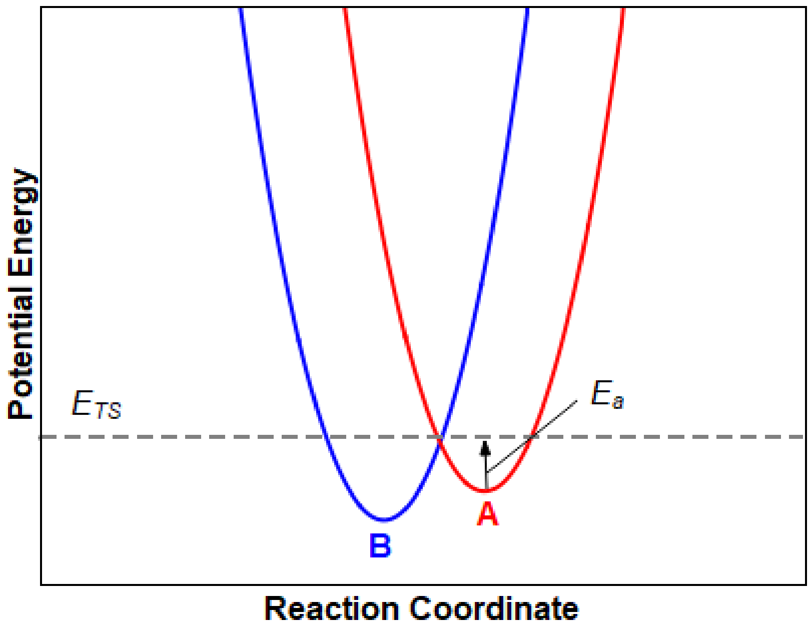

Figure 4.1.3 Marcus theory representation of the fast reduction of A to B where the red and blue parabolae represent the potential energy surfaces of A and B respectively and the grey dashed line represents the energy of the A to B transition state (E_{TS}).[186]

However, if the potential energy surfaces are far apart with respect to the reaction coordinate, (i.e., there is a significant change in geometry when A is reduced to B) then activation energy is high and electron transfer is sluggish (Fig 4.1.3). The value of k_e decreases exponentially with increasing E_a according to the Arrhenius equation (Eqn 4.1.5)

$$k_e = Ae^{-\frac{E_a}{RT}} \qquad \text{(Eqn. 4.1.5)}$$

If the rate of electron transfer is slow due to changes in geometry between A and B, or if there is an electronic rearrangement known as spin crossover, the electrochemical process is irreversible, and the CV is distorted from this ideal shape. The effect of only reducing k_e on a CV is shown in Fig. 4.1.4.

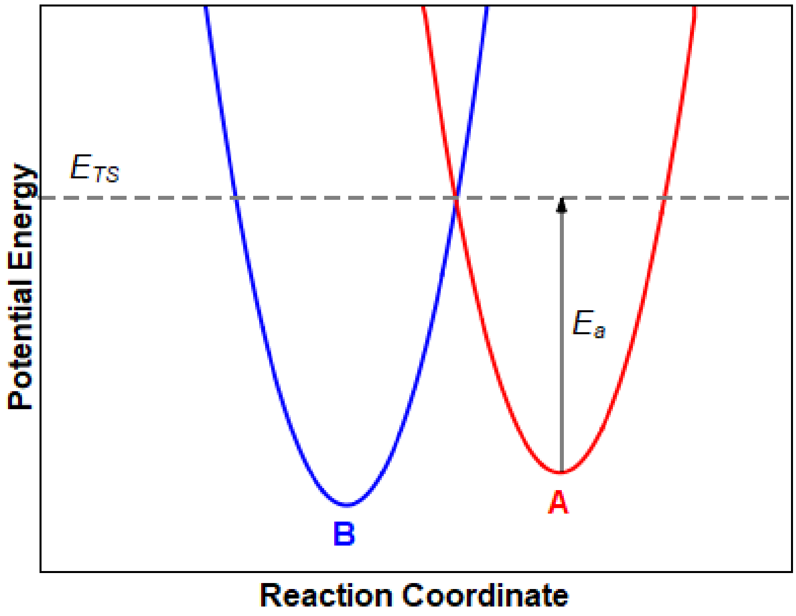

Figure 4.1.4 Marcus theory representation of the slow reduction of A to B where the red and blue parabolae represent the potential energy surfaces of A and B respectively and the grey dashed line represents the energy of the A to B transition state (E_{TS}).[186]

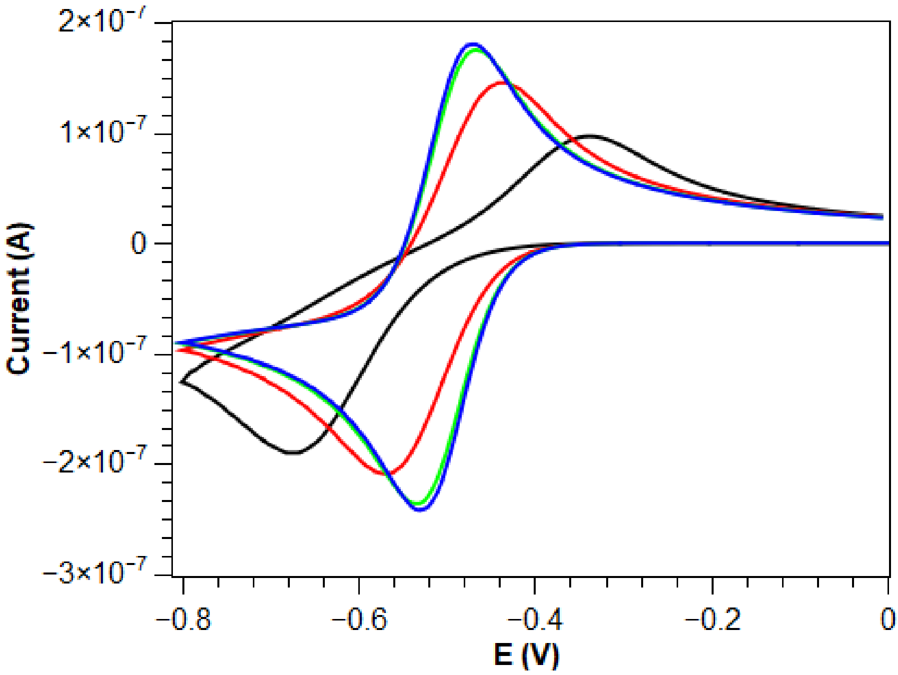

Figure 4.1.5 Simulated CVs of the same A to B reduction process where k_e is 1 (blue), 10^{-3} (green), 10^{-4} (red) and 10^{-5} ms^{-1} at a scan rate of 100 mVs^{-1} Simulated using Limhes ECsim Open Source Software.[191]

4.2 Voltammetry of $Co_2L^{Me}OAc$ in DMF

4.2.1 Cyclic Voltammetry of $Co_2L^{Me}OAc$ in DMF

The complexes synthesised in this work were first electrochemically analysed in dimethylformamide (DMF) due to the solvent's large electrochemical window. **$Co_2L^{Me}OAc$** was first examined under an inert argon atmosphere in the range of -2 – 1 V vs Ag (Figure 4.2.1).

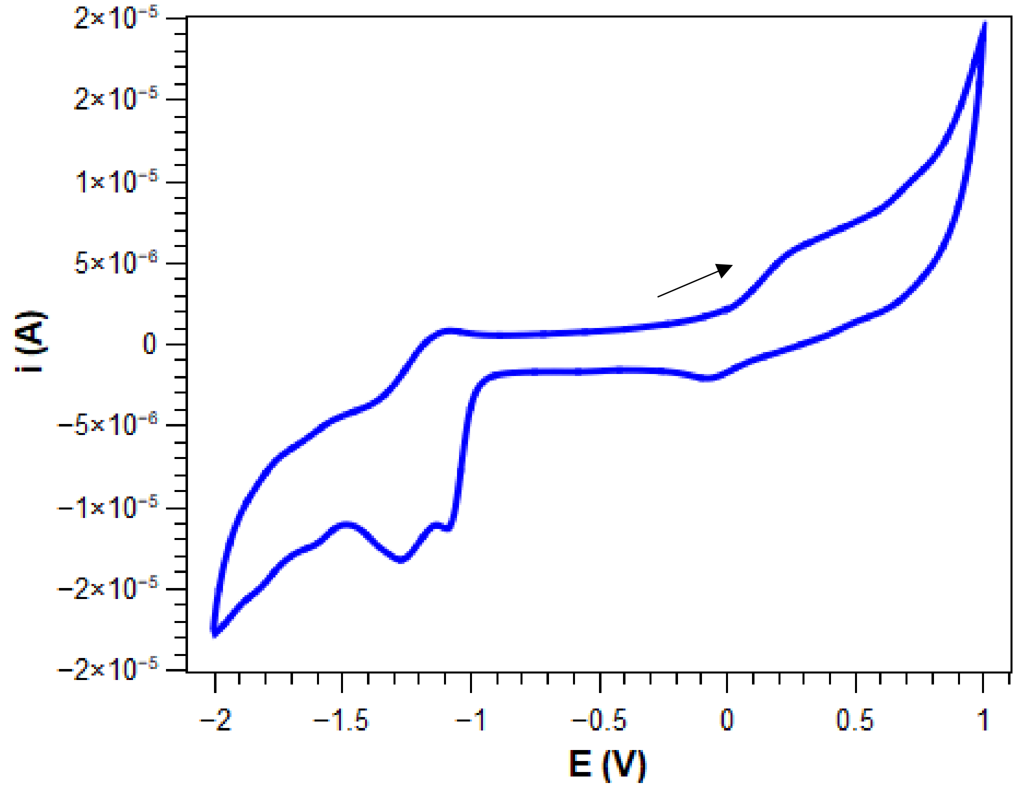

Figure 4.2.1 Cyclic voltammogram of $Co_2L^{Me}OAc$ (1 mM) in argon saturated DMF with $TBAPF_6$ (0.1 M) as the supporting electrolyte and a scan rate of 100 mVs^{-1}. WE = Glassy carbon, RE = Ag wire, CE = Pt wire. Internally referenced to the $Fc^{*0/+}$ couple.

The CV shows a broad oxidative feature from 0 V up to 0.50 V and a second less intense feature at 0.72 V. Upon the reverse scan, there is a small reduction feature at 0.43 V which is likely the reduction of the species generated at 0.73 V, followed by a larger reduction feature at -0.052 V. These two quasireversible processes are likely the sequential $Co^{II}Co^{II}/Co^{II}Co^{III}$ and $Co^{II}Co^{III}/Co^{III}Co^{III}$ couples. The wide peak separations of these events (342 mV for $Co^{II}Co^{II}/Co^{II}Co^{III}$ and 300 mV for $Co^{II}Co^{III}/Co^{III}Co^{III}$) are typical for the $Co^{II/III}$ redox couple due to low k_e values associated with the spin crossover event from high spin Co^{II} to low spin Co^{III}.[193] As the potential is swept more negatively than -1 V, there are two intense and irreversible redox event with E_{pc} values of -1.08 and -1.26 V. These events are likely a combination of Co^{II}Co^{II}/ Co^{II}Co^{I} and Co^{II}Co^{I}/ Co^{I}Co^{I} redox couples, combined with ligand reductions. If the potential is swept to 1.7 V oxidatively (figure 4.2.2), a large, broad, irreversible wave is seen, which, upon reductive scanning to -2 V changes the shape of the reduction events seen. This large oxidative feature is indicative of a destructive ligand oxidation.

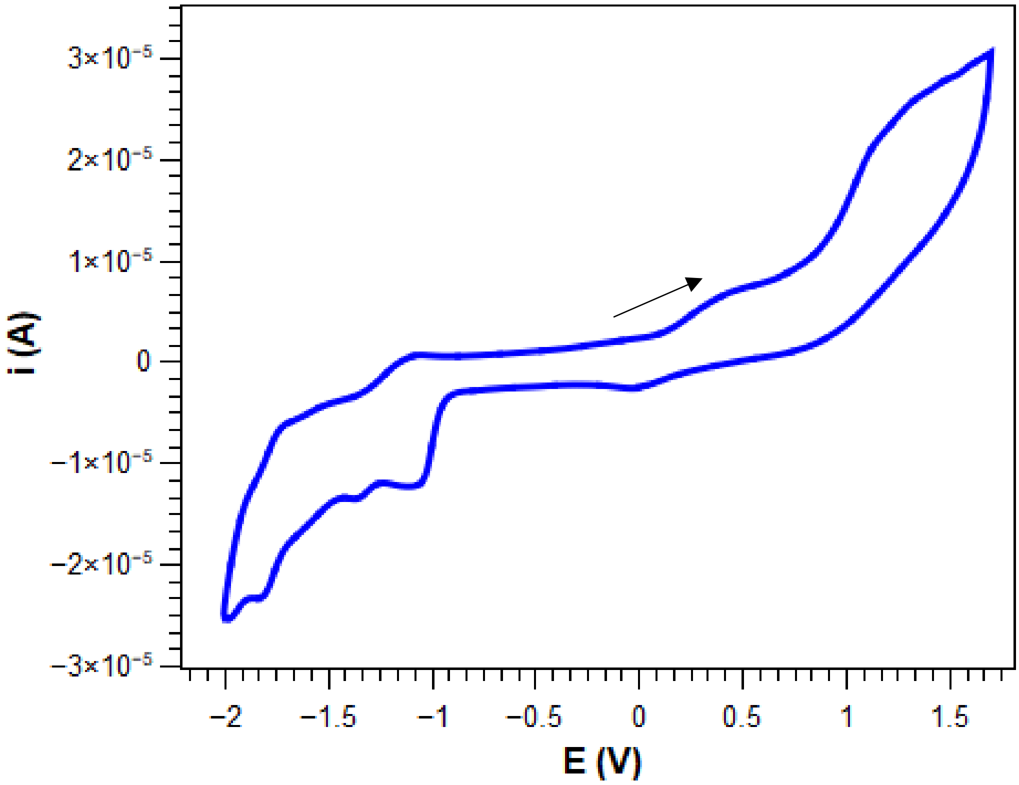

Figure 4.2.2 Cyclic voltammogram of $Co_2L^{Me}OAc$ (1 mM) up to 1.7 V in argon saturated DMF with $TBAPF_6$ (0.1 M) as the supporting electrolyte and a scan rate of 100 mVs^{-1}. WE = Glassy carbon, RE = Ag wire, CE = Pt wire. Potentials were internally referenced to the Fc$^{*0/+}$ couple.

4.2.2 Differential Pulse Voltammetry of Co $Co_2L^{Me}OAc$ in DMF

Since the CV of **$Co_2L^{Me}OAc$** is complex with many overlapping features, differential pulse voltammetry (DPV) experiments were undertaken in an attempt to distinguish these features. These experiments were performed alongside the CV measurements.

The DPV of **$Co_2L^{Me}OAc$** when swept from -0.50 to 1.2 V (figure 4.2.3) shows three distinct oxidation processes consistent with those described in the CV, with one broad wave at 0.20 V, a smaller but now more distinct wave at 0.70 V and finally a very large wave attributed to the ligand oxidation at 1.05 V. Since the differential pulse voltammogram is related to the derivative of the cyclic voltammogram,[194] the peak currents seen in the DPV align with the steepest current/potential slopes on the CV, rather than the peak currents and therefore the peak potential seen in a DPV is an approximation of the $E_{1/2}$ of a reversible process in the CV.

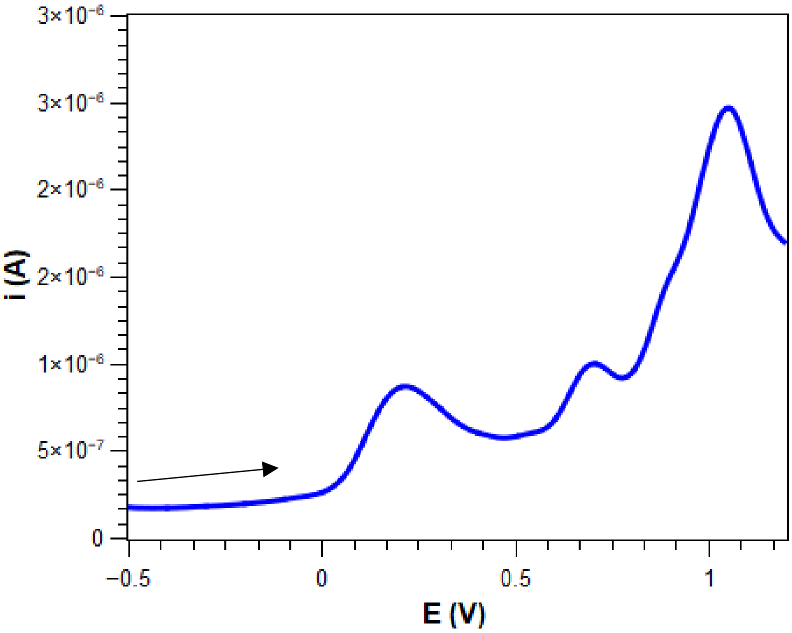

Figure 4.2.3 Differential pulse voltammogram of **$Co_2L^{Me}OAc$** (1 mM) in argon saturated DMF containing $TBAPF_6$ (0.1 M) as the supporting electrolyte. WE = Glassy carbon, RE = Ag wire, CE = Pt wire. Potentials were internally referenced to the $Fc^{*0/+}$ couple.

4.2.3 Comparison With $Zn_3L^{Me}(OAc)_3$

In order to further understand which of the electrochemical features are ligand based, $Zn_3L^{Me}OAc_3$ was used as an electrochemically inert analogue, in which any redox events observed are ligand based. Since Zn(II) is electrochemically inactive in the potential window being studied, the fact that $Zn_3L^{Me}OAc_3$ is trinuclear and not dinuclear should not affect its comparison to the dinuclear **$Co_2L^{Me}OAc$**.

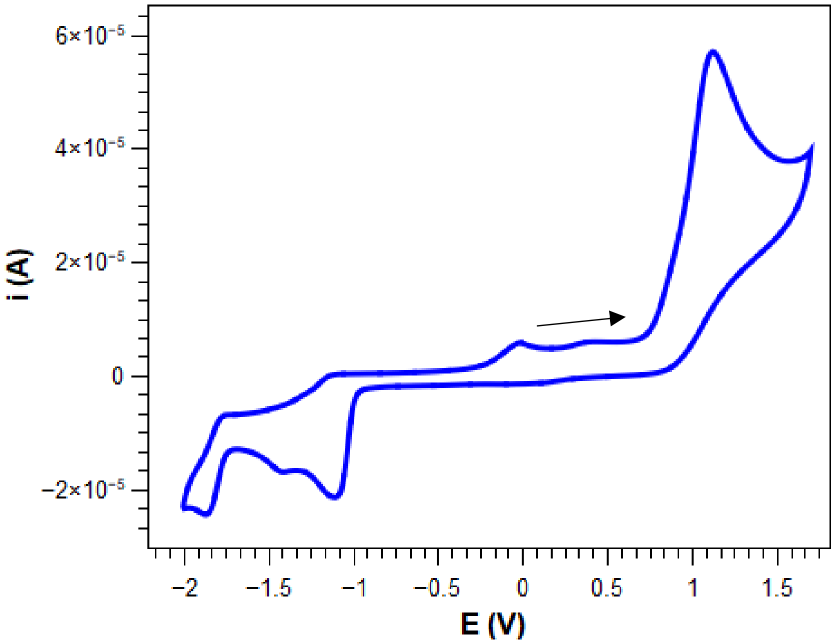

Figure 4.2.4 CV of $Zn_3L^{Me}(OAc)_3$ (2 mM) in argon saturated DMF with $TBAPF_6$ (0.1 M) as the supporting electrolyte and a scan rate of 100 mVs^{-1}. WE = Glassy carbon, RE = Ag wire, CE = Pt wire. Potentials were internally referenced to the $Fc^{*0/+}$ couple.

The CV of $Zn_3L^{Me}(OAc)_3$ shows the expected large irreversible ligand oxidation at 1.05 V and lacks the quasireversible redox features seen with the cobalt analogue at 0.20 and 0.70 V. The sharp irreversible reduction at -1.08 V is still present in the zinc analogue, however the second reduction at -1.26 V is not observed and as a result, this value is assigned to the reduction process from $Co^{II}Co^{II}$ to $Co^{I}Co^{II}$. The smaller ligand reduction feature at -1.42 V is clear in the zinc complex, however this same feature in the CV of **$Co_2L^{Me}OAc$** is most likely masked by the large reduction to $Co^{I}Co^{II}$. The small irreversible oxidative feature at -0.1 V is only observed following the reduction steps between -1 and -1.5 V and is therefore attributed to an ECEC type mechanism relating to a chemical reaction of the reduced ligand.

4.2.4 CV Response of $Co_2L^{Me}OAc$ to O_2 in DMF

In the ORR when catalysed by cobalt complexes, O_2 is normally bound to Co(II) to form Co(III) and thus the initial $Co^{II}Co^{II}/Co^{II}Co^{III}$ couple is the most likely to initiate and terminate the ORR catalytic cycle. For this reason, the quasireversible redox event at 0.20 V was studied in isolation from the other redox events (Figure 4.2.5)

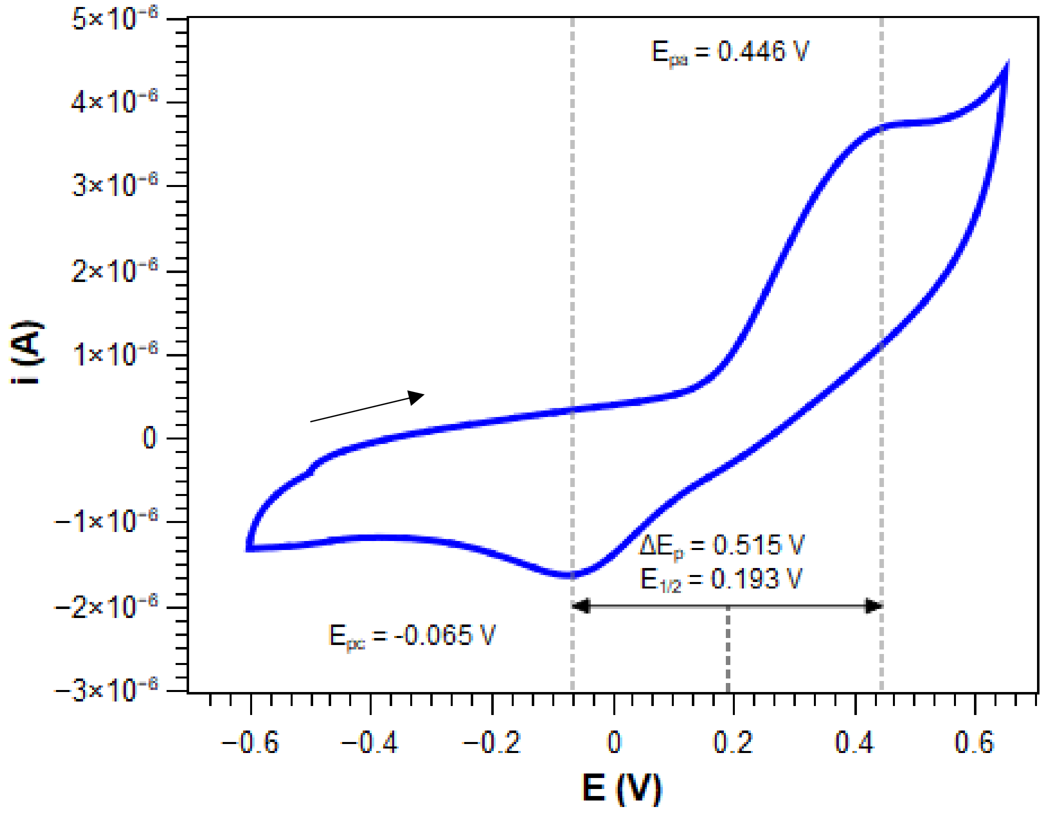

Figure 4.2.5 Isolated CV of the first quasireversible oxidation seen in figure 4.2.1. Potentials were internally referenced to the $Fc^{*0/+}$ couple.

The analyte solution of the CV was saturated with air in order to observe the effects of oxygen binding to the complex. The resulting CV (figure 4.2.6) shows a slight shift in the $E_{1/2}$ and ΔE_p of the redox wave from 0.193 to 0.138 V and from 0.515 to 0.544 V respectively. This is indicative of reversible O_2 binding and is seen for many oxygen binding cobalt complexes to varying degrees.[93,115]

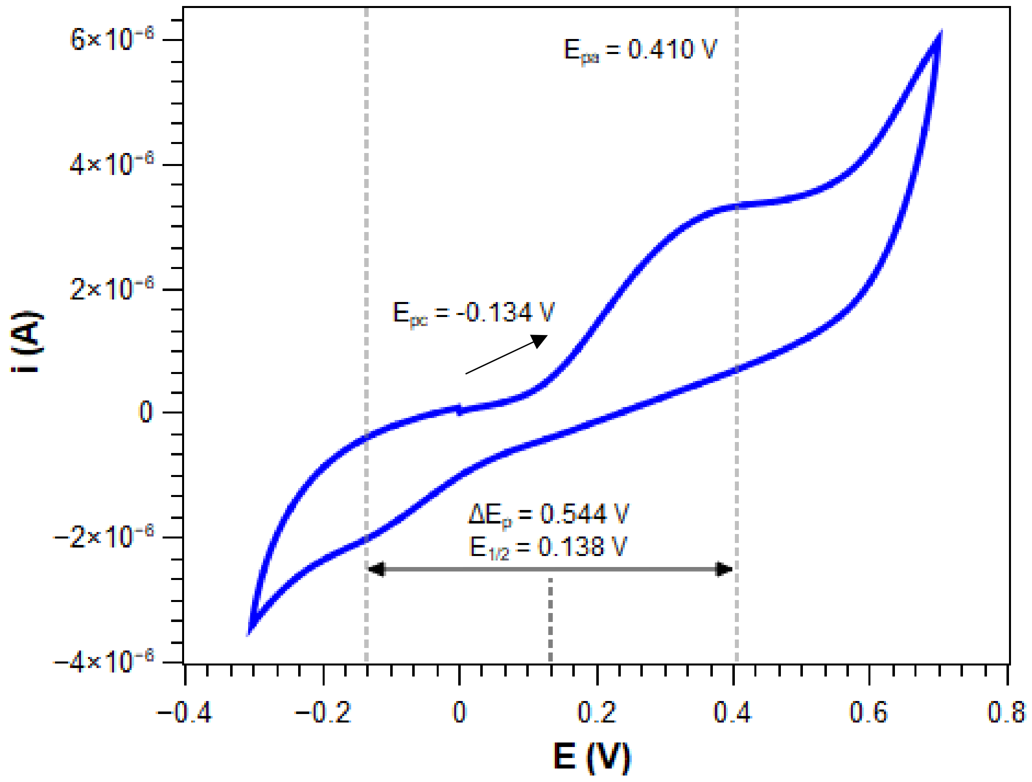

Figure 4.2.6 CV of the $Co^{II}Co^{II}/Co^{II}Co^{III}$ couple of **$Co_2L^{Me}OAc$** in air saturated DMF with $TBAPF_6$ (0.1 M) as the supporting electrolyte and a scan rate of 100 mVs^{-1}. WE = Glassy carbon, RE = Ag wire, CE = Pt wire. Potentials were internally referenced to the $Fc^{*0/+}$ couple.

AcOH was added to the same solution as a preliminary experiment to test the electrocatalytic activity of **$Co_2L^{Me}OAc$** towards the ORR, upon which there are two notable observations. Firstly, while there is a current response from addition of AcOH, the electrocatalytic effect is negligible. This lack of activity is not unexpected since the standard thermodynamic potential of the four-electron ORR in DMF solution is only 0.63 V,[195] in addition, the weak acidity of AcOH will bring this value even lower, therefore the overpotential of the system under these conditions would be extremely low. Similar limited electrocatalytic activities are observed for previously reported low overpotential ORR catalysts.[115,117] Secondly, the $E_{1/2}$ is more positive than before AcOH is added, and the ΔE_p is lower. The higher $E_{1/2}$ shows that the complex is more difficult to oxidise in the presence of AcOH, which is likely a result of ligand protonation, reducing the electron density about the cobalt centres. The reduced ΔE_p indicates a more reversible redox couple, and thus a higher k_e value, suggesting that a proton coupled electron transfer (PCET) step occurs more rapidly than a simple electron transfer.

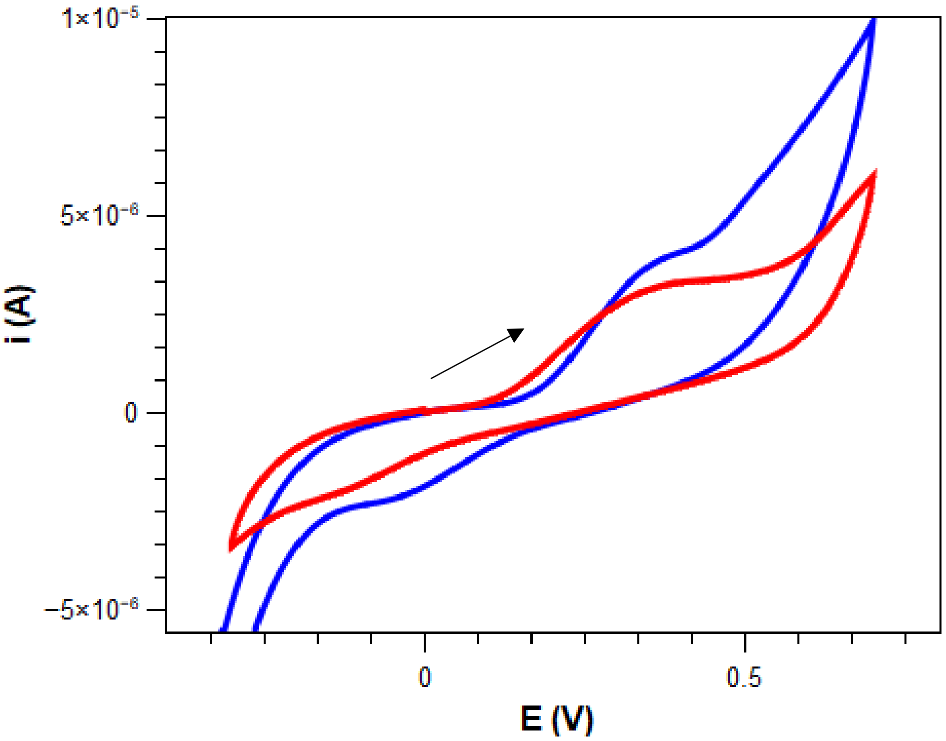

Figure 4.2.7 CVs of CV of the $Co^{II}Co^{II}/Co^{II}Co^{III}$ couple of **$Co_2L^{Me}OAc$** in air saturated DMF both before (red trace) and after (blue trace) addition of AcOH (20 mM) saturated DMF with $TBAPF_6$ (0.1 M) as the supporting electrolyte and a scan rate of 100 mVs^{-1}. WE = Glassy carbon, RE = Ag wire, CE = Pt wire. Potentials were internally referenced to the $Fc^{*0/+}$ couple.

These results show that while **$Co_2L^{Me}OAc$** is able to interact with O_2, the conditions for electrocatalytic ORR must be further optimised to be observed in the cyclic voltammetry.

4.3 Voltammetry of $Co_2L^{CF3}OAc$

Cyclic voltammetry of **$Co_2L^{CF3}OAc$** in the potential range of -0.5 and 1.5 V (figure 4.3.1), where the methyl groups in the *para* position of the 2-iminophenolate moieties of **$Co_2L^{Me}OAc$** have been substituted for trifluoromethyl groups, shows similar redox events as its more electron rich counterpart, with a few key differences.

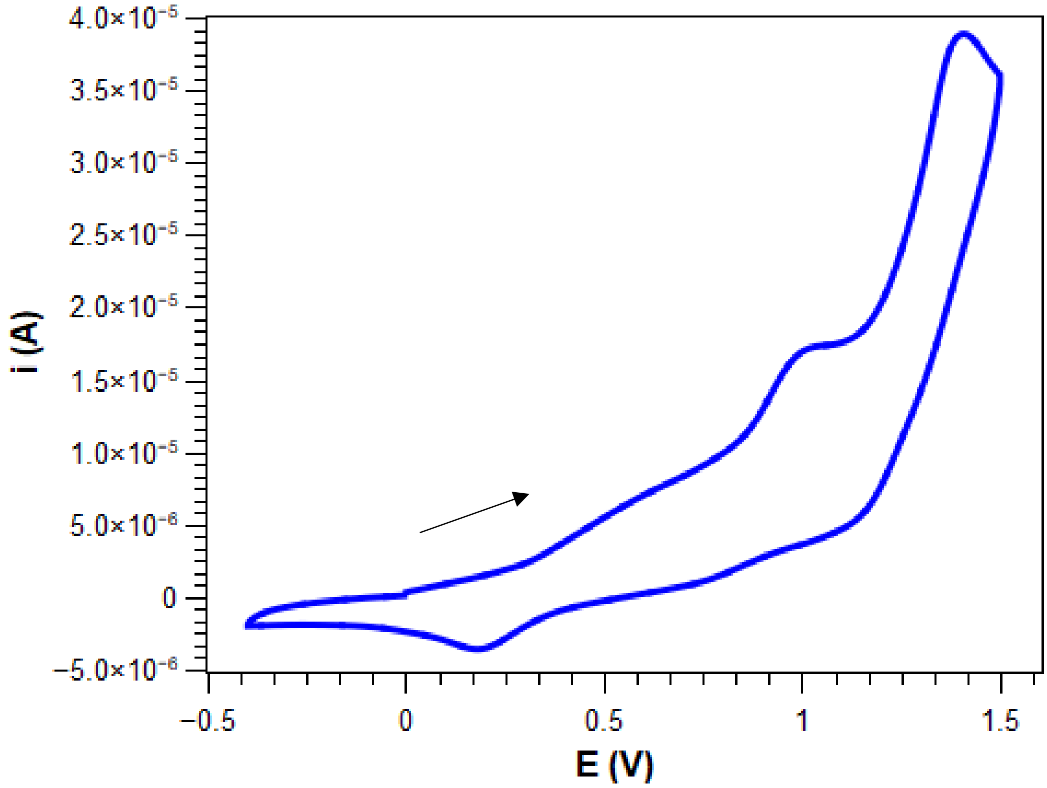

Figure 4.3.1 Cyclic voltammogram of $Co_2L^{CF3}OAc$ (1 mM) in argon saturated DMF with $TBAPF_6$ (0.1 M) as the supporting electrolyte and a scan rate of 100 mVs^{-1}. WE = Glassy carbon, RE = Ag wire, CE = Pt wire. Potentials were internally referenced to the $Fc^{*0/+}$ couple.

The first broad oxidation attributed to the $Co^{II}Co^{II}/Co^{II}Co^{III}$ couple shifts positively to c.a. 0.6 V, which is significantly higher than the value of the same couple for **$Co_2L^{Me}OAc$**, and its corresponding reduction process has an E_{pc} value of 0.18 V, approximately 300 mV higher than the same wave in the CV of **$Co_2L^{Me}OAc$**. The peak separation between the oxidative and reductive processes is 0.42 V, highlighting the increased reversibility of this process in the more electron deficient complex. The second redox process related to the $Co^{II}Co^{III}/Co^{III}Co^{III}$ couple is also anodically shifted where the E_{pa} and E_{pc} are 1.01 and 0.73 V respectively, again approximately 300 mV higher than those seen for **$Co_2L^{Me}OAc$**. Finally, the large ligand oxidation wave is much sharper in the case of **$Co_2L^{CF3}OAc$** and has a peak potential of 1.40 V and an onset potential of 1.15 V. While the peak potential of the ligand oxidation in **$Co_2L^{Me}OAc$** is difficult to assign accurately, the same ligand in **$Zn_3L^{Me}(OAc)_3$** occurs at only 1.05 V. These results clearly show the strong influence of substituting the group at the *para* position of the 2-aminophenol moiety for a more electron withdrawing group upon both the metal and ligand centred processes.

Processes assigned to Co^{II} to Co^{I} and ligand reductions are merged at -1.19 V (figure 4.3.2), where the reduction of the ligand has shifted by -100 mV, and the Co^{II} to Co^{I} reduction has shifted by +100 mV .

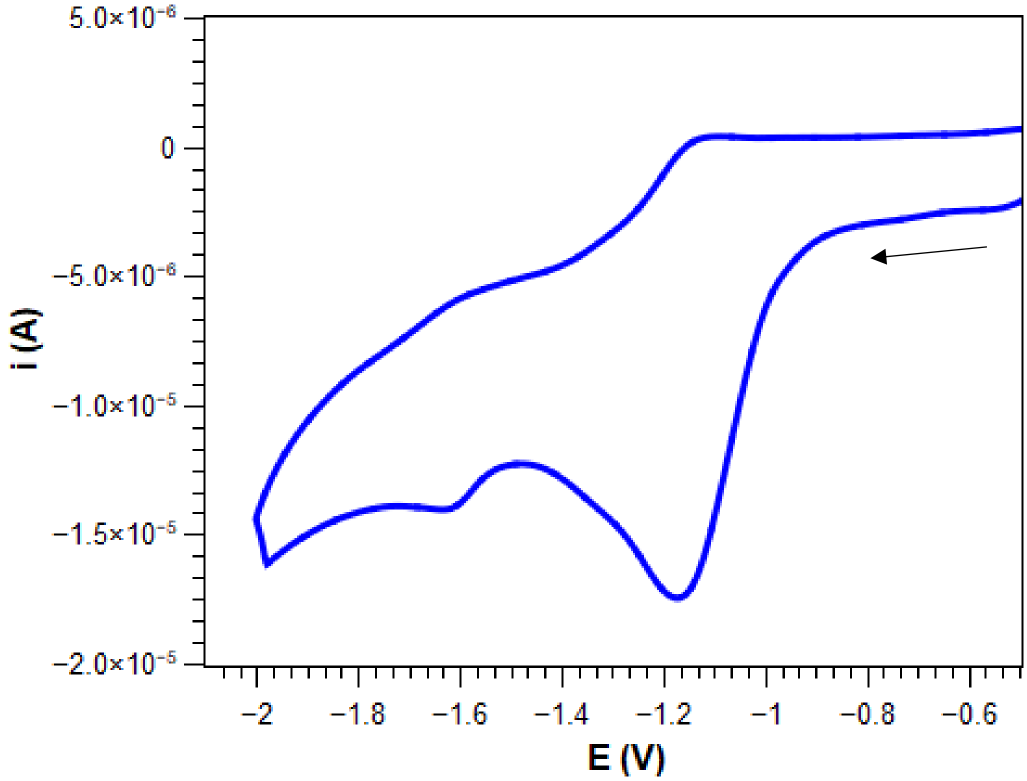

Figure 4.3.2 Cyclic voltammogram of $Co_2L^{CF3}OAc$ (1 mM) in argon saturated DMF with $TBAPF_6$ (0.1 M) as the supporting electrolyte and a scan rate of 100 mVs^{-1}. WE = Glassy carbon, RE = Ag wire, CE = Pt wire. Potentials were internally referenced to the $Fc^{*0/+}$ couple.

The negative shift of the ligand reduction is likely a result of slower electron transfer kinetics to the electrode due to steric bulk provided by trifluoromethyl groups, while the positive shift of the metal centred reduction is likely due to the reduced electron density about the metal centres due to the electron withdrawing effects of the trifluoromethyl group.

4.4 Voltammetry of $Co_3L^{Me}(OAc)_3$

$Co_3L^{Me}(OAc)_3$ was subjected to the same electrochemical characterisation as **$Co_2L^{Me}OAc$** and while **$Co_3L^{Me}(OAc)_3$** is structurally similar to **$Co_2L^{Me}OAc$**, since it is the product of the reaction between **$Co_2L^{Me}OAc$** and an equivalent of $Co(OAc)_2$, one may expect to see similar, or more electrochemical features in the CV (figure 4.4.1)

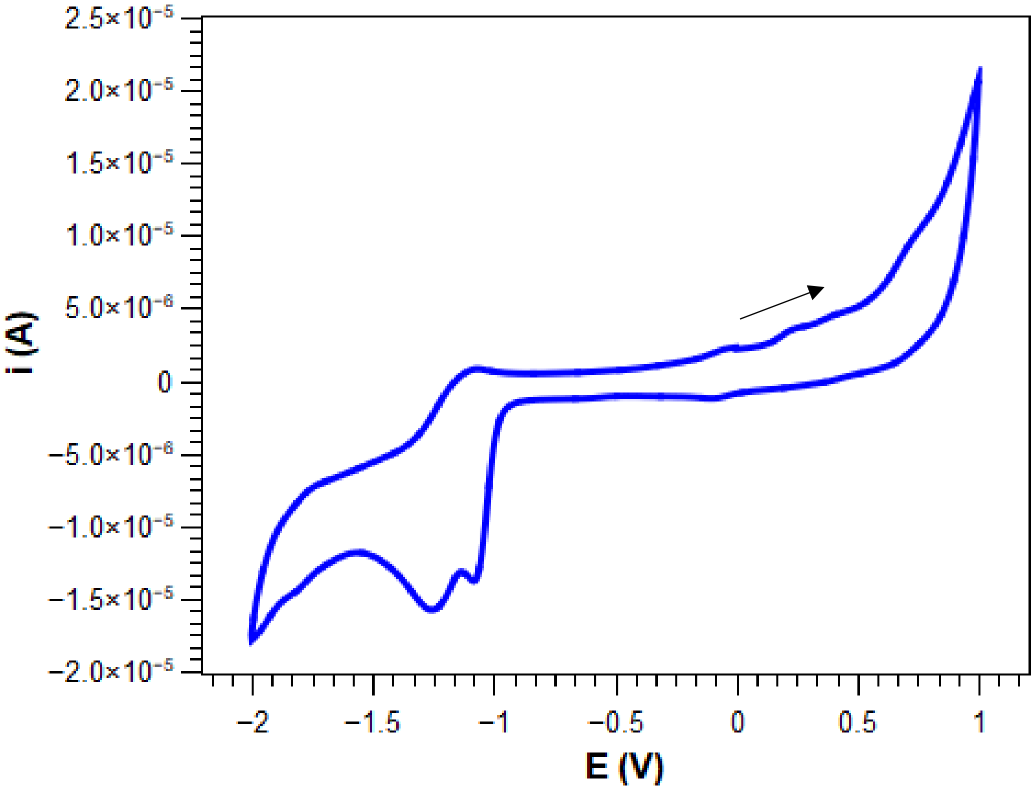

Figure 4.4.1 Cyclic voltammogram of **$Co_3L^{Me}(OAc)_3$** (1 mM) in argon saturated DMF with $TBAPF_6$ (0.1 M) as the supporting electrolyte and a scan rate of 100 mVs^{-1}. WE = Glassy carbon, RE = Ag wire, CE = Pt wire. Potentials were internally referenced to the $Fc^{*0/+}$ couple.

$Co_3L^{Me}(OAc)_3$ demonstrates much reduced current responses to the $Co^{II/III}$ events than **$Co_2L^{Me}OAc$**. The oxidation at -0.2 V, similar to that of **$Zn_3L^{Me}(OAc)_3$** only occurs after the reduction events between -1 and -1.5 V and is equally attributed to a ligand-based oxidation. The second oxidation at 0.26 V is coupled to the small reduction at -0.080 V and is therefore assigned to the $Co^{II}Co^{II}Co^{II}/Co^{III}Co^{II}Co^{II}$ couple. Similarly, the oxidation at 0.72 V is attributed to the $Co^{III}Co^{II}Co^{II}$ to $Co^{III}Co^{III}Co^{II}$ oxidation. However, in the case of **$Co_3L^{Me}(OAc)_3$**, there is a third feature between these two oxidations at 0.41 V. This is attributed to the irreversible oxidation of the third Co(II) ion which bridges the two phenolate moieties of the ligand. The CV also shows the same two reductive features at -1.10 and -1.25 V, which are attributed to the ligand reduction and multi-electron reduction of Co^{II} to Co^{I} respectively.

The peak separation between the oxidative and reductive waves for the $Co^{II}Co^{II}Co^{II}/Co^{III}Co^{II}Co^{II}$ couple is smaller than that for the $Co^{II}Co^{II}/Co^{II}Co^{III}$ couple of **$Co_2L^{Me}OAc$** (0.34 vs 0.52 V respectively) indicating that the former couple is more electrochemically reversible than the latter. This is most likely due to the increased rigidity of the trinuclear complex, reducing the extent of geometric deformation upon oxidation. However, there still remains a large peak separation due to the spin crossover effects discussed previously.

Differential pulse voltammetry (DPV) of **$Co_3L^{Me}(OAc)_3$** under the same conditions (Figure 4.4.2) clearly shows the second and third oxidation events at 0.47 and 0.82 V vs $Fc^{*0/+}$ respectively, the first oxidation relating to the $Co^{II}Co^{II}Co^{III}/Co^{III}Co^{III}Co^{II}$ and $Co^{III}Co^{III}Co^{II}/Co^{III}Co^{III}Co^{III}$ couples. The first oxidative wave in the CV relating to the $Co^{II}Co^{II}Co^{II}/Co^{III}Co^{II}Co^{II}$ could not be observed.

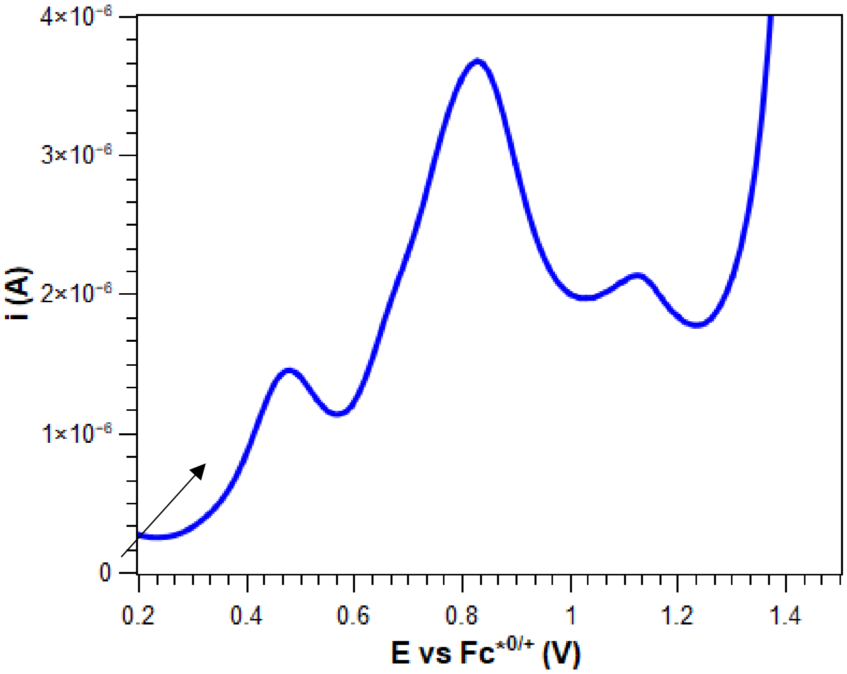

Figure 4.4.2 Differential pulse voltammogram of **$Co_3L^{Me}(OAc)_3$** in argon saturated DMF containing $TBAPF_6$ as the supporting electrolyte, potentials are referenced internally to the $Fc^{*O/+}$ couple. Potentials were internally referenced to the $Fc^{*0/+}$ couple.

4.5 Voltammetry of $Co_4L^{Me}{}_2(BF_4)_2$

The cyclic voltammogram of the tetranuclear defective dicubane core complex **$Co_4L^{Me}{}_2(BF_4)_2$** (Figure 4.5.1) is interestingly bare, where the only redox events occur at either highly oxidising or reducing potentials and is similar to the CV of $Zn_3L^{Me}(OAc)_3$.

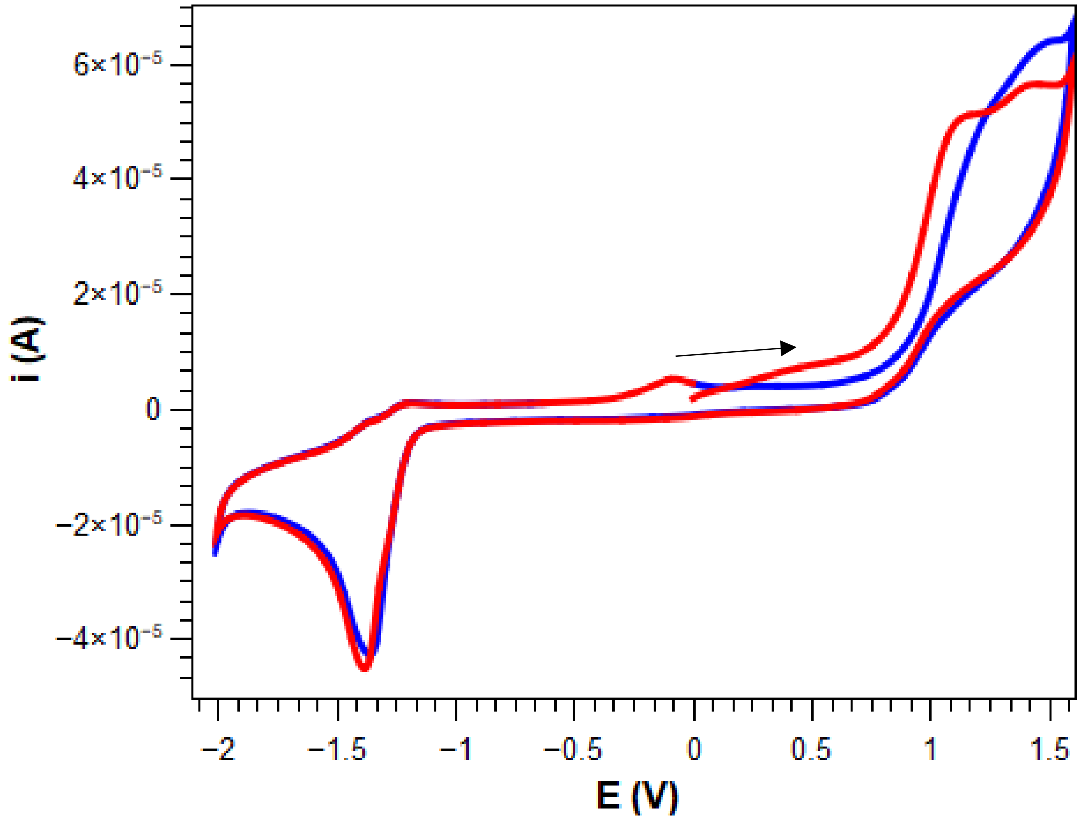

Figure 4.5.1 Cyclic voltammogram of **$Co_4L^{Me}{}_2(BF_4)_2$** (1 mM) in argon saturated DMF with $TBAPF_6$ (0.1 M) as the supporting electrolyte and a scan rate of 100 mVs^{-1} where the red and blue traces show the first and second scans respectively. Potentials were internally referenced to the $Fc^{*0/+}$ couple.

On the first scan, there is a slight increase in current between 0.3 and 0.6 V which could be a result of an oxidation of one of the four cobalt centres, however on the second scan this wave is absent. At 1.1 V there is a large irreversible oxidative feature which is followed by a second small wave at 1.41 V. In the cyclic voltammetry of previous complexes, one peak is seen in oxidations above this potential and are assigned to only ligand oxidations. The presence of two peaks in this range for the tetranuclear complex suggests that one of these must be metal centred. Upon subsequent scans, these two peaks merge into one, showing the chemical instability of the tetranuclear complex following oxidation at such high positive potentials. The sharp ligand reduction at -1.37 V is similar to those seen in previous complexes bearing the same ligand, however, the wave assigned to the reduction of Co^{II} to Co^{I} in previous complexes is not present for $\mathbf{Co_4L^{Me}_2(BF_4)_2}$. The most likely cause for the lack of, and high potential of redox events, despite the high number of classically electrochemically active metal ions in the complex is a very low k_e value (i.e. electron transfer between the electrode and the complex is extremely low). Low k_e values shift the oxidation and reduction potentials to more extreme values, which explains the high potential required for metal centred oxidation. The oxidised species then undergoes rapid chemical reaction to a species which is resistant to reduction, and thus no return wave is seen.

There is a clear trend in the voltammetry of the multinuclear cobalt complexes as the number of metal centres increase. In the dinuclear complex, the redox waves relating to the $Co^{II/III}$ couple are clear, in the trinuclear complex the wave appears but the current response is drastically reduced, and in the tetranuclear complex the only wave appears at highly oxidising potentials. This trend may be explained by the reduced communication with the electrode surface as the size and complexity of the structure increases. Particularly in the tetranuclear case, the cobalt atoms are confined in a bulky ligand system. In addition, while the dinuclear and trinuclear complexes are neutral species under the assumption that AcO^- remains coordinated in solution, the tetranuclear complex bears a 2+ charge with non-coordinating anions, meaning that oxidation from this structure will be a more energy intensive process, requiring a higher overpotential to drive the electron transfer.

4.6 Voltammetry of $Co_2L^{Me}OAc$ in Methanol

4.6.1 Choice of Solvent

The choice of solvent is extremely important when examining catalytic and electrocatalytic reactions. In the case of the ORR, the most common non-aqueous solvents are DMF and acetonitrile. The pKa of proton sources, as well as the thermodynamic potentials of the ORR pathways vary greatly between solvents, and as such, it is of vital importance to consider solvent effects when comparing catalysts with those in the literature. The simplest method to mitigate complications from solvent affects is to examine a catalyst under the same conditions as used in the literature. Since the catalysts in this work aim to build upon salen-like and Schiff base cobalt complexes in which the solvent of choice tends to be methanol, this solvent was chosen both for further electrochemical characterisation and electrocatalytic studies. Methanol, however, is typically a less suitable solvent for voltammetry owing to its narrow potential window. Nonetheless, methanol is a suitable solvent to examine the metal centred redox processes which lie between -0.5 and 1 V.

4.6.2 Internal Referencing

Since the aim of this section is to understand the electrochemical behaviour under catalytic conditions and compare to some of the catalysts found in the literature, it is important to have a consistent reference point. These previous studies in the literature have used decamethylferrocene (Fc*) as an internal reference, since it’s redox potential is extremely resistant to changes in solution acidity, whereas the redox couple of the more classical reference compound ferrocene is prone to drift and change in reversibility upon addition of acids to the analyte solution.

In addition, decamethylferrocene in MeOH has a reduction potential which is conveniently close to the reference potential of the silver wire used as a pseudoreference electrode, and the Fc* redox wave is normally well away from the redox processes of the analyte complexes.

4.6.3 Supporting Electrolyte

While in DMF solutions, $TBAPF_6$ is a suitable supporting electrolyte, its solubility in MeOH is limited at room temperature. The electrolyte was therefore changed to

$TBAClO_4$ and is used throughout this section. In addition, it was important to reduce the concentration of the electrolyte to 50 mM instead of 100 mM, this is because at higher concentrations, $TBAClO_4$ abstracts the acetate bridge of the dinuclear complexes and initiates dimerisation and precipitation of the tetranuclear complex, which has very limited solubility in methanol.

4.6.4 Cyclic Voltammetry of $Co_2L^{Me}OAc$

CV of **$Co_2L^{Me}OAc$** in MeOH (Figure 4.6.1) highlights the two cobalt centred redox processes, relating to the $Co^{II}Co^{II}/Co^{II}Co^{III}$ and $Co^{II}Co^{III}/Co^{III}Co^{III}$ couples, much more clearly than in DMF solution. This could be explained by the fact that MeOH is a protic solvent, and PCET steps may be more facile than simple ET. The second process in particular shows much improved reversibility where a clear reduction wave is seen. In addition, MeOH has a lower viscosity than DMF, and therefore increased diffusion rates result in higher current responses.

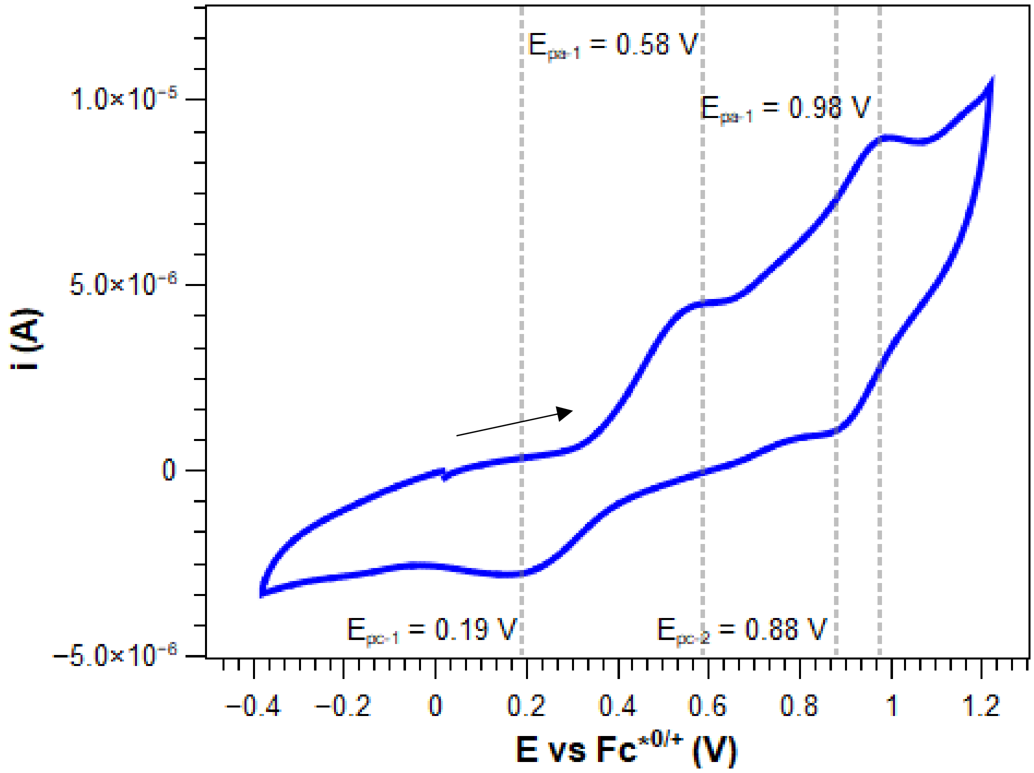

Figure 4.6.1 Cyclic voltammetry of **$Co_2L^{Me}OAc$** (1 mM) in argon saturated MeOH containing $TBAClO_4$ (50 mM) as the supporting electrolyte.

The $Co^{II}Co^{II}/Co^{II}Co^{III}$ couple shows E_{pa} and E_{pc} values of 0.58 and 0.19 V vs $Fc^{*0/+}$ respectively, giving a ΔE_p of 0.39 V and a $E_{1/2}$ of 0.385 V. The peak separation in

MeOH is 125 mV lower than that of the same complex in DMF, demonstrating the increased rates of electron transfer in this solvent system. The $E_{1/2}$ of 0.385 V is higher than even the most electron deficient of the Co^{II}salen family of ORR catalysts studied by Stahl and co-workers previously discussed in chapter 1 of this work. This high $E_{1/2}$ can be attributed to the fact that each cobalt centre is only coordinated by one imine donor, versus two per cobalt centre in mononuclear salen complexes and the rest of the coordination sphere is comprised of relatively weak field O donors.

The second redox process, attributed to the $Co^{II}Co^{III}/Co^{III}Co^{III}$ has an $E_{1/2}$ value of 0.93 V vs $Fc^{*0/+}$, over 500 mV higher than the first couple. This large difference in $E_{1/2}$ for the two processes indicates a very strong electronic communication between the two cobalt centres, which is not unexpected considering they are separated by only an alcoholate bridge. The small ΔE_p (100 mV) of this redox process shows an improved electrochemical reversibility than the first process, though still far from the ideal value for a fully reversible couple (59 mV), the peak separation is still less than is common for a $Co^{II/III}$ couple. It has been suggested that in some dinuclear cobalt complexes, the second Co^{III} may have a more stable high spin state than the first Co^{III} ion, and as a result, peak separation from spin crossover effects on the CV timescale may be reduced.[196]

4.6.1 Cyclic Voltammetry of $Co_2L^{Me}OAc$ under acidic conditions

When the methanolic analyte solution of **$Co_2L^{Me}OAc$** is acidified with AcOH between 15 and 55 mM (figure 4.6.2), there are multiple changes to the voltametric response. Similar to that seen in DMF solutions, the E_{pc} of the first redox process is increased from 0.19 V vs $Fc^{*0/+}$ at 0 mM AcOH, to 0.31 V vs $Fc^{*0/+}$. This positive shift of 120 mV could be related to protonation of the ligand making reduction more facile, however, the E_{pa} of the process is largely unchanged over the whole range of AcOH concentrations, and therefore, the change in E_{pc} most likely arises from an increase in reversibility of the $Co^{II}Co^{II}/Co^{II}Co^{III}$ couple. The ΔE_p value for this process upon addition of AcOH decreases from 0.39 V to 0.28 V, and the $E_{1/2}$ is shifted positively to 0.45 V vs $Fc^{*0/+}$ at 55 mM AcOH, after which concentration no further shift occurs. The potential of the second couple shifts negatively slightly upon addition of AcOH, and the reduction wave is gradually lost over the concentration range.

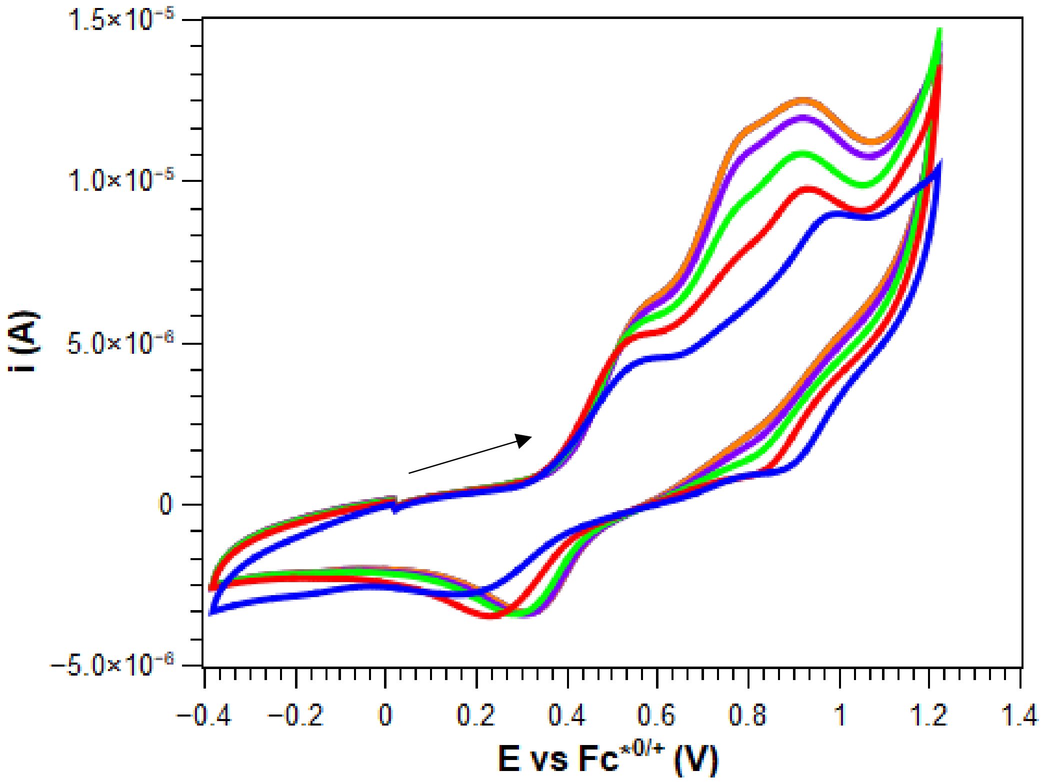

Figure 4.6.2 Cyclic voltammetry of **$Co_2L^{Me}OAc$** (1 mM) in argon saturated MeOH containing $TBAClO_4$ (50 mM) as the supporting electrolyte and AcOH (0 mM (blue trace), 15 mM (red trace), 25 mM (green trace), 45 mM (purple trace) and 55 mM (orange trace) at a scan rate of 100 mVs^{-1}.

Finally, a new irreversible oxidation wave begins to appear just before $Co^{II}Co^{III}/Co^{III}Co^{III}$ oxidation as [AcOH/TBAOAc] is increased. It is difficult to accurately assign the redox process which causes this wave, and it was initially considered to be attributed to coordination effects of acetate to the metal centres increasing the ease of oxidation steps.

To examine the system further, a similar study was undertaken using the slightly stronger proton source benzoic acid (BzOH) (pKa = 9.30) instead of AcOH (pKa = 9.63) (figure 4.6.3). The CV shows similar features when increasing BzOH as with AcOH, where the reductive wave of the first process is shifted positively over the [BzOH] range, and the reduction wave for the second process disappears. The increase in oxidative current, however, is much more pronounced. This observation led to the suspicion of a slow electrocatalytic oxidation reaction upon addition of the proton source, since the binding of the carboxylate does not explain the large increase in current between the two proton sources.

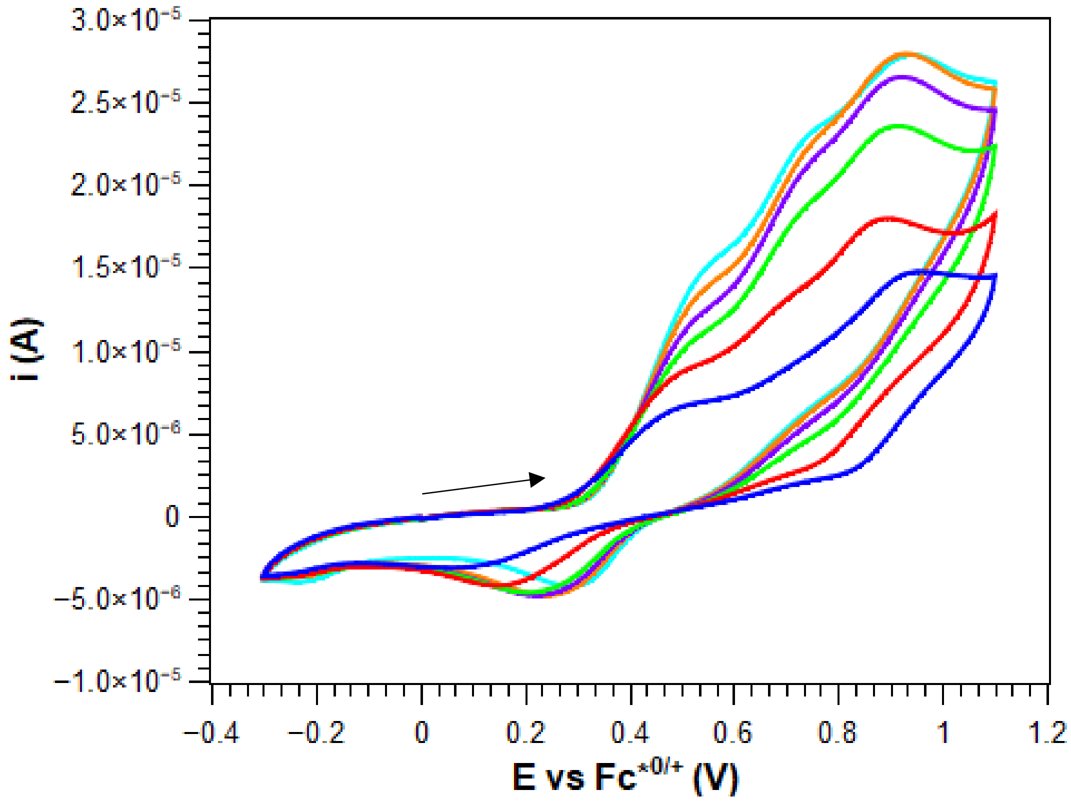

Figure 4.6.3 Cyclic voltammetry of **$Co_2L^{Me}OAc$** (1 mM) in argon saturated MeOH containing $TBAClO_4$ (50 mM) as the supporting electrolyte and BzOH (0 mM (blue trace), 5 mM (red trace), 10 mM (green trace), 15 mM (purple trace) 25 mM (orange trace) and 100 mM (cyan trace) at a scan rate of 100 mVs^{-1}.

Further to this, if instead of AcOH alone, a buffer containing AcOH and TBAOAc in a 1:1 molar ratio is used (Figure 4.6.4), the increase in current is even larger than the previous systems. These findings were initially attributed to slow electrocatalytic oxidation of MeOH to either formaldehyde or formic acid. The current enhancement upon addition of TBAOAc likely arises due to the basic properties of AcO^- in MeOH. While the overall solution is acidic, abstraction of protons from a reactive MeOH intermediate by free AcO^- ions drives the electrocatalytic oxidation of MeOH.

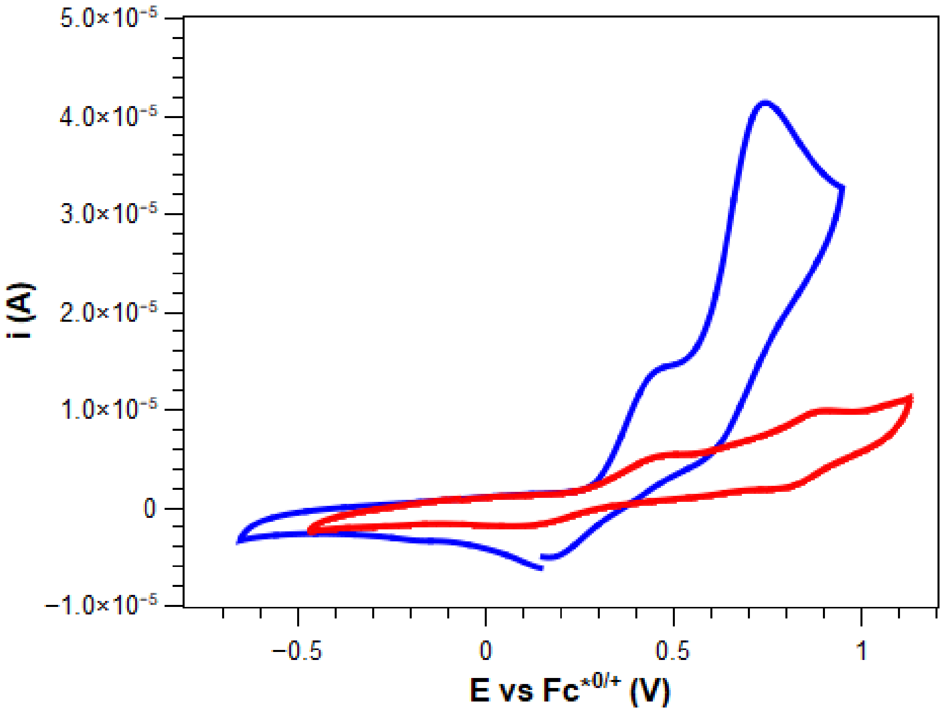

Figure 4.6.4 Cyclic voltammetry of **$Co_2L^{Me}OAc$** (1 mM) in argon saturated MeOH containing $TBAClO_4$ (50 mM) as the supporting electrolyte in the absence (red trace) and presence of AcOH/TBAOAc (25 mM) at a scan rate of 100 mVs^{-1}.

This assignment seems counterintuitive, adding a source of protons to the electrolyte should not facilitate an electrocatalytic oxidation in which protons are released. Nonetheless, there are many examples of electrocatalytic MeOH oxidation in acidic media. Liu and co-workers studied a homogeneous ruthenium containing polyoxometalate catalyst $[Ru_4O_4(OH)_2(H_2O)_4(\gamma\text{-}SiW_{10}O_{36})_2]^{10-}$ in a variety of aqueous alcohol or pure alcohol solutions containing H_2SO_4 as the proton source. Bulk electrolysis of a pure MeOH solution containing 0.50 M H_2SO_4 at 0.88 V vs $Fc^{0/+}$ (c.a. 1.28 V vs $Fc^{*0/+}$) yielded formaldehyde and formic acid at a Faradaic efficiency of 95.8%.

On the other hand, this assignment did not satisfactorily explain the increased electrocatalytic response to BzOH versus AcOH. An electrocatalytic decarboxylation mechanism in which CO_2 is lost from the carboxylic acid to form a radical species was considered. This reaction would proceed faster with a carboxylic acid where the formed radical is stabilised, rather than an unstable methyl radical. In addition, the oxidative electrocatalytic decarboxylation of carboxylic acids has been used in carbon-carbon bond forming reactions known as the Kolbe reaction. This reaction has shown to be effectively carried out in MeOH solvent at potentials similar to those found in this work.[197]

4.6.2 Voltammetry of the $Co_2L^{R}OAc$ family in MeOH

Cyclic voltammetry measurements were performed on the wider family of **$Co_2L^{R}OAc$** complexes. While all but **$Co_2L^{CF3}OAc$** were determined to be of insufficient purity to perform quantitative catalytic studies, the CVs of the whole family showed similar redox features, indicating that the impurity is not electroactive. The measurement of these CVs allowed determination of the electronic effect that substitution at the 4-position of the phenolate moiety had on the redox potentials of the Co^{II}/Co^{III} couple. The $E_{1/2}$ values of **$Co_2L^{Me}OAc$**, **$Co_2L^{CF3}OAc$**, **$Co_2L^{tBu}OAc$** and **$Co_2L^{H}OAc$** in argon saturated MeOH containing AcOH/TBAOAc (20 mM) are shown in Table 4.6.1. The CVs **of $Co_2L^{F}OAc$** and **$Co_2L^{tAm}OAc$** showed irreversible Co^{II}/Co^{III} features and therefore $E_{1/2}$ values are not quoted.

Complex	**Co^{II}/Co^{III} $E_{1/2}$ (mV vs $Fc^{*0/+}$)**
$Co_2L^{Me}OAc$	450
$Co_2L^{CF3}OAc$	530
$Co_2L^{H}OAc$	500
$Co_2L^{tBu}OAc$	430

Table 4.6.1 Half wave potentials of the Co^{II}/Co^{III} couple of the $Co_2L^{R}OAc$ family in argon saturated MeOH containing 20 mM AcOH/TBAOAc with respect to the $Fc^{*0/+}$ couple.

It is seen from the half wave potentials of the $Co_2L^{R}OAc$ family that substitution at the 4-position of the phenolate moiety has a reasonable effect on the reduction potential of the Co^{II}/Co^{III} couple, where the difference between the most electron withdrawing and donating substituents is 100 mV. The difference between the $E_{1/2}$ of **$Co_2L^{Me}OAc$** and **$Co_2L^{CF3}OAc$** (the substances of sufficient purity for quantitative catalytic study) is 80 mV, which should have a significant effect on the TOF of the ORR if a similar rate vs. overpotential trend is seen, as is the case with Co^{II}salen complexes.

4.7 Electrocatalytic response of $Co_2L^{Me}OAc$ to the ORR

4.7.1 ORR at Glassy Carbon without $Co_2L^{Me}OAc$

To understand the electrocatalytic activity of **$Co_2L^{Me}OAc$** under the set of standard catalytic conditions used in this work (25 mM AcOH/TBAOAc, 2 mM O_2, MeOH solution) it is important to first understand the ORR activity at the glassy carbon electrode under the same conditions.

In air saturated MeOH solutions containing 25 mM AcOH/TBAOAc (figure 4.7.1), the cathodic current begins to onset at -0.2 V vs $Fc^{*0/+}$, after which the current response increases exponentially to an initial peak potential of -0.86 V vs $Fc^{*0/+}$. Following this first cathodic peak the current plateaus briefly before reaching a second peak current at -1.50 V vs $Fc^{*0/+}$. The processes at these two peaks are most likely ORR, followed by reduction of protons to H_2 at more negative potentials.

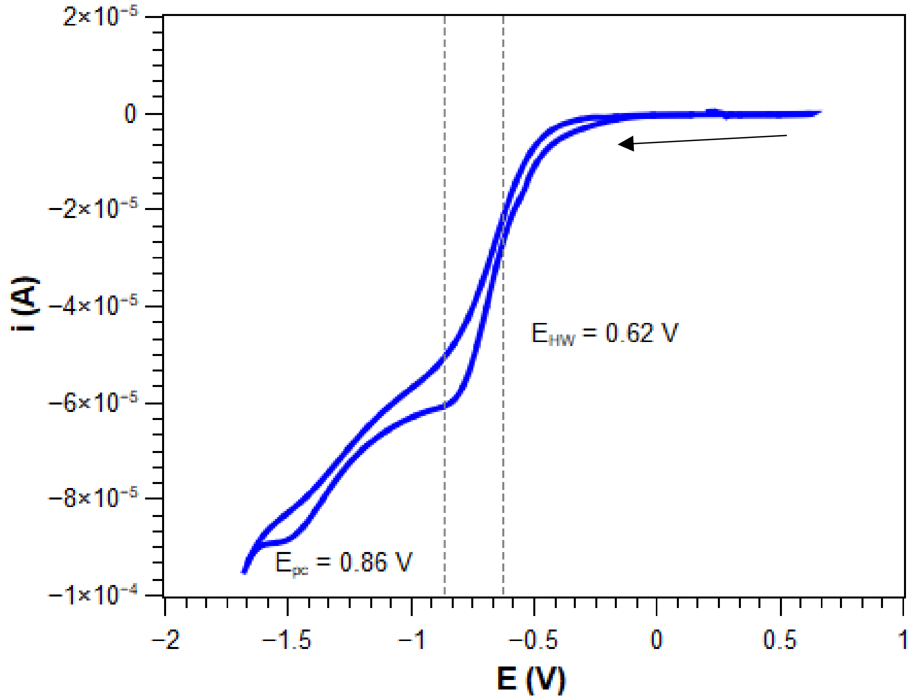

Figure 4.7.1 Cyclic voltammogram of an air saturated MeOH solution (2 mM O_2) containing AcOH/TBAOAc (25 mM) at a scan rate of 10 mVs^{-1} at an unmodified glassy carbon electrode. Potentials were internally referenced to the $Fc^{*0/+}$ couple.

The standard potential of the ORR in MeOH containing AcOH/TBAOAc was determined by Stahl and co-workers by open circuit potentiometry (OCP) measurements of the $H_2/2H^+$ couple at a Pt electrode in MeOH containing 25 mM

AcOH/TBAOAc and 1 atm H_2. The potential of the $H_2/2H^+$ couple was determined to be -0.31 V vs $Fc^{*0/+}$ and the reduction potential of the O_2/H_2O_2 couple was determined by adding 0.68 V (the standard reduction potential of the O_2/H_2O_2 couple) to obtain $E_{O2/H2O2}$ = 0.37 V $Fc^{*0/+}$. Similarly (though not commented upon by Stahl and co-workers) the reduction potential of the O_2/H_2O couple ($E_{O2/2H2O}$) can also be determined by the same method of adding 1.23 V (the standard reduction potential of the $O_2/2H_2O$ couple) to -0.31 V to obtain $E_{O2/2H2O}$ = 0.92 V vs $Fc^{*0/+}$.

If the operating potential of the ORR under these conditions is taken to be the half-wave potential (the potential at which half of the peak current of the ORR is drawn, 0.62 V vs $Fc^{*0/+}$), then the operating overpotential of the ORR is the difference between the half wave potential and $E_{O2/2H2O}$ (1.54 V).

The CV of a MeOH solution containing 1 mM **$Co_2L^{Me}OAc$** and 25 mM AcOH/TBAOAc shows little response to the addition of O_2 similar to that shown in DMF solutions. The negligible ORR response in the CV of **$Co_2L^{Me}OAc$** is mostly due to the low overpotential of the ORR under these conditions. The $E_{1/2}$ of the $Co^{II}Co^{II}/Co^{II}Co^{III}$ couple in the presence of 25 mM **$Co_2L^{Me}OAc$** is 0.45 V vs $Fc^{*0/+}$ and thus the overpotential of the ORR under these conditions if the $Co^{II}Co^{II}/Co^{II}Co^{III}$ couple is the redox event responsible for catalytic turnover would be only 0.47 V, which is a value much lower than that typically associated with electrochemically observable ORR. Another factor which may reduce the cathodic ORR current observed in the CV is a slow electron transfer between the electrode and an O_2-**$Co_2L^{Me}OAc$** intermediate. Two generally used methods to increase electronic communication between the electrode and catalytic intermediates are to immobilise the catalyst onto the electrode, or to use an electron transfer mediator.

4.7.2 Attempted Immobilisation of $Co_2L^{Me}OAc$ onto Electrode Surfaces

Immobilisation of a catalyst onto an electrode surface can be achieved through several routes. Such methods include electropolymerisation of the catalyst directly onto the electrode surface, covalently linking the catalyst to an electrode which has been modified to accept covalent linkages, or adsorption of the catalyst onto a conductive solid such as graphite, graphene or carbon nanotubes.

These methods were examined for feasibility, however none of these methods were found to be effective for enhancing the current response of the ORR. Electropolymerisation tests were performed by sweeping the potential of the glassy carbon electrode far beyond that of the ligand oxidation wave. Upon repeat scans however, the current response from **$Co_2L^{Me}OAc$** was depleted, indicating deposition of a non-conducting substance onto the electrode, whereas if a conducting polymer is deposited onto the electrode, an increase in capacitive current upon subsequent scans is observed.

Adsorption of **$Co_2L^{Me}OAc$** onto a high surface area conductive carbon black was achieved by stirring carbon black with **$Co_2L^{Me}OAc$** in DCM overnight. The resulting material was filtered and washed with further DCM, before drying. The immobilised carbon black-**$Co_2L^{Me}OAc$** was then used as the basis for an ink containing EtOH and H_2O as the liquid phase, and Nafion^{TM} as a proton conducting binder. The ink was deposited onto a GC electrode surface, and while the CV showed redox events from the immobilised complex, no appreciable catalytic activity was observed under any of the conditions tested.

4.7.3 Use of Decamethylferrocene as an Electron Transfer Mediator

Electron transfer mediators (ETM) are used when an electrochemically active species has poor heterogeneous electron transfer kinetics with the electrode surface. An effective ETM must fulfil two main criteria: The ETM must be able to be either oxidised or reduced by the dissolved complex, and the ETM must have rapid electron transfer kinetics to the electrode surface. The use of ETMs has shown excellent effectiveness in protein electrochemistry, both in the ORR and other electrocatalytic reactions. In addition, ETMs have been used with the ORR with synthetic catalysts which show slow electron transfer rates.

We decided to use decamethylferrocene (Fc*) as the ETM for this work, since it has an $E_{1/2}$ more negative than the $Co^{II}Co^{II}/Co^{II}Co^{III}$ couple (i.e. it is more readily oxidised than **$Co_2L^{Me}OAc$**, and thus electron transfer from Fc* to O_2-**$Co_2L^{Me}OAc$** should be facile) and its electrochemical behaviour is resistant to changes in solution acidity, thus any changes in the CV of the solution containing the ETM are due to electrocatalytic events, rather than unexpected reactions between Fc* and protons.

A CV of a solution containing **$Co_2L^{Me}OAc$** (1 mM), Fc* (1 mM) and AcOH/TBAOAc (25 mM) at a scan rate of 100 mVs^{-1} was recorded, and very little change was observed upon addition of O_2 to the solution. The reversibility of the $Fc^{*0/+}$ couple largely remained intact, whereas if electron transfer from Fc* to an O_2-**$Co_2L^{Me}OAc$** intermediate took place rapidly, one would expect to see a reduction in the current attributed to the oxidation of Fc* to Fc^{*+}. In order to give Fc* time to undergo electron transfer to O_2-**$Co_2L^{Me}OAc$**, the scan rate was slowed to 10 mVs^{-1}. Under these conditions, the reduction wave associated with Fc^{*+} to Fc* was enhanced, and its reverse Fc* to Fc^{*+} wave had disappeared completely (**Figure 4.7.2**).

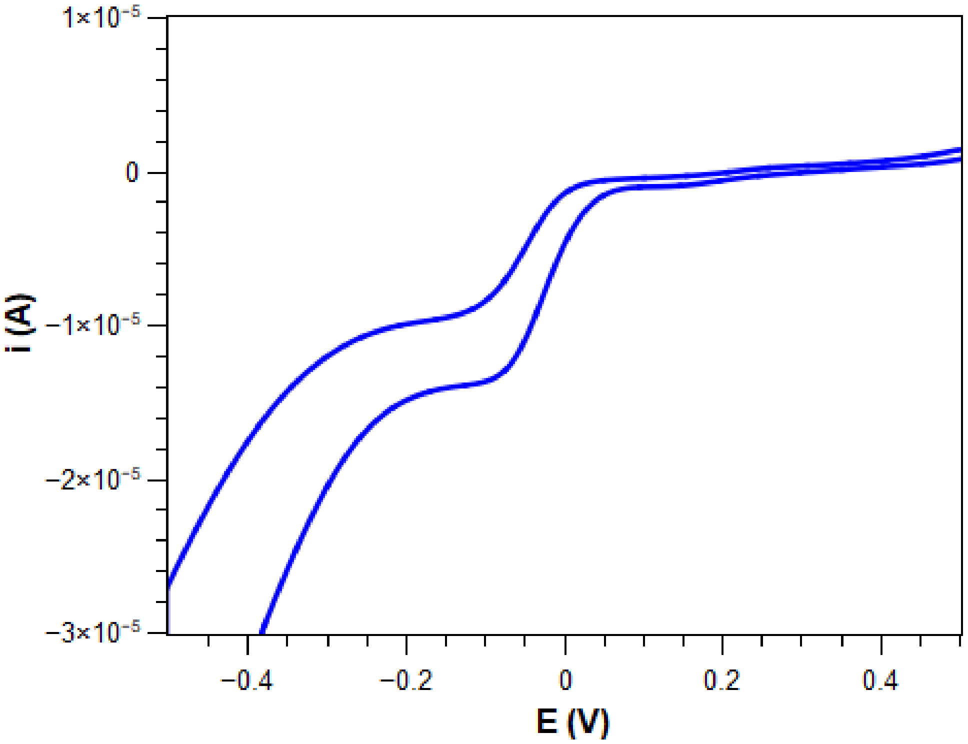

Figure 4.7.2 Cyclic voltammogram of an air saturated MeOH solution containing AcOH/TBAOAc (25 mM) Fc* (1 mM) and **$Co_2L^{Me}OAc$** (1 mM) with $TBAClO_4$ (0.1 M) as the supporting electrolyte at a scan rate of 10 mVs^{-1} demonstrating the ETM properties of Fc* for the electrocatalytic ORR.

Chapter 5
Homogeneous Catalytic Oxygen Reduction

5.1 Introduction

5.1.1 Ferrocene Derivatives as a Homogeneous Reducing Agent

Ferrocene (Fc) derivatives are well known for their highly reversible electron transfer kinetics with good electrochemical stability under acidic conditions, particularly in the case of decamethylferrocene (Fc*). We have shown in the previous chapter that Fc* can act as an electron transfer mediator between **$Co_2L^{Me}OAc$** and the glassy carbon electrode, allowing for electrochemical observation of the ORR under conditions where direct electron transfer from the electrode to the oxidised catalytic intermediates is too slow to give an appreciable current response. In acidic solutions, Fc* can reduce O_2 to H_2O_2 via an outer sphere mechanism slowly without the need for a catalyst (Scheme 5.1.1).[198] Conveniently, the ferricenium oxidation products, Fc^+, show weak *d-d* transitions in the electronic spectra. Normally absorbing light in a wavelength range between 600 and 800 nm, Fc^+ formation can be monitored by electronic spectroscopy with bands well out of the way of the strong ligand-to-metal charge transfer bands usually shown by the catalyst complex in solution. The low extinction coefficient of these *d-d* transitions allows for accurate observation of the formation of Fc^+ with the c.a. 1 mM concentrations required by the catalytic reaction.

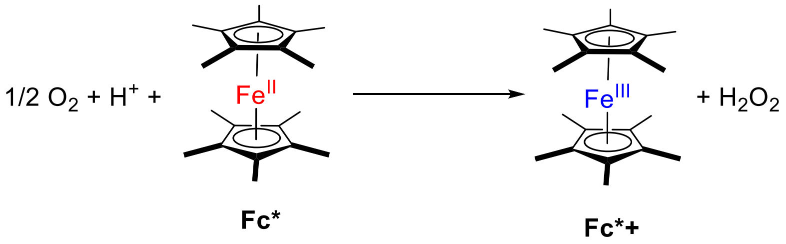

Scheme 5.1.1 Reduction of O_2 to H_2O_2 under acidic conditions by Fc*

Spectrophotometric quantification of the ORR was first studied by Fukuzumi and Guilard in 2004 where a series cobalt cofacial di-porphyrins (**Co_2DPX**) were used to catalyse the four-electron reduction of oxygen in benzonitrile (PhCN) containing $HClO_4$ as the proton source.[112] The ferrocene derivative used must be compatible with the redox potential of the catalyst where to facilitate spontaneous electron transfer from the ferrocene derivative to the oxidised catalyst, the peak oxidation potential of the ferrocene derivative must be more negative than the peak reduction potential of the catalyst. In the case of the cofacial dinuclear systems, the second cobalt redox couple i.e., $Co^{II}Co^{III}/Co^{III}Co^{III}$ was sufficiently high, that the first electron transfer to the doubly oxidised Co_2^{III}(DPX) from decamethylferrocene and dimethylferrocene was too fast to measure accurately where the electron transfer free energy (ΔG^o_{et}) was -0.61 and -0.27 eV, respectively. For unsubstituted ferrocene, ΔG^o_{et} was -0.16 eV for the first electron transfer process and -0.02 eV for the second, accompanied by a k_{et} for the second electron transfer that was an order of magnitude lower than the first electron transfer. Moreover, the rate of electron transfer from ferrocene derivatives to the cobalt catalysts scaled exponentially with - ΔG^o_{et}, producing a linear plot between - ΔG^o_{et} and log(k_{et}). For the less reducing pair of ferrocene derivatives $Fe(C_5H_5)_2$ and $Fe(C_5H_4Me)_2$, the rate of formation of their corresponding oxidised product scaled linearly with [$HClO_4$], [O_2] and [Co_2(DPX)] indicating that the rate limiting step was proton coupled electron transfer from the reduced catalyst to O_2. With the more strongly reducing $Fe(C_5Me_5)_2$ as the reducing agent, its rate of oxidation depended only on [Co_2(DPX)], suggesting that the rate limiting step was an intramolecular process, likely cleavage of the bound O-O bond.

In a similar study by Love and Devoille, a double pillared cobalt Pacman complex reduces oxygen in the presence of trifluoroacetic acid using Fc as the reducing agent.[199] The ORR occurs rapidly and nears completion within 300 s with [**Co_2L**] = 20 µM, [Fc] = 0.1 M and [CF_3CO_2H] = 20 mM with full selectivity to the four-electron pathway. Interestingly, $Fe(C_5H_5)_2$ can be used as the reducing agent even though the reduction potentials of the metal centres are >200 mV lower than that of the oxidation potential of ferrocene. This large disparity of potentials should result in a non-spontaneous electron transfer from ferrocene to cobalt with a positive ΔG^o_{et}. While this non-spontaneous electron transfer may influence the rate of ORR, it is important to consider other factors that may facilitate electron transfer despite the positive free energy. Firstly, [$Fe(C_5H_5)_2$] is in exceptionally large excess to [Co_2L] and thus electron transfer is possible when considering a Boltzmann type distribution of energy within the $Fe(C_5H_5)_2$ population. Secondly, the potential of the $Fe(C_5H_5)_2$/ $Fe(C_5H_5)_2^+$ couple by cyclic voltammetry is the equilibrium potential i.e., the potential when [$Fe(C_5H_5)_2$]/[$Fe(C_5H_5)_2^+$] = 1 and would shift in accordance with the Nernst equation when the concentrations of ferrocene and ferricenium are not equal, for example, if [$Fe(C_5H_5)_2$]/[$Fe(C_5H_5)_2^+$] = 100, then the ferrocene would theoretically be 118 mV more reducing. Of course, in a spectrophotometric reaction, the reducing agent is ideally almost all in its reduced form and is therefore much more reducing than its equilibrium potential.

5.2 Overpotential in the Homogeneous ORR

Determination of ORR overpotential in electrocatalysis is relatively simple and is defined as the difference between the equilibrium potential of the ORR under the non-standard experimental conditions (E_{ORR}) and the $E_{1/2}$ of the wave which becomes the catalytic wave upon addition of O_2. More specifically, the overpotential is the additional potential beyond the equilibrium potential to drive the reaction at a specific rate. Therefore, in an ideal electrocatalytic reaction, one simply selects a potential (normally the half wave potential of catalysis) and calculates the rate of reaction for that potential. Of course, some complication arises from the determination of $E_{O2/H2O}$ or $E_{O2/H2O2}$ under experimental conditions, however extensive study in this area where open circuit potentiometry is used to determine the E_{H_2/H^+} potential, from which the potentials of the two ORR pathways can be derived. In the spectrophotometric ORR however, the determination of overpotential is more complex. The applied potential is dictated by the reduction potential of the reducing agent and is often significantly different from the $E_{1/2}$ of the catalyst. It is equally dubious however, to simply calculate the difference between E_{ORR} and the $E_{1/2}$ of the reducing agent since, as discussed previously, the actual reducing potential of a chemical reductant can vary significantly from the equilibrium potential over the course of a reaction. As a result, it has become convention to simply define overpotential as the difference in catalyst $E_{1/2}$ and $E_{O2/H2O}$ or $E_{O2/H2O2}$. In many cases, this is a reasonable approximation, particularly if the rate of reaction is experimentally determined to be independent of the reducing agent reduction potential, or if the reducing agent and catalyst have close $E_{1/2}$ values.

The validity of this approximation is demonstrated the work by Stahl described in chapter 1 where a cobalt porphyrin catalyses either the four electron or two electron ORR depending on the overpotential of the system which is manipulated by changing the thermodynamic oxygen reduction potential rather than the catalyst $E_{1/2}$.[93] The work showed that when the $E_{O2/H2O2}$ was lower than the catalyst $E_{1/2}$, the ORR proceeded almost exclusively via the four-electron pathway, whereas if the $E_{O2/H2O2}$ was higher than the catalyst $E_{1/2}$, the ORR proceeds via only the two-electron pathway. In other words, the two-electron pathway under weakly acidic conditions is disfavoured because it would be operating at an underpotential, while the four-electron pathway is still thermodynamically available. This switch in selectivity occurs over a relatively minor change in overpotential, c.a. 160 mV, indicating that the overpotential determined by the conventional difference between $E_{O2/H2O}$ and catalyst $E_{1/2}$ is valid, even though the ‘applied’ potential by the reducing agent is 300 mV more negative than the $E_{1/2}$ of the catalyst. This shows than even though the ‘applied potential’ by the reducing agent is higher than the $E_{1/2}$ of the catalyst, the ORR is operating close to the redox event at the metal centre.

5.3 Effect of pK_a towards the ORR

5.3.1 Effect of pK_a on E_{ORR}

To find the ideal conditions for ORR catalysis, one must first understand the Nernstian effects of pKa on the E_{ORR}. Work by multiple groups has shown that the E_{ORR} can be estimated by finding the open circuit potential (OCP) for the non-standard hydrogen electrode under varying acid strengths.[52,97,115] The resulting value from OCP measurements is the E_{H_2/H^+} couple under specific conditions. This is found to scale linearly with pKa following equation 5.3.1

$$E_{H_2/H^+} = E^0{}_{H_2/H^+} - 0.059pKa \qquad \text{Eqn. 5.3.1}$$

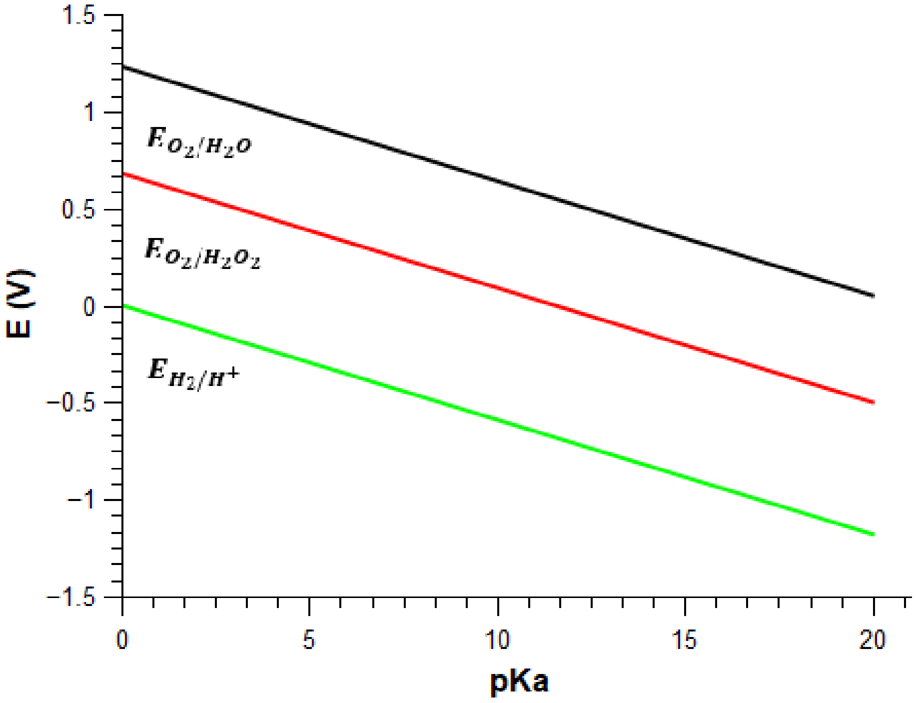

Figure 5.3.1 Plot demonstrating the linear dependence of pKa on the thermodynamic potential of H^+ reduction (green), two-electron O_2 reduction (red) and four-electron O_2 reduction (black) according to Eqn 5.3.1

This relationship between E_{H_2/H^+} and pKa appears to be purely thermodynamic and is independent of solvent aside from the initial variability of acid pKa in different solvents i.e., the gradient is the same, but the intercepts are different between solvent systems. E_{O_2/H_2O} or E_{O_2/H_2O_2} can be estimated from the E_{H_2/H^+} value by adding 1.23 or 0.68 V, respectively. If the E_{H_2/H^+} couple is referenced to Fc$^{*0/+}$ during OCP measurements, then the resulting E_{O_2/H_2O} or E_{O_2/H_2O_2} is also referenced vs Fc$^{*0/+}$. This referencing step is convenient since it allows simple comparison of E_{O_2/H_2O} or E_{O_2/H_2O_2} and $E_{1/2}$ of the catalyst. The concentration of the acid in solution also contributes to a Nernstian shift in E_{O_2/H_2O} or E_{O_2/H_2O_2} and while still significant, these effects are small in comparison to the effect of pKa.

Examining the acid pKa and how it affects the E_{O_2/H_2O} or E_{O_2/H_2O_2} is a valuable tool in determining optimal conditions for the ORR. For example, in MeCN, the pKa of AcOH is quite high (23.5)[200] and often results in exceptionally low values for E_{O_2/H_2O}. If the $E_{1/2}$ of the catalyst is higher than this value under the same conditions, one can expect the ORR to be thermodynamically unfavourable. On the other hand, the pKa of AcOH in MeOH is substantially lower (9.6),[201] and as a result only moves the E_{O_2/H_2O} moderately from its standard potential, and therefore often remains higher than the $E_{1/2}$ of the catalyst, resulting in a thermodynamically favourable ORR.

The E_{H_2/H^+} in MeOH in the presence of 25 mM AcOH/TBAOAc was determined by Stahl and co-workers using the OCP method and was found to be -0.31 V vs Fc*$^{0/+}$. From this value the E_{O_2/H_2O_2} and E_{O_2/H_2O} can be estimated under the same conditions by adding 0.68 or 1.23 V to this value respectively, giving E_{O_2/H_2O_2} as 0.37 V and E_{O_2/H_2O} as 0.92 V. The catalysis in this chapter takes place partly under conditions very close to those studied by Stahl, and therefore these values for E_{O_2/H_2O} and E_{O_2/H_2O_2} will be used to estimate overpotentials where appropriate.

5.3.2 Homoconjugation Effects and Buffering the ORR

For a weak acid, HA, there exists its classical disassociation equilibrium (equation 5.3.2).

$$\mathrm{HA} \overset{K_a}{\rightleftharpoons} \mathrm{H^+} + \mathrm{A^-} \qquad \text{Eqn 5.3.2}$$

However, in many solvent systems this disassociation equilibrium can be perturbed by a secondary equilibrium in which hydrogen bonding between a second HA molecule stabilises the deprotonated product A$^-$, shifting the initial disassociation equilibrium to the right and effectively decreasing the pKa of HA (Scheme 5.3.1).

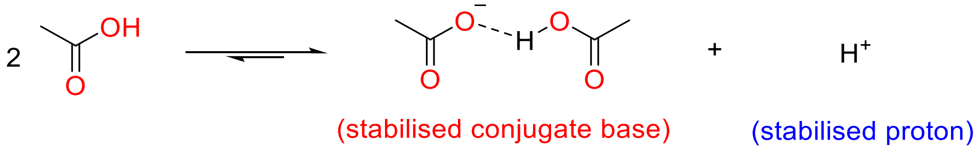

Scheme 5.3.2 Mechanism of increased pKa of acetic acid by stabilisation of the conjugate base through hydrogen bonding to a second acetic acid equivalent

This process is called homoconjugation and is an important consideration when evaluating the thermodynamics of a catalytic system which relies on the pKa of the proton source. These homoconjugation effects can vary in different solvent systems and are particularly potent in acetonitrile solutions. To avoid complications arising from homoconjugation, the solution can be buffered by the addition of a salt containing the conjugate base. This addition effectively saturates the system with A$^-$, and therefore hydrogen bonding interactions between the additional conjugate base and HA dominate over A$^-$ which is generated by deprotonation of HA, thus shifting the original disassociation equilibrium back to its value without homoconjugation (Scheme 5.3.2).

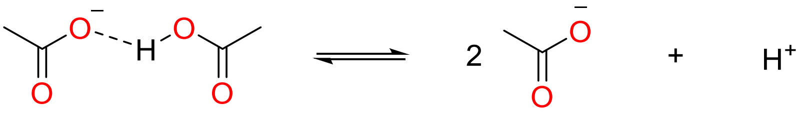

Scheme 5.3.3 Elimination of homoconjugation effects by saturation of the hydrogen bonding to A$^-$ by additional conjugate base

Another vital reason to buffer the acid during catalysis is to establish a known concentration of A$^-$ at the initiation of the ORR, doing so allows for the reaction quotient of the Nernst equation to be determined more accurately than if the concentration of A$^-$ at the start of the reaction is close to zero, thus allowing for a higher level of confidence in the E_{O_2/H_2O} and the resulting overpotential values.

5.4 Reactivity of Catalysts Towards O_2

5.4.1 O_2 Reactivity by Electronic Spectroscopy

The binding of O_2 to cobalt complexes is often observed through changes in their electronic spectra in the presence and absence of O_2. Love and Devoille were able to observe binding of O_2 to the double pillared cofacial dicobalt complex by the growth of a sharp Soret band at 358 nm and a broad feature at 430 nm; whereas under nitrogen the absorbance of both of these features was reduced and the band at 358 nm became broad.[199] Similarly, Pui was able to observe O_2 binding to Co(salen) and similar complexes with the growth of a band at c.a. 380 nm.[202] The electronic spectrum of **$Co_2L^{Me}OAc$** (10 µM) in O_2 saturated MeOH shows a sharp band at 310 nm, and a broader less intense band at 405 nm. Minimal changes are seen upon vigorously sparging the solution with argon for 30 minutes (figure 5.4.1)

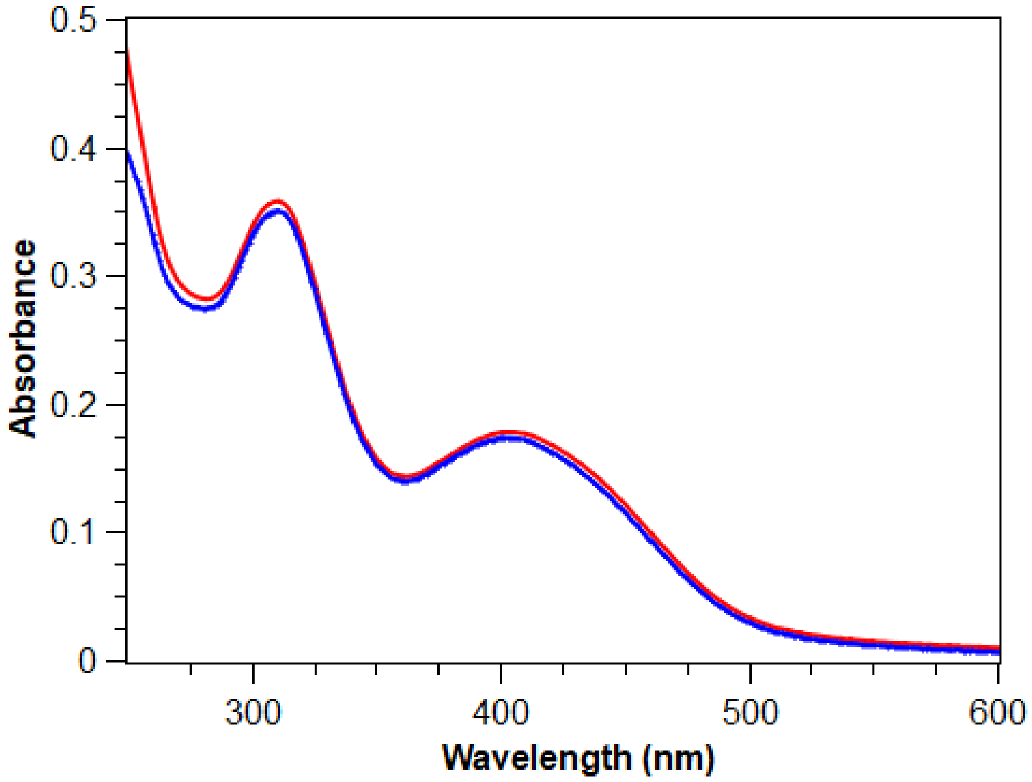

Figure 5.4.1 Electronic spectra of a MeOH solution containing **$Co_2L^{Me}OAc$** (10 µM) under air saturated (blue trace) and argon saturated (red trace) conditions.

Even when the solution was cooled to -78 °C during O_2 saturation, minimal changes in the spectra were observed, suggesting weak and slow O_2 binding in MeOH solution. In an attempt to facilitate O_2 binding further, DMF was used as the solvent. Since

DMF has a greater Lewis basicity than MeOH, coordination of the solvent increases electron density about the cobalt centres, and may facilitate the oxidative binding of O_2. The electronic spectrum of an O_2 saturated 100 μM DMF solution of **$Co_2L^{Me}OAc$** shows a similar broad band to that in MeOH at 430 nm. When the solution is vigorously degassed with argon for 30 minutes, this band is blue shifted to 420 nm, and becomes slightly more intense indicating the removal of bound O_2 in DMF solution. When air was reintroduced to the solution, the band at 420 nm slowly red shifted closer to its original value.

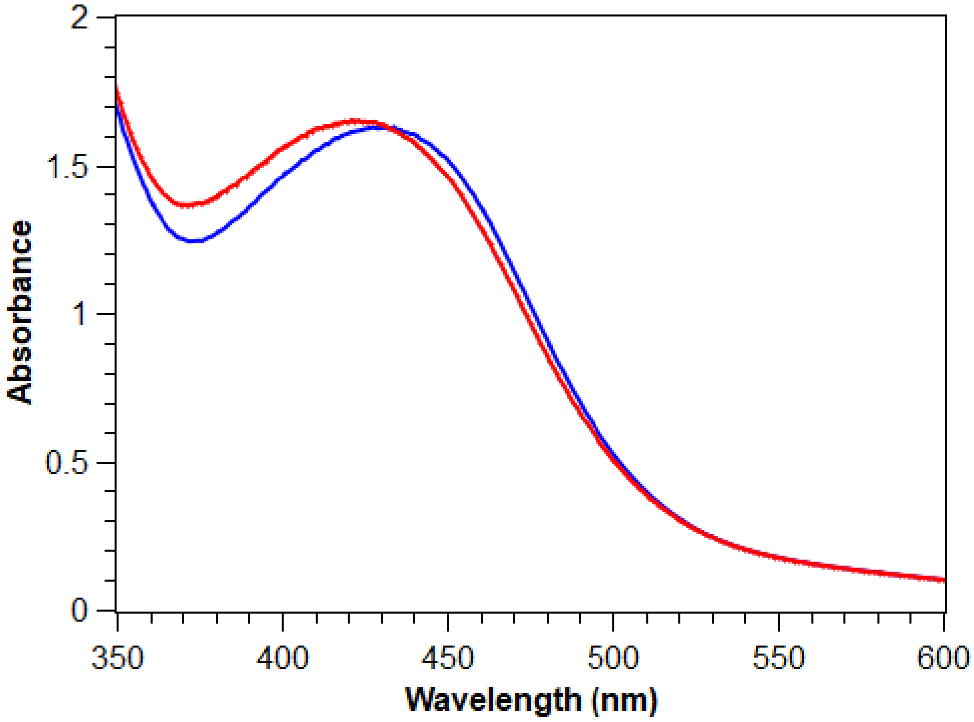

Figure 5.4.2 Electronic spectra of a DMF solution of **$Co_2L^{Me}OAc$** (100μM) under air saturated (blue trace) and argon saturated (red trace) conditions.

While O_2 binding can be tentatively observed in the electronic spectra of **$Co_2L^{Me}OAc$**, the extent of the binding is low compared to other cobalt complexes. This weak O_2 binding is not unexpected however, since the L^{Me} ligand is relatively electron poor with only one N donor per cobalt atom. Complexes which bind O_2 quantitatively normally contain at least two N donors per cobalt centre and as many as 5 N donors per cobalt centre in systems where the bound O_2 can even be observed in the X-ray crystal structure.

5.4.2 O_2 Reactivity by NMR Spectroscopy

The NMR spectrum of **$Co_2L^{Me}OAc$** in D_3COD as seen in Figure 5.4.3 shows significant paramagnetic broadening attributed to the presence of the high spin d^7 cobalt centres present within the complex. This paramagnetism is observed whether the sample is air saturated, or saturated with an inert gas. This indicates that the binding of O_2 to **$Co_2L^{Me}OAc$** is weak, where there is minimal oxidation of the Co^{II} metal ions to Co^{III} under the conditions of the experiment. If an excess of acetic acid is added to the sample however, the paramagnetic features of the spectrum (Figure 5.4.4) are rapidly lost (within the time taken to run the NMR experiment). The loss of paramagnetic broadening suggests that all Co^{II} is converted entirely to Co^{III}. It is possible that protonation of the weakly bound oxygen provides a sufficient kinetic or thermodynamic driving force, shifting the equilibrium far to the oxidised species. It is also notable that upon degassing of the acidic solution of **$Co_2L^{Me}OAc$**, the NMR spectrum remains diamagnetic. This suggests that the reaction with oxygen upon protonation is irreversible. In addition, the typical imine resonance at 10.4 ppm is retained throughout the experiment; this shows that any hydrolysis induced oxidative decomposition of the complex is unlikely.

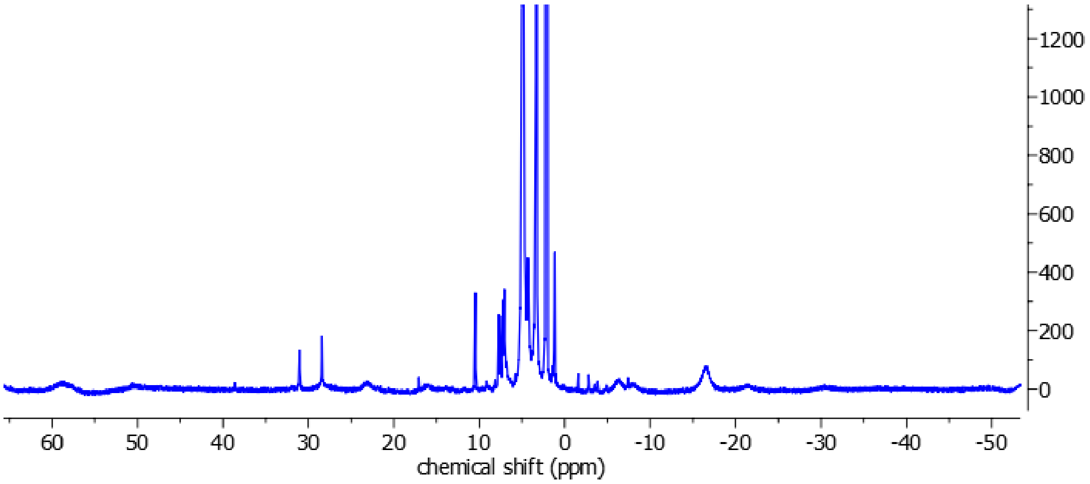

Figure 5.4.3 Paramagnetic ^1H NMR spectrum of an aerated D_3COD solution of **$Co_2L^{Me}OAc$** at 500 MHz

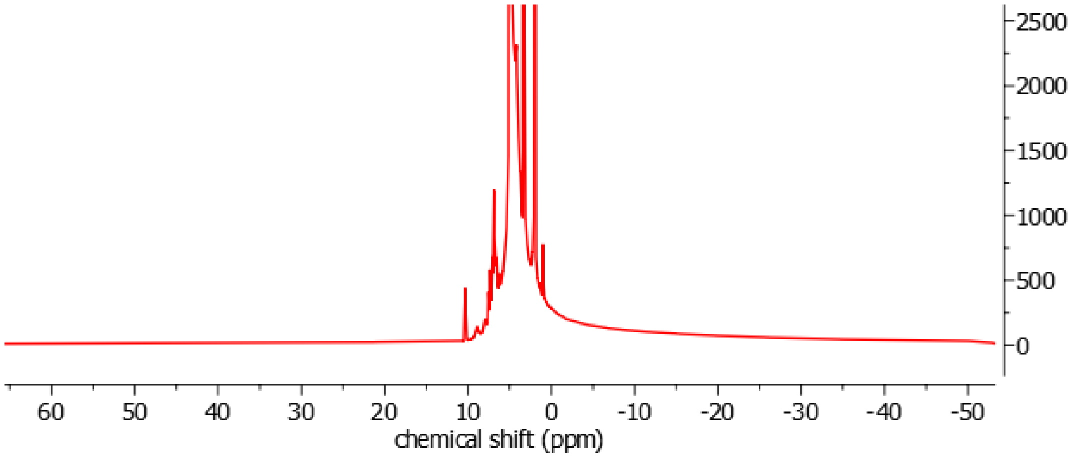

Figure 5.4.4 Diamagnetic ^1H NMR spectrum of an aerated D_3COD solution of **$Co_2L^{Me}OAc$** containing 10 mM AcOH at 500 MHz.

5.4.3 O_2 Reactivity by Electron Paramagnetic Resonance Spectroscopy

The electron paramagnetic resonance (EPR) spectrum of **$Co_2L^{Me}OAc$** (1 mM) in frozen MeOH at 10 K shows a broad feature centred at approximately 2000 G with a g-factor of 3.37. Weak hyperfine coupling interactions arising from coupling of the Co^{II} electronic spin to the ^{59}Co nuclear spin can be determined, however, due to the complexity and low intensity of these interactions, further analysis of the hyperfine coupling was not possible.

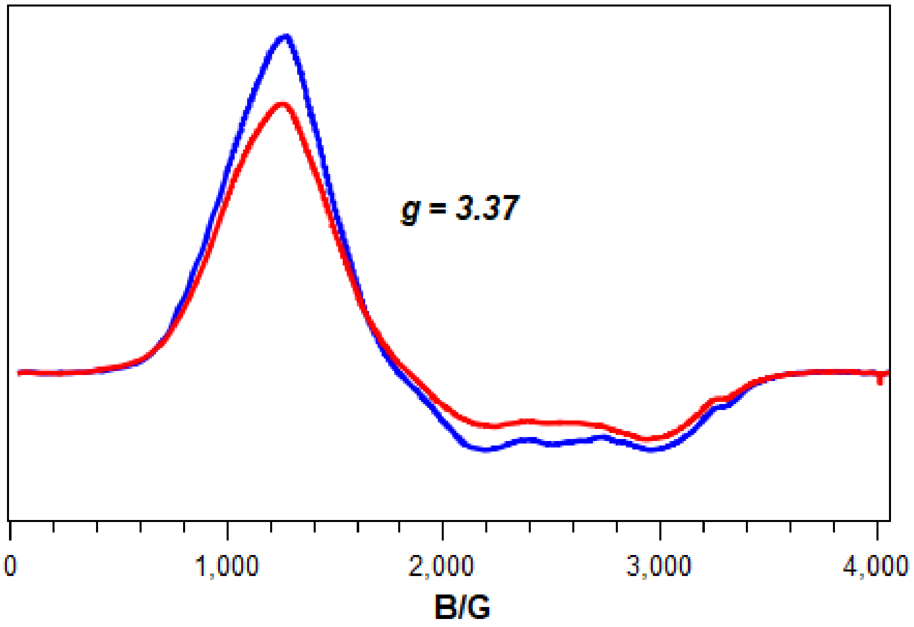

Figure 5.4.5 EPR spectra of **$Co_2L^{Me}OAc$** (1 mM) in frozen argon saturated (blue trace) and air saturated (red trace) methanol.

The sample of **$Co_2L^{Me}OAc$** was thawed and saturated with air before recording a second EPR spectrum. The spectrum under aerobic conditions showed the same feature attributed to the Co^{II}, however, this new signal was approximately 20% less intense. This loss of spin between the two spectra suggests the loss of some of the EPR active cobalt ions, where reaction of O_2 with the complex produces EPR silent Co^{III}. In addition, it is notable no additional signals are observed for the generation of EPR active superoxide radicals, suggesting that the complex either binds O_2 via a two-electron mechanism, generating peroxide, or that the reactive superoxide species is rapidly quenched by the environment.

5.4.4 Clark Electrode O_2 binding studies

For strongly oxygen binding complexes, electrochemical quantification of oxygen binding can be achieved by the use of a Clark electrode in which a platinum electrode is used to produce a cathodic current in the presence of O_2, and binding of oxygen to a metal complex prevents the detection of O_2.[115,203] In aerated MeOH or DMF solutions, the Clark electrode measurements showed no change in current after the addition of 1 mM **$Co_2L^{Me}OAc$**, suggesting that binding of O_2 to the complex is too weak to prevent detection of O_2 at the platinum electrode.

5.5 Initial ORR Investigations and Selectivity Determination

5.5.1 Spectrophotometric Determination of ORR by $Co_2L^{Me}OAc$

Catalytic ORR experiments were performed by rapidly mixing aerated MeOH solutions containing **$Co_2L^{Me}OAc$**, Fc* and AcOH/TBAOAc buffer in a quartz cuvette such that the final concentrations of reactants and catalyst took the form [**$Co_2L^{Me}OAc$**] << **[**Fc*] < [O_2] < [AcOH/TBAOAc] where the reductant Fc* is the limiting reagent. The concentration of O_2 in the MeOH solution was estimated by multiplying the solubility of pure O_2 in MeOH (10 mM) by the partial pressure of O_2 in air (0.2), obtaining a standard oxygen concentration of 2 mM in all ORR experiments unless stated otherwise. The ORR was monitored by the increase in absorbance due to the formation of Fc^{*+} (λ_{max} = 780 nm, ε = 440 $M^{-1}cm^{-1}$) over the course of the reaction. The ORR was complete once the absorbance due to Fc^{*+} had increased until it became close to the theoretical limit for the specific concentration, following which the selectivity could be determined by titration with NaI.

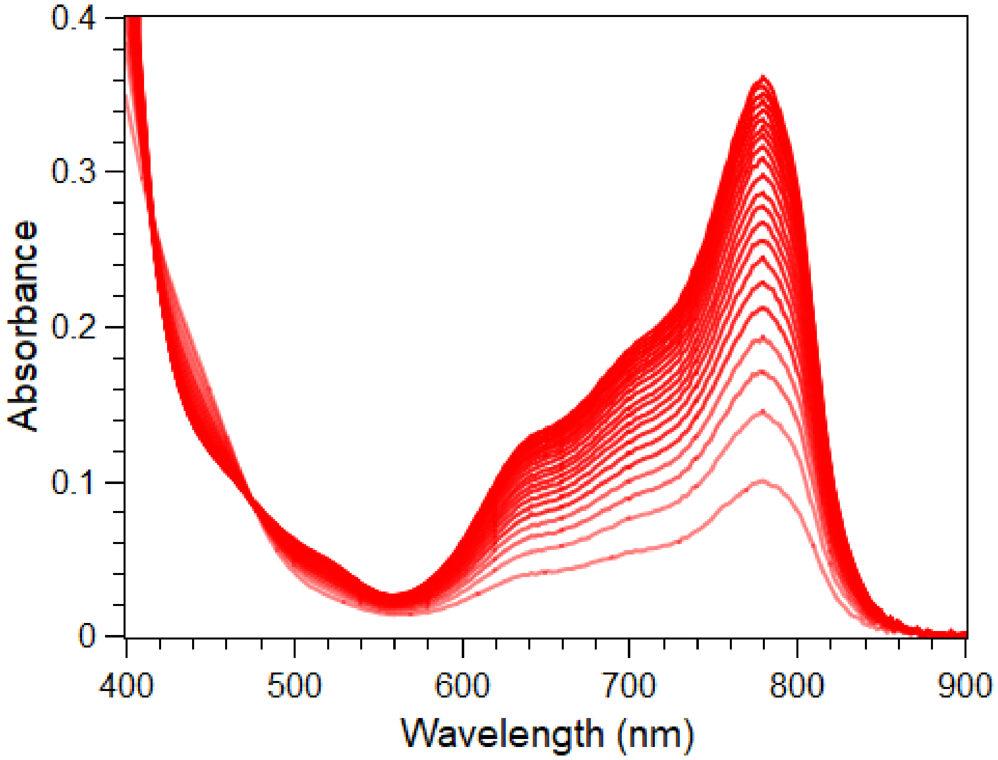

Figure 5.5.1 Temporal changes in the electronic spectra of an aerated MeOH solution containing **$Co_2L^{Me}OAc$** (20µM), AcOH/TBAOAc (16 mM) and Fc* (1 mM) over the course of 435 s with regular intervals of 15 s between scans

When aerated solutions of **$Co_2L^{Me}OAc$**, AcOH/TBAOAc, and Fc* were mixed to give final concentrations of 20 µM, 16 mM, and 1 mM respectively, the generation of Fc^{*+} was monitored by recording an electronic spectrum every 15 seconds until the reaction was complete (Figure 5.5.1). The increase in absorbance over time gives the rate of reaction. The initial rate of reaction was taken as the slope of the absorbance vs time plot (Figure 5.5.2) during the first 100 s of reaction time. This absorbance vs time rate with s^{-1} units could then be converted to a molar rate through the use of the Beer-Lambert law (Eqn. 5.5.1) by dividing the initial change in absorbance over time by the molar extinction coefficient of the Fc^{*+} product (440 $M^{-1}cm^{-1}$) (Eqn 5.5.2)

$$A = \varepsilon c l \qquad \text{(Eqn. 5.5.1)}$$

$$\frac{d[Fc^*]}{dt} = \frac{dA_{780}}{dt}\frac{1}{\varepsilon_{780}} \qquad \text{(Eqn. 5.5.2)}$$

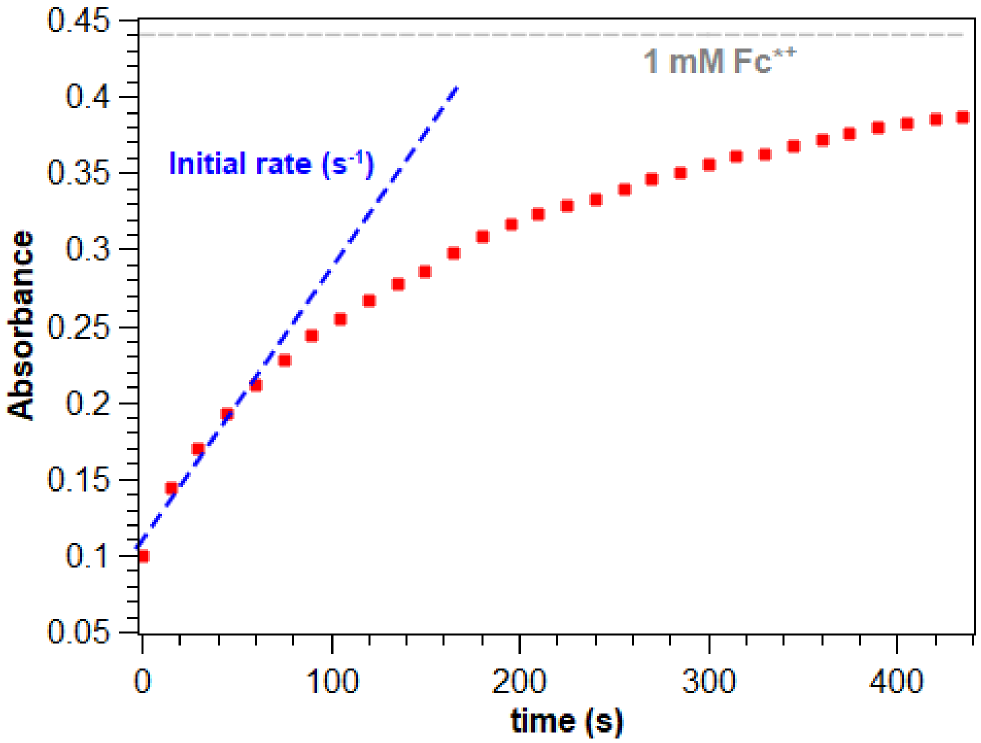

Figure 5.5.2 Absorbance vs time profile of an aerated MeOH solution containing **$Co_2L^{Me}OAc$** (20µM), AcOH/TBAOAc (16 mM) and Fc* (1 mM). The grey dashed line represents the theoretical absorbance of a solution containing 1 mM Fc^{*+}, the blue dashed line represents the initial absorbance rate used to calculate molar reaction rates.

The rate of formation of Fc*$^+$ relates to the overall rate of ORR, however, it is important to understand the relationship between the rate of O_2 consumption and Fc*$^+$ generation. Since the ORR can proceed by either the two-electron or four-electron pathway, the number of Fc* equivalents consumed per O_2 equivalent varies between two and four and depends on the selectivity of the reaction.

To test the selectivity of the ORR under these conditions, iodometric titration using NaI was performed on a reaction mixture after 1 h of reaction time to ensure all Fc* had converted to Fc*$^+$. An aliquot of the reaction solution was then diluted in MeCN, and an electronic spectrum was recorded before and 1 h after the addition of an excess of NaI. The I^- is oxidised by any H_2O_2 present in solution to form I_2 in a 1:1 molar ratio. Generated I_2 then combines with excess I^- to form I_3^- which can be detected in the electronic spectra (λ_{max} = 361 nm, $\varepsilon = 2.8 \times 10^4$ $M^{-1}cm^{-1}$) (figure 5.5.3).

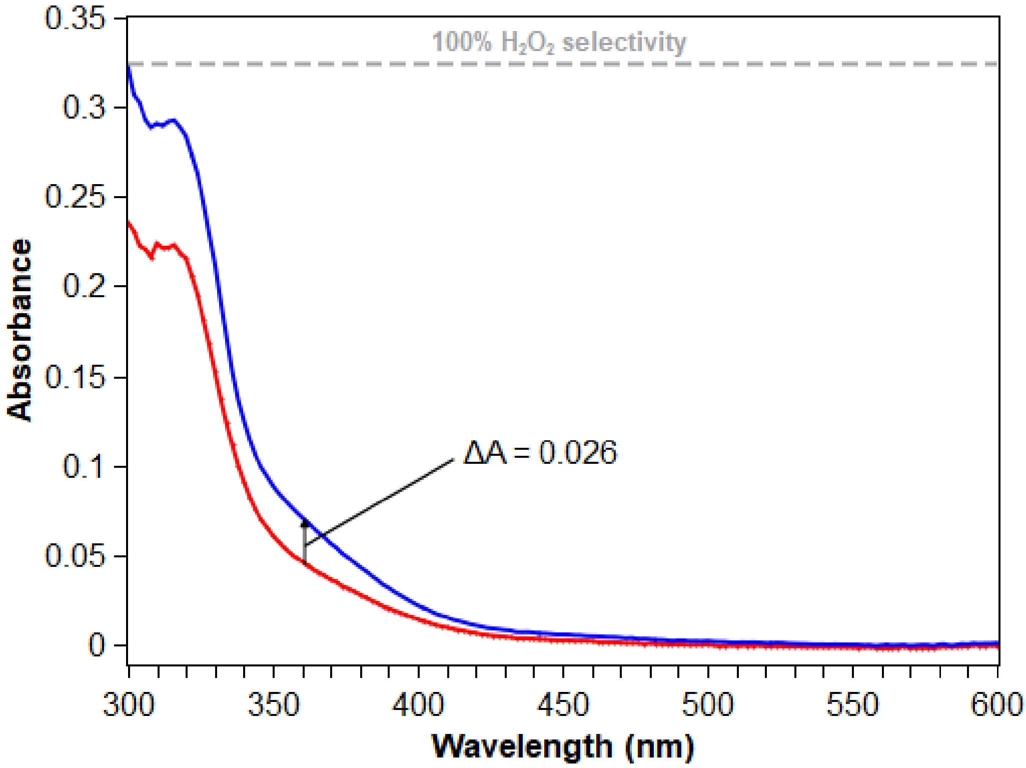

Figure 5.5.3 Electronic spectrum of a 60 μL aliquot of the complete reaction in fig. 1.5.2 diluted in MeCN (2.94 mL) before (red trace) and 1h after (blue trace) addition of excess NaI (ca. 100 mg). The grey dashed line represents the theoretical absorbance value for a catalytic reaction with 100% selectivity for H_2O_2

The iodometric titration shows a 0.026 increase in absorbance at 361 nm upon addition of NaI. The theoretical maximum amount of H_2O_2 produced in the reaction is 0.5 mM (i.e., if all Fc* was used to generate H_2O_2, two equivalents of Fc* would be needed to form one equivalent of H_2O_2). Upon the 50-fold dilution in MeCN, the theoretical maximum of $[H_2O_2]$ is 0.01 mM, and hence the same $[I_3^-]$ value following titration. Converting this $[I_3^-]$ to absorbance gives a theoretical maximum absorbance increase of 0.28 for the two-electron pathway. The actual change in absorbance following titration was only 0.026, only 9.3% of the theoretical value. If it assumed that the only other product available from the oxidation of Fc* is H_2O, this gives a 90.7% selectivity towards the four-electron pathway.

In acidic MeOH in the absence of a catalyst, very slow oxidation of Fc* to Fc^{*+} is still observed, and in order to calculate a true rate of catalysis, this slow background reaction should be subtracted from the total ORR rate to obtain the catalysed rate (Eqn. 5.5.3). This value for the background rate is normally on the order of 10^{-7} Ms^{-1} and has been performed on all rate determinations.

$$\frac{d[Fc^{*+}]}{dt}_{catalysed} = \frac{d[Fc^{*+}]}{dt}_{total} - \frac{d[Fc^{*+}]}{dt}_{background} \qquad \text{(Eqn. 5.5.3)}$$

The turnover frequency (TOF) of the system is determined from the initial catalysed rate of Fc^{*+} generation per unit catalyst, divided by the number of electrons (*n*) transferred per O_2 (Eqn. 5.5.4). Since we have determined >90% selectivity of the system towards the four-electron pathway, we have used four-electrons in this TOF determination.

$$TOF = \frac{\frac{d[Fc^{*+}]}{dt}_{catalysed}}{n * [\boldsymbol{Co_2L^{Me}OAc}]} \qquad \text{(Eqn. 5.5.4)}$$

Using Eqn 5.5.4 with slope of tangent to the curve shown in figure 5.5.2 as the numerator and $4 \times 20 \times 10^{-6}$ as the denominator, a TOF of 0.034 s^{-1} in the presence of 16 mM AcOH/TBAOAc, 1 mM Fc* and 2 mM O_2 is obtained. It is important to note that the TOF only describes the activity of a catalyst under a specific set of conditions, for example, if [AcOH/TBAOAc], [Fc*], or $[O_2]$ were increased from the outset, a higher TOF value may be obtained. This is an important consideration when comparing catalyst systems.

The TOF value of 0.034 s^{-1} is comparable to low overpotential mononuclear Co(salen) catalysts studied by Stahl and co-workers which are completely selective to the two-electron pathway under similar conditions in MeOH with AcOH/TBAOAc. When compared to other ORR catalysts which are selective towards the four-electron pathway, **$Co_2L^{Me}OAc$** shows excellent activity for its high selectivity and low overpotential (480 mV).[94,117]

$Co_2L^{CF3}OAc$ was examined for ORR activity with the same method. The TOF of the ORR in the presence of 20 μM **$Co_2L^{CF3}OAc$** in air saturated MeOH solution containing 20 mM AcOH/TBAOAc and 1 mM Fc* was found to be 5.67×10^{-3} s^{-1} almost an order of magnitude lower than that of **$Co_2L^{Me}OAc$**. The overpotential of the reaction catalysed by **$Co_2L^{CF3}OAc$** was 390 mV, 80 mV lower than the overpotential of **$Co_2L^{Me}OAc$** (470 mV) and demonstrates that the substituent at the 4-position of the phenolate group has a large impact on the TOF of catalysis. In addition, $Co_2L^{CF3}OAc$ showed 93% selectivity towards the four-electron pathway, slightly higher than the value for **$Co_2L^{Me}OAc$**, showing that the substituent of the ligand also may have some influence over the selectivity of the reaction.

The **$Co_2L^{R}OAc$** complexes which were deemed insufficiently pure for quantitative catalytic analysis were also briefly screened for catalytic activity towards the ORR by the same method. It was found that all of these complexes were catalytically active and showed rates of catalysis similar to **$Co_2L^{Me}OAc$** and **$Co_2L^{CF3}OAc$**.

The trinuclear and tetranuclear complexes **$Co_3L^{Me}(OAc)_3$** and **$Co_4L^{Me}{}_2(BF_4)_2$** were also screened for catalytic activity by the same method. No catalytic activity was observed for **$Co_4L^{Me}{}_2(BF_4)_2$**, which may be explained by the poor redox behaviour as seen in the CV, where oxidation of the Co_4 cluster is too slow to bind O_2. In the case of **$Co_3L^{Me}(OAc)_3$**, there was initially no catalytic activity, however after the first 30 seconds of reaction, catalytic activity began to increase. This increase in catalytic activity over time may suggest a pre-activation step to produce a catalytically active species. Since **$Co_3L^{Me}(OAc)_3$** is essentially an adduct of **$Co_2L^{Me}OAc$** and $Co(OAc)_2$, it is possible that under the acidic conditions of catalysis, the third cobalt atom is released into solution, leaving the known catalytically active **$Co_2L^{Me}OAc$** species to facilitate the reaction.

5.6 Spectrophotometric Kinetic Studies

5.6.1 Kinetic Studies with Acetic Acid as a Proton Source

Independently varying the concentrations of reactants of the homogeneous ORR allows for examination of the rate determining step through formation of concentration vs. rate profiles. To achieve this, stock solutions of **$Co_2L^{Me}OAc$**, Fc* and AcOH/TBAOAc were diluted systematically with additional MeOH in the quartz cuvette to the desired final concentrations. Typically, **$Co_2L^{Me}OAc$** and Fc* solutions could be mixed with minimal formation of Fc^{*+}, and the reaction was initiated by quick injection of the buffer solution. The initial rate of formation of Fc^{*+} was determined by recording a spectrum in the range of 900-300 nm immediately upon addition of buffer and then every 15 seconds thereafter. When [**$Co_2L^{Me}OAc$**] was varied between 5 and 40 µM, while [Fc*], [AcOH/TBAOAc] and [O_2] were kept constant, the resulting initial rate vs. concentration profile was linear and showed pseudo-first order kinetics. This indicates that the rate determining step of the ORR catalysed by **$Co_2L^{Me}OAc$** involves one molecule of the catalyst.

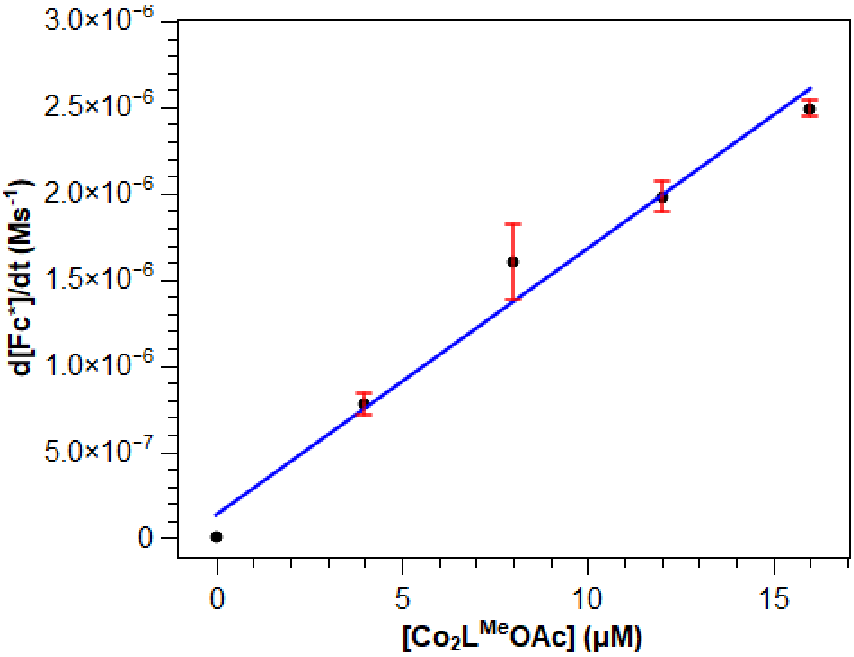

Figure 5.6.1 ORR rate vs [**$Co_2L^{Me}OAc$**] plot in the presence of AcOH/TBAOAc (20 mM), mM Fc* (1 mM) and O_2 (2 mM)

When [O_2] is varied between 2 and 10 mM, no change in ORR rate is observed, this indicates that the O_2 binding step of catalysis is fast in comparison to other events in the catalytic cycle.

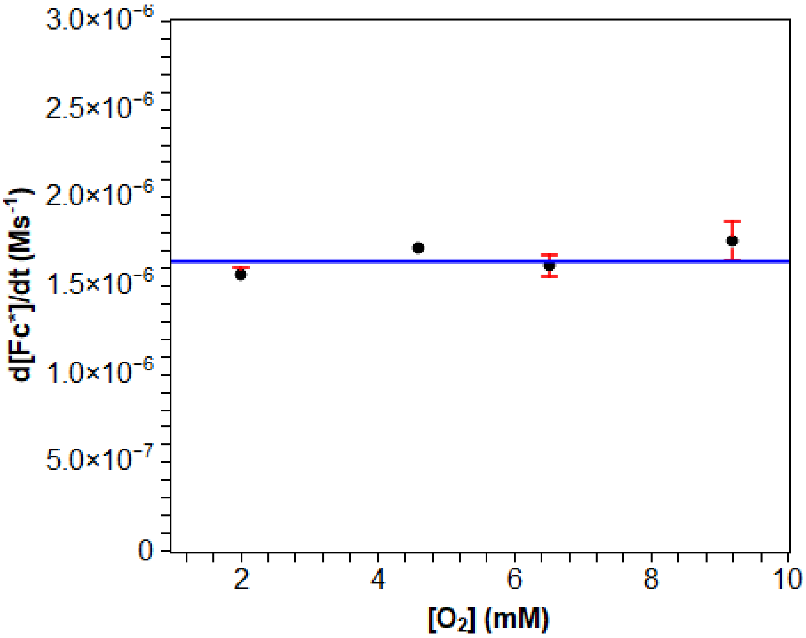

Figure 5.6.2 ORR rate vs [O_2] plot in the presence of **$Co_2L^{Me}OAc$** (20 μM), Fc* (1 mM), and AcOH/TBAOAc (20 mM) and O_2 (2 mM)

When [Fc*] was varied between 0 and 0.8 mM, the rate of formation of Fc^{*+} increased linearly, passing through the origin and reaching a rate of 2.5 μMs^{-1}. The pseudo-first order relationship of this plot indicates the involvement of Fc* in the rate determining step of catalysis. Such a dependence on Fc* can give good insights into the mechanism of the ORR and generally catalyst systems that are selective to the four-electron pathway show a first-order dependence on the reducing agent used, while two-electron selective systems tend to show a zero-order dependence on reducing agent.

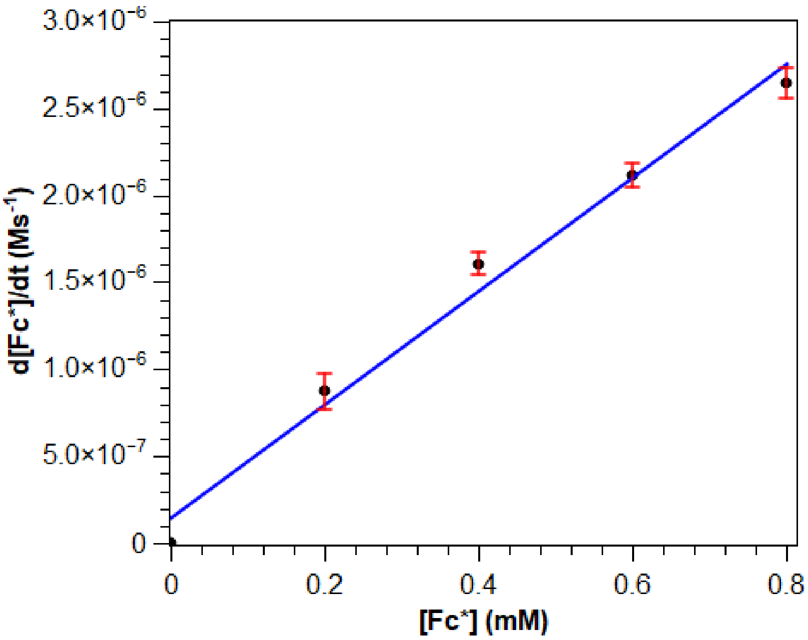

Figure 5.6.3 ORR rate vs [Fc*] plot in the presence of **$Co_2L^{Me}OAc$** (20 μM), AcOH/TBAOAc (20 mM) and O_2 (2 mM)

When [AcOH/TBAOAc] is varied between 0 and 16 mM, a weak, pseudo-first order rate dependence is observed with slight attenuation from linearity as [AcOH/TBAOAc] is increased. This slight attenuation arises from saturation kinetics which are common in enzymatic catalysis

Interestingly, there is a significantly non-zero intercept to this rate vs [AcOH/TBAOAc] profile, meaning that if no external proton source is present, the oxidation of Fc* still proceeds at a rate of almost 1.5 μMs^{-1}. This rate is much faster than the oxidation of Fc* in the presence of AcOH in MeOH without **$Co_2L^{Me}OAc$**, indicating that even only the weakly acidic MeOH can facilitate catalytic turnover.

If the rate of background Fc* oxidation by MeOH is subtracted from the overall rate vs [AcOH/TBAOAc] profile, a much clearer pseudo-first order relationship can be seen .

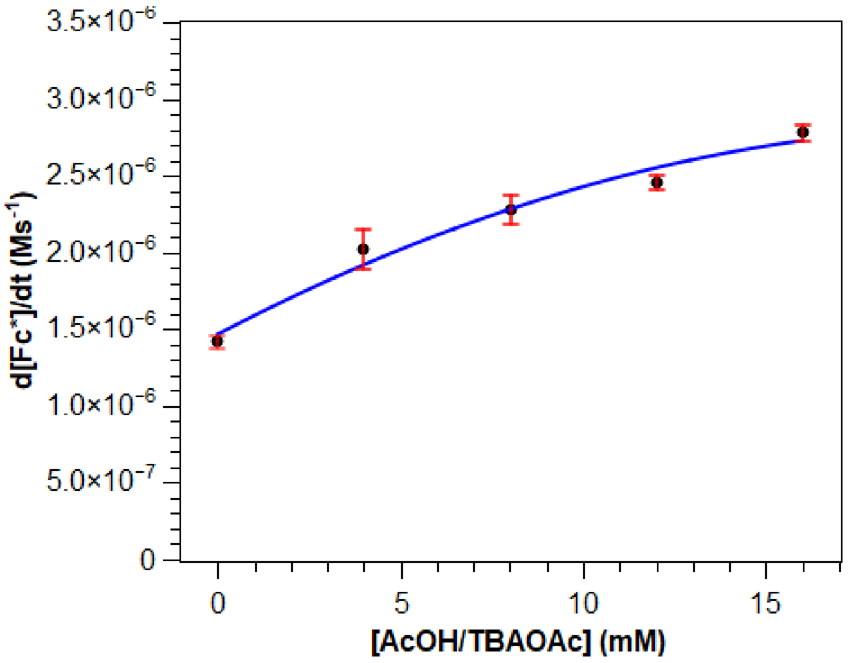

Figure 5.6.4 ORR rate vs [AcOH/TBAOAc] plot in the presence of **$Co_2L^{Me}OAc$** (20 μM), Fc* (1 mM) and O_2 (2 mM)

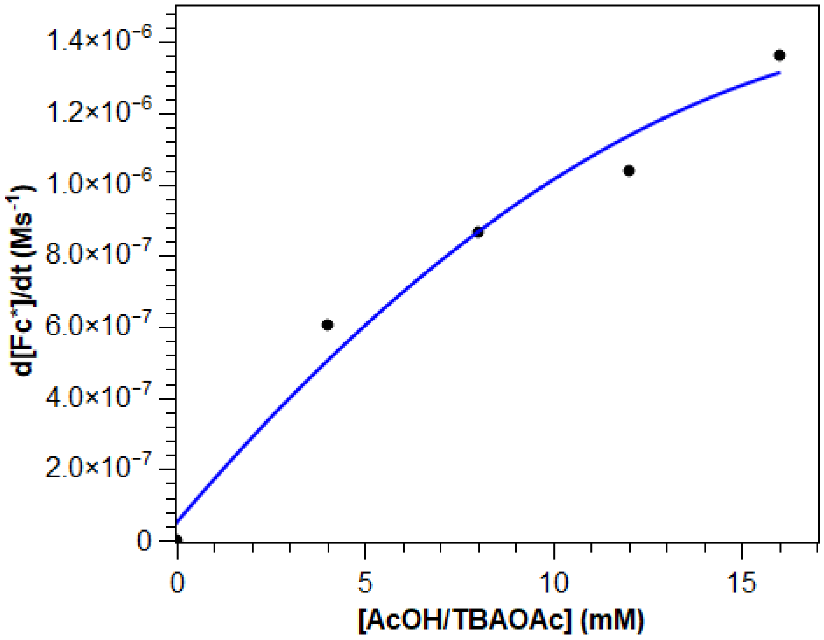

Figure 5.6.5 ORR rate vs [AcOH/TBAOAc] plot with the rate of background ORR where MeOH is the proton source subtracted to give the true effect of AcOH/TBAOAc on rate

If AcOH is used as the proton source in the absence of TBAOAc, a negative linear dependence on [AcOH] is observed, with highest reaction rates being achieved at the lowest [AcOH] tested. In addition, the rate between reactions where the only difference is the presence or absence of TBAOAc differed by up to 10^{-6} Ms^{-1} where the ORR was slower in the presence of TBAOAc. There are a few possible explanations for this phenomenon: Firstly, binding of AcO^- to the active site of the catalyst competes with the binding of O_2 resulting in partial deactivation of the catalyst, effectively lowering [$Co_2L^{Me}OAc$] at higher [AcOH] values. When TBAOAc is added, the pacification of the catalyst reaches a saturation limit, i.e., the occupation of active sites by OAc^- is maximised and therefore the rate of ORR is reduced. The positive dependence on [AcOH/TBAOAc] would then be attributed to only increasing [H^+] since the effects of increasing [OAc^-] are already at their maximum.

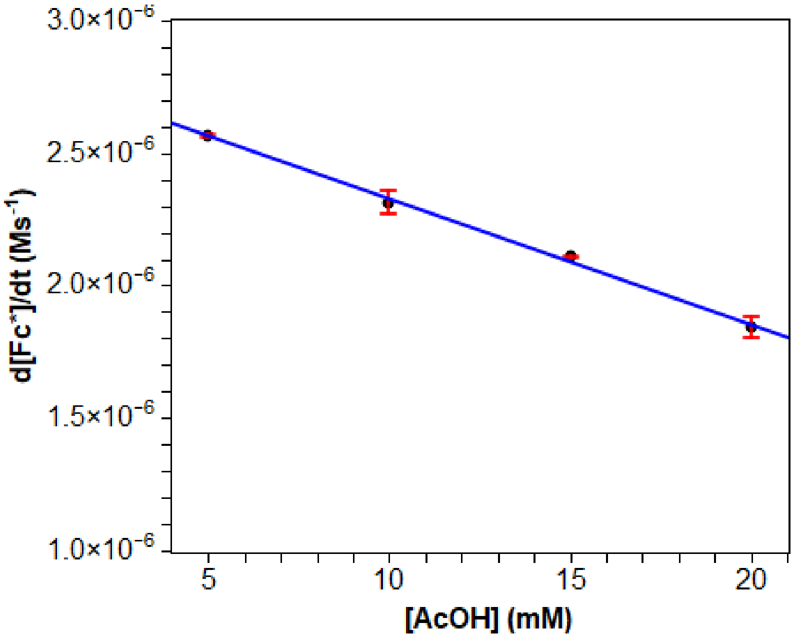

Figure 5.6.6 Unbuffered ORR rate vs [AcOH] plot in the presence of **$Co_2L^{Me}OAc$** (20 μM), Fc* (1 mM) and O_2 (2 mM)

Secondly, as seen by cyclic voltammetry data, E^{red} of the catalyst shifts positively upon introduction of AcOH. This increase in E^{red} effectively reduces the overpotential of the catalyst and would be accompanied by a lower rate of ORR. However, the trend between overpotential and rate is often exponential rather than linear, so reducing the overpotential by increasing AcOH would likely not explain the negative linear effect on ORR rate. Also, if the increasing E^{red} of the catalyst was a cause for the lowering rate of ORR, one would also expect the same negative dependence whether TBAOAc is present or not. Thirdly, there could be two competing mechanisms of ORR, and the ratio of the two pathways changes over the course of increasing [AcOH]. If the slower pathway is favoured at higher [AcOH] values, and the faster pathway is favoured at lower [AcOH] values, then it would be expected that the ORR rate would decrease with increasing [AcOH]. If the change in mechanism is a result of increasing [AcO^-] then introduction of TBAOAc should increase [AcO^-] to fully favour the slower pathway. The result would be complete observation of the slower pathway, with increasing [H^+], which effects the rate in a positive linear fashion, depending on the involvement of H^+ in the rate determining step of ORR turnover.

5.6.2 ORR with Benzoic Acid as the Proton Source

In order to further examine the effect of carboxylate binding to the catalyst upon the rate and mechanism of the ORR, similar studies were undertaken with benzoic acid (BzOH) as the proton source. BzOH is a slightly stronger acid than AcOH, and as a result its conjugate base (BzO^-) has a lower electron density at the carboxylate moiety and coordinates less strongly to metal centres. If the negative trend observed in the rate vs. [AcOH] profile is due to coordination of AcO^- to the catalyst effecting the mechanism, then changing the conjugate base present to the more weakly coordinating BzO^- then the reduction in rate with increasing acid concentration should be lessened.

Under the same conditions as the previous set of studies with unbuffered AcOH, this time with BzOH ranging between 3 and 30 mM and the resulting rate vs [BzOH] profile was constructed.

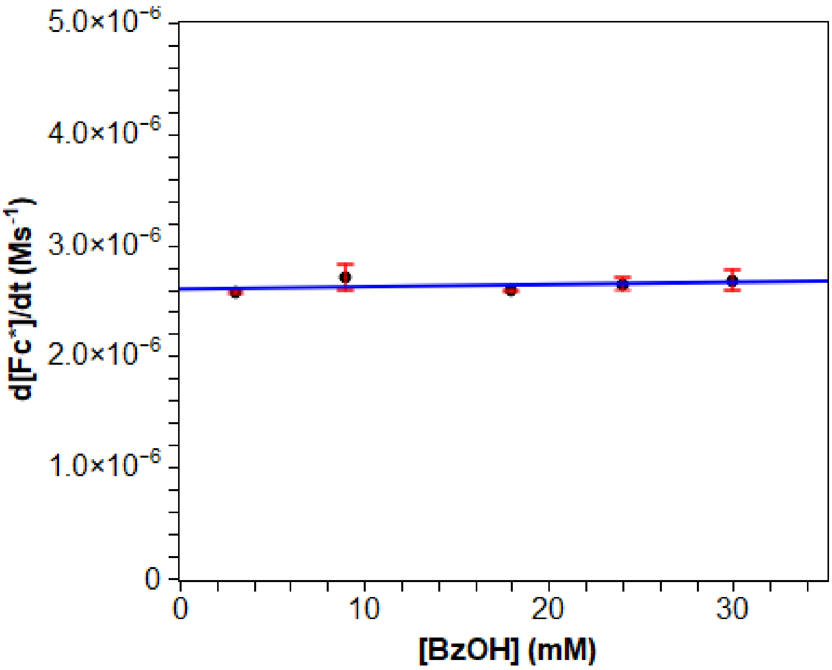

Figure 5.6.7 ORR rate vs [BzOH] plot in the presence of $\mathbf{Co_2L^{Me}OAc}$ (20 µM) Fc* (1 mM), and O_2 (2 mM)

Comparing ORR where BzOH is the proton source against that with AcOH, a few distinct differences are seen. Firstly, the rate of ORR with BzOH is higher than with AcOH across all [BzOH] values as a result from the slightly lower pKa of BzOH vs AcOH. Secondly, the ORR has a pseudo-zero order dependence on [BzOH], whereas with AcOH the rate of ORR is always affected even if TBAOAc is present, this also likely arises from the reduced pKa of BzOH, such that protonation becomes so rapid that [BzOH] no longer has an effect on the rate limiting step of the ORR. Finally, the negative rate vs [AcOH] dependence seen with AcOH is completely quenched when using BzOH as the proton source, indicating that there is no longer a change in the mechanism of the ORR across the range of [BzOH] values used.

To test if the mechanism of the ORR with BzOH as the proton source was the same as using a higher concentration of AcOH, the rate dependencies of the remaining three reaction components were examined.

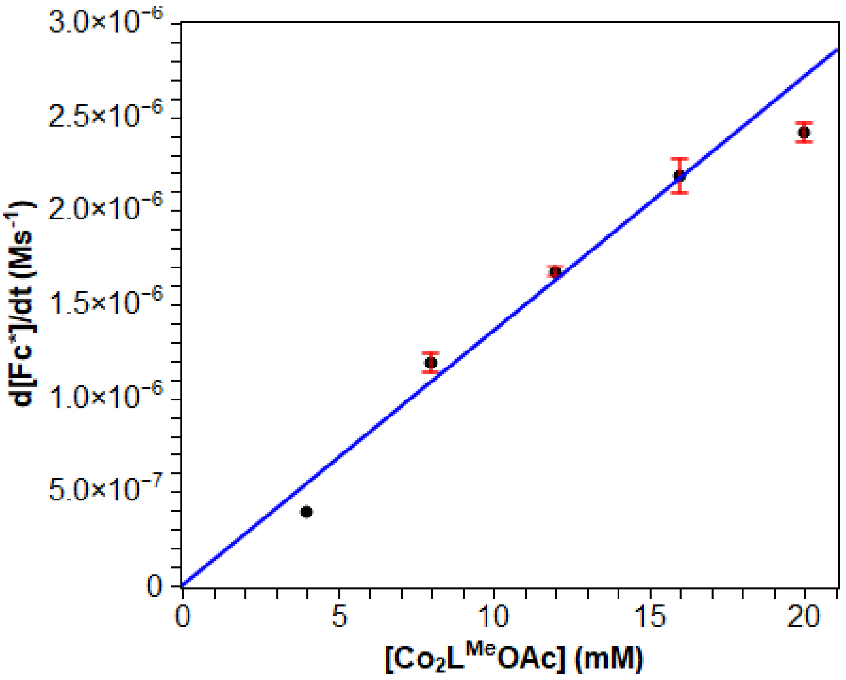

Figure 5.6.8 ORR rate vs [**$Co_2L^{Me}OAc$**] plot in the presence of BzOH (30 μM) Fc* (1 mM), and O_2 (2 mM)

Upon varying [**$Co_2L^{Me}OAc$**] between 4 and 20 mM, the rate of ORR increases from approximately 5×10^{-7} to 2.5×10^{-6} Ms^{-1} showing a linear relationship which intercepts at the origin, indicating that the catalyst is involved in the rate determining step, similar to when AcOH is used as the proton source.

Varying the [O_2] present in solution by mixing known quantities of O_2, air and N_2 saturated solutions shows an increase in rate between 2 and 4 mM, followed by rapid attenuation of the rate at higher [O_2] values. Comparing this trend with that observed with AcOH as the proton source, which shows no significant change across the whole range of [O_2] values, it can be suggested that the rate of O_2 binding to the catalyst is more significant to the overall rate, particularly at low concentrations, of reaction in the presence of BzOH than in the presence of AcOH.

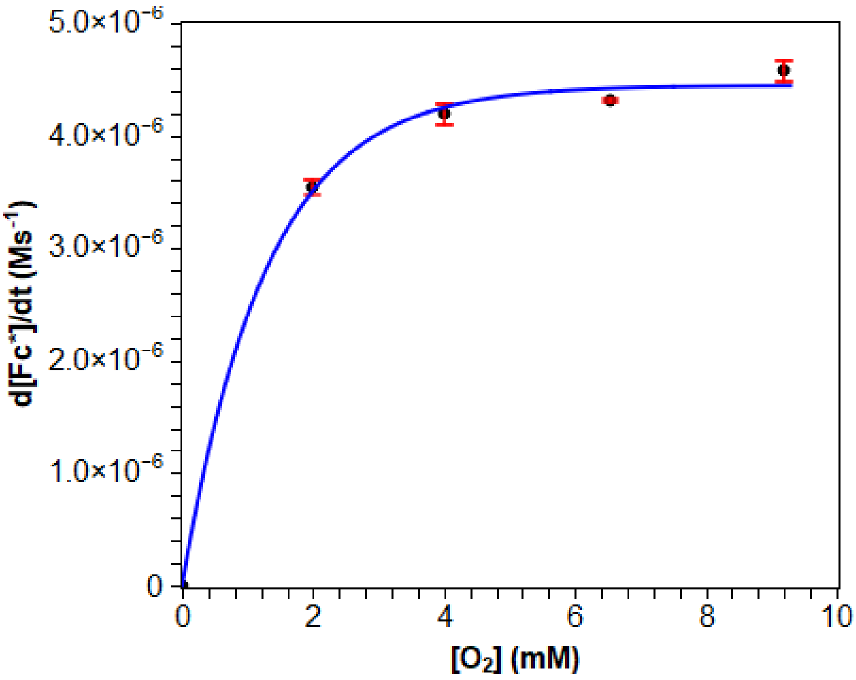

Figure 5.6.9 ORR rate vs [O_2] plot in the presence of **$Co_2L^{Me}OAc$** (20 μM) Fc* (1 mM), and BzOH (30 mM)

When [Fc*] is varied between 0 and 1 mM, a similar dependence to when AcOH is used is seen, however, the attenuation of the rate occurs quickly, approaching the plateau at 1 mM rather than 5 mM. Once higher Fc* concentrations are reached, the effect of adding more reducing agent is diminished, indicating that in the presence of BzOH, the electron transfer (ET) step from Fc* is faster than that in the presence of AcOH. This increased ET rate is likely due to the worse electron donating and coordinating properties of BzO^- vs AcO^-, and therefore makes reduction of the catalyst by Fc* more facile.

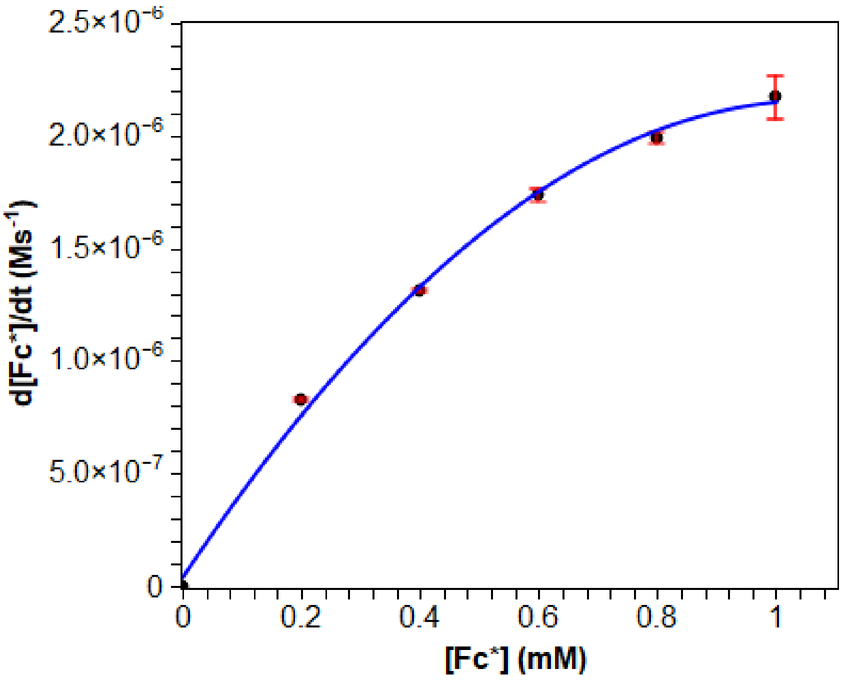

Figure 5.6.10 ORR rate vs [Fc*] plot in the presence of **$Co_2L^{Me}OAc$** (20 μM), BzOH (30 mM) and O_2 (2 mM)

Overall, in the presence of carboxylic acids, the rate of the ORR catalysed by **$Co_2L^{Me}OAc$** is always dependent on the concentration of both the catalyst and reducing agent. This indicates that the rate limiting step is an electron transfer. In the case of unbuffered AcOH, the rate shows an inverse dependence, indicating deactivation of the catalyst which likely arises from competitive binding of AcO^- to the active site. In the presence of an AcOH/TBAOAc buffer, the dependence is positive and linear, however for BzOH, there is a zero-order dependence. This indicates that between the two proton sources, the increased acidity means that protonation becomes sufficiently fast as to no longer take part in the rate determining step.

5.6.3 Use of NH_4PF_6 as a Proton Source

Since the presence of carboxylates clearly have an effect on the mechanism of ORR catalysed by **$Co_2L^{Me}OAc$**, we decided to use a proton source which does not involve a strongly coordinating conjugate base which has a similar acidity to AcOH in MeOH. NH_4PF_6 fits these criteria reasonably well, with a pKa of 10.6 in MeOH, and the neutral NH_3 as conjugate base. With PF_6^- as the counter ion, very limited coordination of either the conjugate base or the counter ion should take place in comparison to AcO$^-$ or BzO$^-$.

Similar rates of ORR are observed with NH_4PF_6 as AcOH, the dependence of ORR rate on [NH_4PF_6] (figure 5.6.11) shows a similar trend to that of AcOH where the linear dependence quickly attenuates at higher [NH_4PF_6] values. With NH_4PF_6 however, the rate is attenuated towards the plateau much more quickly than with AcOH, reaching saturation kinetics at [NH_4PF_6] values greater than 10 mM, whereas with AcOH the attenuation is very shallow. In addition, the negative rate dependence as seen with unbuffered AcOH is not present with NH_4PF_6, indicating that no inhibition of the catalyst by the conjugate base takes place with this non-coordinating proton source. The same background ORR rate with no additional proton source present gives the same non-zero intercept as with AcOH/TBAOAc and the same background rate subtraction was performed to see the effect of increasing [NH_4PF_6] more clearly (figure 5.6.12)

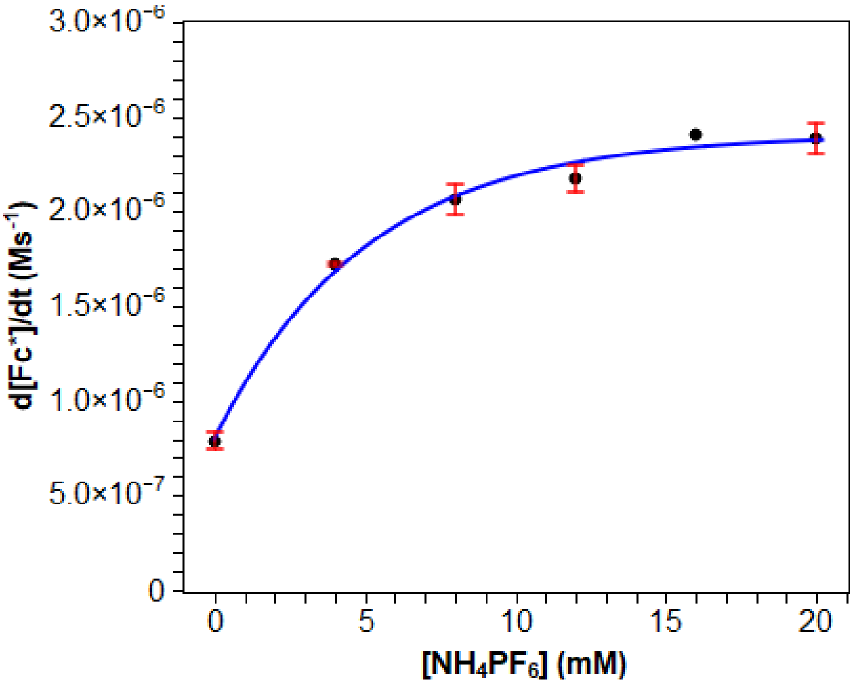

Figure 5.6.11 ORR rate vs [NH_4PF_6] profile in the presence of **$Co_2L^{Me}OAc$** (20 µM), Fc* (1 mM) and O_2 (2 mM)

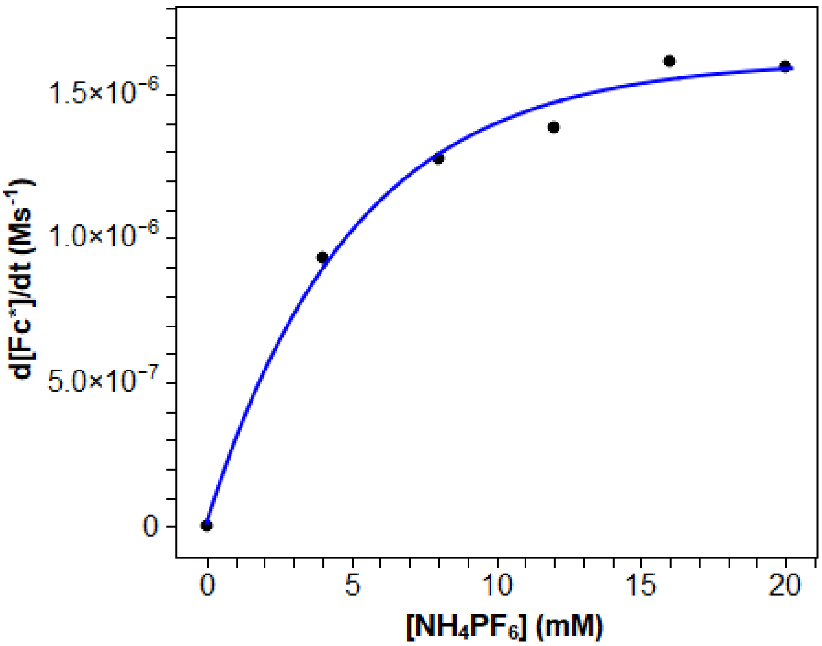

Figure 5.6.12 ORR rate vs [NH_4PF_6] profile in the presence of **$Co_2L^{Me}OAc$** (20 µM), Fc* (1 mM) and O_2 (2 mM) corrected to include only the influence of increasing [NH_4PF_6]

Interestingly the ORR in the presence of NH_4PF_6 as the proton source, iodometric titration of the complete reaction mixture (figure 5.6.13) reveals a complete switch in selectivity moving from 90% H_2O selective in the presence of AcOH to 93% H_2O_2 selective in the presence of NH_4PF_6. To the best of our knowledge, this is the first case in which the selectivity of the ORR can be almost fully biased towards either the two electron or four electron pathways by changing the anions present in solution.

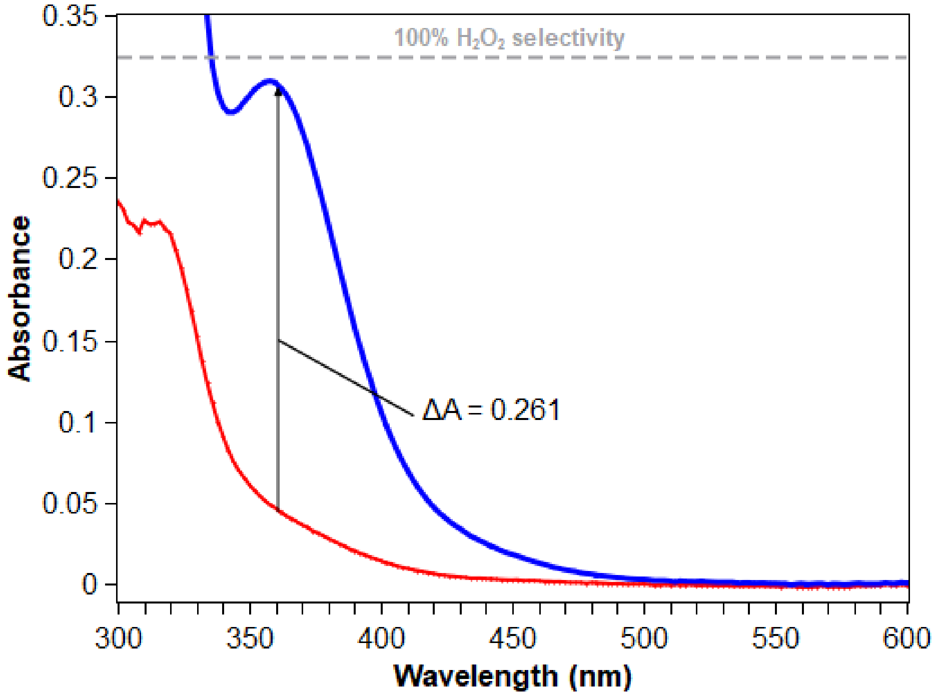

Figure 5.6.13 Electronic spectrum of a 60 µL aliquot of the complete with NH_4PF_6 reaction in fig. 1.5.2 diluted in MeCN (2.94 mL) before (red trace) and 1h after (blue trace) addition of excess NaI (ca. 100 mg). The grey dashed line represents the theoretical absorbance value for a catalytic reaction with 100% selectivity for H_2O_2

To further test if the switch in selectivity observed when changing AcOH to NH_4PF_6 is due to the anions present, or the minor changes in pKa upon changing the acid identity, an AcO^- containing analogue of NH_4PF_6 with the same pKa, NH_4OAc was used.

Upon completion of the ORR with NH_4OAc as the proton source, the selectivity determined by iodometric titration (Figure 5.6.14) was found to switch back to an even higher H_2O selectivity of 97%

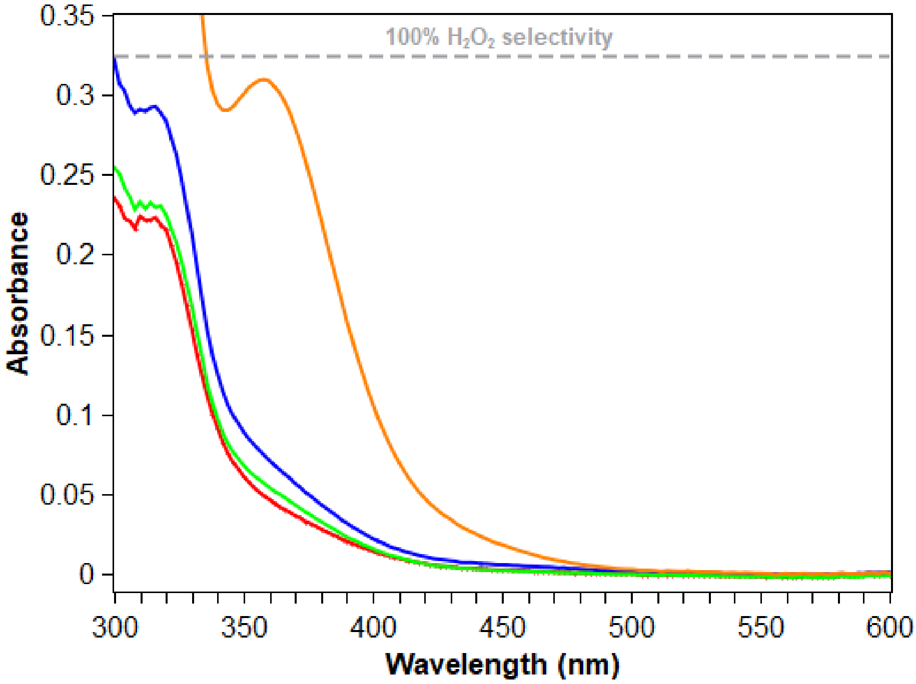

Figure 5.6.14 Spectral changes before (red trace) and after iodometric titration of ORR solutions where the proton source was AcOH (blue trace), NH_4PF_6 (orange trace) or NH_4OAc (green trace)

.

When **$Co_2L^{CF3}OAc$** was studied for the ORR where NH_4PF_6 was used as the proton source, no reaction occurred. Since NH_4PF_6 seems to only facilitate the two-electron pathway, it is possible that the $E_{1/2}$ of **$Co_2L^{CF3}OAc$** is more positive than the E_{O_2/H_2O_2} under these conditions, and therefore it may be the case that **$Co_2L^{CF3}OAc$** would be operating at an underpotential and is therefore thermodynamically unfeasible.

5.7 Proposed ORR Mechanisms

5.7.1 Mechanism with a Peroxo Bridged Intermediate

Summarising the kinetics observed for the ORR catalysed by **$Co_2L^{Me}OAc$** in the presence of AcOH/TBAOAc as the proton source, conclusions about the ORR mechanism can be drawn. The ORR shows a first order dependence on [**$Co_2L^{Me}OAc$**], [Fc*] and [AcOH/TBAOAc] while the rate is independent of [O_2]. Therefore, the rate determining step of the ORR is likely a proton coupled electron transfer (PCET) to a catalyst intermediate, while the rate of oxygen binding under these conditions is rapid in comparison. Since the catalyst is in its fully reduced $Co^{II}Co^{II}$ state before addition of O_2, as shown by Evans' method NMR studies, and that Fc* is not strongly reducing enough to facilitate the Co^{II} to Co^{I} reduction, the PCET step must occur after oxidation by O_2 to the catalyst to form a Co^{III} intermediate which is able to be reduced by Fc*. Aerobic NMR studies show that **$Co_2L^{Me}OAc$** becomes diamagnetic upon addition of AcOH, and therefore all the cobalt centres must be oxidised from Co^{II} to Co^{III} in acidic aerobic media supporting the idea that O_2 binds in a bridging mode between the two cobalt atoms. Differences between concentration vs rate profiles under buffered and non-buffered conditions indicate the binding of acetate to the catalyst has a significant effect on the ORR rate, where the ORR proceeds more slowly when $[AcO^-]$ is high. For this section, only the mechanism for reactions containing a large $[AcO^-]$ will be discussed, and elucidation of the mechanism when the extent of AcO^- binding is lower will be discussed in coming sections. Finally, the high selectivity for the four-electron pathway means that the mechanism must involve the cleavage of the O-O bond.

With these results in mind, in combination with previously reported proposed mechanisms for the ORR by similar catalysts, we suggest the following mechanism for the ORR in MeOH containing AcOH/TBAOAc.

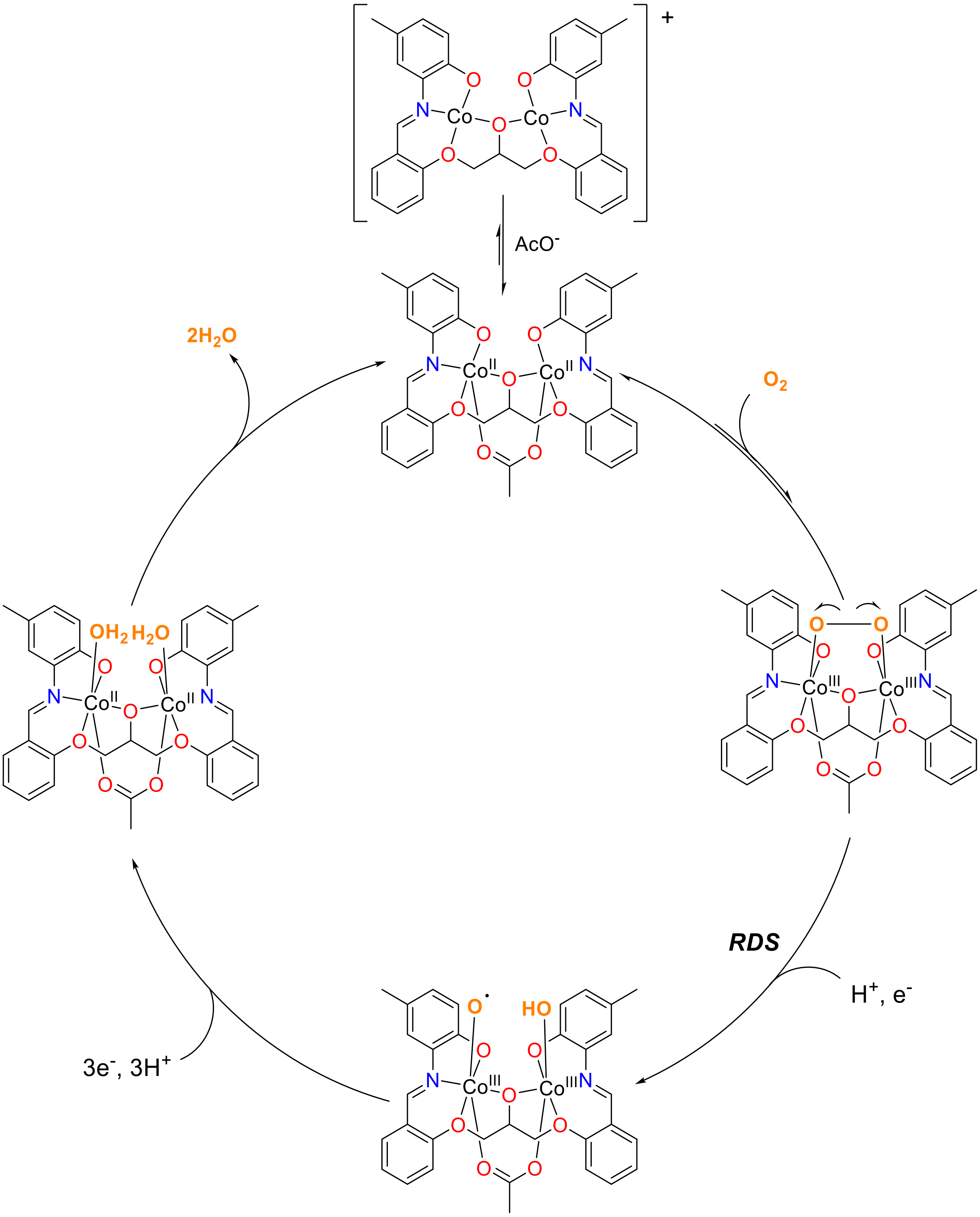

Scheme 5.7.1 Proposed mechanism of the ORR catalysed by **$Co_2L^{Me}OAc$** where the binding of oxygen forms a peroxo bridge between the two cobalt ions.

5.7.2 Mechanism with One Catalytically Active Cobalt Centre

Since the oxidation potential of the second cobalt centre is large compared to the first oxidation, it is entirely possible that the second cobalt does not participate directly in the binding of O_2, but instead acts as a site for binding of acetate. The bound acetate may, in turn, act as a proton relay towards the distal O atom of the superoxide bound to the first cobalt centre.

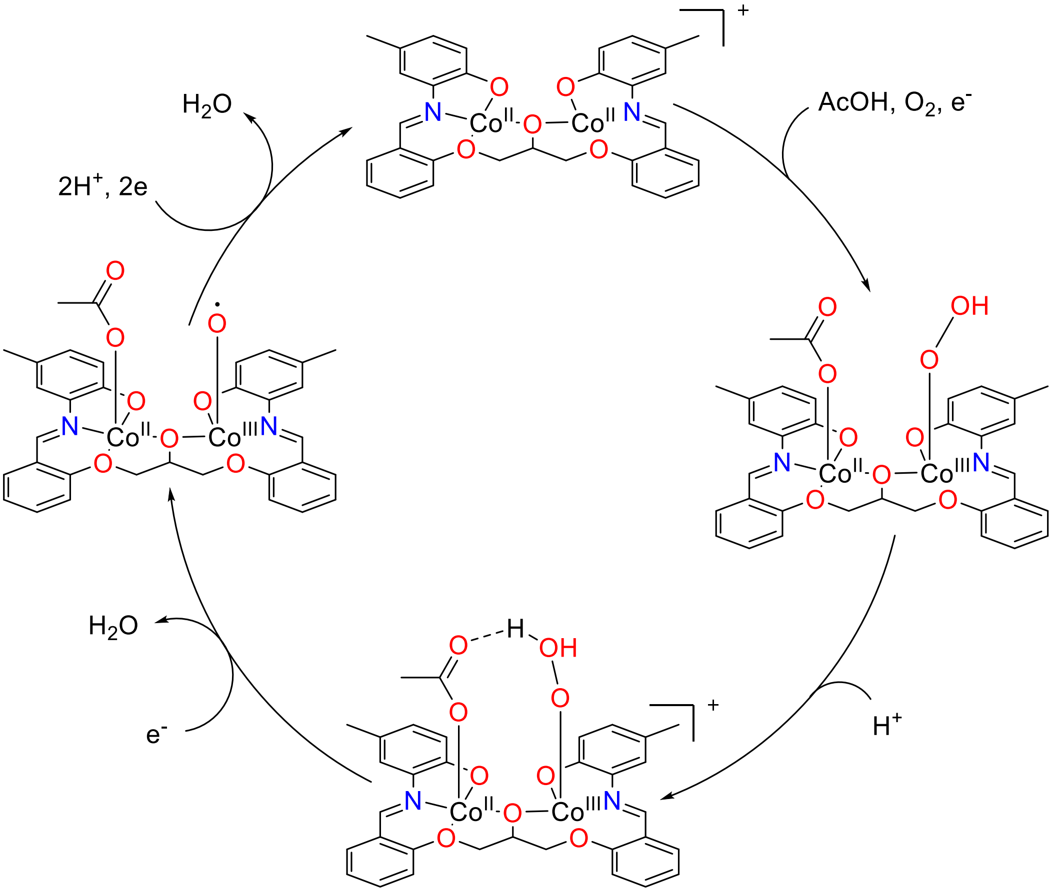

Scheme 5.7.2 Postulated mechanism involving oxygen binding to only one cobalt centre, where acetate coordinated to the second cobalt centre acts as a proton relay to facilitate the four-electron reduction of O_2.

A similar mode of action is seen for the reverse reaction, the oxygen evolution reaction, in a study by Cao, Lai and co-workers, in which a mononuclear Cu complex bearing a tridentate pyridine diamide ligand facilitates the electrocatalytic OER in the presence of carbonate ions.[204] The axial coordination of carbonate to the complex acts as both a proton shuttle to remove protons from a first-sphere aqua ligand, as well as a hydrogen bond acceptor for a second water molecule. This combined effect results in O-O bond formation and subsequent release of O_2.

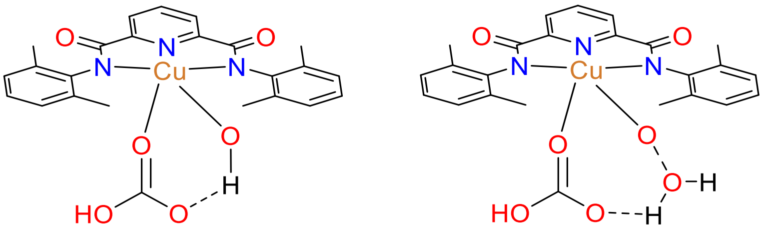

Figure 5.7.1 Electrocatalytic WOC studied by Cao and co-workers which uses a coordinated carbonic acid ligand as a proton source.

5.7.3 Mechanism with NH_4PF_6 and Peroxo Bridging

The ORR catalysed by **$Co_2L^{Me}OAc$** when NH_4PF_6 is used as the proton source produces H_2O_2 almost quantitatively. It was also determined that the cause for this change in selectivity between carboxylic acid proton sources and NH_4PF_6 was the absence of the acetate conjugate base. For this pathway, we propose an ORR pathway where acetate is not coordinated to the cobalt ions, and therefore electron donation from the acetate anion is lost when the non-coordinating NH_4PF_6 is used. It has been proposed that increased electron density about the metal centre of an ORR catalyst can facilitate O-O bond cleavage by increased donation to the π^* orbitals of the bound O_2, and therefore if this increased electron density is missing, protonation of the peroxo species and subsequent release of H_2O_2 may be preferred over O-O bond cleavage. With this in mind, we propose the following mechanism for H_2O_2 selective oxygen reduction by **$Co_2L^{Me}OAc$** in the presence of NH_4PF_6, where protonation of each bound oxygen atom occurs without breakage of the O-O bond.

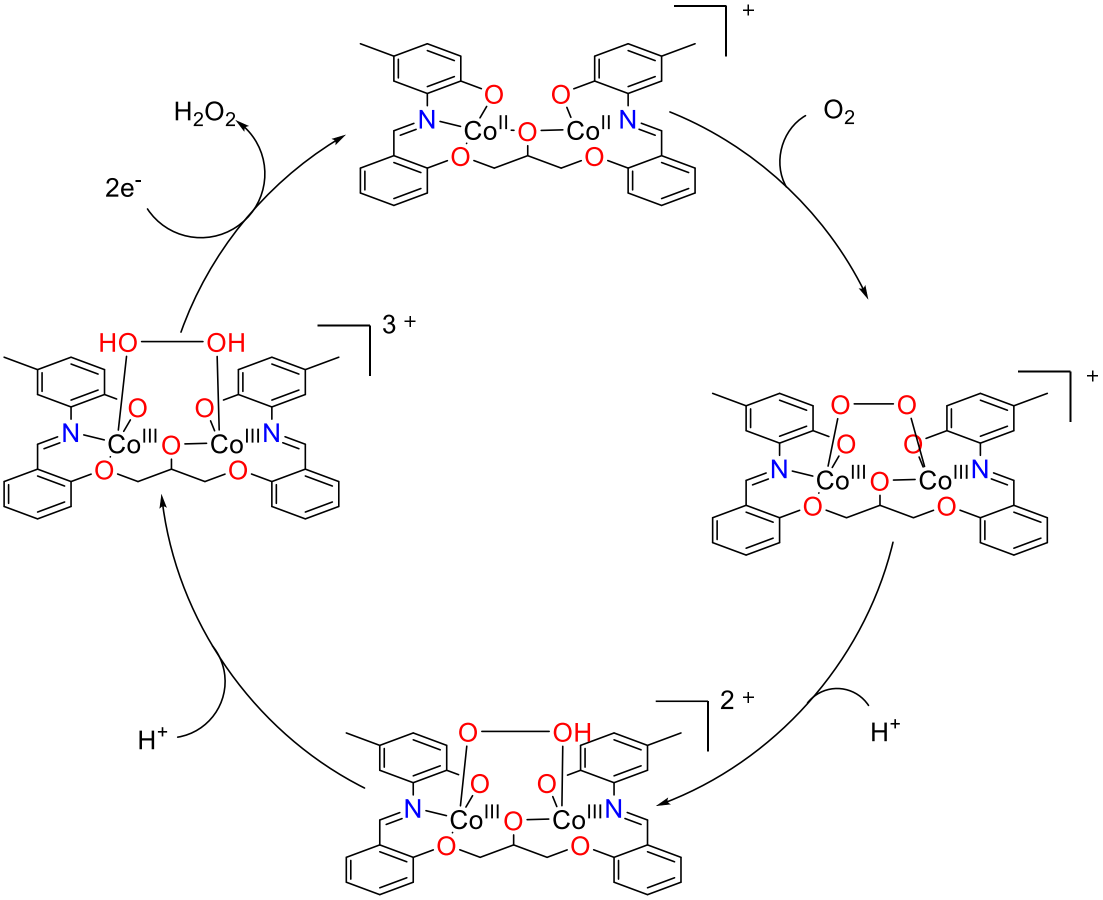

Scheme 5.7.3 Proposed mechanism of the two-electron selective ORR catalysed by **$Co_2L^{Me}OAc$** in the presence of NH_4PF_6

5.7.4 Mechanism with NH_4PF_6 and One Catalytically Active Centre

Like the mechanism proposed in Scheme 5.7.2, it is possible that only one cobalt centre is able to bind oxygen. This also applies to the ORR in the presence of NH_4PF_6. The absence of a carboxylic acid would mean that there would be no proton relay activity which would direct protons to the distal oxygen atom of the hydroperoxo complex. As a result, protonation of the proximal oxygen atom and subsequent release of H_2O_2 may be preferred over O-O bond cleavage.

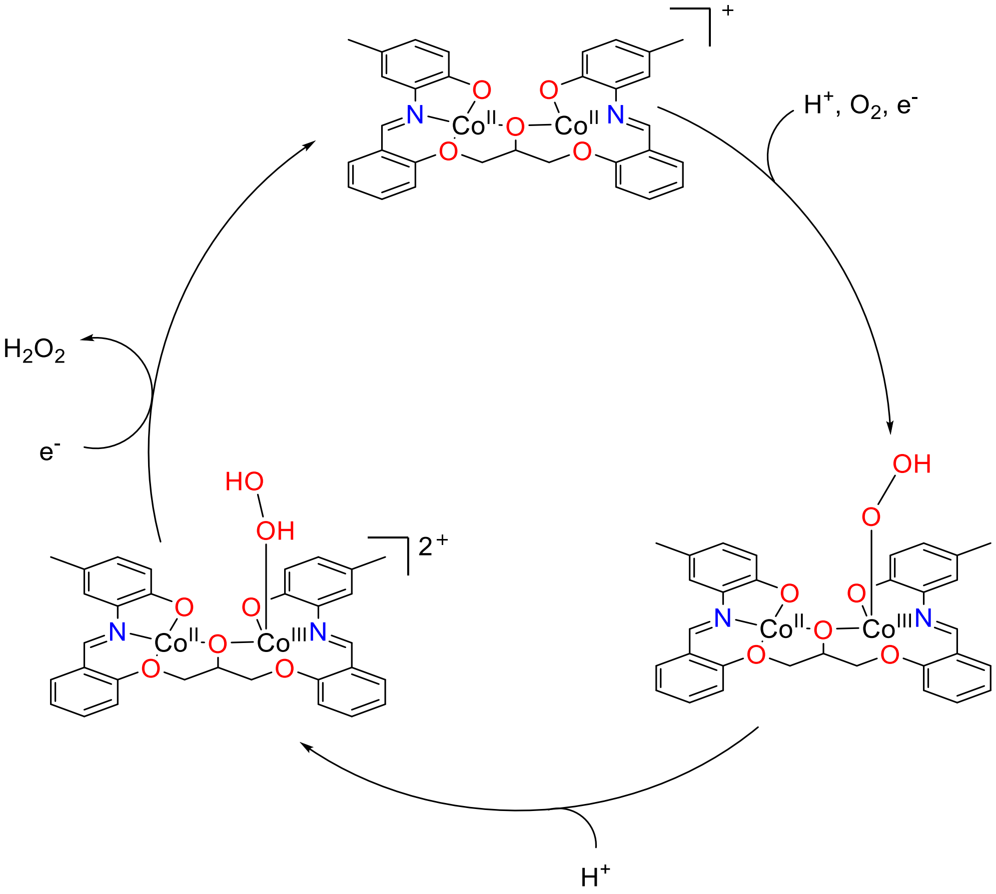

Scheme 5.7.4 Proposed mechanism of the two-electron selective ORR where only one cobalt centre takes part in catalysis and no proton relay is available

It is also possible that the conjugate base of NH_4PF_6, NH_3, may coordinate to the vacant coordination site of the second cobalt ion. In this case, NH_3 may be in close proximity to the proximal oxygen atom of the bound hydroperoxide. It is possible that this coordinated NH_3 is able to form am N-H—O hydrogen bonding interaction which may further facilitate protonation of the proximal oxygen atom.

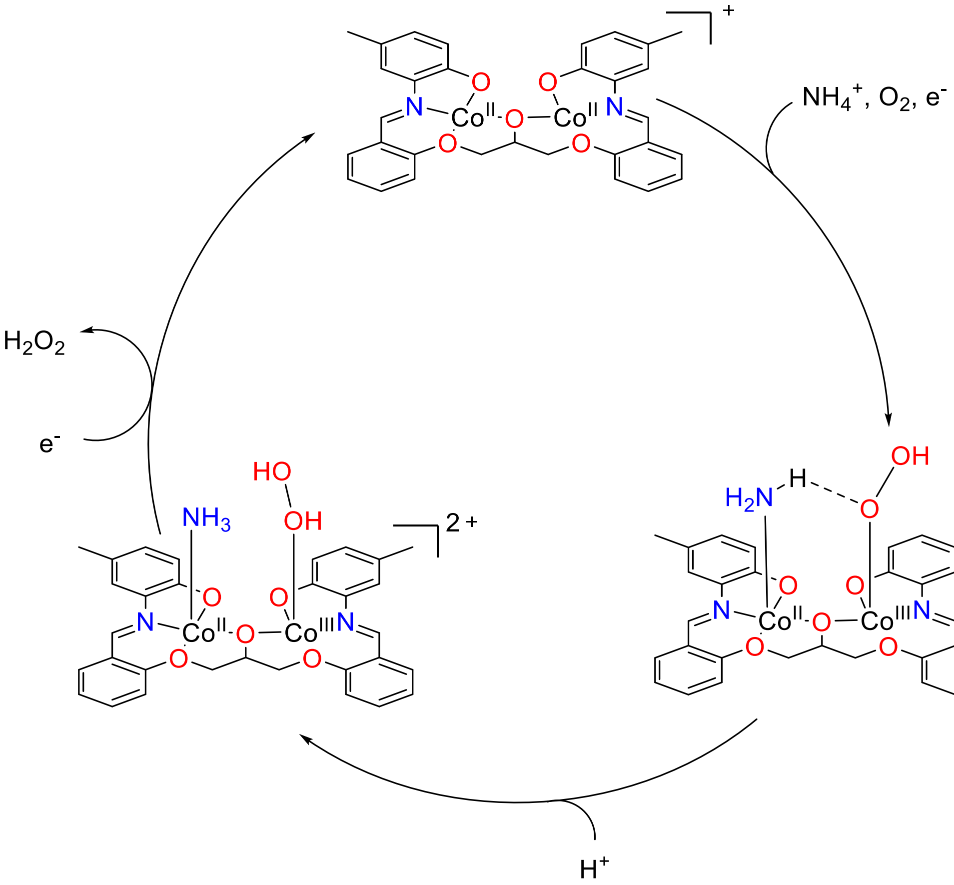

Scheme 5.7.5 Proposed mechanism of the two-electron pathway selective ORR where coordination of NH_3 to the second cobalt centre promotes protonation of the proximal oxygen atom and facilitates H_2O_2 release.

There are reasonable arguments for both mechanisms involving peroxo bridged intermediates and those containing only one oxygen binding site. For the proposed peroxo-bridged mechanisms, it would be expected that the only cobalt species present in the catalytic resting state would be diamagnetic Co^{III}. This is supported by the fact that the NMR spectrum of **$Co_2L^{Me}OAc$** shows no paramagnetic broadening in the presence of air and AcOH. On the other hand, on the time scale taken to run the NMR experiment, it is possible that all cobalt centres are aerobically oxidised independently without peroxo bridging in the presence of acetic acid. In addition, EPR evidence supports the slow binding of O_2 to form a fully EPR silent complex rather than a species with a single Co^{II}.

The main argument for the proposed mechanisms where only one cobalt centre binds oxygen is that the oxidation of the second cobalt centre proceeds at a much more positive potential than the first, that is to say, electron transfer from the second Co^{II} ion to oxygen should be significantly slower than that for the first Co^{II} ion. Therefore, binding of the second oxygen atom may be slower than catalytic turnover. In addition, these mechanisms conveniently explain the drastic switch in selectivity between the two proton sources by the presence or absence of carboxylate as a proton relay. The mechanisms proposed in Schemes 5.7.2, 5.7.4 and 5.7.5 also would allow for the acetate originally present in the complex to remain coordinated, whereas the proposed mechanism shown in Scheme 5.7.3 relies on full decoordination of acetate to explain H_2O_2 selectivity.

5.8 Catalytic Aerobic Oxidation of 3,5-di-*tert*-butylcatechol

Catechol oxidase is a metalloenzyme found in many fruits and vegetables and contains a multinuclear copper active site. The enzyme is responsible for the oxidation of aryl dialcohols to their respective quinone substance and the respective oxidative browning of fruits. Catechol oxidases are important in the production of melanin pigments and other UV protective dye compounds in biology. Monitoring the catechol oxidase activity of synthetic complexes is often a useful measure of determining the potential of a catalyst system towards other aerobic oxidation reactions which may have important industrial applications. Catechol oxidase activity is measured conveniently by mixing solutions of a potential catalyst complex and appropriate catechol in the presence of oxygen.

The most commonly used catechol compound for these tests is 3,5-di-*tert*-butyl catechol (DTBC) since it is relatively stable towards oxidation without catalysis in alcohol solutions and does not absorb visible light in its reduced form. When oxidised, the resulting 3,5-di-*tert*-butyl-*o*-quinone absorbs visible light with a characteristic peak in its electronic spectrum with a λ_{max} of 400 nm and an extinction coefficient of 1560 $M^{-1}cm^{-1}$.

In addition, this oxidation of catechol is of course in essence, another form of the ORR where the soluble reductant is a quinone instead of decamethylferrocene which does not require the use of an external proton source.

$Co_2L^{Me}OAc$ was examined for catechol oxidase activity by mixing air saturated MeOH solutions of the complex and 3,5-di-*tert*-butyl catechol such that the reaction mixture contained 40 µM of **$Co_2L^{Me}OAc$** and 10 mM DTBC. The absorbance at 400 nm was recorded over the course of 100 minutes, with 5 minute intervals between scans. At the start of the reaction, the absorbance at 400 nm was 0.32, which arises from absorption by the catalyst itself. Over the course of 100 minutes, the absorbance increased almost linearly up to a value of 0.92, indicating the oxidation of DTBC to DTBQ. A control experiment where the catalyst was excluded showed negligible oxidation of DTBC over the 100 minute period.

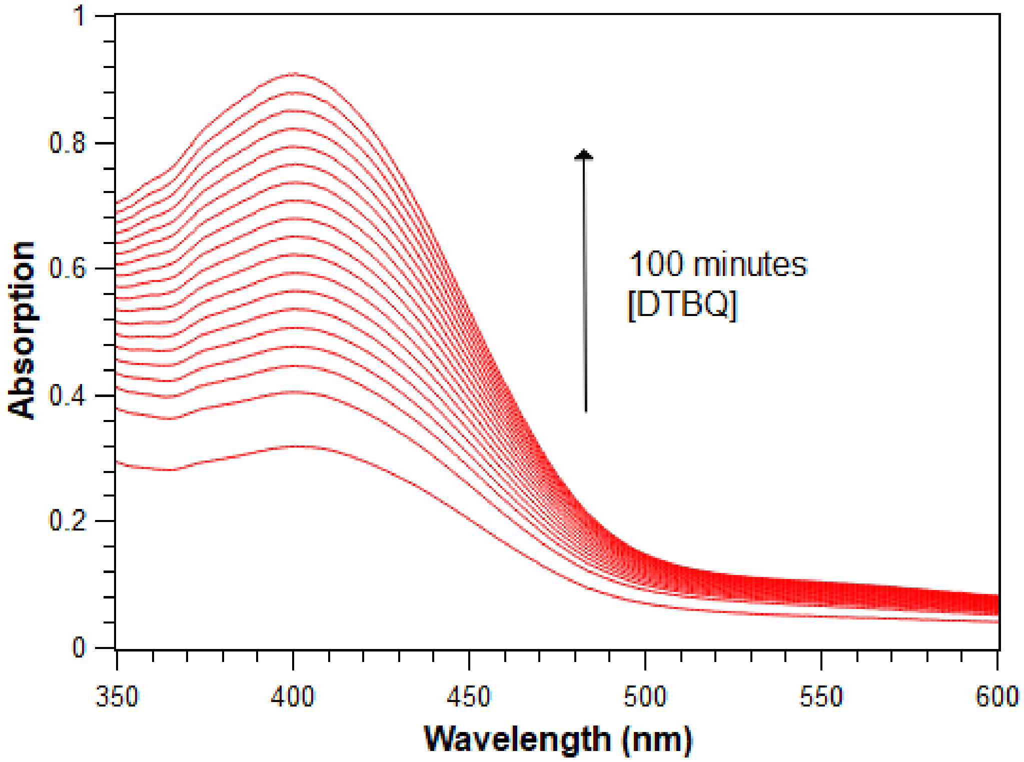

Figure 5.8.1 Changes in the electronic spectra of an air saturated MeOH solution containing **$Co_2L^{Me}OAc$** (40 µM) and TBHC (10 mM) at room temperature over 100 minutes.

To determine the TOF of oxidase catalysis, a range of catalyst concentrations were examined. The rate vs [**$Co_2L^{Me}OAc$**] profile (figure 5.8.2) was calculated by converting the absorbance change over time to concentration change over time by the Beer-Lambert law and showed a linear dependence between the rate of quinone formation and catalyst concentration. The slope of figure 5.8.2 is the TOF of catalytic aerobic oxidation of DTBC and was found to be 0.016 s^{-1} or 52 h^{-1}. While the highest recorded TOF for DTBC oxidation catalysis was on the order of 10^3 h^{-1},[205] the rate observed was similar to many other catalysts found in the literature.[206,207] The modest rate of oxidation is to be expected, since as discussed in relation to the ORR, the $E_{1/2}$

of the catalytically relevant electron transfer steps is much closer to the E_{ORR} than other catalyst systems, and therefore there is less of a driving force for oxygen reduction. In this system, the overpotential of the reaction is not as relevant, since it is not the aim to obtain as high of a thermodynamic efficiency as possible, so the use of a catalyst with a higher overpotential for the reduction of oxygen may be more suitable.

The oxidation of DTBC under relatively simple catalytic conditions does however demonstrate the potential for versatility in catalyst, and shows that this dinuclear Schiff base system may have uses outside of the ORR where homogeneous aerobic oxidation catalysts may be used for a number of oxidative organic transformations.

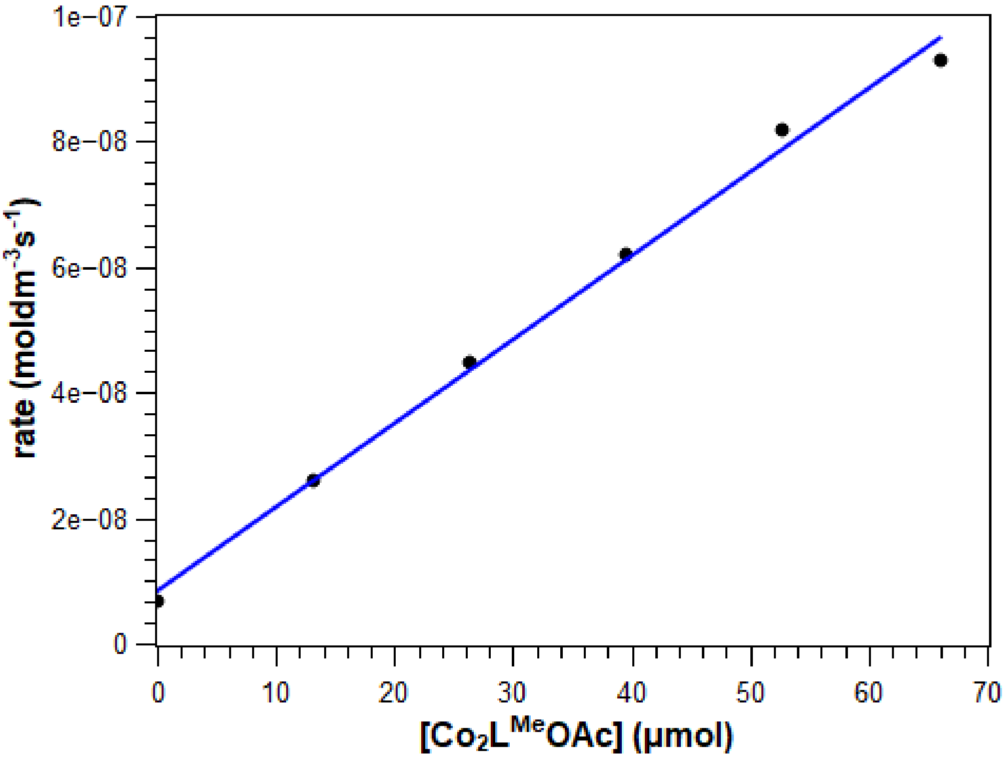

Figure 5.8.2 Rate vs. [**$Co_2L^{Me}OAc$**] profile for the aerobic oxidation of TBHC (10 mM) in air saturated MeOH.

Chapter 6

General Conclusions

In this work, we have developed an easily synthesised family of multinuclear complexes. The main complex studied for its ORR activity was the dinuclear **$Co_2L^{Me}OAc$** which could be synthesised in one step from the easily obtained BFPP dialdehyde, 2-amino-4-methylphenol and cobalt (II) acetate. The complex bears two cobalt (II) ions in close proximity in a N_2O_5 donor set and are bridged by an alkoxide moiety and furnished with a bridging acetate ligand. In addition, it was possible to obtain a trinuclear **$Co_3L^{Me}(OAc)_3$** in which a third cobalt ion coordinates between the two phenolate moieties. Synthesis of this trinuclear complex allowed for examination of the structure by XRD and provided further information on the dinuclear species, for which diffraction quality crystals could not be obtained. In the case that the coordinating acetate ligand was abstracted and replaced with a non-coordinating anion, quantitative conversion to a MeOH insoluble tetranuclear dimer of two $[Co_2L^{Me}]^+$ units took place. XRD studies showed that this dimer bears a defective dicubane core geometry. This easily obtained tetranuclear structure may have interesting applications as a single molecule magnet, however the required magnetometry experiments to determine this behaviour were not performed in this work.

Cyclic and differential pulse voltammetry was used to examine the redox behaviour of the di, tri, and tetranuclear complexes. In DMF solution, **$Co_2L^{Me}OAc$** showed a redox wave which was typical of the Co^{II}/Co^{III} couple with a large peak separation owing to the spin crossover effects common to this electron transfer. Ligand contributions to the redox behaviour were examined using a trinuclear $Zn_3L^{Me}(OAc)_3$ analogue which removed any metal centred electron transfer steps. For tri and tetranuclear complexes, the wave relating to the Co^{II}/Co^{III} electron transfer were diminished and became less reversible. The voltammetry of **$Co_2L^{Me}OAc$** was also examined in MeOH solution, since this was the solvent most suitable for homogeneous catalytic studies. In this solution, it was possible to more clearly see a second reversible couple following the Co^{II}/Co^{III} step. This step was assigned to the sequential oxidation of the second cobalt atom of the dinuclear core. It was found that electrocatalytic activity towards the ORR was too slow to be determined by cyclic voltammetry by foot-of-the-wave analysis, however, when decamethylferrocene (Fc*) was added to the solution as an electron transfer mediator, the electrocatalytic ORR could be observed, but not quantitatively assessed.

The ORR catalysed by **$Co_2L^{Me}OAc$** was assessed by an increasingly popular method which uses Fc* as a chemical reductant, where the generation of Fc^{*+} could be measured by spectrophotometry. This method allowed close examination of the TOF of catalysis, as well as the determination of the rate determining step by independently varying concentrations of the reaction components. It was found that in MeOH solution containing and AcOH/TBAOAc buffer, that the rate was dependent on [**$Co_2L^{Me}OAc$**], and [Fc*] but also showed a weak dependence on [AcOH/TBAOAc] with a non-zero intercept. The selectivity of the ORR determined by iodometric titration, and it was found that **$Co_2L^{Me}OAc$** facilitates the four-electron reduction of O_2 with a 91% selectivity. Interestingly, this selectivity changes to almost quantitative two-electron pathway selectivity when NH_4PF_6 is used as the proton source. To determine if this selectivity change was related to the slight pKa difference between the two acids, or if it was due to the coordinating properties of the conjugate base, the selectivity was also determined when NH_4OAc was used as the proton source, In this case, selectivity was biased back towards the four-electron pathway, suggesting that the carboxylate is essential to four-electron selectivity. Multiple mechanisms were proposed, and based on the evidence gathered, we tentatively postulate that the mechanism of the ORR proceeds where only one cobalt centre takes part in the binding of oxygen, while the other may bind a conjugate base which dictates the selectivity of the reaction.

It was also shown that **$Co_2L^{Me}OAc$** can catalyse the aerobic oxidation of 3,5-di-*tert*-butylcatechol to 3,5-di-*tert*-butyl-*o*-quinone in MeOH solution at a rate comparable to other catechol oxidase inspired catalysts, indicating its possible use in other organic transformations.

Overall, we have shown that **$Co_2L^{Me}OAc$** is an easily obtained complex and multiple analogous structures can be obtained from simple modification of the reaction conditions. **$Co_2L^{Me}OAc$** is able to catalyse the ORR with low overpotential, whilst retaining a moderate TOF. In addition, the selectivity of the ORR was found to be dependent on the anion present in the reaction solution and could be easily controlled. To the best of our knowledge, this was the first case where the ORR selectivity can be controlled completely by the anion present in solution and may prove important when understanding structure activity relationships when developing new two or four-electron selective ORR catalysts, whether they be homogeneous or heterogeneous.

This work could be further developed by performing rigorous DFT calculations to support the proposed catalytic pathways and better understand the role of the anion in the selectivity of the ORR. It would also prove interesting to examine a catalyst with a similar overall structure as **$Co_2L^{Me}OAc$**, but modify the ligand such that the cobalt centres are more electron rich, resulting in faster catalysis which may be observed by electroanalytical methods. Finally, this work could be further developed by immobilising the catalyst onto an electrode surface, possibly via electropolymerisation with an appropriate functional group such as pyrrole or thiophene, with the goal of examining the system's longevity and reusability under the conditions found in a true fuel cell.

Chapter 7

Experimental

7.1 General Information

7.1.1 Reagents for Multinuclear Complex Synthesis

Salicyclaldehyde derivatives, epichlorohydrin and most 2-aminophenol derivatives (reagent grade) were purchased from Merck. 2-amino-4-trifluoromethylphenol was purchased from Fluorochem and all were used as received. Metal salts were purchased from AlfaAesar. Anhydrous methanol (sureseal) was purchased from Merck and was used without need for further drying. Ammonium hexafluorophosphate, sodium tetrafluoroborate and sodium perchlorate were purchased from Merck as crystalline solids and were used as received.

Cis,cis-cyclohexane-1,3,5-triol dihydrate was purchased from Bujno Chemicals (Poland) and was dehydrated *in vacuo* at 80 ^{o}C overnight and stored under argon until use. *p*-toluenesolfonyl chloride was purchased from Merck and was purified by dissolving 30 g in ethyl acetate (200 mL before washing with a 10% w/v aqueous NaOH solution (2×100 mL). The organic phase was then washed with water (100 mL) then brine (20 mL). The organic phase was dried over anhydrous $MgSO_4$ and filtered. The solvent volume was reduced to 100 mL and was placed in the freezer (-20 ^{o}C) overnight. During this time, large white crystals of pure *p*-toluenesolfonyl chloride formed. The crystals were filtered and washed with further ice-cold ethyl acetate (2×20 mL) then dried in air. The pure product was stored under argon. Sodium azide and sodium hydride (40% in mineral oil) were purchased from Alfa Aesar, 2-bromomethylpyridine hydrobromide and Pd/C (10%) were purchased from Merck and was used as received. Pyridine was distilled over KOH under nitrogen and stored over 4Å molecular sieves. Anhydrous DMF was purchased from Merck and used as received.

7.1.2 Instrumentation

^{1}H and ^{13}C-NMR{^{1}H} spectra were obtained on a Bruker Ascend 500 spectrometer (500 MHz) and all shifts are quoted with respect to TMS using the residual solvent signal as an internal reference. FT-IR were obtained on a Perkin Elmer FT-IR spectrum BX. UV-Vis spectra were obtained on an Agilent Cary 60 UV-Vis spectrophotometer. Cyclic voltammetry and differential pulse voltammetry measurements were carried out using an Autolab PGstat 30 potentiostat/gavlanostat.

A 3 mm diameter glassy carbon electrode was used as the working electrode for all voltammetry experiments and was polished on a felt pad with alumina before each experiment. The counter electrode was platinum wire and was cleaned between experiments by washing with acetone and burning any remaining organic materials using a Bunsen burner. A silver pseudo reference electrode was used and was calibrated to an internal reference of either ferrocene or decamethylferrocene after measurement. X-Ray diffraction measurements were carried out using a Rigaku XtalLab Synergy S. Crystal structures were refined using Olex2,[208] the structure was solved with the SHELXT[209] structure solution program using Intrinsic Phasing and refined with the SHELXL[210] refinement package using Least Squares minimisation. Hydrogen atoms were modelled using the riding method.

7.2 Synthesis of Multinuclear Complexes

7.2.1 1,3-bis(2-formylphenoxy)-2-propanol BFPP

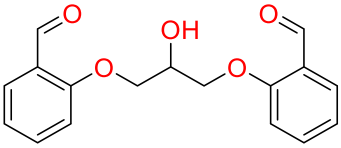

Salicylaldehyde (23 mL, 0.2 mol) was dissolved in degassed aqueous NaOH (8.8 g in 200 mL) resulting in a vivid yellow solution. The mixture was heated to 60 °C before dropwise addition of (±)-epichlorohydrin (8 mL, 0.1 mol) over 30 min. The mixture was stirred at 60 ^{o}C for a further two hours, after which a viscous yellowish-brown oil had formed. The reaction flask was cooled in ice water with rapid stirring for two hours, causing the oil to solidify into a pale-yellow cake. The cake was broken and washed with liberal quantities of deionised water, removing some of the yellow colour. The solid was then dissolved in the minimum volume of hot methanol, cooled to room temperature and then precipitated by the dropwise addition of ice-cold water with rapid stirring. The precipitate was filtered, washed with further water and dried in air to give 11.8 g, 39 mmol of off-white BFPP (39 % yield). In some instances, the oil did not solidify upon cooling, in this case, the supernatant aqueous solution was decanted, and the oil was dissolved in the minimum of hot methanol, boiling off some of this methanol resulted in precipitation of the solid product, which was then purified by the above method. δ_H (500 MHz, Chloroform-d) 10.40 (2 H, s), 7.81 (2 H, dd, J = 7.7, 1.8 Hz), 7.57 (2 H, ddd, J = 8.3, 7.3, 1.8 Hz), 7.09 (2 H, t, J = 7.5 Hz), 7.04 (2 H, ddd, J =

1867.8, 8.5, 0.9 Hz), 4.52 (1 H, p, J= 5.7, 5.1, 0.0 Hz), 4.33 (4 H, d, J = 5.2 Hz). δ_C (126 MHz, Chloroform-d) 189.58, 160.15, 135.98, 130.12, 125.01, 121.43, 112.96, 69.26, 68.26. ATR-IR (cm^{-1}) 1676 (C=O), 3456 (O-H)

7.2.2 $\mathbf{Co_2L^{Me}OAc}$

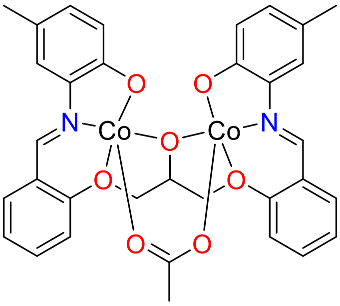

BFPP (300 mg, 1 mmol) and cobalt (II) acetate tetrahydrate (498 mg, 2 mmol) were refluxed in methanol (30 mL) for 20 minutes, forming a purple solution. 2-amino-4-methylphenol (246 mg, 2 mmol) in methanol (5 mL) was added dropwise and the solution immediately turned deep orange-brown. The mixture was refluxed for a further two hours before being concentrated to ca. 10 mL. Diethyl ether (20 mL) was added dropwise with rapid stirring and a brown solid precipitated. The suspension was filtered and the collected solid was washed with diethyl ether (20 mL), dried, then washed with water (3×10 mL) and dried in air, then under vacuum overnight to obtain $\mathbf{Co_2L^{Me}OAc}$ as a yellowish brown solid (514 mg, 71%) *m/z* ESI$^+$: 625.1 [M – OAc]$^+$ requires 625. Elemental analysis found: C, 55.37; H, 4.77; N, 3.83 $C_{33}H_{30}Co_2N_2O_7 \cdot 2H_2O$ requires C, 55.01; H, 4.76; N, 3.39. ATR-IR (cm^{-1}): 1598 (C=N), 1575 (C-O, acetate bridging).

7.2.3 $Co_2L^{CF3}OAc$

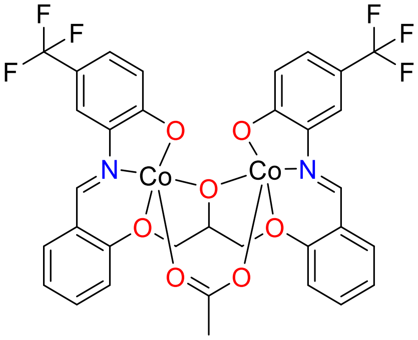

Using the same method as **$Co_2L^{Me}OAc$** except using 2-amino-4-trifluoromethylphenol (2 mmol, 354 mg) the title compound was obtained as an orange-brown solid. (460 mg, 0.58 mmol 58%) Elemental analysis found: C, 48.73; H, 3.41; N, 3.92 $C_{33}H_{24}Co_2N_2O_7{\cdot}H_2O$ requires C, 48.91; H, 3.23; N, 3.46 *m/z* ESI$^+$: 733.21 $[M – OAc]^+$ requires 733.1. ATR-IR (cm^{-1}): 1600 (C=N), 1573 (C-O, acetate bridging).

7.2.4 $Co_2L^{tBu}OAc$

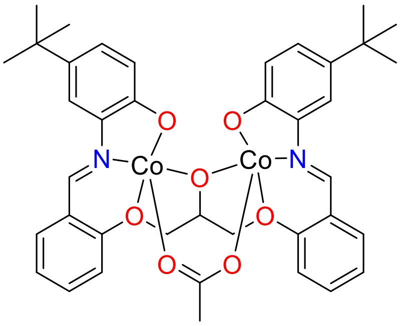

Using the same method as **$Co_2L^{Me}OAc$** except using 2-amino-4-*tert*-butylphenol (2 mmol, 218 mg) the title compound was obtained as a yellow-brown solid. *m/z* ESI$^+$: 709.16 $[M – OAc]^+$ requires 709.15. Elemental analysis showed significant impurity, attempts to further purify the complex failed. ATR-IR (cm^{-1}): 1598 (C=N), 1572 (C-O, acetate bridging).

7.2.5 $\mathbf{Co_2L^{H}OAc}$

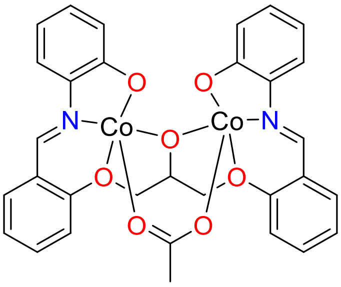

Using the same method as $\mathbf{Co_2L^{Me}OAc}$ except using 2-aminophenol (2 mmol, 330 mg) the title compound was obtained as a yellow-brown solid. *m/z* ESI$^+$: 597.14 [M – OAc]$^+$ requires 597.1. Elemental analysis showed significant impurity, attempts to further purify the complex failed. ATR-IR (cm^{-1}): 1600 (C=N), 1575 (C-O, acetate bridging).

7.2.6 $\mathbf{Co_2L^{tAm}OAc}$

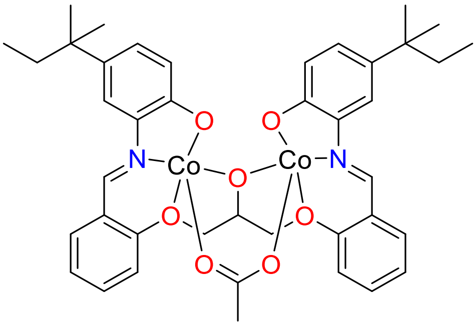

Using the same method as $\mathbf{Co_2L^{Me}OAc}$ except using 2-amino-4-*tert*-amylphenol (2 mmol, 358 mg) the title compound was obtained as a yellow-brown solid. *m/z* ESI$^+$: 737.20 [M – OAc]$^+$ requires 737.27. Elemental analysis showed significant impurity, attempts to further purify the complex failed. ATR-IR (cm^{-1}): 1598 (C=N), 1573 (C-O, acetate bridging).

7.2.7 Co_2L^FOAc

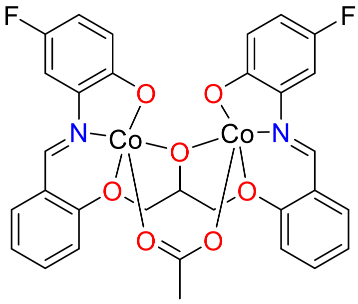

Using the same method as **$Co_2L^{Me}OAc$** except using 2-amino-4-fluorophenol (2 mmol, 254 mg) the title compound was obtained as a yellow-brown solid. *m/z* ESI$^+$: 633.01 [M – OAc]$^+$ requires 633.01. Elemental analysis showed significant impurity, attempts to further purify the complex failed. ATR-IR (cm^{-1}): 1600 (C=N), 1572 (C-O, acetate bridging).

7.2.8 $Co_3L^{Me}(OAc)_3$

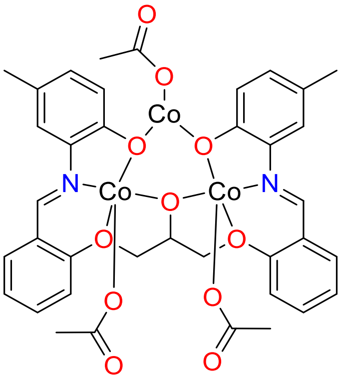

BFPP (301 mg, 1 mmol) and cobalt (II) acetate tetrahydrate (747 mg, 3 mmol) were stirred in ethanol (25 mL) at room temperature for 30 minutes forming a purple suspension. 2-amino-4-methylphenol (246 mg, 2 mmol) was added to the suspension, resulting in an immediate colour change to dark brown. Over the next 5 minutes of stirring, the suspension became homogeneous, and after an hour a brown precipitate begans to form. The mixture was stirred for a total of four hours before filtering. The collected solid was washed with cold ethanol (2×10 mL) then diethyl ether (20 mL) and dried in air to give **$Co_3L^{Me}OAc_3$** as a brown solid (682 mg 0.79 mmol, 79%) X-Ray quality crystals were obtained from slow evaporation of a concentrated MeOH solution of the product. MALDI-TOF-MS: 801 [M – OAc$^-$]$^+$ Elemental analysis found:

C, 51.98; H, 4.23; N, 3.25 $C_{33}H_{30}Co_2N_2O_7 \cdot 2H_2O$ requires C, 51.59; H, 4.21 N, 3.25 ATR-IR (cm^{-1}): 1598 (C=N), 1578, 1556 (C-O, acetate monodentate and bridging).

7.2.9 $Zn_3L^{Me}(OAc)_3$

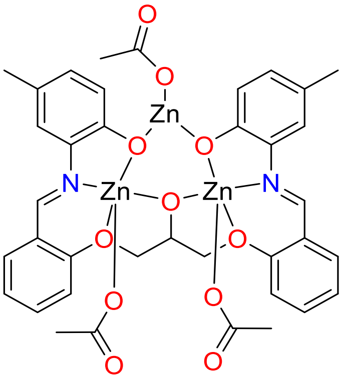

To a solution of zinc (II) acetate dihydrate (367 mg, 2 mmol) and BFPP (300 mg, 1 mmol) in MeOH (25 mL) was added 2-amino-4-methylphenol (246 mg, 2 mmol). The solution immediately turned vivid yellow. The solution was stirred at room temperature for two hours, over which time a yellow solid had precipitated. The mixture was filtered and the collected solid was washed with cold MeOH (2 × 10 mL) then diethyl ether (2 × 10 mL) and dried in air to obtain the complex as a bright yellow solid. (620 mg, 0.70 mmol, 70%) Single crystals suitable for X-Ray diffractometry were obtained by vapour diffusion of diethyl ether into a concentrated DMF solution of the complex. Elemental analysis found: C 48.87; H, 4.41; N, 3.30 $C_{37}H_{36}N_2O_{11}Zn_3 \cdot 2H_2O$ requires: C, 48.47; H, 4.40; N, 3.06. *m/z* (MALDI-TOF) 821 $[M - OAc^-]^+$ requires 821.7. ATR-IR (cm^{-1}): 1600 (C=N), 1585, 1575 (C-O, acetate).

7.2.10 $Co_4L^{Me}(BF_4)_2$

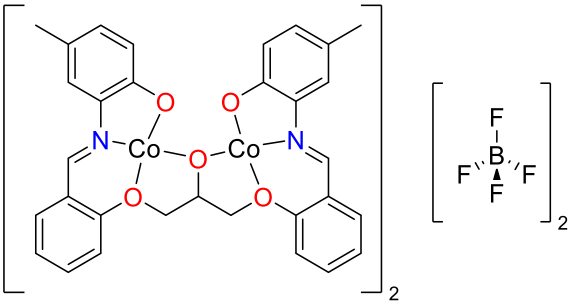

To a refluxing methanol (25 mL) solution of BFFP (301 mg, 1 mmol) and cobalt acetate tetrahydrate (498 mg, 2 mmol) was added a solution of 2-amino-4-

methylphenol (246 mg, 2 mmol) in methanol (10 mL). After refluxing for two hours, a solution of $NaBF_4$ (1 mmol) in methanol (20 mL) was added dropwise without stirring. After a couple of hours dark-brown cubic crystals began to form. The crystals were filtered from the supernatant and washed with MeOH (2 × 10 mL) then water (2×10 mL) and dried in air overnight. (1.20 g, 0.84 mmol, 84%) Elemental analysis found: C, 48.64; H, 4.28; N, 3.67. $C_{64}H_{54}B_2Co_4F_8N_4O_{16}\cdot 6H_2O$ requires C, 48.59; H, 4.34; N; 3.66. ATR-IR (cm^{-1}): 1600 (C=N), 3614 (O-H coordinated MeOH).

7.3 Mononuclear Salen Complexes Bearing Pendant Bases

7.3.1 Cis,cis-3,5-ditosyloxycyclohexanol (3-1)

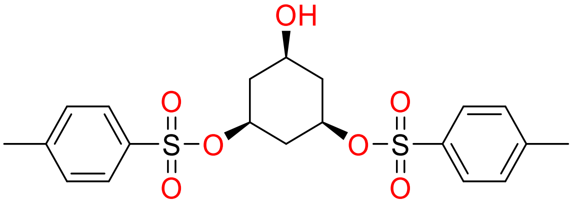

Cis,cis-1,3,5-cyclohexanetriol monohydrate was dried at 60°C under high vacuum overnight, or until the mass of one water equivalent had been removed. Under a nitrogen atmosphere, the cyclohexanetriol (10 g, 75 mmol)was dissolved in pyridine (175 mL) and was cooled to 0°C. Freshly purified and dried tosyl chloride (29.3g, 157 mmol) was also dissolved in pyridine (50 mL) under a nitrogen atmosphere and cooled to 0°C during this time the solution turns yellow due to activation of the tosyl chloride by pyridine. The latter solution was added to the former dropwise by cannula transfer, and the solution was left stirring at 0°C for 6 hours then was allowed to warm slowly to room temperature overnight, during which time a white precipitate appears. The solution was filtered and washed with ethyl acetate before washing with HCl (20 mL), water (20 mL), sat. $NaHCO_3$ (20 mL), then brine. The organic phase was dried over anhydrous $MgSO_4$ and concentrated *in vacuo*. The remaining white tar like residue was then co-evaporated with toluene several times. The residue was then triturated with hexane resulting in a white powder. The powder was purified by column chromatography through silica gel (1:1 EtOAc : Hexane) to yield the name ditosylate (18.8g, 42 mmol, 57%) δ_H (400 MHz, Chloroform-*d*) 7.75 (4 H, d, J = 11.5 Hz), 7.35 (4 H, d, J = 7.7 Hz), 4.35 (2 H, tt, J = 11.3, 4.4 Hz), 3.55 (1 H, tt, J = 11.1, 4.1 Hz), 2.46 (6 H, s), 2.26 – 2.15 (3 H, m), 1.63 (1 H, q, J = 11.6 Hz), 1.44 (1 H, q, J = 11.5, 11.5, 11.0 Hz). δ C (101 MHz, $CDCl_3$) δ 145.13, 133.85, 130.01, 127.62, 77.34, 77.02, 76.70, 74.10, 65.03, 40.34, 37.71, 21.70.

7.3.2 *Cis,trans*-diazidocyclohexanol (3-2)

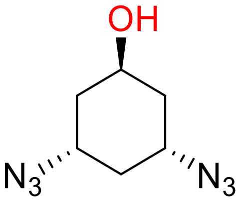

Compound **3-1** (11.9 g, 27.2 mmol) was dissolved in DMF under nitrogen atmosphere. Sodium azide (17.7 g, 272 mmol) was then added to the solution and the mixture was heated to 80°C overnight. After cooling, the solids were removed by filtration and the filtrate was diluted with EtOAc (40 mL) then washed with water (20 mL) then brine (10 mL). The aqueous phase was then back extracted with EtOAc (40 mL). The organic phases were combined and dried over anhydrous $MgSO_4$ then concentrated *in vacuo* before co-evaporation with toluene. The resulting yellow oil was found to be sufficient for the next step without further purification. N.B., the oil contained a large amount of remaining DMF which was not removed due to the high azide number of the compound. δ H (500 MHz, Chloroform-*d*) 4.35 – 4.29 (1 H, m), 3.81 – 3.73 (2 H, m), 2.30 (1 H, dtt, J = 12.4, 4.2, 2.1 Hz), 2.07 (2 H, dtt, J = 13.8, 3.8, 1.9 Hz), 1.42 (2 H, ddt, J = 13.1, 11.8, 2.6 Hz), 1.34 (1 H, qd, J = 11.8, 2.2 Hz) δ C (126 MHz, $CDCl_3$) δ 66.44, 54.50, 37.34, 36.92.

7.3.3 2-[(3,5-diazidocyclohexyloxy)methyl]pyridine (3-3)

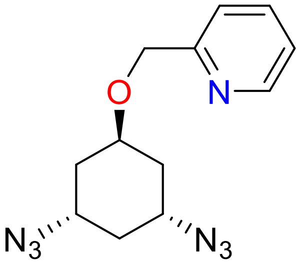

To a flame dried Schlenk flask was added compound **3-2** (470 mg, 2.57 mmol), dry DMF (20 mL) and a few crystals of tetrabutylammonium iodide under N_2. Sodium hydride (40% dispersion in mineral oil) (411 mg, 10.2 mmol) was added in a single portion. Gas evolution is observed immediately, and the suspension was stirred for 20 minutes. During this time, 2-bromomethylpyridine hydrobromide (1.30 g, 5.14 mmol) was dissolved in water (5 mL) and a saturated solution of sodium bicarbonate was added until a pH of 10 was reached. The solution was extracted exhaustively with dichloromethane before drying over $MgSO_4$. After filtering, the solvent was removed *in vacuo* and the remaining pink oil was added directly to the deprotonated solution. N.B it is important to carry out this freebasing step quickly due to the instability of the neutralised reagent. The reaction was stirred for 2 h at room temperature before slow addition of methanol (3 mL) to stop the reaction. The mixture was taken up in ethyl acetate (80 mL) and was washed with water (3×50 mL). The aqueous phase was back extracted with ethyl acetate (2×50 mL) then the combined organic phases were dried over $MgSO_4$ and concentrated *in vacuo*. The resulting oil was purified by column chromatography over silica gel (1:1 EtOAc : Hexane) to isolate the diazide as a yellow oil (463 mg, 64%) δ_H ($CDCl_3$, 400MHz): δ = 8.56 (d, J =4.3 Hz, 4 H), 7.69 - 7.69 (m, 1 H), 7.72 (td, J = 7.7, 1.8 Hz, 4 H), 7.41 (d, J = 7.8 Hz, 1 H), 7.22 (ddd, J = 7.5, 4.9, 0.6 Hz, 1 H), 4.63 (s, 2 H), 4.03 (quin, J = 3.0 Hz, 1 H), 3.69 - 3.80 (m, 3 H), 2.27 - 2.39 ppm (m, 3 H). m/z (ESI^+): calcd. for $C_{12}H_{15}N_7O$: 274.1416, found: 274.1418 $[M]^+$. FTIR (ATR) cm^{-1}: 2932 (w) (C_{aryl}-H), 2084 (s) (N_3), 1590 (w), 1435 (w), 1244 (m)

7.3.4 2-[(3,5-diaminocyclohexyloxy)methyl]pyridine (3-4)

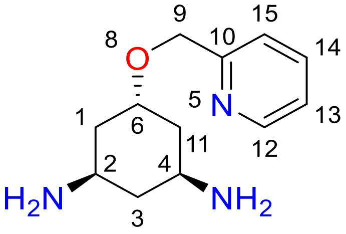

To a Parr hydrogenation vessel equipped with a stirrer bar, a solution of compound **3-3** (150 mg) in ethanol (10 mL) was mixed with 10% Pd/C (13 mg). The vessel was sealed and pressurised with H_2 to 6 bar and vented three times before pressurising to a static pressure of 6 bar. The suspension was stirred at room temperature for 18 h after which the pressure was released and the suspension was filtered through a plug of celite before removing the solvent *in vacuo* yielding the product as a colourless oil (119 mg, 98%). ^1H NMR (CD_3OD ,500MHz): δ = 8.47 - 8.49 (m, 2 H, 12), 7.86 (td, J = 7.7, 1.8 Hz, 2 H, 13), 7.56 (d, J = 7.8 Hz, 1 H, 15), 7.32 - 7.35 (m, 1 H, 13), 4.62 (s, 2 H, 9), 3.94 (quin, J = 3.0 Hz, 1 H 6 axial), 3.07 (tt, J = 11.7, 3.8 Hz, 2 H, 2, 4 equatorial), 2.17 - 2.23 (m, 2 H, 1, 5 equatorial), 2.09 (ddt, J = 9.9, 5.8, 1.9 Hz, 1 H, 11 equatorial), 1.16 - 1.23 (m, 2 H, 1, 5 axial), 1.00 ppm (q, J = 11.8 Hz, 1 H, 3 axial) m/z (ESI$^+$): calcd. for $C_{12}H_{19}N_3O$: 221.15, found: 222.16 $[M + H]^+$ ATR-IR (cm^{-1}): 1619 (N-H).

7.3.5 Salcn-Py Ligand

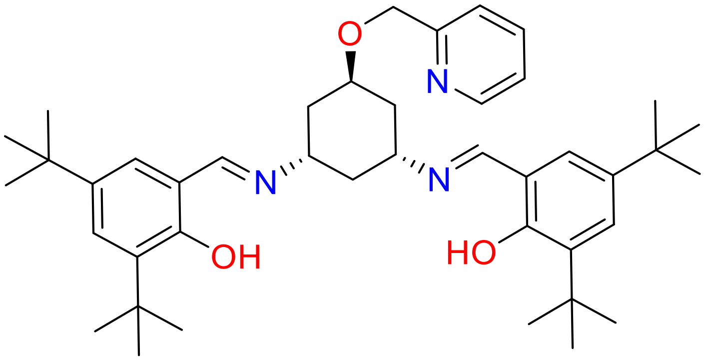

Compound **3-4** (60 mg, 0.27 mmol) and 3,5-di-*t*-butylsalicylaldehyde (150 mg, 00 mmol) were dissolved in methanol (10 mL) and refluxed for 18 h. The reaction mixture was cooled before the yellow precipitate was filtered and washed with cold methanol. The dried **Salcn-Py** was collected as pastel yellow solid (100 mg, 0.15 mmol 55%) ^{1}H NMR ($CDCl_3$, 500 MHz): δ = 13.74 (s, 1 H), 8.59 (br. d, J = 4.6 Hz, 1 H), 8.44 (s, 2 H), 7.76 (td, J = 7.7, 1.6 Hz, 1 H), 7.53 (d, J = 8.0 Hz, 1 H), 7.38 (d, J = 2.2 Hz, 2 H), 7.21 - 7.26 (m, 1 H), 7.09 (d, J = 2.4 Hz, 2 H), 4.71 (s, 2 H), 4.08 - 4.13 (m, 1 H), 3.75 - 3.85 (m, 2 H), 2.26 (d, J = 13.2 Hz, 2 H), 2.10 (d, J = 13.2 Hz, 1 H), 1.98 (q, J = 12.2 Hz, 1 H), 1.76 (t, J = 12.7 Hz, 2 H), 1.42 - 1.49 (m, 18 H), 1.31 ppm (s, 14 H) Elemental analysis found: C, 77.03; H, 8.71; N, 6.41. $C_{49}H_{52}N_3O_3$ requires: C, 77.14; H, 9.09; N, 6.43.). m/z (ESI$^+$): calcd. for $C_{49}H_{52}N_3O_3$: 653.46; found: 654.4627 $[M + H]^+$ ATR-IR (cm^{-1}): 1627 (C=N).

7.3.6 CoSalcn-Py

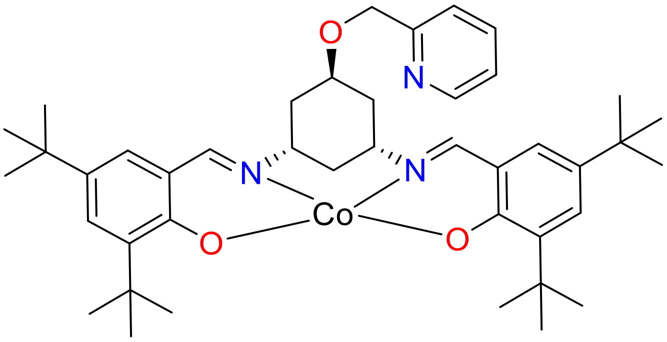

Salcn-Py (50 mg, 0.076 mmol) was dissolved in DCM (2 mL) in a 10 mL vial. To this was added a solution of cobalt(II) acetate dihydrate (18.9 mg, 0.076 mmol) in MeOH (2 mL). The vial was capped, and the solution was stirred for two hours, over which time a colour change to orange-brown was observed. After the two hours, the vial was opened slightly to allow for slow evaporation of the DCM solvent overnight. After this time, an orange-brown microcrystalline material had deposited from solution and the mixture was filtered and washed with additional methanol (2 × 5 mL) to obtain the complex as an orange-brown microcrystalline powder. (43 mg, 61 mmol, 80%) ESI-MS: 711.379 $[M + H]^+$ Elemental analysis found: C, 70.56; H, 7.61; 5.94 $C_{49}H_{50}N_3O_3Co$ requires: C, 70.96; H, 8.08; N, 5.91; ATR-IR (cm^{-1}): 1587 (C=N).

7.3.7 CuSalcn-Py

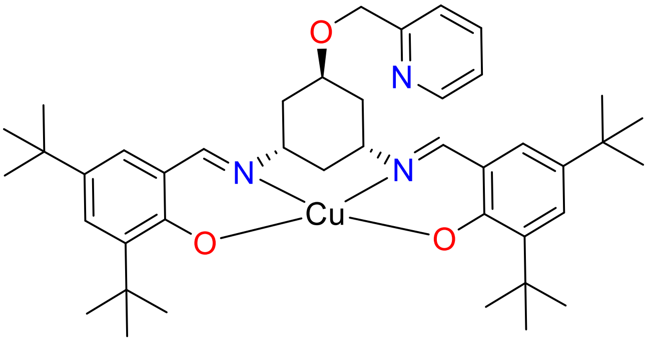

Following the same procedure shown in **7.3.6**, except with copper(II) acetate monohydrate (15.1 mg, 0.076 mmol) and the complex was obtained as dark green needles suitable for X-Ray diffractometry studies (51 mg, 0.072 mmol 94%). Elemental analysis found: C, 70.29; H, 7.95; N 6.20. $C_{42}H_{57}CuN_3O_3$ requires: C, 70.51; H, 8.03; N, 5.87.

7.4 Catalysis Methods

7.4.1 Determination of catalytic rate law

To establish a catalytic rate equation, the initial rate of ORR was measured under variable concentrations of catalyst, decamethylferrocene, AcOH/TBAOAc and O_2:

Rate dependence on [$Co_2L^{Me}OAc$]

A 0.3 mL air saturated methanolic solution of **$Co_2L^{Me}OAc$** (50, 100, 200, 300 and 400 µM) was added to a quartz UV cuvette along with a 1.7 mL air saturated methanolic solution of Fc* (1.76 mM). A 1 mL air saturated methanolic solution containing 60 mM each AcOH and TBAOAc was rapidly injected into the cuvette before capping and vigorously shaking for 10 seconds. A UV/Vis trace was then immediately recorded in the range of 900-300 nm and then every 15 seconds thereafter. The ORR was monitored by the growth of the absorbance at 780 nm. Each run was repeated in triplicate to enable estimation of errors. (Initial concentrations in reaction mixture: 1 mM Fc*, 20 mM AcOH/TBAOAc, 2 mM O_2 and 5, 10, 20, 30 or 40 µM **$Co_2L^{Me}OAc$**)

Rate dependence on [AcOH/TBAOAc]

A 0.3 mL air saturated methanolic solution of **$Co_2L^{Me}OAc$** (200 µM) was added to a quartz UV cuvette along with a 1.7 mL air saturated methanolic solution of Fc* (1.76 mM). Additional air saturated methanol (0.8, 0.6, 0.4 or 0.2 mL) was added along with 0.2, 0.4, 0.6 or 0.8 mL air saturated methanolic solution containing 30 mM each AcOH and tetrabutylammonium acetate (TBAOAc) to give final concentrations of 2, 4, 6 or 8 mM respectively before capping and vigorously shaking for 10 seconds. A UV/Vis trace was then immediately recorded in the range of 900-300 nm and then every 15 seconds thereafter. The ORR was monitored by the growth of the absorbance at 780 nm. Each run was repeated in triplicate to enable estimation of errors. (Initial concentrations in reaction mixture: 1 mM Fc*, 2, 4, 6 or 8 mM AcOH/TBAOAc, 2 mM O2 and 20 µM **$Co_2L^{Me}OAc$**)

Rate dependence on [AcOH] (unbuffered)

A 0.3 mL air saturated methanolic solution of **$Co_2L^{Me}OAc$** (200 µM) was added to a quartz UV cuvette along with a 1.7 mL air saturated methanolic solution of Fc* (1.76 mM). Additional air saturated methanol (1, 0.75, 0.5, 0.25 mL) was added along with 0, 0.25, 0.5 or 0.75 mL air saturated methanolic solution containing 60 mM AcOH to give final concentrations of 2, 4, 6 or 8 mM respectively before capping and vigorously shaking for 10 seconds. A UV/Vis trace was then immediately recorded in the range of 900-300 nm and then every 15 seconds thereafter. The ORR was monitored by the growth of the absorbance at 780 nm. Each run was repeated in triplicate to enable estimation of errors. (Initial concentrations in reaction mixture: 1 mM Fc*, 5, 10, 15 or 20 mM AcOH, 2 mM O_2 and 20 µM **$Co_2L^{Me}OAc$**)

Rate dependence on [Fc*]

A 0.3 mL air saturated methanolic solution of **$Co_2L^{Me}OAc$** (50 µM) was added to a quartz UV cuvette along with a 0.34, 0.68, 1.02, 1.36 or 1.7 mL air saturated methanolic solution of Fc* (0.88 mM).

Additional air saturated methanol 1.36, 1.02, 0.68 or 0.34 mL was added to obtain final Fc* concentrations of 0.1, 0.2, 0.3, 0.4 and 0.5 mM respectively. A 1 mL air saturated methanolic solution containing 30 mM each AcOH and TBAOAc was rapidly injected into the cuvette before capping and vigorously shaking for 10 seconds. A UV/Vis trace was then immediately recorded in the range of 900-300 nm and then every 15 seconds thereafter. The ORR was monitored by the growth of the absorbance at 780 nm. Each run was repeated in triplicate to enable estimation of errors. (Initial concentrations in reaction mixture: 0.1, 0.2, 0.3, 0.4 or 0.5 mM Fc*, 10 mM AcOH/TBAOAc, 2 mM O_2 and 5 µM **$Co_2L^{Me}OAc$**)

Rate dependence on [O_2]

9 mM: A 0.3 mL air saturated methanolic solution of **$Co_2L^{Me}OAc$** (300 µM) was added to a quartz UV cuvette along with a 1.7 mL O2 saturated methanolic solution of Fc* (1.76 mM). A 1 mL O_2 saturated methanolic solution containing 60 mM each AcOH and TBAOAc was rapidly injected into the cuvette before capping and vigorously shaking for 10 seconds. A UV/Vis trace was then immediately recorded in the range of 900-300 nm and then every 15 seconds thereafter. The ORR was monitored by the growth of the absorbance at 780 nm. Each run was repeated in triplicate to enable estimation of errors. (Initial concentrations in reaction mixture: 1 mM Fc*, 20 mM AcOH/TBAOAc, 9 mM O_2 and 30 µM **Co2LMeOAc**)

6.5 mM: A 0.3 mL air saturated methanolic solution of **$Co_2L^{Me}OAc$** 300 µM) was added to a quartz UV cuvette along with a 1.7 mL O_2 saturated methanolic solution of

Fc* (1.76 mM). A 1 mL air saturated methanolic solution containing 60 mM each AcOH and TBAOAc was rapidly injected into the cuvette before capping and vigorously shaking for 10 seconds. A UV/Vis trace was then immediately recorded in the range of 900-300 nm and then every 15 seconds thereafter. The ORR was monitored by the growth of the absorbance at 780 nm. Each run was repeated in triplicate to enable estimation of errors. (Initial concentrations in reaction mixture: 1 mM Fc*, 20 mM AcOH/TBAOAc, 6.5 mM O2 and 30 µM **$Co_2L^{Me}OAc$**)

4 mM: A 0.3 mL air saturated methanolic solution of **$Co_2L^{Me}OAc$** 300 µM) was added to a quartz UV cuvette along with a 1.7 mL air saturated methanolic solution of Fc* (1.76 mM). A 1 mL O_2 saturated methanolic solution containing 60 mM each AcOH and TBAOAc was rapidly injected into the cuvette before capping and vigorously shaking for 10 seconds. A UV/Vis trace was then immediately recorded in the range of 900-300 nm and then every 15 seconds thereafter. The ORR was monitored by the growth of the absorbance at 780 nm. Each run was repeated in triplicate to enable estimation of errors. (Initial concentrations in reaction mixture: 1 mM Fc*, 20 mM AcOH/TBAOAc, 4 mM O_2 and 30 µM **$Co_2L^{Me}OAc$**)

2 mM: A 0.3 mL air saturated methanolic solution of **$Co_2L^{Me}OAc$** 300 µM) was added to a quartz UV cuvette along with a 1.7 mL air saturated methanolic solution of Fc* (1.76 mM). A 1 mL air saturated methanolic solution containing 60 mM each of AcOH and TBAOAc was rapidly injected into the cuvette before capping and vigorously shaking for 10 seconds. A UV/Vis trace was then immediately recorded in the range of 900-300 nm and then every 15 seconds thereafter. The ORR was monitored by the growth of the absorbance at 780 nm. Each run was repeated in triplicate to enable estimation of errors. (Initial concentrations in reaction mixture: 1 mM Fc*, 20 mM AcOH/TBAOAc, 2 mM O_2 and 30 µM **$Co_2L^{Me}OAc$**)

Chapter 8

References

1 J. Hansen, R. Ruedy, M. Sato and K. Lo, *Rev. Geophys.*, 2010, **48**, 4004.

2 N. Höhne, M. J. Gidden, M. den Elzen, F. Hans, C. Fyson, A. Geiges, M. L. Jeffery, S. Gonzales-Zuñiga, S. Mooldijk, W. Hare and J. Rogelj, *Nat. Clim. Chang. 2021 1110*, 2021, **11**, 820–822.

3 N. J. L. Lenssen, G. A. Schmidt, J. E. Hansen, M. J. Menne, A. Persin, R. Ruedy and D. Zyss, *J. Geophys. Res. Atmos.*, 2019, **124**, 6307–6326.

4 The Paris Agreement | UNFCCC, https://unfccc.int/process-and-meetings/the-paris-agreement/the-paris-agreement, (accessed 26 August 2022).

5 *Nationally determined contributions under the Paris Agreement Synthesis report by the secretariat* Summary*, .

6 Statistical Review of World Energy | Energy economics | Home, https://www.bp.com/en/global/corporate/energy-economics/statistical-review-of-world-energy.html, (accessed 26 August 2022).

7 Solar PV module prices, https://ourworldindata.org/grapher/solar-pv-prices, (accessed 26 August 2022).

8 E. Vartiainen, C. Breyer, D. Moser, E. Román Medina, C. Busto, G. Masson, E. Bosch and A. Jäger-Waldau, *Sol. RRL*, 2022, **6**, 2100487.

9 Irena, *Geopolitics of the Energy Transformation: The Hydrogen Factor*, 2022.

10 K. M. Camp, D. Mead, S. B. Reed, C. Sitter and D. Wasilewski, *Mon. Labor Rev.*, 2020, **2020**, 1–14.

11 The impact of Coronavirus (COVID-19) and the global oil price shock on the fiscal position of oil-exporting developing countries - OECD, https://read.oecd-ilibrary.org/view/?ref=136_136801-aw9nps8afk&title=The-impact-of-Coronavirus-COVID-19-and-the-global-oil-price-shock-on-the-fiscal-position-of-oil-exporting-developing-countries, (accessed 26 August 2022).

12 The Potential Impact on the UK of a Disruption in Russian Gas Supplies to Europe - Oxford Institute for Energy Studies, https://www.oxfordenergy.org/publications/the-potential-impact-on-the-uk-of-

a-disruption-in-russian-gas-supplies-to-europe/, (accessed 26 August 2022).

13 REPowerEU, https://ec.europa.eu/commission/presscorner/detail/en/IP_22_3131, (accessed 26 August 2022).

14 Net Zero Hydrogen Fund strand 1 and strand 2 - GOV.UK, https://www.gov.uk/government/publications/net-zero-hydrogen-fund-strand-1-and-strand-2, (accessed 26 August 2022).

15 J.-P. Rodrigue, *Geogr. Transp. Syst.*, , DOI:10.4324/9780429346323.

16 C. Ronneau, *Énergie, pollution de l'air et développement durable*, Presses universitaires de Louvain, Louvain-la-Neuve, 2004.

17 Hydrogen Storage | Department of Energy, https://www.energy.gov/eere/fuelcells/hydrogen-storage, (accessed 27 August 2022).

18 Hydrogen Storage | Department of Energy, https://www.energy.gov/eere/fuelcells/hydrogen-storage, (accessed 20 September 2022).

19 Hydrogen timeline | Worcester Bosch, https://www.worcester-bosch.co.uk/hydrogen-timeline, (accessed 26 August 2022).

20 X. Yu and S. Ye, *J. Power Sources*, 2007, **172**, 133–144.

21 M. Lopez-Haro, L. Guétaz, T. Printemps, A. Morin, S. Escribano, P. H. Jouneau, P. Bayle-Guillemaud, F. Chandezon and G. Gebel, *Nat. Commun. 2014 51*, 2014, **5**, 1–6.

22 S. Banerjee and D. E. Curtin, *J. Fluor. Chem.*, 2004, **125**, 1211–1216.

23 M. B. Karimi, F. Mohammadi and K. Hooshyari, *Int. J. Hydrogen Energy*, 2019, **44**, 28919–28938.

24 C. Song and J. Zhang, *PEM Fuel Cell Electrocatal. Catal. Layers Fundam. Appl.*, 2008, 89–134.

25 Y. Nie, L. Li and Z. Wei, *Chem. Soc. Rev.*, 2015, **44**, 2168–2201.

26 A. Züttel, *Naturwissenschaften*, 2004, **91**, 157–172.

27 B. Bogdanović, R. A. Brand, A. Marjanović, M. Schwickardi and J. Tölle, *J Alloy. Compd.*, 2000, **302**, 36.

28 Y. Sun, M. Delucchi and J. Ogden, *Int. J. Hydrogen Energy*, 2011, **36**, 11116–11127.

29 C. He, S. Desai, G. Brown and S. Bollepalli, *Electrochem. Soc. Interface*, 2005, **14**, 41–44.

30 C. Sealy, *Mater. Today*, 2008, **11**, 65–68.

31 M. S. Thorum, J. M. Hankett and A. A. Gewirth, *J. Phys. Chem. Lett.*, 2011, **2**, 295–298.

32 Q. Li, R. He, J.-A. Gao, J. O. Jensen and N. J. Bjerrum, *J. Electrochem. Soc.*, 2003, **150**, A1599.

33 E. B. Maxted, *Adv. Catal.*, 1951, **3**, 129–178.

34 *High-temperature Solid Oxide Fuel Cells: Fundamentals, Design and Applications - Google Books*, .

35 S. C. Singhal, *Solid State Ionics*, 2000, **135**, 305–313.

36 O. Yamamoto, *Electrochim. Acta*, 2000, **45**, 2423–2435.

37 D. R. Nhuchhen, S. P. Sit and D. B. Layzell, *Appl. Energy*, 2022, **306**, 118001.

38 M. Bischoff, *J. Power Sources*, 2006, **160**, 842–845.

39 A. Kulkarni and S. Giddey, *J. Solid State Electrochem. 2012 1610*, 2012, **16**, 3123–3146.

40 A. L. Dicks, *Curr. Opin. Solid State Mater. Sci.*, 2004, **8**, 379–383.

41 N. Sammes, R. Bove and K. Stahl, *Curr. Opin. Solid State Mater. Sci.*, 2004, **8**, 372–378.

42 P. Stonehart, *J. Appl. Electrochem. 1992 2211*, 1992, **22**, 995–1001.

43 A. S. Aricò, A. Stassi, E. Modica, R. Ornelas, I. Gatto, E. Passalacqua and V.

Antonucci, *J. Power Sources*, 2008, **178**, 525–536.

44 T. J. Schmidt, *ECS Trans.*, 2006, **1**, 19–31.

45 B. Niu, S. Luo, C. Lu, W. Yi, J. Liang, S. Guo, D. Wang, F. Zeng, S. Duan, Y. Liu, L. Zhang and B. Xu, *Solid State Ionics*, 2021, **361**, 115569.

46 HyPoint - we make zero emission air transport possible, https://hypoint.com/, (accessed 27 August 2022).

47 C. Costentin, S. Drouet, M. Robert and J. M. Savéant, *J. Am. Chem. Soc.*, 2012, **134**, 11235–11242.

48 A. M. Appel and M. L. Helm, *ACS Catal.*, 2014, **4**, 630–633.

49 J. K. Nørskov, J. Rossmeisl, A. Logadottir, L. Lindqvist, J. R. Kitchin, T. Bligaard and H. Jónsson, *J. Phys. Chem. B*, 2004, **108**, 17886–17892.

50 R. R. Knowles, *ACS Cent. Sci.*, 2015, **1**, 224.

51 S. Anantharaj, P. E. Karthik and S. Noda, *Angew. Chemie Int. Ed.*, 2021, **60**, 23051–23067.

52 C. Costentin, G. Passard and J. M. Savéant, *J. Am. Chem. Soc.*, 2015, **137**, 5461–5467.

53 T. A. Betley, Y. Surendranath, M. V. Childress, G. E. Alliger, R. Fu, C. C. Cummins and D. G. Nocera, *Philos. Trans. R. Soc. B Biol. Sci.*, 2007, **363**, 1293–1303.

54 J. P. Collman, Y. L. Yan, T. Eberspacher, X. Xie and E. I. Solomon, *Inorg. Chem.*, 2005, **44**, 9628–9630.

55 G. ScMfer, A. Weiss, E. I. Stiefel, W. E. Newton, G. D. Watt, K. L. Hadfield, W. A. Bulen, J. P. Collman, J. I. Brauman, K. M. Doxsee, T. R. Halbert, S. E. Hayes and K. S. Suslick, *34) R. Eisenberg, Prog. Horg. Chem*, 1976, **15**, 353.

56 J. P. Collman, J. I. Brauman and K. S. Suslick, *J. Am. Chem. Soc.*, 1975, **97**, 7185–7186.

57 A. Dedieu and M. M. Rohmer, *J. Am. Chem. Soc.*, 1977, **99**, 8050–8051.

58 A. A. A. Emara, A. M. Ali, A. F. El-Asmy and E. S. M. Ragab, *J. Saudi*

Chem. Soc., 2014, **18**, 762–773.

59 A. Bhagi-Damodaran, M. A. Michael, Q. Zhu, J. Reed, B. A. Sandoval, E. N. Mirts, S. Chakraborty, P. Moënne-Loccoz, Y. Zhang and Y. Lu, *Nat. Chem. 2016 93*, 2016, **9**, 257–263.

60 K. D. Karlin, R. W. Cruse, Y. Gultneh, A. Farooq, J. C. Hayes and J. Zubieta, *J. Am. Chem. Soc.*, 1987, **109**, 2668–2679.

61 E. I. Solomon, J. W. Ginsbach, D. E. Heppner, M. T. Kieber-Emmons, C. H. Kjaergaard, P. J. Smeets, L. Tian and J. S. Woertink, *Faraday Discuss.*, 2011, **148**, 11.

62 R. Boča, *J. Mol. Struct.*, 1980, **65**, 173–183.

63 P. L. Holland, *Dalt. Trans.*, 2010, **39**, 5415–5425.

64 M. F. Perutz, *Proc. R. Soc. London. Ser. B. Biol. Sci.*, 1980, **208**, 135–162.

65 Acad Sci and B. D. K, *Proc. R. Soc. London. Ser. B - Biol. Sci.*, 1939, **127**, 167–191.

66 M. Saraste, *Q. Rev. Biophys.*, 1990, **23**, 331–366.

67 R. C. Zangar, D. R. Davydov and S. Verma, *Toxicol. Appl. Pharmacol.*, 2004, 199, 316–331.

68 X. Y. Zhou, C. Xu, P. P. Guo, W. L. Sun, P. J. Wei and J. G. Liu, *Chemistry*, 2021, **27**, 9898–9904.

69 S. Samanta, P. K. Das, S. Chatterjee and A. Dey, *https://doi.org/10.1142/S1088424615300049*, 2015, **19**, 92–108.

70 J. P. Collman, J. I. Brauman, E. Rose and K. S. Suslick, *Proc. Natl. Acad. Sci. U. S. A.*, 1978, **75**, 1052.

71 H. W. Kim, V. J. Bukas, H. Park, S. Park, K. M. Diederichsen, J. Lim, Y. H. Cho, J. Kim, W. Kim, T. H. Han, J. Voss, A. C. Luntz and B. D. McCloskey, *ACS Catal.*, 2020, **10**, 852–863.

72 X. Lu, Y.-M. Lee, M. Sankaralingam, S. Fukuzumi and W. Nam, *Cite This Inorg. Chem*, 2020, **59**, 18010–18017.

73 S. Fukuzumi, S. Mandal, K. Mase, K. Ohkubo, H. Park, J. Benet-Buchholz, W. Nam and A. Llobet, *J. Am. Chem. Soc.*, 2012, **134**, 9906–9909.

74 X. Zhao and Y. Liu, *J. Am. Chem. Soc.*, 2021, **143**, 9423–9428.

75 J. Y. Zhang, C. Xia, H. F. Wang and C. Tang, *J. Energy Chem.*, 2022, **67**, 432–450.

76 J. M. Campos-Martin, G. Blanco-Brieva and J. L. G. Fierro, *Angew. Chemie Int. Ed.*, 2006, **45**, 6962–6984.

77 S. R. Samms, S. Wasmus and R. F. Savinell, *J. Electrochem. Soc.*, 1996, **143**, 1498–1504.

78 T. Tsuneda, *Sci. Reports 2020 101*, 2020, **10**, 1–13.

79 M. K. Debe, *Nat. 2012 4867401*, 2012, **486**, 43–51.

80 H. Claus, *Micron*, 2004, **35**, 93–96.

81 G. Gupta, V. Rajendran and P. Atanassov, *Electroanalysis*, 2004, **16**, 1182–1185.

82 M. R. Tarasevich, A. I. Yaropolov, V. A. Bogdanovskaya and S. D. Varfolomeev, *J. Electroanal. Chem.*, 1979, **104**, 393–403.

83 N. Mano, V. Soukharev and A. Heller, *J. Phys. Chem. B*, 2006, **110**, 11180–11187.

84 E. C. M. Tse, D. Schilter, D. L. Gray, T. B. Rauchfuss and A. A. Gewirth, *Inorg. Chem.*, 2014, **53**, 8505–8516.

85 H. Schweiger, E. Vayner and A. B. Anderson, *Electrochem. Solid-State Lett.*, 2005, **8**, A585.

86 H. S. Carr and D. R. Winge, *Acc. Chem. Res.*, 2003, **36**, 309–316.

87 M. R. A. Blomberg, *Biochemistry*, 2016, **55**, 489–500.

88 J. P. Collman, N. K. Devaraj, R. A. Decréau, Y. Yang, Y. L. Yan, W. Ebina, T. A. Eberspacher and C. E. D. Chidsey, *Science (80-.).*, 2007, **315**, 1565–1568.

89 S. Mukherjee, A. Mukherjee, A. Bhagi-Damodaran, M. Mukherjee, Y. Lu and A. Dey, *Nat. Commun. 2015 61*, 2015, **6**, 1–9.

90 S. Chatterjee, K. Sengupta, S. Hematian, K. D. Karlin and A. Dey, *J. Am. Chem. Soc.*, 2015, **137**, 12897–12905.

91 C. Du, Y. Gao, H. Chen, P. Li, S. Zhu, J. Wang, Q. He and W. Chen, *J. Mater. Chem. A*, 2020, **8**, 16994–17001.

92 S. Hiroto, Y. Miyake and H. Shinokubo, *Chem. Rev.*, 2017, **117**, 2910–3043.

93 Y. H. Wang, P. E. Schneider, Z. K. Goldsmith, B. Mondal, S. Hammes-Schiffer and S. S. Stahl, *ACS Cent. Sci.*, 2019, **5**, 1024–1034.

94 M. L. Pegis, B. A. McKeown, N. Kumar, K. Lang, D. J. Wasylenko, X. P. Zhang, S. Raugei and J. M. Mayer, *ACS Cent. Sci.*, 2016, **2**, 850–856.

95 M. L. Rigsby, D. J. Wasylenko, M. L. Pegis and J. M. Mayer, *J. Am. Chem. Soc.*, 2015, **137**, 4296–4299.

96 M. L. Pegis, C. F. Wise, B. Koronkiewicz and J. M. Mayer, *J. Am. Chem. Soc.*, 2017, **139**, 11000–11003.

97 M. L. Pegis, C. F. Wise, D. J. Martin and J. M. Mayer, *Oxygen Reduction by Homogeneous Molecular Catalysts and Electrocatalysts*, American Chemical Society, 2018, vol. 118.

98 J. P. Coliman, C. S. Bencosme, R. P. Kreh, R. R. Durand and F. C. Anson, *J. Am. Chem. Soc.*, 1983, **105**, 2699–2703.

99 H. Y. Liu, M. J. Weaver, C. B. Wang and C. K. Chang, *J. Electroanal. Chem. Interfacial Electrochem.*, 1983, **145**, 439–447.

100 N. Mihara, Y. Yamada, H. Takaya, Y. Kitagawa, S. Aoyama, K. Igawa, K. Tomooka and K. Tanaka, *Chem. – A Eur. J.*, 2017, **23**, 7508–7514.

101 R. R. Durand, C. S. Bencosme, J. P. Coliman and F. C. Anson, *J. Am. Chem. Soc.*, 1983, **105**, 2710–2718.

102 J. P. Collman, M. Marrocco, P. Denisevich, C. Koval and F. C. Anson, *J. Electroanal. Chem.*, 1979, **101**, 117–122.

103 D. Ramprasad, A. G. Gilicinski, T. J. Markley and G. P. Pez, *Inorg. Chem.*, 1994, **33**, 2841–2847.

104 H. Arima, M. Wada, T. Nakazono and T. Wada, *Inorg. Chem.*, 2021, **60**, 9402–9415.

105 C. Matsubara, N. Kawamoto and K. Takamura, *Analyst*, 1992, **117**, 1781–1784.

106 C. Di Giovanni, C. Gimbert-Suriñach, M. Nippe, J. Benet-Buchholz, J. R. Long, X. Sala and A. Llobet, *Chem. – A Eur. J.*, 2016, **22**, 361–369.

107 P. G. Cozzi, *Chem. Soc. Rev.*, 2004, **33**, 410–421.

108 C. Baleizão and H. Garcia, *Chem. Rev.*, 2006, **106**, 3987–4043.

109 N. S. Finney, P. J. Pospisil, S. Chang, M. Palucki, R. G. Konsler, K. B. Hansen and E. N. Jacobsen, *Angew. Chemie Int. Ed. English*, 1997, **36**, 1720–1723.

110 A. Böttcher, M. W. Grinstaff, J. A. Labinger and H. B. Gray, *J. Mol. Catal. A Chem.*, 1996, **113**, 191–200.

111 W. K. Wilmarth, S. Aranoff and M. Calvin, *J. Am. Chem. Soc.*, 1946, **68**, 2263–2266.

112 S. Fukuzumi, K. Okamoto, C. P. Gros and R. Guilard, *J. Am. Chem. Soc.*, 2004, **126**, 10441–10449.

113 L. Tahsini, H. Kotani, Y. M. Lee, J. Cho, W. Nam, K. D. Karlin and S. Fukuzumi, *Chem. - A Eur. J.*, 2012, **18**, 1084–1093.

114 C. W. Anson and S. S. Stahl, *J. Am. Chem. Soc.*, 2017, **139**, 18472–18475.

115 Y. H. Wang, M. L. Pegis, J. M. Mayer and S. S. Stahl, *J. Am. Chem. Soc.*, 2017, **139**, 16458–16461.

116 Y. H. Wang, Z. K. Goldsmith, P. E. Schneider, C. W. Anson, J. B. Gerken, S. Ghosh, S. Hammes-Schiffer and S. S. Stahl, *J. Am. Chem. Soc.*, 2018, **140**, 10890–10899.

117 A. W. Nichols, J. S. Kuehner, B. L. Huffman, P. R. Miedaner, D. A. Dickie

and C. W. Machan, *Chem. Commun.*, 2021, **57**, 516–519.

118 A. W. Nichols, E. N. Cook, Y. J. Gan, P. R. Miedaner, J. M. Dressel, D. A. Dickie, H. S. Shafaat and C. W. Machan, *J. Am. Chem. Soc.*, 2021, **143**, 13065–13073.

119 Z. Liu and F. C. Anson, *Inorg. Chem.*, 2001, **40**, 1329–1333.

120 Z. Liu and F. C. Anson, *Inorg. Chem.*, 2000, **39**, 274–280.

121 C. B. Li, P. Gong, Y. Yang and H. Y. Wang, *Catal. Letters*, 2018, **148**, 3158–3164.

122 X. Feng, Z. Xu, J. Zhao, H. A. Hansen and Q. Deng, *Int. J. Hydrogen Energy*, 2022, **47**, 27000–27011.

123 M. Yagi and M. Kaneko, *Chem. Rev.*, 2001, **101**, 21–35.

124 S. Singh, B. Phukan, C. Mukherjee and A. Verma, *RSC Adv.*, 2014, **5**, 3581–3589.

125 P. Bose, C. Mukherjee and A. K. Golder, *Inorg. Chem. Front.*, 2019, **6**, 1721–1728.

126 L. Canali, E. Cowan, H. Deleuze, C. L. Gibson and D. C. Sherrington, *Chem. Commun.*, 1998, 2561–2562.

127 P. S. Savle, M. J. Lamoreaux, J. F. Berry and R. D. Gandour, *Tetrahedron: Asymmetry*, 1998, **9**, 1843–1846.

128 J. E. Armstrong, P. M. Crossland, M. A. Frank, M. J. Van Dongen and W. R. McNamara, *Dalt. Trans.*, 2016, **45**, 5430–5433.

129 R. J. Dirisio, J. E. Armstrong, M. A. Frank, W. R. Lake and W. R. McNamara, *Dalt. Trans.*, 2017, **46**, 10418–10425.

130 M. Asahi, S. ichi Yamazaki, Y. Morimoto, S. Itoh and T. Ioroi, *Inorganica Chim. Acta*, 2018, **471**, 91–98.

131 S. Fu, Y. Liu, Y. Ding, X. Du, F. Song, R. Xiang and B. Ma, *Chem. Commun.*, 2014, **50**, 2167–2169.

132 D. S. Nesterov and O. V. Nesterova, *Catal. 2018, Vol. 8, Page 602*, 2018, **8**,

602.

133 X. Guo, N. Wang, X. Li, Z. Zhang, J. Zhao, W. Ren, S. Ding, G. Xu, J. Li, U.-P. Apfel, W. Zhang, R. Cao, X. J. Guo, N. Wang, X. L. Li, S. P. Ding, G. L. Xu, W. Zhang, R. Cao, Z. Y. Zhang, J. P. Zhao, W. J. Ren, J. F. Li and U. Apfel, *Angew. Chemie Int. Ed.*, 2020, **59**, 8941–8946.

134 T. Leblond and P. H. Dinolfo, *ACS Appl. Mater. Interfaces,* 2020, **11**, 47.

135 J. Chen, A. K. Vannucci, C. A. Mebi, N. Okumura, S. C. Borowski, M. Swenson, L. T. Lockett, D. H. Evans, R. S. Glass and D. L. Lichtenberger, *Organometallics*, 2010, **29**, 5330–5340.

136 D. Brazzolotto, M. Gennari, N. Queyriaux, T. R. Simmons, J. Pécaut, S. Demeshko, F. Meyer, M. Orio, V. Artero and C. Duboc, *Nat. Chem. 2016 811*, 2016, **8**, 1054–1060.

137 H. Chen, Z. Sun, X. Liu, A. Han and P. Du, *J. Phys. Chem. C*, 2015, **119**, 8998–9004.

138 S. Mukhopadhyay, O. Basu, A. Kar and S. K. Das, *Inorg. Chem.*, 2020, **59**, 472–483.

139 S. Fukuzumi, J. Jung, Y. Yamada, T. Kojima and W. Nam, *Chem. – An Asian J.*, 2016, **11**, 1138–1150.

140 Y. H. Wang, B. Mondal and S. S. Stahl, *ACS Catal.*, 2020, **10**, 12031–12039.

141 S. A. Hosseini-Yazdi, A. A. Khandar, M. K. Tabatabai and L. Noohinejad, *Zeitschrift für Anorg. und Allg. Chemie*, 2010, **636**, 2650–2657.

142 R. Golbedaghi, L. L. G. Justino, R. Fausto, S. Safarabadi and M. Alvandi, *Inorganica Chim. Acta*, 2019, **495**, 118941.

143 V. T. Kasumov, E. Taş, Y. Yakar, F. Köksal and R. Köşoeoğlu, *Zeitschrift fur Naturforsch. - Sect. B J. Chem. Sci.*, 2002, **57**, 495–502.

144 V. T. Kasumov and F. Köksal, *Spectrochim. Acta Part A Mol. Biomol. Spectrosc.*, 2003, **59**, 1151–1160.

145 S. R. Pour, A. Abdolmaleki and M. Dinari, *J. Mater. Sci.*, 2019, **54**, 2885–2896.

146 F. L. Jin, X. Li and S. J. Park, *J. Ind. Eng. Chem.*, 2015, **29**, 1–11.

147 K. V. Sashidhara, A. Kumar and K. Bhaskara Rao, *Tetrahedron Lett.*, 2011, **52**, 5659–5663.

148 V. Zeleňák, Z. Vargová and K. Györyová, *Spectrochim. Acta Part A Mol. Biomol. Spectrosc.*, 2007, **66**, 262–272.

149 G. E. Jackson, L. G. Scott, G. E. Jackson and L. G. Scott, , DOI:10.10520/AJA03794350_1038.

150 K. De Buysser, G. G. Herman, E. Bruneel, S. Hoste and I. Van Driessche, *Chem. Phys.*, 2005, **315**, 286–292.

151 B. Weber and F. A. Walker, *Inorg. Chem.*, 2007, **46**, 6794–6803.

152 W. F. Ruettinger, C. Campana and G. C. Dismukes, *J. Am. Chem. Soc.*, 1997, **119**, 6670–6671.

153 T. Ama, M. M. Rashid, T. Yonemura, H. Kawaguchi and T. Yasui, *Coord. Chem. Rev.*, 2000, **198**, 101–116.

154 S. M. J. Aubin, M. W. Wemple, D. M. Adams, H. L. Tsai, G. Christou and D. N. Hendrickson, *J. Am. Chem. Soc.*, 1996, **118**, 7746–7754.

155 Y. Umena, K. Kawakami, J. R. Shen and N. Kamiya, *Nat. 2011 4737345*, 2011, **473**, 55–60.

156 R. M. Cinco, A. Rompel, H. Visser, G. Aromí, G. Christou, K. Sauer, M. P. Klein and V. K. Yachandra, *Inorg. Chem.*, 1999, **38**, 5988–5998.

157 A. C. Stewart and D. S. Bendall, *Biochem. J.*, 1980, **188**, 351–361.

158 F. Evangelisti, R. Güttinger, R. Moré, S. Luber and G. R. Patzke, *J. Am. Chem. Soc.*, 2013, **135**, 18734–18737.

159 W. Hillier and T. Wydrzynski, *Biochim. Biophys. Acta - Bioenerg.*, 2001, **1503**, 197–209.

160 X. Jiang, I. Li, B. Yang, X. I.-Z. Wei, B.-W. Dong, Y. Ikao, M. A.-Y. Huang, C.-H. Tung, L.-Z. Wu,] X Jiang, J. Li, B. Yang, X.-Z. Wei, M.-Y. H. Uang, C.-H. Tung, L.-Z. Wu, B.-W. Dong and Y. Kao, *Angew. Chemie Int. Ed.*,

2018, **57**, 7850–7854.

161 G. Charles Dismukes, R. Brimblecombe, G. A. N. Felton, R. S. Pryadun, J. E. Sheats, L. Spiccia and G. F. Swiegers, *Acc. Chem. Res.*, 2009, **42**, 1935–1943.

162 H. Seino and M. Hidai, *Chem. Sci.*, 2011, **2**, 847–857.

163 Z. Asadi, L. Zarei, M. Golchin, E. Skorepova, V. Eigner and Z. Amirghofran, *Spectrochim. Acta. A. Mol. Biomol. Spectrosc.*, , DOI:10.1016/J.SAA.2019.117593.

164 S. Sagar, S. Sengupta, A. J. Mota, S. K. Chattopadhyay, A. Espinosa Ferao, E. Riviere, W. Lewis and S. Naskar, *Dalt. Trans.*, 2017, **46**, 1249–1259.

165 A. Das, S. Goswami and A. Ghosh, *New J. Chem.*, 2018, **42**, 19377–19389.

166 M. Murrie, *Chem. Soc. Rev.*, 2010, **39**, 1986–1995.

167 G. Christou, D. Gatteschi, D. N. Hendrickson and R. Sessoli, *MRS Bull.*, 2000, **25**, 66–71.

168 D. Aravena and E. Ruiz, *Dalt. Trans.*, 2020, **49**, 9916–9928.

169 E. C. Yang, W. Wernsdorfer, L. N. Zakharov, Y. Karaki, A. Yamaguchi, R. M. Isidro, G. Di Lu, S. A. Wilson, A. L. Rheingold, H. Ishimoto and D. N. Hendrickson, *Inorg. Chem.*, 2006, **45**, 529–546.

170 A. Ferguson, J. Lawrence, A. Parkin, J. Sanchez-Benitez, K. V. Kamenev, E. K. Brechin, W. Wernsdorfer, S. Hill and M. Murrie, *Dalt. Trans.*, 2008, 6409–6414.

171 I. Nemec, R. Herchel, M. Machata and Z. Trávníček, *New J. Chem.*, 2017, **41**, 11258–11267.

172 M. B. Coban, E. Gungor, H. Kara, U. Baisch and Y. Acar, *J. Mol. Struct.*, 2018, **1154**, 579–586.

173 I. Nemec, R. Herchel, M. Machata and Z. Trávníček, *New J. Chem.*, 2017, **41**, 11258–11267.

174 J. M. Campos-Martin, G. Blanco-Brieva and J. L. G. Fierro, *Angew. Chemie Int. Ed.*, 2006, **45**, 6962–6984.

175 A. C. Brezny, S. I. Johnson, S. Raugei and J. M. Mayer, *J. Am. Chem. Soc.*, 2020, **142**, 4108–4113.

176 S. Narayan Chowdhury, S. Biswas, P. Das, S. Paul and A. N. Biswas, *Cite This Inorg. Chem*, 2020, **59**, 14012–14022.

177 C. T. Carver, B. D. Matson and J. M. Mayer, *J. Am. Chem. Soc.*, 2012, **134**, 5444–5447.

178 J. Han, N. Wang, X. Li, W. Zhang and R. Cao, *J. Phys. Chem. C*, 2021, **125**, 24805–24813.

179 R. McGuire, D. K. Dogutan, T. S. Teets, J. Suntivich, Y. Shao-Horn and D. G. Nocera, *Chem. Sci.*, 2010, **1**, 411–414.

180 D. K. Dogutan, S. A. Stoian, R. McGuire, M. Schwalbe, T. S. Teets and D. G. Nocera, *J. Am. Chem. Soc.*, 2011, **133**, 131–140.

181 R. Götz, H. K. Ly, P. Wrzolek, M. Schwalbe and I. M. Weidinger, *Dalt. Trans.*, 2017, **46**, 13220–13228.

182 S. N. Child, R. Raychev, N. Moss, B. Howchen, P. N. Horton, C. C. Prior, V. S. Oganesyan and J. Fielden, *Dalt. Trans.*, 2019, **48**, 9576–9580.

183 S. F. Martin and J. A. Dodge, *Tetrahedron Lett.*, 1991, **32**, 3017–3020.

184 and Azides, J. E. Leffler, R. D. Temple, G. I. Derkach, I. N. Zhmurova, A. V Kirsanov, V. I. Shevchenko, A. S. Stepanek, H. Staudinger, J. Meyer, H. Staudinger, E. Hauser, H. Chim Ada, H. Ulrich and A. A. Sayigh, *Tetrahedron Lett.*, 1965, **591**, 841.

185 S. N. Maiti, P. Spevak and A. V. Narender Reddy, *Synth. Commun.*, 1988, **18**, 1201–1206.

186 R. G. Compton and C. E. Banks, *Underst. Voltammetry, 2nd Ed.*, 2010, 1–430.

187 N. Elgrishi, K. J. Rountree, B. D. McCarthy, E. S. Rountree, T. T. Eisenhart and J. L. Dempsey, *J. Chem. Educ.*, 2018, **95**, 197–206.

188 P. T. Kissinger and W. R. Heineman, *J. Chem. Educ.*, 1983, **60**, 702–706.

189 J. F. Rusling and S. L. Suib, *Adv. Mater.*, 1994, **6**, 922–930.

190 Z. Liu, F. Peng, H. Wang, H. Yu, W. Zheng and X. Wei, *J. Nat. Gas Chem.*, 2012, **21**, 257–264.

191 R. Becker, .

192 T. P. Silverstein, *J. Chem. Educ.*, 2012, **89**, 1159–1167.

193 P. Harding, D. J. Harding, R. Daengngern, T. Thurakitsaree, B. M. Schutte, M. J. Shaw and Y. Tantirungrotechai, *Polyhedron*, 2012, **42**, 291–301.

194 M. Lovrlc, J. J. O and J. Osteryoung, *B. E.; Angerstein-Kozlowska, H. Acc. Chem. Fies*, 1983, **55**, 73–91.

195 M. L. Pegis, J. A. S. Roberts, D. J. Wasylenko, E. A. Mader, A. M. Appel and J. M. Mayer, *Inorg. Chem.*, 2015, **54**, 11883–11888.

196 T. LeBlond and P. H. Dinolfo, *Inorg. Chem.*, 2020, **12**, 50.

197 B. Zhang, Y. Gao, Y. Hioki, M. S. Oderinde, J. X. Qiao, K. X. Rodriguez, H. J. Zhang, Y. Kawamata and P. S. Baran, *Nature*, 2022, **606**, 313–318.

198 B. Su, I. Hatay, P. Y. Ge, M. Mendez, C. Corminboeuf, Z. Samec, M. Ersoz and H. H. Girault, *Chem. Commun.*, 2010, **46**, 2918–2919.

199 A. M. J. Devoille and J. B. Love, *Dalt. Trans.*, 2011, **41**, 65–72.

200 A. Kütt, S. Tshepelevitsh, J. Saame, M. Lõkov, I. Kaljurand, S. Selberg and I. Leito, *European J. Org. Chem.*, 2021, **2021**, 1407–1419.

201 E. L. M. Miguel, P. L. Silva and J. R. Pliego, , DOI:10.1021/jp501379p.

202 A. Pui, *Croat. Chem. Acta*, 2002, **75**, 165–173.

203 Z. Li and B. H. Graham, *Methods Mol. Biol.*, 2012, **837**, 63–72.

204 F. Chen, N. Wang, H. Lei, D. Guo, H. Liu, Z. Zhang, W. Zhang, W. Lai and R. Cao, *Inorg. Chem.*, 2017, **56**, 13368–13375.

205 B. Sreenivasulu, M. Vetrichelvan, F. Zhao, S. Gao and J. J. Vittal, *Eur. J. Inorg. Chem.*, 2005, **2005**, 4635–4645.

206 Á. Kupán, J. Kaizer, G. Speier, M. Giorgi, M. Réglier and F. Pollreisz, *J.*

Inorg. Biochem., 2009, **103**, 389–395.

207 J. Reim and B. Krebs, *J. Chem. Soc. Dalt. Trans.*, 1997, 3793–3804.

208 O. V. Dolomanov, L. J. Bourhis, R. J. Gildea, J. A. K. Howard and H. Puschmann, *urn:issn:0021-8898*, 2009, **42**, 339–341.

209 G. M. Sheldrick and IUCr, *urn:issn:2053-2733*, 2015, **71**, 3–8.

210 G. M. Sheldrick and IUCr, *urn:issn:2053-2296*, 2015, **71**, 3–8.

Appendix A: ^{1}H NMR spectra of selected compounds

BFPP

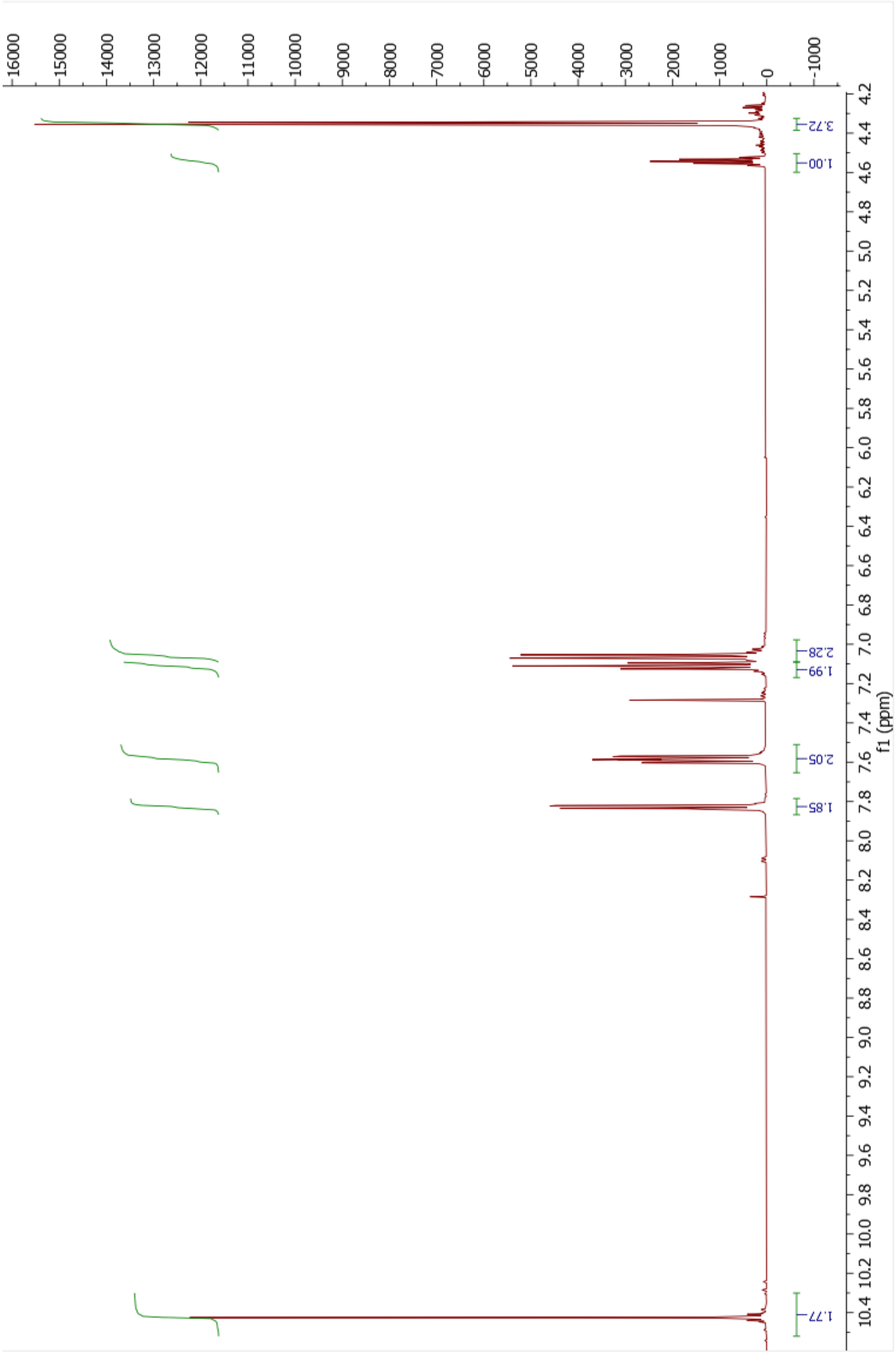

Cis,cis-3,5-ditosyloxycyclohexanol (3-1)

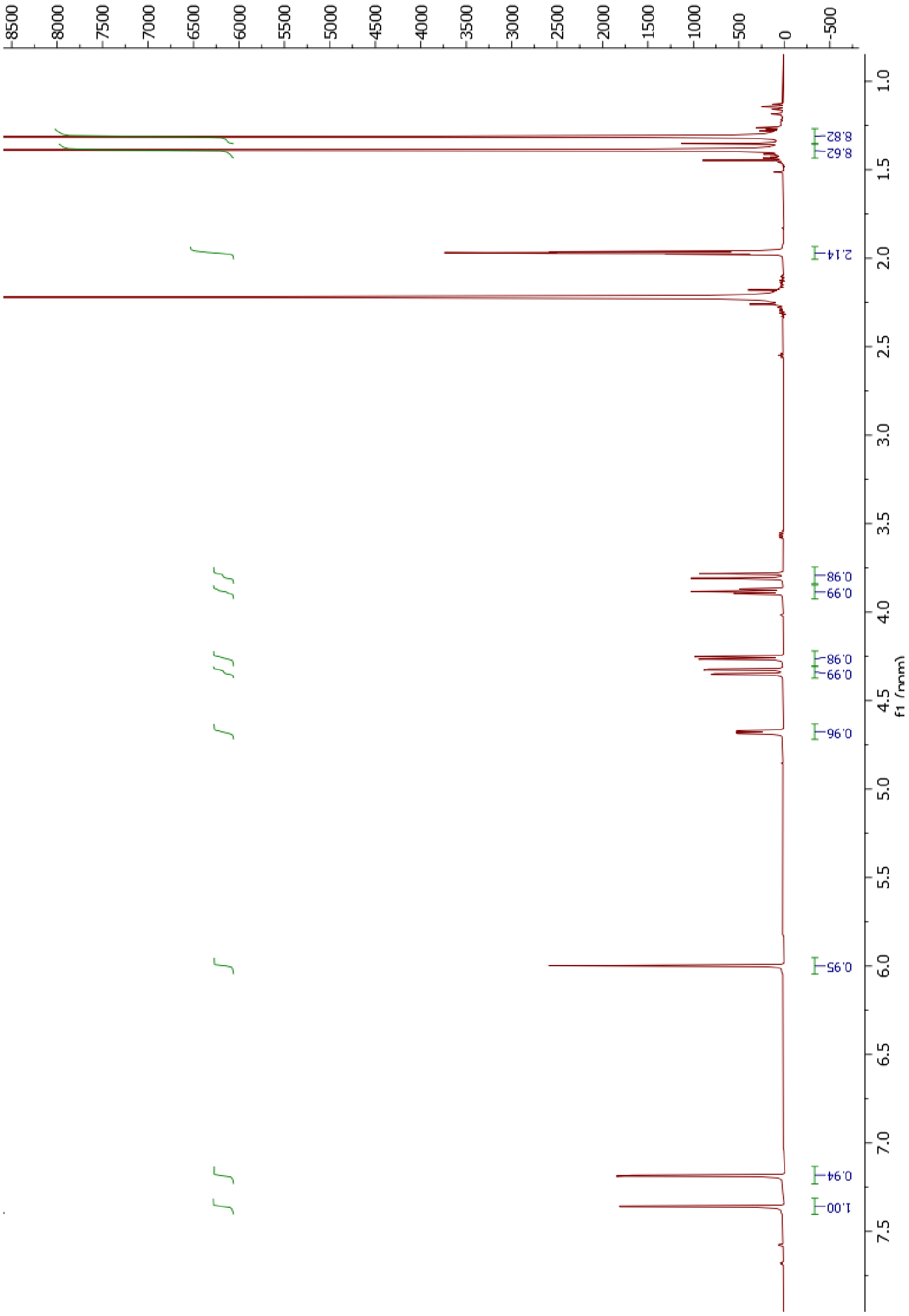

Cis,trans-diazidocyclohexanol (3-2)

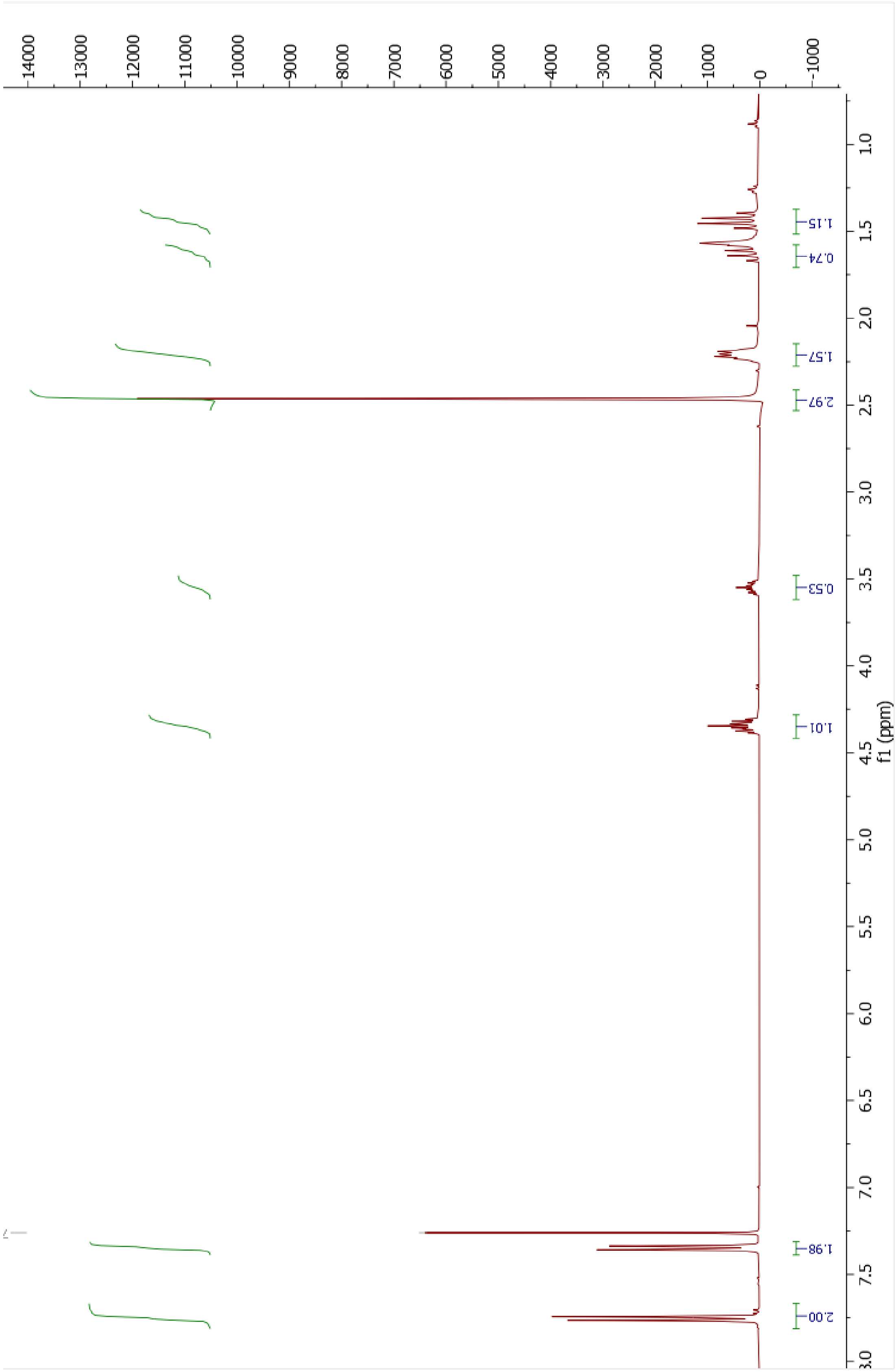

2-[(3,5-diazidocyclohexyloxy)methyl]pyridine (3-3)

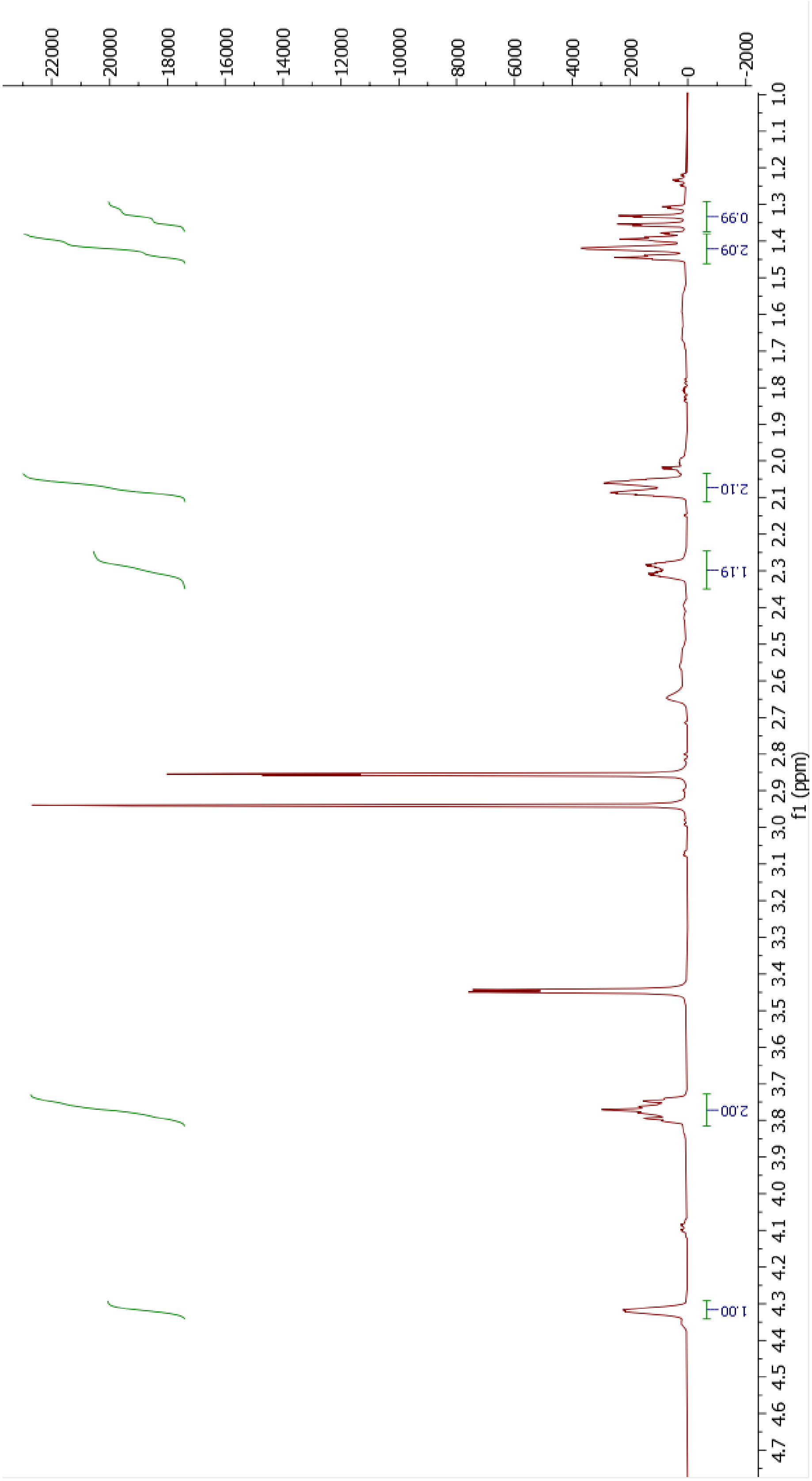

2-[(3,5-diaminocyclohexyloxy)methyl]pyridine (3-4)

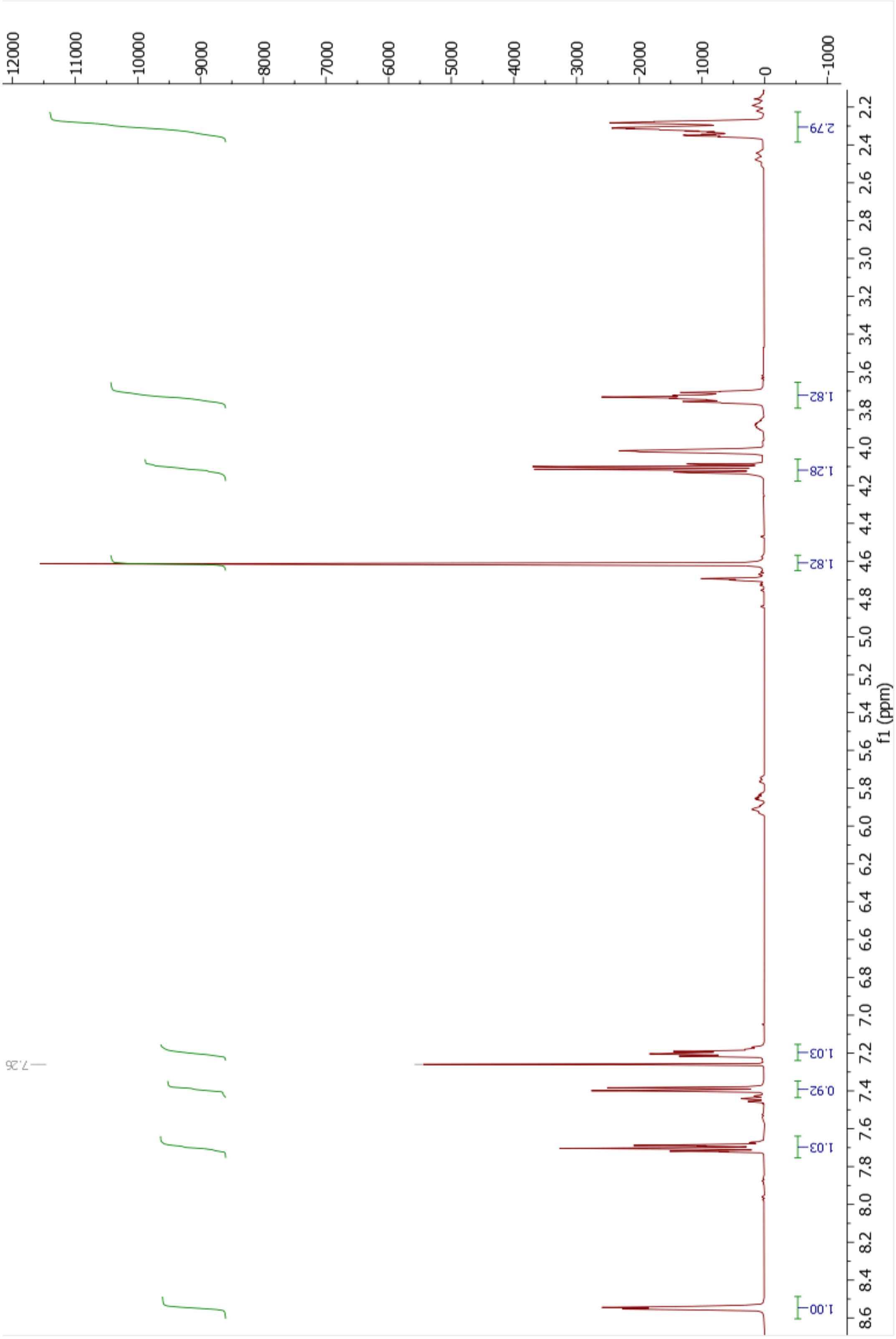

Pyridyl salcn ligand (Salcn-Py)

Appendix 2 Crystal data and structure refinement

Table A.7.4.1 Crystal data and structure refinement for trinuclear complexes

Identification code	**$Co_3L^H(OAc)_3$**	**$Co_3L^{Me}(OAc)_3$**	**$Co_3L^{tBu}Cl_3$**	**$Zn_3L^{Me}(OAc)_3$**
Empirical formula	$C_{35}Co_3N_2O_{11}$	$C_{39.5}H_{46}Co_3N_2O_{13.5}$	$C_{43}H_{53}Cl_3Co_3N_2O_8$	$C_{43}H_{50}N_4O_{13}Zn_3$
Formula weight	832.41	941.57	1009.01	1026.98
Temperature/K	99.97(12)	100.00(14)	100.00(10)	100.00(10)
Crystal system	orthorhombic	triclinic	triclinic	triclinic
Space group	Pbcn	P-1	P-1	P-1
a/Å	16.4684(7)	11.5896(4)	10.04480(10)	12.7619(5)
b/Å	13.0932(6)	13.2720(5)	11.39190(10)	12.9167(5)
c/Å	15.3826(8)	14.6041(4)	20.7525(2)	12.9920(5)
α/°	90	102.365(3)	74.9920(10)	83.678(4)
β/°	90	105.032(3)	76.9610(10)	89.752(3)
γ/°	90	93.290(3)	78.4360(10)	89.047(3)
Volume/Å^3	3316.9(3)	2103.93(13)	2208.95(4)	2128.30(14)
Z	4	2	2	2
ρ_{calc}g/cm^3	1.667	1.486	1.517	1.603
μ/mm^{-1}	12.187	9.718	10.829	2.576
F(000)	1696	972	1042	1060
Crystal size/mm^3	0.02 × 0.02 × 0.02	0.15 × 0.15 × 0.015	0.12 × 0.1 × 0.08	0.06 × 0.05 × 0.09
Radiation	Cu Kα (λ = 1.54184)	Cu Kα (λ = 1.54184)	Cu Kα (λ = 1.54184)	Cu Kα (λ = 1.54184)
2Θ range for data collection/°	8.628 to 155.42	6.452 to 158.382	8.128 to 154.568	6.886 to 153.98
Index ranges	$-10 \le h \le 20$, $-16 \le k \le 16$, $-19 \le l \le 18$	$-14 \le h \le 13$, $-16 \le k \le 16$, $-18 \le l \le 17$	$-12 \le h \le 12$, $-14 \le k \le 14$, $-25 \le l \le 24$	$-14 \le h \le 15$, $-16 \le k \le 16$, $-15 \le l \le 12$
Reflections collected	13678	24333	59490	8663
Independent reflections	3378 [R_{int} = 0.0526, R_{sigma} = 0.0430]	8246 [R_{int} = 0.0790, R_{sigma} = 0.0700]	9050 [R_{int} = 0.0532, R_{sigma} = 0.0290]	5885 [R_{int} = 0.0339, R_{sigma} = 0.0544]
Data/restraints/parameters	3378/0/245	8246/3/545	9050/4/553	5885/0/577
Goodness-of-fit on F^2	1.02	1.078	1.072	1.1
Final R indexes [I>=2σ (I)]	R_1 = 0.0570, wR_2 = 0.1502	R_1 = 0.0783, wR_2 = 0.2146	R_1 = 0.0375, wR_2 = 0.0995	R_1 = 0.0465, wR_2 = 0.1387
Final R indexes [all data]	R_1 = 0.0737, wR_2 = 0.1635	R_1 = 0.0915, wR_2 = 0.2298	R_1 = 0.0400, wR_2 = 0.1009	R_1 = 0.0518, wR_2 = 0.1423
Largest diff. peak/hole / e Å^{-3}	1.23/-0.61	1.43/-1.22	0.75/-0.60	0.65/-0.57

Table A.7.4.2 Crystal data and structure refinement for tetranuclear complexes

Identification code	**$Co_4L^{Me}{}_2(BF_4)_2$**	**$Co_4L^{OMe}{}_2(PF_6)_2$**	**$Co_4L^{H}{}_2(PF_6)_2$**	**$Ni_4L^{Me}{}_2(PF_6)_2$**
Empirical formula	$C_{68}H_{76}B_2Co_4F_8N_4O_{16}$	$C_{64}H_{59}B_2Co_4F_8N_4O_{16}$	$C_{70}H_{64}Cl_2Co_4N_{10}O_{18}$	$C_{68}H_{72}Cl_4F_{12.54}N_4Ni_4O_{14}P_2$
Formula weight	1614.66	1549.49	1639.93	229.93
Temperature/K	100.15	100.15	99.99(13)	100.15
Crystal system	triclinic	monoclinic	triclinic	monoclinic
Space group	P-1	$P2_1/n$	P-1	$P2_1/n$
a/Å	12.7253(2)	12.6615(3)	10.84530(10)	13.40000(10)
b/Å	13.2722(2)	13.6404(2)	12.9074(2)	11.65970(10)
c/Å	22.5229(4)	18.8519(4)	13.6533(2)	23.9114(3)
α/°	97.2080(10)	90	79.4380(10)	90
β/°	97.696(2)	103.053(2)	82.4040(10)	96.0070(10)
γ/°	108.398(2)	90	68.1340(10)	90
Volume/Å^3	3519.64(11)	3171.75(11)	1739.42(4)	3715.40(6)
Z	2	2	1	16
ρ_{calc}g/cm^3	1.524	1.622	1.566	1.644
μ/mm^{-1}	1.017	1.125	8.717	1.282
F(000)	1660	1578	840	1873
Crystal size/mm^3	0.31 × 0.27 × 0.25	0.12 × 0.18 × 0.19	0.2 × 0.2 × 0.18	0.18 × 0.21 × 0.23
Radiation	MoKα (λ = 0.71073)	MoKα (λ = 0.71073)	Cu Kα (λ = 1.54184)	MoKα (λ = 0.71073)
2Θ range for data collection/°	3.71 to 62.138	4.374 to 61.692	6.602 to 154.096	3.89 to 61.988
Index ranges	$-18 \le h \le 17$, $-18 \le k \le 16$, $-29 \le l \le 30$	$-16 \le h \le 15$, $-19 \le k \le 17$, $-23 \le l \le 25$	$-13 \le h \le 13$, $-15 \le k \le 16$, $-17 \le l \le 17$	$-19 \le h \le 17$, $-16 \le k \le 15$, $-33 \le l \le 34$
Reflections collected	57745	33507	39401	107324
Independent reflections	18079 [R_{int} = 0.0449, R_{sigma} = 0.0472]	8042 [R_{int} = 0.0302, R_{sigma} = 0.0259]	7117 [R_{int} = 0.0358, R_{sigma} = 0.0225]	10617 [R_{int} = 0.0406, R_{sigma} = 0.0220]
Data/restraints/parameters	18079/18/957	8042/3/469	7117/38/483	10617/39/533
Goodness-of-fit on F^2	1.04	1.048	1.031	1.702
Final R indexes [I>=2σ (I)]	R_1 = 0.0486, wR_2 = 0.1283	R_1 = 0.0457, wR_2 = 0.1228	R_1 = 0.0327, wR_2 = 0.0872	R_1 = 0.0935, wR_2 = 0.2569
Final R indexes [all data]	R_1 = 0.0681, wR_2 = 0.1377	R_1 = 0.0545, wR_2 = 0.1281	R_1 = 0.0348, wR_2 = 0.0885	R_1 = 0.1001, wR_2 = 0.2609
Largest diff. peak/hole / e Å^{-3}	1.56/-0.54	1.58/-0.84	0.42/-0.42	7.81/-7.03

Table A.7.4.3 Crystal data and structure refinement for CuSalcn-py

Identification code	**CuSalcn-py**
Empirical formula	$C_{42.5}H_{58}CuN_3O_{3.5}$
Formula weight	730.46
Temperature/K	100.00(10)
Crystal system	triclinic
Space group	P-1
a/Å	12.2206(4)
b/Å	12.67530(10)
c/Å	14.4424(2)
α/°	112.0610(10)
β/°	107.766(3)
γ/°	93.322(2)
Volume/Å^3	1936.35(8)
Z	2
ρ_{calc}g/cm^3	1.253
μ/mm^{-1}	1.127
F(000)	782
Crystal size/mm^3	0.25 × 0.15 × 0.15
Radiation	Cu Kα (λ = 1.54184)
2Θ range for data collection/°	7.06 to 154.162
Index ranges	$-15 \leq h \leq 15$, $-15 \leq k \leq 15$, $-18 \leq l \leq 18$
Reflections collected	36660
Independent reflections	36660 [R_{int} = ?, R_{sigma} = 0.0554]
Data/restraints/parameters	36660/16/523
Goodness-of-fit on F^2	1.088
Final R indexes [I>=2σ (I)]	R_1 = 0.0637, wR_2 = 0.1911
Final R indexes [all data]	R_1 = 0.0736, wR_2 = 0.1955
Largest diff. peak/hole / e Å^{-3}	0.97/-0.72

Appendix 3 Additional structural data

Table A.4 Bond angles relating to the coordination environment of $Co_3L^{Me}(OAc)_3$

Atom	Atom	Atom	Angle/°
O4	Co2	O7	129.21(11)
O1	Co2	O4	151.27(12)
O1	Co2	O7	79.02(12)
O1	Co2	O6	115.45(11)
O1	Co2	N1	80.69(13)
O3	Co2	O4	77.82(11)
O3	Co2	O1	105.79(11)
O3	Co2	O7	80.70(12)
O3	Co2	O6	112.07(13)
O3	Co2	N1	146.43(13)
O6	Co2	O4	88.01(11)
O6	Co2	O7	58.95(11)
N1	Co2	O4	81.66(12)
N1	Co2	O7	132.54(12)
N1	Co2	O6	93.32(13)
O3	Co3	O2	104.73(12)
O3	Co3	O5	75.45(11)
O3	Co3	N2	134.49(13)
O3	Co3	O8	112.16(13)
O2	Co3	O5	149.87(12)
O2	Co3	N2	81.47(13)
N2	Co3	O5	78.08(12)
O8	Co3	O2	122.60(13)
O8	Co3	O5	83.02(12)
O8	Co3	N2	100.43(14)
O1	Co1	O7	82.00(12)
O1	Co1	O10	91.92(13)
O1	Co1	O11	102.74(13)
O1	Co1	O12	167.73(13)
O2	Co1	O1	87.91(12)
O2	Co1	O7	84.74(11)
O2	Co1	O10	176.90(12)
O2	Co1	O11	115.43(12)
O2	Co1	O12	88.00(14)
O7	Co1	O11	159.20(12)
O10	Co1	O7	98.30(12)
O10	Co1	O11	61.59(12)
O12	Co1	O7	86.11(14)
O12	Co1	O10	92.78(15)
O12	Co1	O11	89.46(14)

Co2	O1	Co1	104.30(13)
Co3	O3	Co2	118.47(14)
Co3	O2	Co1	116.97(14)
Co1	O7	Co2	94.48(12)

Table A.5 Bond angles relating to the coordination environment of Co$_3$L^{tBu}Cl$_3$

Atom	Atom	Atom	Angle/°
O3	Co1	Cl3	108.13(5)
O3	Co1	O5	155.91(6)
O2	Co1	Cl3	118.42(5)
O2	Co1	O3	103.68(6)
O2	Co1	O5	78.14(6)
O2	Co1	N2	127.91(7)
O5	Co1	Cl3	91.23(4)
N2	Co1	Cl3	108.21(5)
N2	Co1	O3	81.34(6)
N2	Co1	O5	79.00(6)
O2	Co2	Cl2	111.47(5)
O2	Co2	O1	105.03(6)
O2	Co2	O4	79.88(6)
O2	Co2	N1	140.52(7)
O1	Co2	Cl2	105.75(5)
O1	Co2	O4	158.20(6)
O1	Co2	N1	81.83(6)
O4	Co2	Cl2	91.59(4)
N1	Co2	Cl2	103.45(5)
N1	Co2	O4	81.35(6)
O3	Co3	Cl1	121.45(5)
O3	Co3	O1	101.26(7)
O3	Co3	O6	101.01(7)
O1	Co3	Cl1	121.67(5)
O1	Co3	O6	95.36(7)
O6	Co3	Cl1	111.38(5)
Co3	O3	Co1	119.34(7)
Co2	O2	Co1	130.63(7)
Co3	O1	Co2	117.29(7)

Table A.6 Bond angles relating to the coordination environment of Co$_3$L^{H}(OAc)$_3$

Atom	Atom	Atom	Angle/°
O3	Co1	O3^{1}	60.41(15)
O1^{1}	Co1	O3	96.49(11)
O1	Co1	O3	156.42(12)
O1	Co1	O3^{1}	96.50(11)
O1	Co1	O1^{1}	106.88(17)
O1	Co1	O6^{1}	85.46(11)
O1^{1}	Co1	O6^{1}	90.61(11)
O1^{1}	Co1	O6	85.46(11)
O1	Co1	O6	90.61(11)

O6	Co1	O3^1	91.33(11)
O6	Co1	O3	94.38(11)
O6^1	Co1	O3	91.33(11)
O6^1	Co1	O3^1	94.38(11)
O6	Co1	O6^1	173.39(15)
O1^1	Co2	N1^1	82.30(12)
O1^1	Co2	O4^1	164.11(13)
O5	Co2	O1^1	102.97(12)
O5	Co2	N1^1	132.60(14)
O5	Co2	O4^1	92.18(14)
O2	Co2	O1^1	100.72(13)
O2	Co2	O5	112.86(9)
O2	Co2	N1^1	112.20(11)
O2	Co2	O4^1	77.31(14)
N1^1	Co2	O4^1	83.91(12)
Co2^1	O1	Co1	113.30(14)

Table A.7 Bond angles relating to the coordination environment of Co$_4$L$^{Me}_2$(BF$_4$)$_2$

Atom	Atom	Atom	Angle/°
O4	Co2	O3	75.09(6)
O4	Co2	O11	159.28(6)
O4	Co2	N3	80.05(7)
O1	Co2	O4	101.31(6)
O1	Co2	O3	79.22(6)
O1	Co2	O5	161.70(7)
O1	Co2	O11	76.81(6)
O1	Co2	N3	98.67(7)
O3	Co2	O11	123.91(6)
O5	Co2	O4	88.43(6)
O5	Co2	O3	88.54(6)
O5	Co2	O11	99.43(6)
O5	Co2	N3	98.25(7)
N3	Co2	O3	154.03(7)
N3	Co2	O11	79.86(6)
O2	Co1	O3	83.45(6)
O2	Co1	O7	97.94(7)
O2	Co1	O10	163.32(7)
O1	Co1	O2	113.34(6)
O1	Co1	O3	80.17(6)
O1	Co1	O7	85.94(7)
O1	Co1	O10	80.41(6)
O1	Co1	N4	165.12(7)
O7	Co1	O3	165.35(7)
O7	Co1	O10	92.26(7)
O10	Co1	O3	90.02(6)
N4	Co1	O2	81.54(7)

N4	Co1	O3	102.01(7)
N4	Co1	O7	92.60(8)
N4	Co1	O10	84.86(7)
O4	Co3	O12	121.54(6)
O2	Co3	O4	90.26(6)
O2	Co3	O3	87.10(6)
O2	Co3	O12	101.13(6)
O2	Co3	N2	96.48(7)
O3	Co3	O4	76.66(6)
O3	Co3	O12	159.53(6)
O3	Co3	N2	80.64(7)
O6	Co3	O4	79.42(6)
O6	Co3	O2	165.90(7)
O6	Co3	O3	99.67(6)
O6	Co3	O12	76.69(6)
O6	Co3	N2	96.82(7)
N2	Co3	O4	155.94(7)
N2	Co3	O12	79.83(6)
O5	Co4	O4	83.47(6)
O5	Co4	O9	161.73(7)
O5	Co4	O8	96.19(7)
O5	Co4	N1	81.31(7)
O6	Co4	O4	78.43(6)
O6	Co4	O5	114.17(6)
O6	Co4	O9	80.52(6)
O6	Co4	O8	87.61(7)
O6	Co4	N1	164.46(7)
O9	Co4	O4	89.33(6)
O8	Co4	O4	164.43(6)
O8	Co4	O9	95.21(7)
N1	Co4	O4	103.02(7)
N1	Co4	O9	84.01(7)
N1	Co4	O8	92.27(7)
Co2	O4	Co3	105.04(7)
Co2	O4	Co4	89.55(6)
Co3	O4	Co4	91.70(6)
Co3	O2	Co1	97.82(7)
Co1	O1	Co2	106.68(7)
Co1	O3	Co2	90.69(6)
Co3	O3	Co2	103.21(6)
Co3	O3	Co1	91.62(6)
Co2	O5	Co4	98.45(7)
Co4	O6	Co3	106.80(7)

Table A.8 Bond lengths relating to the coordination environment of $Co_4L^{OMe}{}_2(BF_4)_2$

Atom	Atom	Length/Å

Co2	O1	1.9870(17)
Co2	O6^1	2.2355(16)
Co2	O6	2.0740(17)
Co2	O3	2.2604(18)
Co2	O2^1	2.0257(17)
Co2	N2	2.1130(19)
Co1	O1	1.9723(17)
Co1	O6^1	2.2255(16)
Co1	O2	2.0441(18)
Co1	O4	2.1822(18)
Co1	O5	2.161(2)
Co1	N1	2.060(2)

Table A.9 Bond angles relating to the coordination environment of $Co_4L^{OMe}_2(BF_4)_2$

Atom	Atom	Atom	Angle/°
O1	Co2	O6	100.10(7)
O1	Co2	O6^1	78.84(6)
O1	Co2	O3	77.52(7)
O1	Co2	O2^1	162.13(7)
O1	Co2	N2	99.35(7)
O6	Co2	O6^1	75.88(7)
O6	Co2	O3	160.61(6)
O6^1	Co2	O3	121.73(6)
O6	Co2	N2	80.39(7)
O2^1	Co2	O6	88.92(7)
O2^1	Co2	O6^1	88.59(7)
O2^1	Co2	O3	98.93(7)
O2^1	Co2	N2	97.33(8)
N2	Co2	O6^1	155.43(7)
N2	Co2	O3	81.03(7)
O1	Co1	O6^1	79.39(6)
O1	Co1	O2	113.59(7)
O1	Co1	O4	80.81(7)
O1	Co1	O5	89.99(8)
O1	Co1	N1	164.97(8)
O2	Co1	O6^1	84.42(6)
O2	Co1	O4	163.51(7)
O2	Co1	O5	93.48(8)
O2	Co1	N1	81.36(8)
O4	Co1	O6^1	90.79(6)
O5	Co1	O6^1	167.22(7)
O5	Co1	O4	94.53(8)
N1	Co1	O6^1	104.63(7)
N1	Co1	O4	84.63(8)
N1	Co1	O5	87.46(8)
Co1	O1	Co2	107.03(8)
Co2	O6	Co2^1	104.12(7)
Co2	O6	Co1^1	89.91(6)
Co1^1	O6	Co2^1	91.06(6)
Co2^1	O2	Co1	96.65(7)

Table A.10 Bond lengths relating to the coordination environment of $Co_4L^{H}_2(ClO_4)_2$

Atom	Atom	Length/Å
Co2	O1	1.9909(12)
Co2	O5^1	2.2080(12)
Co2	O5	2.0955(13)
Co2	O2^1	2.0196(13)
Co2	O3	2.2675(13)
Co2	N2	2.0990(15)
Co1	O1	1.9590(12)
Co1	O5^1	2.2271(12)
Co1	O2	2.0439(13)
Co1	O4	2.1813(13)
Co1	N1	2.0480(15)
Co1	N3	2.1912(15)

Table A.11 Bond angles relating to the coordination environment of $Co_4L^{H}_2(ClO_4)_2$

Atom	Atom	Atom	Angle/°
O1	Co2	O5	100.22(5)
O1	Co2	O5^1	78.86(5)
O1	Co2	O2^1	163.71(5)
O1	Co2	O3	77.04(5)
O1	Co2	N2	97.52(5)
O5	Co2	O5^1	75.62(5)
O5	Co2	O3	160.08(5)
O5^1	Co2	O3	122.30(5)
O5	Co2	N2	79.89(5)
O2^1	Co2	O5	87.73(5)
O2^1	Co2	O5^1	89.52(5)
O2^1	Co2	O3	100.19(5)
O2^1	Co2	N2	97.87(5)
N2	Co2	O5^1	154.10(5)
N2	Co2	O3	80.93(5)
O1	Co1	O5^1	79.05(5)
O1	Co1	O2	113.90(5)
O1	Co1	O4	80.85(5)
O1	Co1	N1	164.73(6)
O1	Co1	N3	93.73(6)
O2	Co1	O5^1	83.67(5)
O2	Co1	O4	162.87(5)
O2	Co1	N1	81.37(6)
O2	Co1	N3	91.76(6)
O4	Co1	O5^1	91.09(5)
O4	Co1	N3	96.05(6)
N1	Co1	O5^1	103.36(5)
N1	Co1	O4	84.01(6)
N1	Co1	N3	85.83(6)
N3	Co1	O5^1	168.94(5)
Co1	O1	Co2	107.12(6)
Co2	O5	Co2^1	104.38(5)
Co2	O5	Co1^1	90.44(5)

Co2^1	O5	Co1^1	91.53(5)
Co2^1	O2	Co1	98.12(5)

Table A.12 Bond angles relating to the coordination environment of $Zn_3L^{Me}(OAc)_3$

Atom	Atom	Atom	Angle/°
O3	Zn3	O4	76.38(11)
O3	Zn3	O2	92.20(12)
O3	Zn3	N1	132.45(13)
O6	Zn3	O3	98.64(13)
O6	Zn3	O4	90.30(14)
O6	Zn3	O2	127.22(14)
O6	Zn3	N1	121.90(13)
O2	Zn3	O4	142.27(13)
O2	Zn3	N1	82.70(14)
N1	Zn3	O4	79.45(13)
O3	Zn2	O1	103.99(12)
O3	Zn2	O5	78.10(12)
O3	Zn2	O9	107.52(13)
O3	Zn2	N2	138.99(14)
O1	Zn2	O5	160.91(12)
O1	Zn2	N2	83.06(14)
O9	Zn2	O1	99.88(13)
O9	Zn2	O5	97.46(13)
O9	Zn2	N2	110.95(13)
N2	Zn2	O5	83.35(14)
O1	Zn1	O8	91.32(12)
O1	Zn1	O10	103.42(13)
O1	Zn1	O11	139.61(14)
O8	Zn1	O10	150.98(14)
O2	Zn1	O1	99.62(13)
O2	Zn1	O8	104.60(14)
O2	Zn1	O10	97.49(13)
O2	Zn1	O11	118.45(14)
O11	Zn1	O8	91.65(13)
O11	Zn1	O10	60.97(13)
Zn2	O3	Zn3	108.31(14)
Zn1	O1	Zn2	112.04(14)

Table A.13 Bond angles relating to the coordination environment of NiL^{Me}

O1	Ni1	O4	94.03(17)
O1	Ni1	O3	167.24(16)
O1	Ni1	N2	95.39(16)
O2	Ni1	O4	163.59(17)
O2	Ni1	O1	100.24(18)
O2	Ni1	O3	87.18(17)
O2	Ni1	N1	98.3(2)
O2	Ni1	N2	84.2(2)
O3	Ni1	O4	80.34(16)

N1	Ni1	O4	91.29(18)
N1	Ni1	O1	83.40(17)
N1	Ni1	O3	85.27(16)
N1	Ni1	N2	177.4(2)
N2	Ni1	O4	86.47(18)
N2	Ni1	O3	95.68(16)

Table A.14 Bond angles relating to the coordination environment of $Ni_4L^{Me}_2(PF_6)_2$

Atom	Atom	Atom	Angle/°
O2	Ni1	O4^1	79.91(7)
O2	Ni1	O1	106.16(8)
O2	Ni1	O3	83.87(8)
O2	Ni1	O6	85.68(8)
O2	Ni1	N1	170.61(9)
O1	Ni1	O4^1	83.74(7)
O1	Ni1	O3	168.57(8)
O1	Ni1	O6	95.37(8)
O3	Ni1	O4^1	92.85(7)
O3	Ni1	O6	90.77(8)
O6	Ni1	O4^1	164.67(8)
N1	Ni1	O4^1	103.25(8)
N1	Ni1	O1	83.07(8)
N1	Ni1	O3	87.13(8)
N1	Ni1	O6	91.80(9)
O2	Ni2	O4	99.50(8)
O2	Ni2	O4^1	79.54(7)
O2	Ni2	O1^1	165.54(8)
O2	Ni2	O5	77.93(7)
O2	Ni2	N2	95.29(8)
O4	Ni2	O4^1	77.76(8)
O4	Ni2	O5	160.68(7)
O4^1	Ni2	O5	119.93(7)
O1^1	Ni2	O4^1	89.08(7)
O1^1	Ni2	O4	86.61(7)
O1^1	Ni2	O5	100.53(7)
O1^1	Ni2	N2	98.62(8)
N2	Ni2	O4	80.97(8)
N2	Ni2	O4^1	156.90(8)
N2	Ni2	O5	80.22(8)
Ni1	O2	Ni2	105.13(9)
Ni2^1	O4	Ni1^1	93.64(7)
Ni2	O4	Ni1^1	91.86(7)
Ni2	O4	Ni2^1	102.24(8)
Ni2^1	O1	Ni1	97.45(8)

Table A.14 Bond lengths relating to the coordination environment of CuSalcn-Py

Atom	Atom	Length/Å
Cu1	O1	1.932(4)
Cu1	O2	1.921(4)
Cu1	N1	1.985(5)
Cu1	N2	1.986(5)

Table A.15 Bond angles relating to the coordination environment of CuSalcn-Py

Atom	Atom	Atom	Angle/°
O1	Cu1	N1	91.69(17)
O1	Cu1	N2	164.6(2)
O2	Cu1	O1	84.91(16)
O2	Cu1	N1	161.2(2)
O2	Cu1	N2	92.35(17)
N1	Cu1	N2	95.57(19)